A Dual/High-Voltage Automotive Electrical Power System with Superior Transient Performance

by

Vahe Caliskan

B.S., University of Illinois at Chicago (1990)
M.S., University of Illinois at Chicago (1993)

Submitted to the Department of Electrical Engineering and Computer Science
in partial fulfillment of the requirements for the degree of

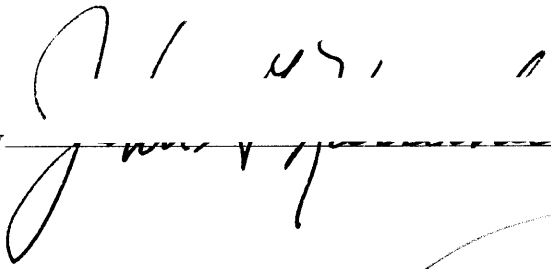## Doctor of Science in Electrical Engineering

at the

MASSACHUSETTS INSTITUTE OF TECHNOLOGY

September 2000

Author_____
Department of Electrical Engineering and Computer Science
September 7, 2000

Certified by_____
John G. Kassakian
Professor of Electrical Engineering
Thesis Supervisor

Accepted by_____
Arthur C. Smith
Chairman, Departmental Committee on Graduate Students

A Dual/High-Voltage Automotive Electrical Power System with Superior Transient Performance

by

Vahe Caliskan

Abstract

Today's automotive electrical power system is based on an engine-driven alternator regulated at 14 V which charges a 12 V battery and delivers power to the loads. Installed electrical power is growing rapidly with model year, and future electrical power requirements are expected to exceed the capability of the present 14 V system by about 2005. A high/dual-voltage electrical system is necessary to meet these requirements.

A new alternator system which substantially improves the present Lundell alternator design is proposed. This new system can double the output power and greatly improve efficiency without the need to rewind the machine. Inherent load-dump transient suppression and jump-start charging features are also achieved. The attributes of this novel system have been experimentally demonstrated.

The main goal of this thesis is to investigate and develop analytical system and subsystem models for dual/high-voltage automotive electrical systems. Detailed time-domain and simplified averaged models for synchronous machines and three-phase rectifiers with constant-voltage loads are developed. A load-matching technique based on a switched-mode rectifier is introduced and used in conjunction with the developed machine/rectifier models to design the new high-power, high-efficiency alternator system.

Analytical models for two dual-voltage systems, one based on interleaved dc/dc converters and the other on a dual-stator Lundell alternator, are developed and used to investigate their characteristics. The analytical models for the dc/dc converter system are used in the design of a prototype which experimentally demonstrates the high performance features of the system while verifying the analytical results. A comparison of the characteristics of dual/high-voltage architectures is presented and it is shown that the load-matching technique can be used in a number of dual-voltage systems to improve performance. An attractive complete dual-voltage system, which incorporates the new alternator and a dc/dc converter, is introduced.

Thesis Supervisor: John G. Kassakian
Title: Professor of Electrical Engineering

Dedication

To My Parents:

Varujan and Yeranuhi

Acknowledgements

As I near the completion of my graduate work, I have had some time to reflect on my six years here at MIT and the total of fourteen years I spent in college. It is hard for me to believe that I have spent an entire decade in graduate school! The extended amount of time that I have spent in school would not have been as fruitful were it not for the individuals who I have interacted with. In the little amount of space that I have here, I would like to thank the many people without whom this work would not be complete.

First and foremost I would like to thank my academic and thesis advisor Professor John Kassakian for his guidance of my graduate work. I feel very fortunate and privileged to have had the opportunity to work with John and have gained a great deal of insight into engineering from my experience. This has been a result of not only my academic work but also from our interaction with the automotive industry on an international level.

I would also like to thank the members of my thesis committee: Professors Jeff Lang and Bernie Lesieutre of MIT and Professor Thomas Jahns of University of Wisconsin–Madison. The comments of the thesis committee have greatly improved the presentation of the research results. In addition to my committee, Dr. Thomas Keim and Dr. David Perreault have had a tremendous impact on the material presented in the thesis. Dave has been the driving force behind the practical implementation and experimental verification of much of the work in this thesis.

In addition to the work presented here, I have also had the opportunity to do research outside my thesis area. For this I must thank Professor George Verghese of MIT and Professor Aleksandar Stankovic of Northeastern University both of whom also served on my Area Exam committee.

I want to thank my past and present colleagues in Laboratory for Electromagnetic and Electronic Systems many of whom have had to put up with me and my unique brand of humor. Over the years, I have used my "humor" to try to lighten-up our working environment and daily occupational pressures which can be overwhelming at times. Here's a list of my colleagues (I hope I am not forgetting anyone!), in alphabetical order, in some cases with a nickname followed by a signature quote: Khurram Afridi, Chalee Asavathiratham, Kojo Ofori-Atta, Babak Ayazifar, Mary Jane Boyd, Andre Brown, Jamie "Hoss" Byrum ("Hey Fred!"), Woo Sok Chang, Albert "Alfred" Chow, Tim "$\sqrt{3}$" Denison, James "Late Night Player" Geraci, Ankur Garg, Jesko Hagee, James "Per Unit" Hockenberry, Ilija Jergovic, Irene Kuo, Ian Lorilla, Ed Lovelace, Kathy Millis, Jama "Total Package" Mohamed ("There will be a small charge"), John Ofori, Joshua "Phineas" Phinney, Brian Perreault, John Rodriguez, Steve Nagle, Amy Ng, Tim "Fred" Neugebauer ("General Gau's Chicken"), Ernst Scholtz ("I know Tom Jones"), Steve Shaw, Isaac Trefz ("Hey all youse, let's rage!"), Feng Zhang, Mingjuan "Flo" Zhu ("Vahe, I have a question for you").

Contents

List of Figures

List of Tables

In this introductory chapter, a brief motivation for the problems to be investigated is presented. The overall goals and contributions of the thesis are outlined. An organization of the thesis document is also presented.

1.1 Motivation

The demand for increased electrical power and fuel efficiency improvements in automobiles have resulted in growing interest in alternative electrical system architectures. The purpose of this thesis is to investigate a promising set of architectures, providing the operational characteristics and identifying the limitations of their power supply. "Power supply" refers to the electrical power generation subsystem of a vehicle's electrical system. It includes such components as the generator, batteries, rectifiers and converters.

The present automotive electrical system is based on an engine driven alternator which charges a 12 V battery and delivers power to the loads. The typical distribution voltage is around 14 V and is constrained by the charging voltage of a lead-acid battery. As a result, it is more appropriate to refer to today's automotive electrical power system as a 14 V system rather than a 12 V system. Presently, the average electrical power demand in vehicles is about 800 W [1]. With the introduction of loads such as electromechanical engine valves, electric power steering, water pump and engine cooling fan, the average power demand could increase to 2.5 kW by the year 2005 [1, 2]. In the past, the increase in electrical power requirements has been met by an appropriate increase in the power rating of the alternator and the charge capacity of the battery. This approach will not be feasible due to a decrease of available space in engine compartments and an increase in the fuel efficiency requirements. Further complicating the problem will be the introduction of advanced loads with high peak power requirements such as active suspension (12 kW) and heated windshield (2.5 kW). These loads cannot be powered effectively with the present 14 V system. In fact, these high peak power loads, as well as some others, could benefit from a power supply architecture with a higher distribution voltage. However, simply changing the present 14 V system

to a higher voltage is not practical in the short term since there is a large infrastructure already in place that supports and services the 14 V components [1]. The demand for higher power while keeping the electrical system compatible with the 14 V infrastructure leads one to investigate dual-voltage architectures. Dual-voltage architectures refer to automotive electrical systems which combine today's 14 V bus with a second bus operating at a voltage of 42 V (connected to a 36 V lead-acid battery). Nevertheless, a power supply architecture with a single high-voltage bus will be the most effective option in the long term while the dual-voltage architectures will be necessary for a smooth transition to the single-voltage system.

1.2   Goals of the Thesis

The goal of this thesis is to develop and investigate dual/high voltage architectures which will eventually replace today's automotive electrical power system. In order to evaluate these systems, it is first necessary to develop proper mathematical models and abstractions of the subsystems contained within these architectures. Once mathematical models have been developed, we can proceed with the analysis and comparison of the architectures. The overall objectives of this thesis are to:

- Investigate and develop analytical system and subsystem models to aid in the analysis of dual/high voltage automotive electrical systems;

- Implement computer simulation models based on the analytical results to predict and evaluate system performance and support the practical implementation of such systems;

- Demonstrate experimentally (whenever possible) the performance of alternative architectures (systems and subsystems) to verify the validity of the developed models.

These items represent the common approach that is used throughout the thesis, that is, implementation of simulation models based on analytical results which are then verified by experimental data and/or hardware prototypes. The next section presents the thesis outline including the topic discussed in each of the chapters and appendices.

1.3   Outline of Thesis

Chapter 2 provides background on conventional automotive electrical systems and highlights those of their limitations which have resulted in investigation of dual/high voltage systems. A brief de-

scription of previous work on dual/high voltage automotive electrical systems is also given. A very common subsystem that is encountered in any automotive electrical system is a three-phase rectifier that is driving constant-voltage loads (which represent the storage battery and associated loads). In Chapter 3, it is shown that these rectifiers are fundamentally different from those driving constant-current (inductive loads). A simplified analysis method is developed to predict system operational characteristics. In Chapter 4, both detailed and averaged models for Lundell alternators are developed. The detailed models are necessary for transient simulations while the averaged models are useful for predicting steady-state performance and are more appropriate for hand calculations. Using the models developed in Chapters 3 and 4, a new high voltage architecture is introduced in Chapter 5. The key subsystem in this architecture is a dual-controlled alternator which possesses such features as enhanced power output, transient suppression and jump-start. Two dual-voltage architectures, namely the dc/dc converter architecture and the dual-stator alternator architecture, are investigated in Chapters 6 and 7, respectively. Chapter 6 develops averaged models for an interleaved converter system which is at the heart of the dc/dc converter architecture. The development of a dual-stator alternator model and its possible use in a dual-voltage architecture are discussed in Chapter 7. Chapter 8 provides a comparison of dual/high voltage architectures presented in the thesis. Chapter 9 presents conclusions drawn from the results presented in the thesis and suggests topics for further research. The simplified analysis method introduced in Chapter 3 for three-phase rectifiers is also applicable to single-phase systems and is developed in Appendix A. Appendices B and C show analysis details to support the alternator model developed in Chapter 4. Appendices D and E provide the Saber and Matlab models that were implemented based on the analytical work in the thesis.

1.4   Contributions of the Thesis

There are several new analytical techniques and system models that are presented in this thesis. These models and techniques serve as the basis for the analysis of dual/high voltage architectures and support the design of such systems. The major contributions of the thesis are as follows:

- An averaged model for rectifiers with constant-voltage loads (Chapter 3). We make use of the averaged model for a three-phase diode rectifier with constant voltage load in Chapter 5 although the results for a three phase phase-controlled rectifier and a single phase diode rectifier are also provided (Chapter 3 and Appendix A, respectively).

- Detailed time-domain and simplified averaged models for synchronous machines with particular emphasis on the Lundell alternator. Computer implementation of models for steady-state

and transient simulation of an alternator with constant-voltage load (Chapter 4).

- A high-power, high-efficiency alternator system design which makes use of the newly developed models. Experimental verification of enhanced power output, transient suppression and jump-start features (Chapter 5).

- Analytical models for an alternative automotive power system based on interleaved dc/dc converters. Computer implementation of models to simulate the steady-state, transient and small-signal behavior of the alternative power supply which support the design of a prototype system (Chapter 6).

- Analytical models of a dual-stator alternator based on the structure of a Lundell alternator. Computer implementation of the model to simulate steady-state and transient characteristics. Use of averaging techniques developed in Chapter 3 to predict system limitations. Illustration of passive transient protection (Chapter 7).

- Comparison of operational characteristics of dual/high voltage candidate architectures based on several attributes (e.g., system complexity, transient behavior, etc.). Extensions and applications of the load-matching technique developed in Chapter 5 to dual-voltage architectures. Introduction of an optimized dual-voltage system based on the combination of a load-matching switched-mode rectifier and an interleaved dc/dc converter system (Chapter 8).

Background on Dual/High Voltage Automotive Electrical Systems

The study of alternative architectures is motivated by a number of factors among which are the limitations of today's electrical system. The present 14 V single voltage system is inefficient and has reached limits where further performance improvements are costly or impractical. The introduction of new and advanced loads has increased the power demand and it has become clear that the present system is incapable of meeting this demand. The increase in the corporate average fuel efficiency (CAFE) requirements has led to the increased efficiency specifications for the electrical system and the exploration/development of efficient techniques for power conversion [3].

2.1 Disadvantages/Limitations of the Present 14 V System

As mentioned earlier, the present automotive electrical system is based on an engine-driven alternator which charges a 12 V battery and delivers power to the loads. There are a number of disadvantages of this system.

First, the claw-pole alternator is electrically very inefficient. Typical peak efficiencies are in the 50–60% range and occur near the engine idle speed of approximately 500–600 rpm. To increase the automotive power supply efficiencies, one must first make certain that the generator efficiencies are as high as possible without compromising other system parameters.

Second, due to the presence of the battery, the distribution voltage varies with the battery voltage. The voltage of a typical automotive lead-acid battery can be as low as 6 V during cold cranking and as high as 16 V when being charged at a high rate at low temperatures. Generally speaking, the battery voltage is a function of temperature, state of charge and rate of charge/discharge. This wide operating voltage range forces the overdesign of loads and electronic control units (ECU), and also reduces the life and reliability of incandescent lamps.

Third, the present system is capable of producing transients with peak voltages up to 100 V

lasting nearly 500 ms when a large current-consuming load is suddenly disconnected from the distribution bus at high alternator speeds. This transient, referred to as *load dump*, is the dominant fault condition which loads and ECUs must survive. Even though the load dump is a low probability event and may never occur during the lifetime of a vehicle, it will occur in a fraction of the population of vehicles and thus must be protected against. As with the wide voltage range, load dump protection leads to overdesign of components that are connected to the distribution bus. For example, every ECU that is connected to the distribution bus must have its own transient absorption/protection circuitry.

2.2   Introduction of Advanced Loads

As pointed out earlier, the average electrical power demand in vehicles is about 800 W [1]. With the introduction of advanced loads such as electromechanical engine valves, electric power steering, water pump and engine cooling fan, the average power demand could increase to 2.5 kW by the year 2005 [1, 2]. In the past, the solution to the increased electrical power requirements has been to increase the size of the alternator and the battery. This approach will not be feasible due to decreasing available space in engine compartments and an increase in the fuel efficiency requirements. Further complicating the problem is the introduction of advanced loads with high peak power requirements such as active suspension (12 kW) and heated windshield (2.5 kW). These loads cannot be powered effectively from the present 14 V system. In addition to advanced load power requirements, there are a number of loads such as the electrically heated catalytic converter which are only feasible at voltages above 60 V [2].

2.3   Higher Fuel Efficiency

The conventional automotive electrical power system today has an average power demand of about 800 W. To generate this electrical power, approximately 1.4 L of gasoline is consumed for 100 km of driving at an average speed of 35 km/h [2]. This consumption due to the electrical system represents nearly 50% of the total fuel consumption allowed in a new generation of vehicles being pursued by the German Automotive Industry Association (VDA). The goal of the VDA is to introduce a 3 L/100 km (78 mpg) vehicle by the year 2000. A very similar fuel efficiency figure (80 mpg) is being pursued by the US Partnership for a New Generation of Vehicles (PNGV). In order to reach the fuel efficiencies sought after by the PNGV and VDA, the conversion efficiency of the automotive electrical system must also be improved.

Due to the limitations of the present 14 V automotive electrical system, further efficiency improvements are costly or impractical. With the introduction of advanced loads, it is inevitable that the 14 V system will be replaced. The next two sections will present some desirable features of alternative automotive electrical power systems and briefly introduce several candidate architectures.

2.4   Characteristics of Alternative Architectures

In this section, the characteristics of an alternative automotive power supply architecture will be described. The new power supply must include a high voltage bus, allow for the use of existing 14 V loads and have well-regulated voltages on both of the buses. The reasons for these requirements will be given.

2.4.1   High Voltage

As mentioned earlier, the introduction of some of the advanced loads leads to considering a higher electrical system distribution voltage [4]. Increasing the dc distribution voltage has a positive effect on most loads. For example, the wire cross-sectional areas can be reduced leading to reduced cost, weight and losses. Furthermore, some of the future loads (e.g., heated windshield) are only economically feasible when operated with high dc voltages. The upper limit on the dc voltage is approximately 60 V. This limitation is primarily set by the safe contact levels for humans [5]–[8]. If voltages higher than 60 V are to be used, insulation and shielding are necessary. The 60 V limit eliminates the consideration of systems with a nominal battery voltage greater than 48 V (four 12 V batteries in series) since the charging voltage can exceed the limit at low temperatures [9].

The benefits of using semiconductors as smart switches in future automotive electrical systems are well known [10, 11]. A recent study has found that a voltage in the vicinity of 40 V has a number of advantages [12]. Since this level is approximately three times the system voltage of today's vehicles, a dc level of 42 V has been chosen for the high voltage bus [13].

2.4.2   Dual Voltage

Changing the present 14 V electrical system to a single higher voltage power supply system is not practical since there is a large infrastructure already in place that supports and services the 14 V components [1]. If the electrical power supply is to meet the higher power requirements while

keeping the system compatible with the existing 14 V components, one must consider having two separate dc voltage levels (14 V and 42 V) during the transition period as more loads migrate to the high voltage bus. This consideration leads to the investigation of dual-voltage power supply architectures. This and considerations of semiconductor technology has led to a consensus among the European and U.S. auto manufacturers and suppliers on a future 14/42 V electrical system [13].

2.4.3 Voltage Regulation

The dual-voltage electrical system that was mentioned in the last subsection has a 42 V bus supporting high power loads, such as heaters and high power motors, and a low voltage bus for backward compatibility for existing 14 V loads such as lamps and electronic control units (ECU). One of the key features of the new dual-voltage system is the extent of voltage regulation required for each of the buses [14]. These limits are presented in Table 2.1 for each bus along with descriptions for each of the various levels. The 42 V bus voltage limits are widely accepted in the automotive industry while the 14 V limits are only accepted by a subset of the industry and are not likely to be widely adopted. The tight voltage limit specifications for the low voltage bus in Table 2.1 will be more agreeable if high power loads are removed from the 14 V bus and the 14 V bus is isolated from the generator. It should be noted that $V_{42,\text{OP-min}}$ and $V_{14,\text{OP-min}}$ in Table 2.1 refer to minimum operating voltages for loads that are not required for starting and safety. On the other hand, the failsafe minimum voltages are the absolute lower limits for all critical loads.

Table 2.1: Dual-Voltage Electrical Power System Voltage Limits.

Description of electrical system parameters for each bus	42 V Bus		14 V Bus	
	Parameter	Value	Parameter	Value
Maximum dynamic overvoltage during fault	$V_{42,\text{OV-dyn}}$	55 V	$V_{14,\text{OV-dyn}}$	20 V
Maximum static overvoltage	$V_{42,\text{OV-stat}}$	52 V	$V_{14,\text{OV-stat}}$	16 V
Maximum operating voltage (engine running)	$V_{42,\text{E-max}}$	43 V	$V_{14,\text{E-max}}$	14.3 V
Nominal operating voltage (engine running)	$V_{42,\text{E-nom}}$	41.4 V	$V_{14,\text{E-nom}}$	13.8 V
Minimum operating voltage (engine running)	$V_{42,\text{E-min}}$	33 V	$V_{14,\text{E-min}}$	12 V
Minimum operating voltage	$V_{42,\text{OP-min}}$	33 V	$V_{14,\text{OP-min}}$	11 V
Failsafe minimum voltage	$V_{42,\text{FS}}$	25 V	$V_{14,\text{FS}}$	9 V

The benefits of voltage regulation have been previously reported and was one of the key issues discussed in a recent doctoral dissertation [2]. For example, brushed permanent magnet motor size and cost can be reduced if the operating voltages are better regulated. In addition,

incandescent lamps will have longer life and higher light output if the applied voltage is regulated to a constant value. Most importantly, reducing the voltage deviations of a distribution bus lowers the required die area of semiconductors intended to be used as smart switches. In fact, it turns out that the use of smart semiconductors in an automotive environment will not be cost effective if the voltage levels are poorly regulated (as in today's vehicles).

2.5   Candidate Dual/High-Voltage Architectures

In this subsection, the candidate dual-voltage architectures are introduced and a brief description is presented. Simplified schematics for the candidate architectures are depicted in Figures 2.1–2.3.

2.5.1   DC-DC Converter Architecture

This architecture is based on a high voltage alternator followed by a rectifier to provide the high voltage level (42 V). The high voltage bus is regulated by controlling the field current of the machine. The lower voltage (14 V) is derived from the high voltage bus by the use of a dc/dc converter. A simplified schematic of the dc/dc converter architecture is shown in Figure 2.1.
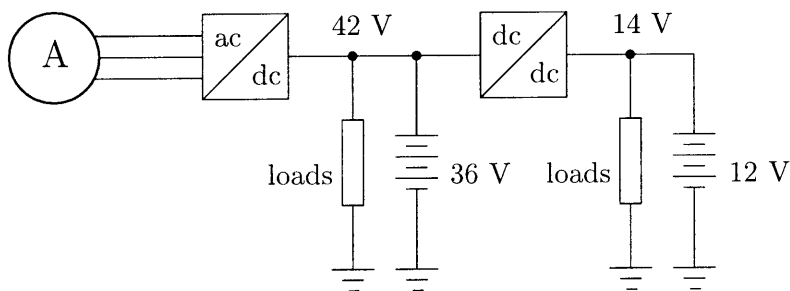
Figure 2.1: Dc/Dc Converter Architecture.

There is a large body of literature on the analysis of dc/dc converters. Nevertheless, there are a number of unique aspects of this application which must be addressed. For example, the converter topology that is selected will affect the transients observed in the system. Thus, it is important that the transient performance of candidate dc/dc converter topologies are included as a key item in the selection process. Another important item is the output current ripple of the converter. There are strict standards and guidelines (e.g., SAE J1113/41) as to the amount of ripple that can be injected to a dc voltage bus; therefore, the design of the dc/dc converter will affect the extent to which one has to filter the ripple, which directly influences the way that the

output EMI filters have to be designed. Active filter design for the dc/dc converter and system optimization are the subjects of two recent theses in this area [15, 16].

Another important requirement for the dc/dc converter is that it has to operate with or without a battery at its outputs. This has an impact on the type of control used with the converter, and regulation strategies must be investigated to ensure reliable operation under both conditions. The dc/dc converter system should also be able to communicate with a vehicle energy management system which manages the power delivered to loads connected to each bus. An example of this would be the dc/dc converter output current limitation. If the energy management system detects that the battery on the low voltage bus is sufficiently charged, it reduces the maximum amount of current that can be delivered by the converter. The response of the converter system to fault conditions has an impact on the design and protection required by the loads that have to survive the transient. The most important of these system faults is the load dump – a sudden disconnect of a large current consuming load. Transient performance and current-limiting are important considerations when choosing a control strategy for the converter system. A control system meeting these requirements will be presented and its performance will be analyzed.

To evaluate the architecture of Figure 2.1, a mathematical model for the dc/dc converter system is needed. The actual dc/dc converter is a switched system and therefore has a periodic time-varying structure. This fact makes the converter quite difficult to analyze, but averaged models overcome this difficulty. In addition to providing a large signal nonlinear description of the converter, the averaged models can be linearized to produce small-signal models useful for control design. Averaged models for the converter system will be derived and used for control design. The overall system model will be used to evaluate closed-loop system performance with average current-mode control.

To validate the analytical results, the architecture will be simulated with Saber [17]. The models developed to assess closed-loop system performance will be implemented in MAST (a multi-discipline modeling language for Saber). Both switched and averaged models will be used for the simulations. The simulations of the averaged system will be used to verify the controller operation and assess the stability of the overall design. The switched simulations, on the other hand, will be used to evaluate short-time phenomenon such as peak current/voltage for switching devices. The simulation models are also suitable for studying the transient behavior of the system under sudden changes in the system parameters on one or both of the buses. Experimental transient results from a prototype converter system will be used to verify the analytical and simulation results. The modeling and analysis of the dc/dc architecture is presented in Chapter 6.
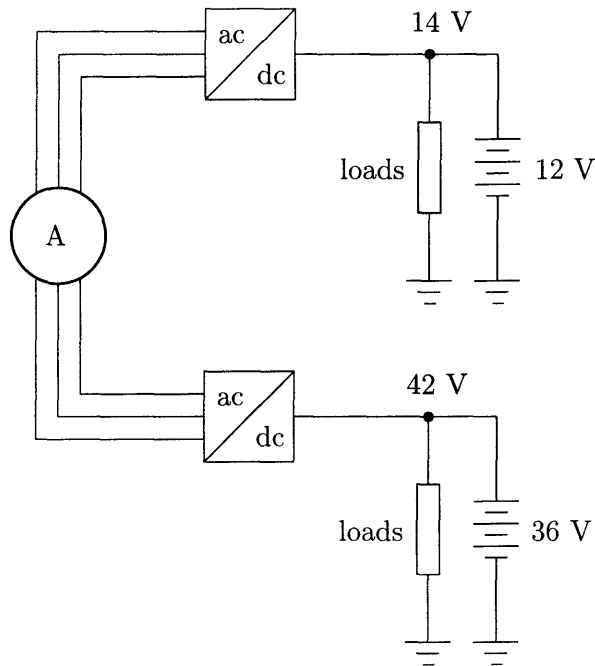
Figure 2.2: Dual-Stator Alternator Architecture.

2.5.2 Dual-Stator Alternator Architecture

This architecture, shown in Figure 2.2, is based on a dual winding machine providing both high and low voltage three phase outputs. Each winding of the machine is followed by a rectifier to produce the desired dc voltage level. One possible way to control the dc bus voltages is to regulate the alternator field current for the 42 V bus and use a phase-controlled rectifier to regulate the 14 V bus.

The first characteristic that must be determined for this architecture is its steady-state control characteristics, that is, the average output current of each rectifier as a function of the control variables (field current, delay angle). Since the windings of the machine share a common magnetic circuit, the steady-state characteristics include the effects of cross-regulation – the degree by which regulation is affected on one bus due to loading of the other. In addition to the steady-state characteristics of the system, one also needs to investigate the dynamics of the architecture, that is, the behavior of the system due to transients. These transients can be due to the normal switching of loads or a fault, such as the condition when a large current consuming load is suddenly turned off. The transient voltage variations on each bus have a strong impact on our ability to use low cost semiconductors as switches in the architecture. Today's automotive electrical system is poorly regulated and voltages several times higher than the system voltage can appear on the main

distribution bus. If the architecture of Figure 2.2 is a viable solution, the distribution voltage has to be substantially better regulated than today's system.

In order to determine the static and dynamic behavior of this architecture, we must first develop a mathematical model for the dual-stator alternator. The mathematical model is described in terms of inductance and resistance matrices for the two sets of three-phase stator windings plus the field winding. The inductance matrix elements capture the leakage and magnetizing inductances in addition to modeling the effects of pole saliency. The model for the machine will be used as the foundation of a simulation model for the dual-stator architecture to be implemented in Saber. We will use the analytical descriptions to model the machine in Saber's MAST programming language. Once the generic template for the model has been developed, it can be exercised by using it in any simulation.

Analytical models need to be developed for the two rectifiers as well. It is interesting to note that the analysis of diode and thyristor based rectifiers with voltage source loads does not appear presently in the literature. Most of the analysis for uncontrolled and controlled polyphase rectifiers assume a current source load and therefore are not suitable for our application. The problem of the dual rectifiers is further compounded by the fact that they are not driven independently. In other words, the two sets of windings driving the rectifiers are coupled; therefore, we expect the two rectifiers to interact. The rectifier analytical models will be used in the implementation of suitable simulation models.

After these alternator and rectifier models have been developed, we can use the alternator and rectifier models that we have discussed earlier in this section to study the dynamics of the architecture. The only additional models that we need for realistic dynamic simulations are the models for the two controllers: field current and thyristor firing-angle. Once these are available, we can study the dynamics of the architecture subjected to any transient sourcing and loading conditions. The modeling and analysis of the dual-stator alternator architecture is presented in Chapter 7.

2.5.3   Dual-Rectifier Architecture

The dual-rectifier architecture is shown in Figure 2.3. It is composed of a high voltage alternator followed by two rectifiers which produce two dc voltage levels. As in the dual-stator alternator architecture, the dc bus voltages can be regulated by field control (42 V bus) and firing angle control (14 V bus). Also, as with the dual-stator alternator architecture, the operational characteristics of this type of system are not widely understood at present.
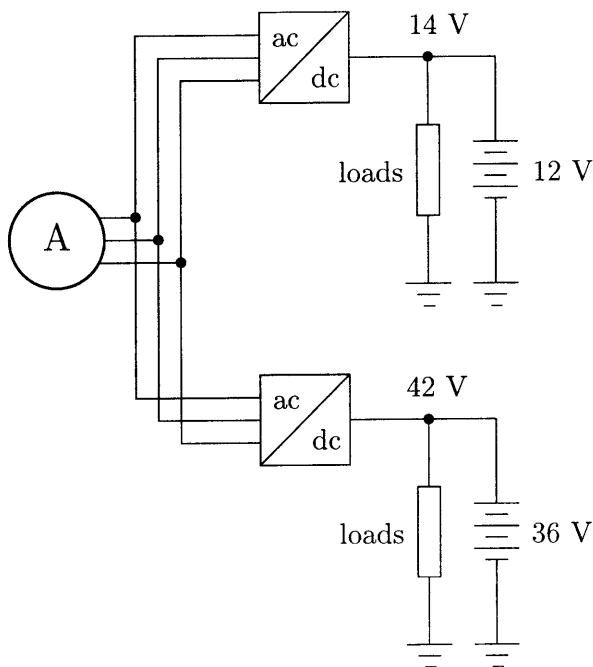
Figure 2.3: Dual-Rectifier Architecture.

As in the dual-stator architecture, we must first determine the steady-state control characteristics of the system – the average output current of each rectifier as a function of the control variables (field current, delay angle). The situation in this architecture is quite different from the approach used for the dual-stator architecture, since rectifiers share an input fed from a common machine reactance. Since there is a common input terminal, there will be interactions between the two rectifiers in this architecture.

To investigate this architecture, we first develop the mathematical model of the machine. The machine likely to be used in this architecture is the high-voltage version of the conventional clawpole (Lundell) alternator. The mathematical description of the conventional alternator is a combination of two subsystems: a three-phase synchronous machine with a field winding and a field current regulator. The three-phase synchronous machine is modeled using inductance and resistance matrices. Saliency is usually neglected in this description for the sake of simplicity but can be included if more accuracy is desired. The field current regulator is modeled as a proportional controller driving a chopper circuit. Moderate modifications of these components allows sufficiently accurate modeling of the high voltage alternator.

This architecture, like the dual-stator architecture, has two rectifiers driving voltage source loads. However, in this case, the rectifiers share a common three-phase input. As in the previous case, an analysis of the rectifiers driving the voltage-source loads appear to be missing from the

literature and needs to be developed. The existence of a common three-phase input with shared machine reactance complicates the treatment of the rectifiers since there will be interactions between the rectifiers which will ultimately affect their control characteristics.

In addition, since the rectifiers are sharing a common input, the current that is generated by the machine will alternately flow in one or the other rectifier. This behavior is inherent to this architecture and results in very large ripples at each rectifier output. Reducing the current ripples requires substantial amount of filtering that can make this architecture less attractive than the dc/dc converter and dual-stator architectures. Due to these disadvantages, this architecture is not analyzed in this thesis; however, a new architecture that overcomes the above-mentioned disadvantages is presented in Chapter 8. The models developed in this thesis can be used to investigate issues such as current ripple and filter implementations and requirements. Analysis of current ripple and its attenuation by means of passive filters for the dual-rectifier architecture using the models presented in this thesis are the subjects of a recent thesis [18].

2.6 Previous Work on Dual-Voltage Architectures

Over the years, a number of alternative dual-voltage power supply architectures have been proposed [19]–[27]; however, most of these have not been analyzed in detail and have only been assessed at a high level. Although they have been proposed as 14/28 V systems, they could be adapted to the 14/42 V requirement. In this section, a review of a few representative dual-voltage architectures is presented and disadvantages that exclude these from consideration as candidate dual-voltage architecture are highlighted.

2.6.1 Transformer/Rectifier Architecture

The transformer/rectifier architecture (shown in Figure 2.4) uses a conventional 14 V alternator and a three phase rectifier unit to charge a 12 V battery and provide power to the 14 V loads [28, 29]. The higher voltage is established by the use of a step-up transformer with the proper turns ratio. The advantage of this system is its simplicity; however, it does have a few drawbacks. One drawback is the cross-regulation of the two dc buses. This causes the dc voltage levels to fluctuate about their nominal values. Another drawback is the fact that the output current in the high voltage bus is limited by the transformer rating. In addition, due to this current limitation, it is quite difficult to keep charge balance in the battery stack. The regulation characteristics of the system could be improved by using a three-phase thyristor rectifier to control the lower voltage while field current is used to regulate the higher voltage.
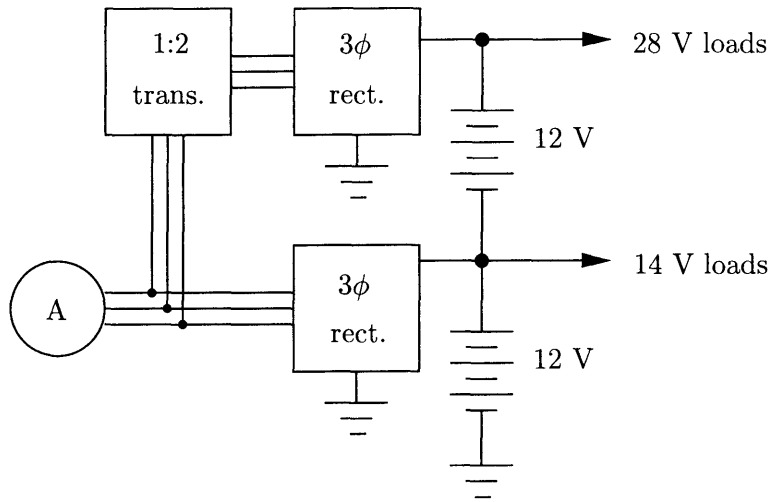
Figure 2.4: Transformer-Rectifier Architecture.

2.6.2   Dual-Reference Alternator Architecture

The dual-reference alternator architecture is shown in Figure 2.5 [28, 29]. In this system, the starter motor is energized from the 28 V bus and once the engine starts and is running above idle, the alternator output voltage will be regulated at 28 V. In this mode of operation, both of the batteries are charged. When the upper battery voltage recovers to its pre-cranking value, the alternator is controlled to regulate its output at 14 V. At this time, the thyristor connecting the alternator output to the 14 V bus is fired and the alternator starts charging the lower battery. The alternator field current is allowed to decay until the charging current reaches zero, at this point the thyristor is reverse biased and turns off. One of the drawbacks of the system is the fact that only one of the buses can be regulated at any given time. In addition, the output current of the alternator flows either through a diode or a thyristor and there is a considerable conduction loss associated with this system. As in the transformer-rectifier architecture, battery stack charge balance is also quite difficult to maintain.

2.6.3   Dual-Voltage Alternator Architecture

The dual-voltage alternator architecture (shown in Figure 2.6) is based on a conventional high voltage alternator with three thyristors operated to control the 14 V bus [30, 31]. The high voltage (28 V) bus is regulated by controlling the field current. The advantage of the system is its simplicity and the fact that the additional thyristors and control circuitry can be mounted directly on the existing alternator housing. This architecture is a specific implementation of the dual-rectifier
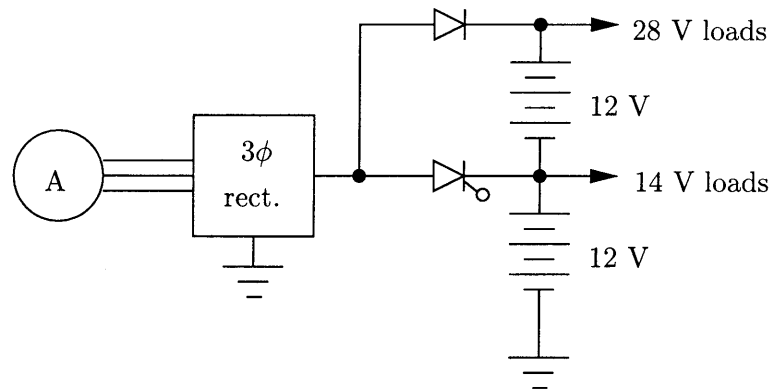
Figure 2.5: Dual-Reference Alternator Architecture.
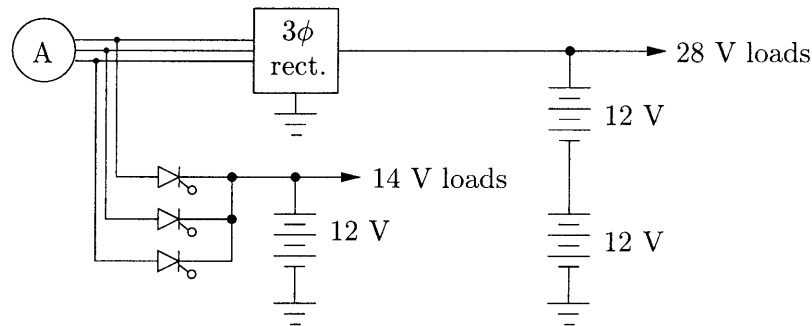
Figure 2.6: Dual-Voltage Alternator Architecture.

architecture shown in Figure 2.3 and therefore also has the disadvantage of producing very large ripples at each rectifier output. Reduction of the current ripple requires filtering which adds to the cost, weight and complexity of the system.

2.7 Summary

In this chapter, it has been shown that the introduction of new automotive loads and the restrictions of the present 14 V electrical system have forced automakers to consider alternative architectures. It has become clear that a high voltage (42 V) system is needed to support the features required and envisioned for the modern automobile. It has also become evident that the industry cannot make the transition to the high-voltage electrical system instantaneously due to the 14 V infrastructure that exists today. As a result, dual-voltage electrical systems have become attractive candidates for the transition period as the industry converts more and more loads to the high-voltage system.

The Lundell or claw-pole alternator is likely to be the generator that is chosen in any of the

candidate architectures since it presently is the most economical choice. However, as mentioned earlier in this chapter, the efficiency of the Lundell alternator is relatively low and it has a number of serious limitations. Among these limitations is the 80 V, 500 ms load dump transient which will get worse as we increase the system output voltage. This transient must be suppressed if the Lundell alternator is to be used in a high-voltage electrical system. The low efficiency of the Lundell alternator is also a disadvantage, especially when fuel efficiency restrictions are considered. In order to quantitatively investigate a high-voltage architecture based on a Lundell alternator, one must develop analytical models for the entire alternator system including the rectifiers. In Chapters 3 and 4, we develop these models for three-phase generator/rectifier systems. The rectifier systems presented are loaded by constant-voltage sources (as is the case in an automotive electrical system) rather than constant-current sources. In Chapter 5, the models of Chapters 3 and 4 are used to develop a high-efficiency high-voltage alternator system which has increased output and efficiency relative to the conventional system. The models of Chapters 3 and 4 are also used as the basis for models developed for the dc/dc converter architecture (Chapter 6) and the dual-stator alternator architecture (Chapter 7).

Analysis of Three-Phase Rectifiers with Constant-Voltage Loads

---

This chapter presents a quantitative analysis of the operating characteristics of three-phase bridge rectifiers with ac-side reactance and constant-voltage loads. We describe the operating characteristics of the three-phase diode bridge rectifier in continuous conduction mode. Simple approximate expressions are derived for the output current characteristic, as well as the input power factor. The output current control characteristic is also derived for the three-phase thyristor bridge converter with constant-voltage load. The derived analytical expressions are applied to a practical example and simulations are used to validate the analytical results. We also show that the derived expressions are far more accurate than calculations based on traditional constant-current models.

3.1   Background

In a number of power electronics applications, one encounters a three-phase bridge rectifier supplied from an inductive ac source driving a constant-voltage load, as illustrated in Figure 3.1. For example, this often occurs in battery charger/power supply systems, such as employed in automotive and aerospace applications. The three-phase source with series inductance represents the alternator back emf and armature inductance, while the constant-voltage load represents the battery and system loads. A similar situation occurs when a transformer-driven rectifier is loaded with a capacitive (rather than inductive) output filter. Here, the ac-side inductance is due to line and transformer leakage reactances, while the dc-side filter acts as a constant-voltage load. In all such applications, the rectifier input and output currents are functions of the system voltage levels and the ac-side reactance, and are also functions of firing angle if thyristor devices are used (Figure 3.2).

While one might expect that analytical models for the operational characteristics of the systems of Figures 3.1 and 3.2 would be readily available in the literature, this appears not to be the case. The behavior of single-phase diode rectifier circuits with ac-side impedance and capacitive loading have been treated in the work of Schade and others [32]–[37]. Most treatments of three-phase rectifier circuits only consider operation with inductive (constant-current) loading of the rectifier.

Schaefer [38] does devote a chapter to rectifiers with ac-side reactance and capacitive loading, with a primary focus on single-phase circuits and the three-phase midpoint connection circuit. The three-phase bridge rectifier is treated for the light-load (discontinuous conduction mode) case, but the chapter stops short of fully analyzing the bridge rectifier in continuous conduction, noting that the analysis is complex. The literature seems to be even more sparse regarding operating characteristics of thyristor bridges with constant-voltage loads, though the principles involved are sometimes described [38] and the challenging nature of firing angle control in this case is occasionally mentioned [38, 39].

This chapter presents a quantitative analysis of the operating characteristics of bridge rectifiers with ac-side reactance and constant-voltage loads [40]. Section 3.2 describes the operating characteristics of the three-phase diode bridge rectifier in continuous conduction mode. Simple approximate expressions are derived for the output current characteristic (output current as a function of input reactance and input and output voltages), as well as the input power factor and distortion. In Section 3.3, the output current control characteristic is derived for the three-phase thyristor bridge converter with constant-voltage load. Section 3.4 applies these newly-derived analytical expressions to a practical example, and validates the results against simulations.

3.2   Three-Phase Diode Rectifier with Constant-Voltage Load

A three phase rectifier with a voltage source load V_o is shown in Figure 3.1. Also included are line inductances L_s each in series with sinusoidal voltages v_{sa}, v_{sb} and v_{sc} which are a three phase set of voltages with magnitude V_s and angular frequency ω. The diodes in the full bridge rectifier are assumed ideal except for a finite on-voltage, V_d. Assuming that the source currents i_a, i_b and i_c are continuous (i.e., do not stay at zero over part of the cycle), it can be shown that the line-line voltages v_{ab}, v_{bc} and v_{ca} are given by

$$v_{ab} = \frac{V_o + 2V_d}{2} \left[\text{sgn}(i_a) - \text{sgn}(i_b)\right] \tag{3.1}$$

$$v_{bc} = \frac{V_o + 2V_d}{2} \left[\text{sgn}(i_b) - \text{sgn}(i_c)\right] \tag{3.2}$$

$$v_{ca} = \frac{V_o + 2V_d}{2} \left[\text{sgn}(i_c) - \text{sgn}(i_a)\right] \tag{3.3}$$

where sgn($\bullet$) is the signum function. Based on the above line-line voltages, the combination of the
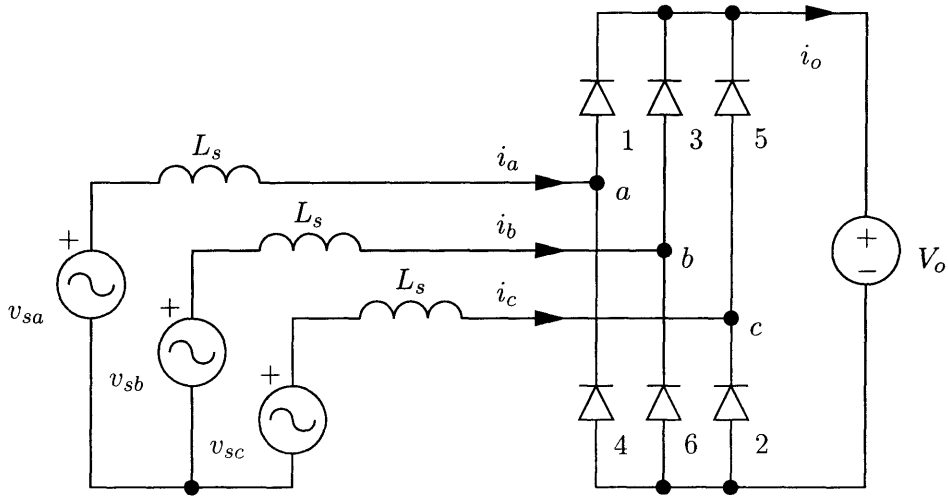
Figure 3.1: Three-phase diode bridge rectifier.
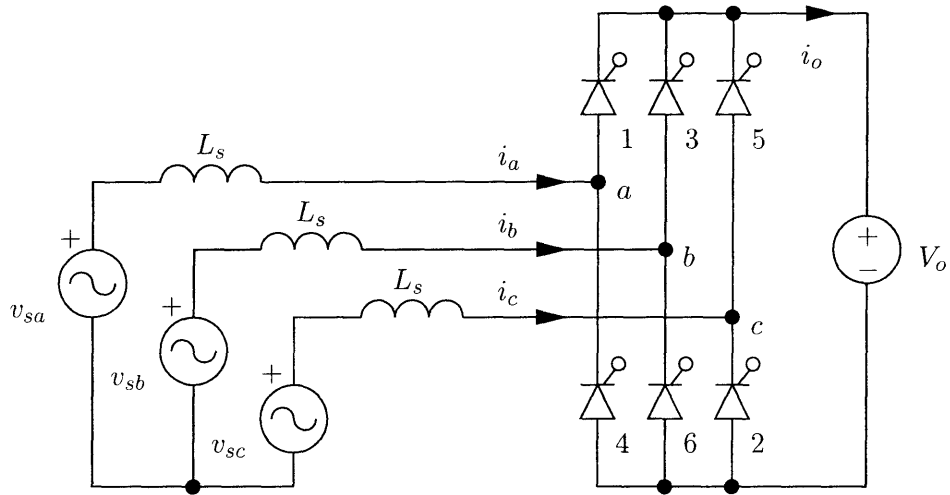
Figure 3.2: Phase-controlled three-phase bridge rectifier.

full bridge rectifier and voltage source load can be replaced by three line-neutral voltages given by

$$v_a = (V_o/2 + V_d)\operatorname{sgn}(i_a) \tag{3.4}$$

$$v_b = (V_o/2 + V_d)\operatorname{sgn}(i_b) \tag{3.5}$$

$$v_c = (V_o/2 + V_d)\operatorname{sgn}(i_c) \tag{3.6}$$

Now, let us approximate phase currents by their fundamental components v_{a1}, v_{b1} and v_{c1}, respectively, since the fundamental component is the only one contributing to power transfer. This approximation yields

$$v_a \approx v_{a1} = V_{o1}\sin(\omega t - \phi) \tag{3.7}$$

$$v_b \approx v_{b1} = V_{o1}\sin(\omega t - \phi - 2\pi/3) \tag{3.8}$$

$$v_c \approx v_{c1} = V_{o1}\sin(\omega t - \phi + 2\pi/3) \tag{3.9}$$

where $V_{o1} = \frac{4}{\pi}(V_o/2 + V_d)$ and ϕ is the phase angle between each voltage source and and its corresponding voltage sink for each phase. An equivalent circuit showing the fundamental components of the voltages and currents in the rectifier system is shown in Figure 3.3. Given expressions (3.7)–(3.9), we can also approximate the inductor currents i_a, i_b and i_c by their fundamental components i_{a1}, i_{b1} and i_{c1}, respectively. Furthermore, since we know voltages v_{a1}, v_{b1} and v_{c1} are in phase with their respective line currents due to the switching pattern of the rectifier, the inductor currents will have the form

$$i_a \approx i_{a1} = I_{s1}\sin(\omega t - \phi) \tag{3.10}$$

$$i_b \approx i_{b1} = I_{s1}\sin(\omega t - \phi - 2\pi/3) \tag{3.11}$$

$$i_c \approx i_{c1} = I_{s1}\sin(\omega t - \phi + 2\pi/3) \tag{3.12}$$

where I_{s1} is the magnitude of the fundamental component of the line currents yet to be determined. Line currents i_{a1}, i_{b1} and i_{c1} are in phase with respective line-neutral voltages v_{a1}, v_{b1}, v_{c1}; therefore, we may replace line-neutral voltages by equivalent resistances (R) defined by

$$R \triangleq \frac{V_{o1}}{I_{s1}} \tag{3.13}$$

The equivalent circuit for our simplified three phase full bridge rectifier is shown in Figure 3.4. To determine the magnitude of the fundamental component of the line current, we only need to

examine one of the phases. For example, the phasor line current in phase a is given by

$$\mathbf{I}_a \overset{\triangle}{=} I_{s1}e^{-j\phi} = \frac{V_s}{\sqrt{R^2 + (\omega L_s)^2}}e^{-j\tan^{-1}(\omega L_s/R)} \tag{3.14}$$

Substituting the expression for I_{s1} into (3.13), equivalent resistance R may now be written as

$$R \overset{\triangle}{=} \frac{V_{o1}}{I_{s1}} = \frac{V_{o1}\sqrt{R^2 + (\omega L_s)^2}}{V_s} \tag{3.15}$$

Solving for R in (3.15) yields

$$R = \frac{\omega L_s V_{o1}}{\sqrt{V_s^2 - V_{o1}^2}} \tag{3.16}$$

Note that our approximation for the equivalent resistance is valid if and only if $\frac{V_s}{V_{o1}} > 1$. Using the expression for the equivalent resistance R in (3.16), the magnitude of the fundamental of the line current I_{s1} and the phase angle ϕ can be expressed as

$$I_{s1} = \frac{\sqrt{V_s^2 - V_{o1}^2}}{\omega L_s} \tag{3.17}$$

$$\phi = \tan^{-1}\sqrt{(V_s/V_{o1})^2 - 1} \tag{3.18}$$

The average output current delivered to the voltage source load V_o can be approximated as

$$\langle i_o \rangle \approx \frac{3}{\pi}I_{s1} = \frac{3}{\pi}\frac{\sqrt{V_s^2 - V_{o1}^2}}{\omega L_s} \tag{3.19}$$

The power factor k_p may now be computed using the expression for ϕ

$$k_p \approx \cos\phi = \frac{V_{o1}}{V_s} \tag{3.20}$$

In our derivation of the equivalent resistance R given in (3.16), we included the impact of the line inductances but neglected series resistances to simplify the analysis and illustrate the details of the procedure. The inclusion of series resistance into the analysis is straightforward; however, it does complicate the expressions. For example, if we assume that each phase has a line inductance L_s
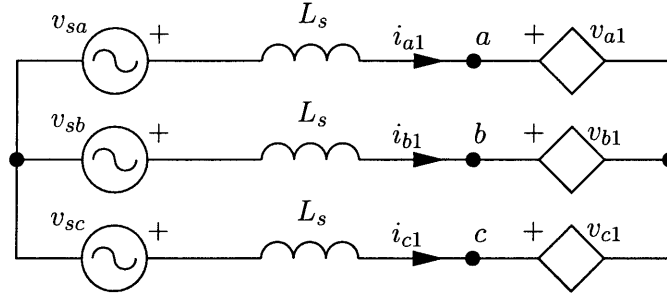
Figure 3.3: Averaged model for three phase rectifier consisting of fundamental components of voltages and currents.
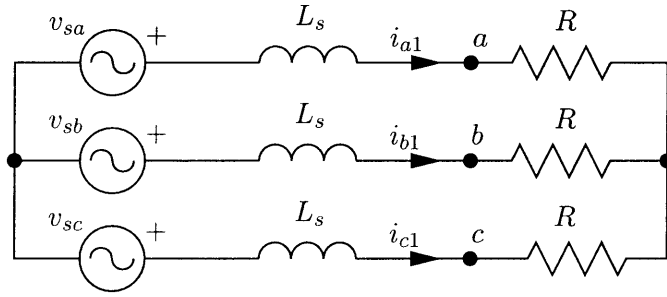
Figure 3.4: Averaged model for three phase rectifier using equivalent resistance R.

and series resistance R_s associated with it, the expression for the equivalent resistance R becomes

$$R = \frac{V_{o1}^2 R_s + V_{o1}\sqrt{(\omega L_s)^2\left(V_s{}^2 - V_{o1}^2\right) + R_s^2 V_s^2}}{V_s{}^2 - V_{o1}^2} \tag{3.21}$$

Using (3.21), one can derive new expressions for I_{s1} and ϕ which include the impact of the series resistance R_s.

$$I_{s1} = \frac{V_s{}^2 - V_{o1}^2}{V_{o1} R_s + \sqrt{(\omega L_s)^2\left(V_s{}^2 - V_{o1}^2\right) + R_s^2 V_s^2}} \tag{3.22}$$

$$\phi = \tan^{-1}\left[\frac{\omega L_s\left(V_s{}^2 - V_{o1}^2\right)}{R_s V_s{}^2 + V_{o1}\sqrt{(\omega L_s)^2\left(V_s{}^2 - V_{o1}^2\right) + R_s^2 V_s^2}}\right] \tag{3.23}$$

Now, the expression for the average output current $\langle i_o \rangle$ may be re-evaluated and is given by

$$\langle i_o \rangle \approx \frac{3}{\pi} I_{s1} = \frac{3}{\pi} \frac{V_s{}^2 - V_{o1}{}^2}{V_{o1} R_s + \sqrt{(\omega L_s)^2 \left(V_s{}^2 - V_{o1}^2\right) + R_s^2 V_s^2}} \qquad (3.24)$$

It should be noted that for typical values of the series resistance R_s in automotive alternators, the maximum error introduced by using (3.19) instead of (3.24) is 15-20% and occurs at the low end of the speed range (idle speed of 1800 rpm). As the alternator speed increases the inductive reactance dominates the impedance of the machine and the output current is not significantly altered by R_s. For instance, in the example presented in Section 3.4, neglecting the 33 mΩ series resistance results in an average output current 78.8 A at 1800 rpm (by using (3.19)) whereas (3.24) gives 65 A (17% error).

3.3   Phase-Controlled Three-Phase Rectifier with Constant-Voltage Load

A simplified schematic of a phase-controlled three phase rectifier with voltage sink is shown in Figure 3.2. The analysis of this system is much more difficult due to the presence of thyristors and the introduction of firing angle α as an additional (control) variable. For purposes of our analysis, we define α as the electrical firing angle delay relative to the forward voltage that appears across the thyristor. To simplify the analysis, we will assume that the on-voltage of the thyristors is zero. In order to compute the average output current, we only need to consider one of the phase currents (for example, thyristor 3 connected to phase b) over a half of its period of conduction. Over a half period of conduction, the current i_b contributes to the average output current over two thyristor conduction intervals: when thyristors 3 and 5 are on (conduction angle length α) and when thyristors 1, 3 and 5 are on (conduction angle length $\frac{\pi}{3} - \alpha$). Integrating i_b over each of these intervals yields:

$$Q_{3,5} \triangleq \int_0^\alpha i_b(\omega t) d(\omega t) = \left(i_{x1} - \frac{\sqrt{3} V_s}{2\omega L_s} \sin\theta\right)\alpha + \frac{\sqrt{3} V_s}{2\omega L_s}\left(\cos\theta - \cos(\theta + \alpha)\right) - \frac{V_o}{4\omega L_s}\alpha^2 \qquad (3.25)$$

$$\begin{aligned} Q_{1,3,5} \triangleq \int_\alpha^{\frac{\pi}{3}} i_b(\omega t) d(\omega t) &= \left[i_{x4} - \frac{V_s}{\omega L_s}\cos\left(\alpha + \theta - \frac{2\pi}{3}\right)\right] \cdot \left(\frac{\pi}{3} - \alpha\right) \\ &+ \frac{V_s}{\omega L_s}\sin\left(\theta - \frac{\pi}{6}\right) - \frac{V_s}{\omega L_s}\sin\left(\alpha + \theta - \frac{2\pi}{3}\right) - \frac{V_o}{6\omega L_s}\left(\frac{\pi}{3} - \alpha\right)^2 \end{aligned} \qquad (3.26)$$

where i_{x1}, i_{x4} and θ are defined as follows

$$i_{x1} = \frac{V_s}{\omega L_s}\left(\cos(\theta + \alpha) - \cos\left(\theta + \frac{\pi}{3}\right)\right) - \frac{V_o}{3\omega L_s}\left(\frac{\pi}{3} - \alpha\right) \tag{3.27}$$

$$i_{x4} = i_{x1} + \frac{\sqrt{3}V_s}{2\omega L_s}\left(\sin(\theta + \alpha) - \sin\theta\right) - \frac{V_o\alpha}{2\omega L_s} \tag{3.28}$$

$$\theta = \cos^{-1}\left(\frac{V_o(\frac{4\pi}{3} - \alpha)}{-12V_s\sin(\frac{\alpha}{2} - \frac{\pi}{6}) + 6\sqrt{3}V_s\sin(\frac{\alpha}{2})}\right) - \frac{\alpha}{2} \tag{3.29}$$

The average output current due to i_b conducting through thyristor 3 over a full conduction period is

$$\langle i_o\rangle\Big|_{i_b} = \frac{1}{2\pi}\left(2\left[Q_{3,5} + Q_{1,3,5}\right]\right) \tag{3.30}$$

Therefore, the average output current for the entire thyristor bridge is

$$\langle i_o\rangle = 3\langle i_o\rangle\Big|_{i_b} = \frac{3}{\pi}\left[Q_{3,5} + Q_{1,3,5}\right] \tag{3.31}$$

The expressions for the average output current (3.31) will be compared with results of computer simulations in Section 3.4.

3.4   Example Applications

In this section, we present some numerical examples that verify the validity of the models developed in the last two sections. We will compare our analytical results with ones obtained from a circuit simulator. We choose parameters that are appropriate for modeling Lundell-type automotive alternators.

First, consider the full bridge rectifier given in Figure 3.1 with the following parameter values typical of an automotive alternator: $V_o = 14.5$ V, $L_s = 180$ μH, $R_s = 33$ mΩ, $V_d = 1$ V. The results of our comparison are shown in Figures 3.5–3.7. Figure 3.5 shows the average output current $\langle i_o\rangle$ versus the magnitude of the source voltage V_s with the source frequency f ($\omega = 2\pi f$) fixed at 180 Hz. Figure 3.6 shows the average output current $\langle i_o\rangle$ versus the source frequency f with the source voltage V_s fixed at 20 V. Figure 3.7 depicts the power factor k_p [41] versus the source voltage V_s with the source frequency f fixed at 180 Hz. In Figures 3.5 and 3.6, analytical results are obtained by

the use of (3.19) and the symbol ($\times$) represents the results from circuit simulation. The predictions using the classical constant-current loaded model [41] are showed by a dashed line. In Figure 3.7, (3.20) was used to generate the analytical results. As can be seen from these comparisons, there is good agreement between the simulated and analytical results. It can also be seen that the model developed here is much more accurate than the classical constant-current model for the case of a constant-voltage load.

Next, consider the phase-controlled rectifier shown in Figure 3.2 with the same parameter values, i.e., $V_s = 24$ V, $f = 180$ Hz, $V_o = 14.5$ V, $L_s = 180$ μH. The results for this case are shown in Figure 3.8. The plot shows the average output current $\langle i_o \rangle$ versus the firing angle α of the thyristors. The solid line obtained by the use of (3.31) while the symbol ($\times$) represents the results from circuit simulation. Once again, there is good agreement between the analytical and simulation results. We thus conclude that the proposed models are accurate and useful for modeling real systems.

3.5 Summary

In this chapter we presented an analysis of the operating characteristics of three-phase bridge rectifiers with ac-side reactance and constant-voltage loads operating in continuous conduction mode, and showed that classical models based on constant-current loads are not very accurate for such systems. Analytical expressions were derived for the output current characteristics and power factor of three-phase diode bridge rectifiers with constant-voltage loads. The effect of ac side series resistance was determined. We also derived analytical models for the output current characteristics of thyristor bridge rectifiers. The analytical expressions were compared to computer simulations and shown to be quite accurate. The models developed in this chapter for the three-phase diode rectifier will be used to analyze a high-voltage high-efficiency alternator in Chapter 5. Chapter 5 will also present experimental results that will further verify the accuracy of our models.
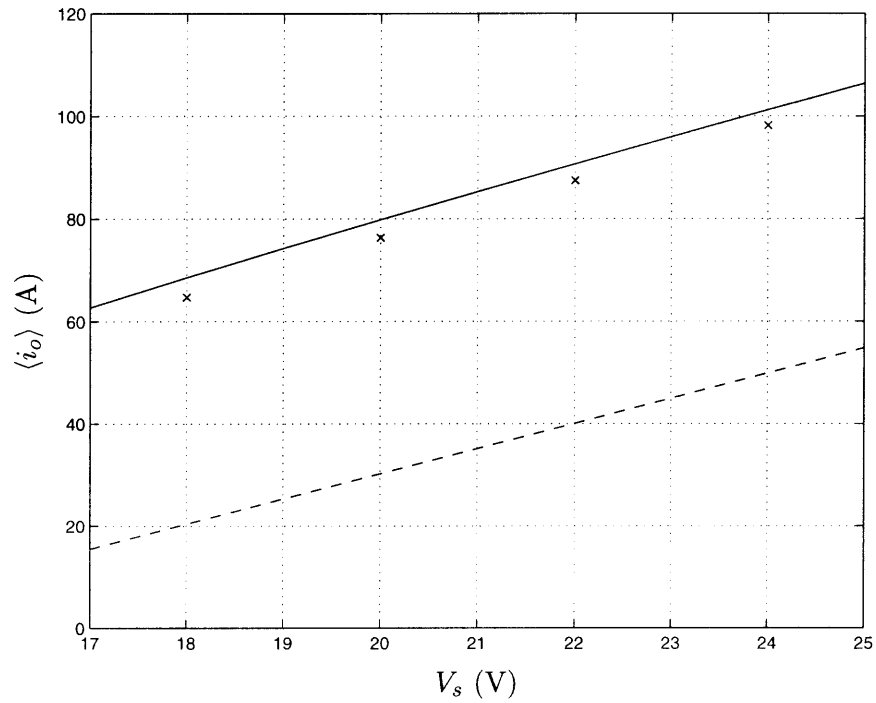
Figure 3.5: Average output current $\langle i_o \rangle$ versus source voltage magnitude V_s with $f = 180$ Hz (solid: analytical, $\times$: simulation, dashed: analytical for classical constant-current loaded model).
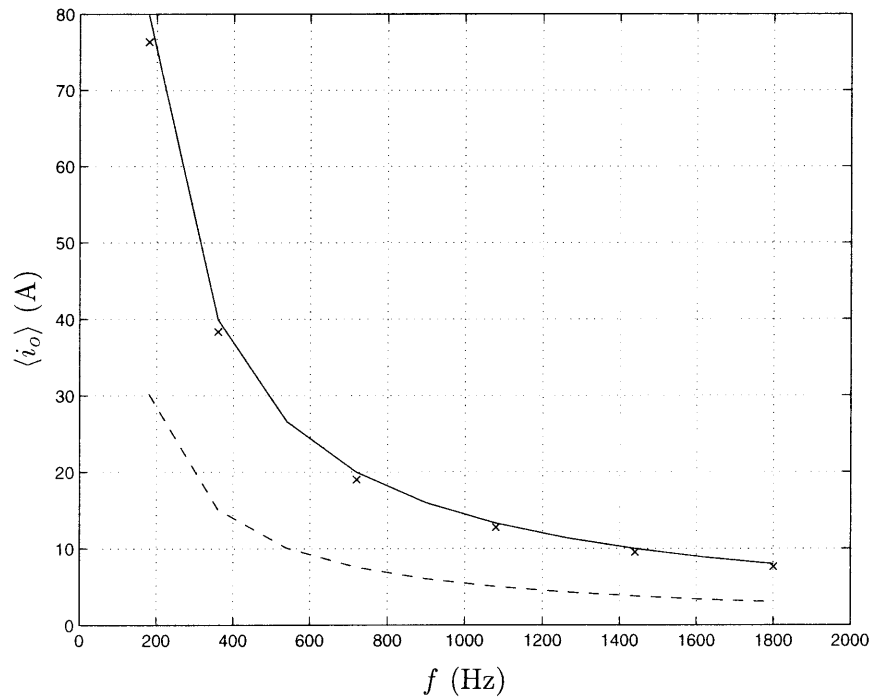
Figure 3.6: Average output current $\langle i_o \rangle$ versus frequency f with $V_s = 20$ V (solid: analytical, $\times$: simulation, dashed: analytical for classical constant-current loaded model).
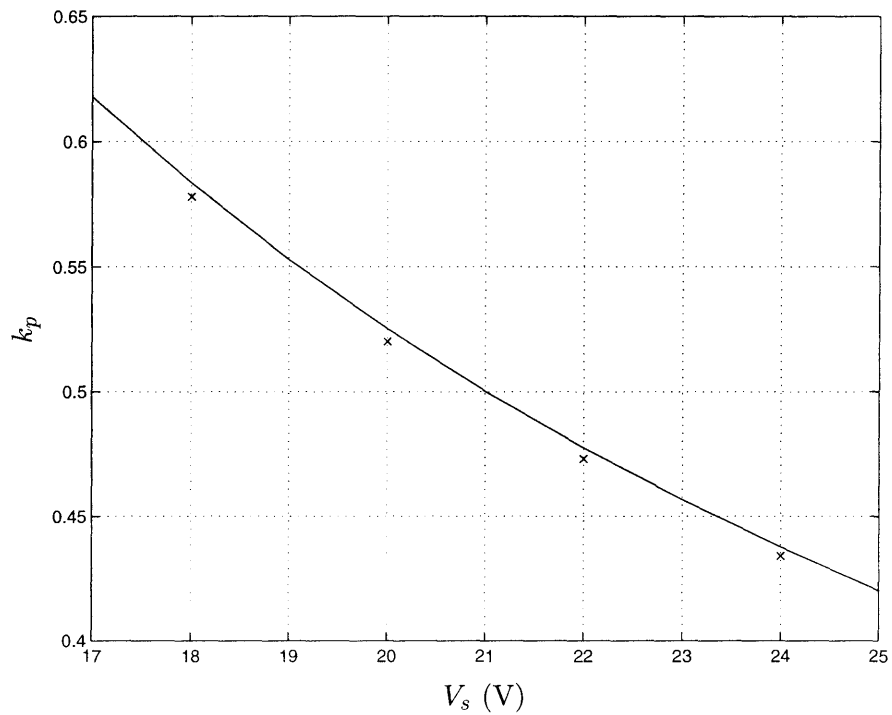
Figure 3.7: Power factor k_p versus source voltage magnitude V_s with $f = 180$ Hz (solid: analytical, ×: simulation).
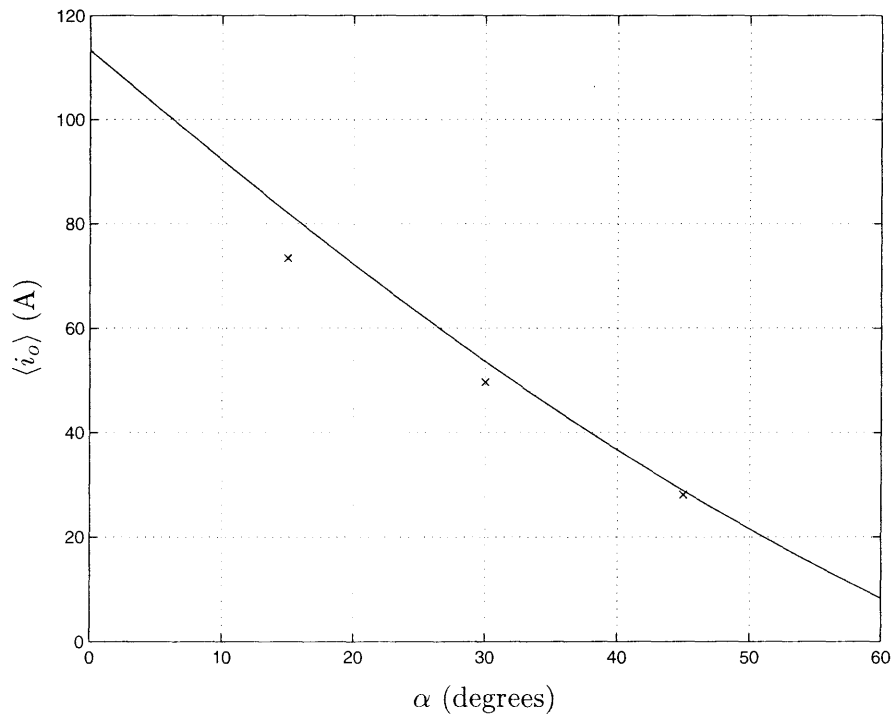
Figure 3.8: Average output current $\langle i_o \rangle$ versus firing angle α for $V_s = 24$ V, $f = 180$ Hz, $V_o = 14.5$ V, $L_s = 180$ μH (solid: analytical, ×: simulation).

Modeling and Simulation of a Lundell (Claw-Pole) Alternator

The Lundell alternator is at the heart of today's automotive electrical system. This type of alternator is also referred to as a claw-pole alternator due to the claw-shaped pole halves that make up the rotor assembly. Its reliability and low manufacturing cost have made the Lundell alternator the workhorse of power generation for motor vehicles.

This chapter describes the mathematical modeling of the Lundell alternator. After a brief overview of the automotive power generation system, analytical models for the alternator are developed based on a three-phase synchronous machine. Using simplifying assumptions, averaged models for the alternator are then derived.

4.1   Introduction

A simplified automotive electrical system is shown in Figure 4.1. The major components of the system include the alternator, battery and the starter motor. The main purpose of the battery is to provide the initial power to engage the starter motor which cranks the engine. In the figure, we explicitly show the cable that connects the alternator and the battery since it does cause a significant voltage drop and must be taken into consideration when placing loads in the electrical system. Placing the loads closer to the alternator results in less voltage drop but larger voltage
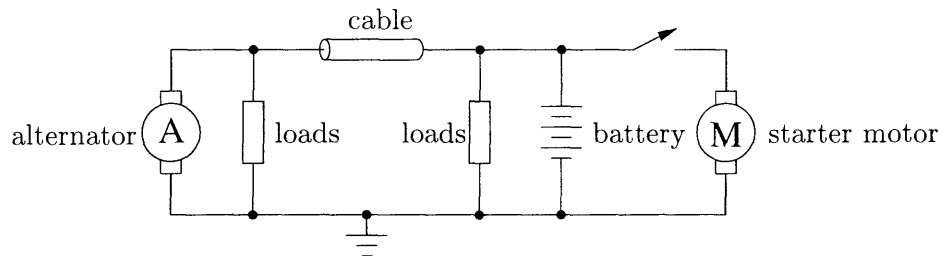
Figure 4.1: Simplified automotive electrical system.
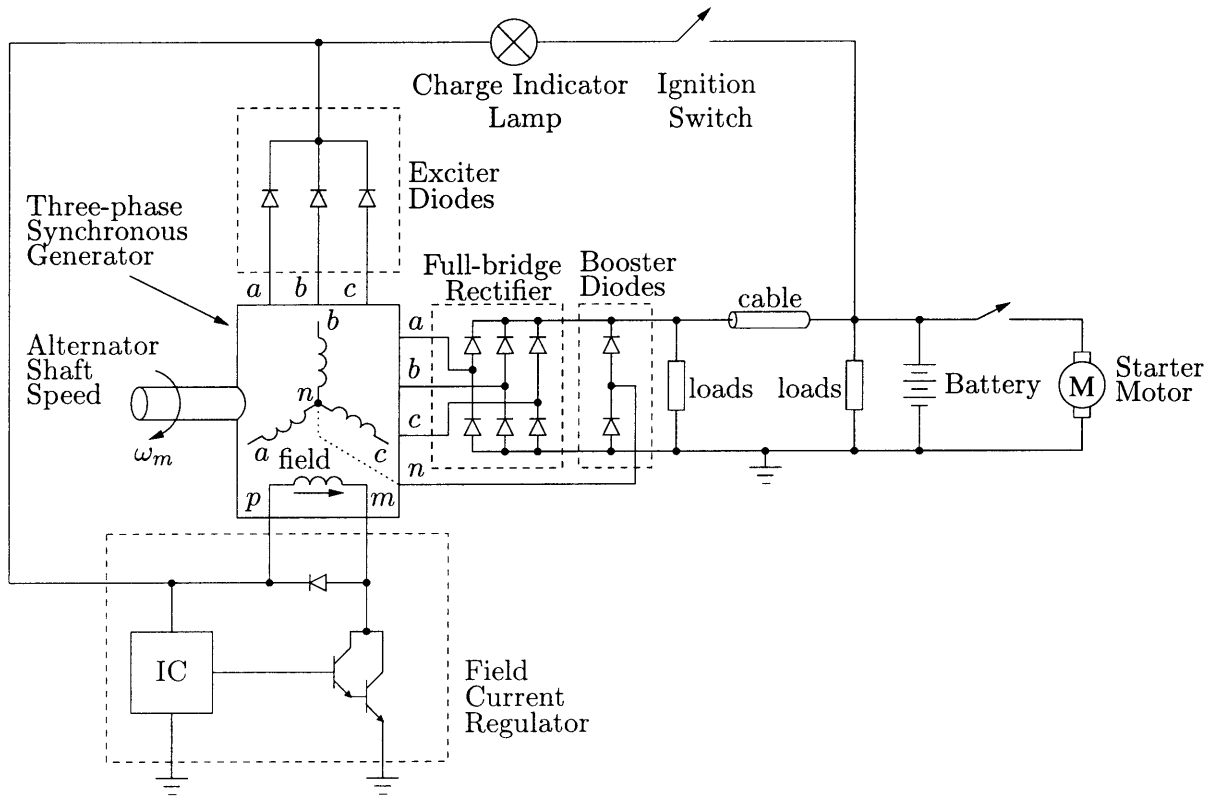
Figure 4.2: Simplified schematic of an automotive electrical system which shows the alternator subsystems including the full-bridge rectifier and field current regulator.

variations. For electronic loads, this overvoltage could be disadvantageous. It is common practice to place voltage insensitive loads, such as heaters, closer to the alternator and voltage sensitive, low current loads closer to the battery [42].

The alternator consists of three subsystems: a three-phase synchronous generator with a field winding, a rectification system (a three-phase full-bridge rectifier, booster and exciter diodes) and a field current regulator. The generator produces a three-phase set of ac voltages which are rectified by the full-bridge rectifier to produce the dc output voltage. The booster diodes which are placed at the output of the three-phase rectifier are optional but are present in most automotive alternators produced today. The midpoint of the booster diode pair is connected to the synchronous generator neutral and uses the third harmonic of the phase voltages to inject third harmonic current into the output to increase the average output current [43].

The output voltage is controlled by a regulator which adjusts the field current which in turn controls the back-emf of the machine. A simplified schematic of the automotive electrical system illustrating the subsystems of the alternator system is shown in Figure 4.2. Referring to Figure 4.2,

it should be noted that when the engine is initially cranked, the alternator field current is drawn from the battery via the ignition switch and the charge indicator lamp. Once the engine (and the alternator) starts rotating, the field current is drawn from the machine windings through the exciter diodes. The alternator voltage is controlled by the field current regulator which adjusts the average value of the field current by using PWM control.

With the engine running, the alternator is to deliver all of the power demanded by the loads and charge the battery. However, this cannot be done under all operating conditions (load power, engine speed, temperature) without severely oversizing the alternator. At times when the alternator cannot supply the demanded current, the battery delivers the balance. This condition often occurs when the engine is idling, for example, when the vehicle is stopped at a red light. It is important that the charge that is taken out of the battery be put back in order to keep the state-of-charge at a level that will not affect the cranking capabilities.

Due to the recent increase in the installed electrical loads in automobiles, there has been much concern over the power delivering capability of present automotive electrical systems. Given a set of loads and driving conditions, one needs to determine if the electrical system is *sized* properly so that there is no deficit in the battery state-of-charge. The term *size* refers to the rated output current (power) and charge capacity of the alternator and battery, respectively. Of course, the conclusions one reaches about the system are highly dependent on the speed profile of the vehicle. There exist a set of time vs. speed profiles referred to as *drive cycles* that are used to compare different sizing strategies. What are difficult to agree on are *load profiles* – that is, which load gets turned on, when and for how long. Load profiles are not deterministic as they depend heavily on environmental conditions and driver psychology. The load flow study of the system is important not only to understand sizing requirements but also from an energy management point of view.

In order to study the transient and steady-state characteristics of the alternator system, proper analytical models need to be developed. For transient time-domain analyses, detailed models are necessary to capture, for example, the switching transitions of rectifier diodes and load dump faults. However, the detailed models are not suitable for longer term analyses and simulations for load flow studies. Thus, simple yet accurate averaged alternator models also need to be developed. The rest of this chapter is devoted to the development of these models which are used as the bases for computer simulations that will be used in subsequent chapters.

4.2 Three-Phase Synchronous Generator

In this section we develop the governing equations and equivalent circuits that characterize a Lundell alternator. In particular we concentrate on modeling the three-phase synchronous generator by approximating it as a cylindrical-rotor machine. This allows the development of a model that is analytically tractable and avoids the complications that arise from treating the complex geometry of the claw-shaped poles of the rotor. The accuracy of this approximation is discussed later in the chapter by a comparison between analytical and experimental results.

There are two commonly used three-phase synchronous machine models based on the shape of the rotor: cyclindrical and salient-pole. We will use both of these models in the thesis but, unless otherwise noted, will concentrate on the cylindrical-rotor model. A schematic diagram of a three-phase two-pole cylindrical-rotor synchronous machine is shown in Figure 4.3. This machine can be considered as two poles of a more general p-pole machine. The coils indicated by aa', bb' and cc' represent the distributed stator windings which produce sinusoidal mmf waves in the air gap. The magnetic axes of the phases are displaced from each other by $120°$. The field coil denoted by ff' is also a representation of a distributed winding that produces a sinusoidal mmf. The alternator shaft (rotor) mechanical speed, ω_m, is usually considered an independent input and is related to the rotor angular position, θ_m, by

$$\frac{d\theta_m(t)}{dt} = \omega_m(t) \tag{4.1}$$

The rotor electrical angle, θ, is proportional to the rotor angular position, θ_m and is defined as

$$\theta(t) \stackrel{\triangle}{=} \left(\frac{p}{2}\right) \theta_m(t) \tag{4.2}$$

where p is the number of poles of the rotor. One can similarly relate the electrical angular frequency,
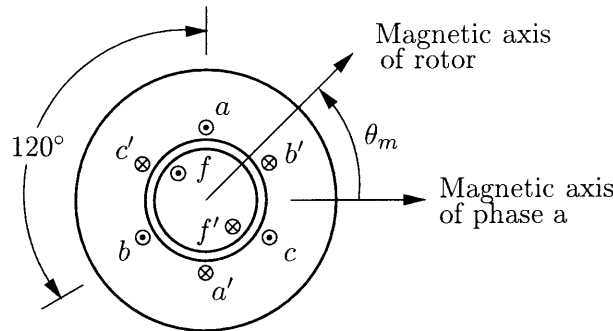
Figure 4.3: Schematic diagram of a three-phase cylindrical-rotor synchronous machine [44].

ω, of the phase voltages and currents to θ as

$$\frac{d\theta(t)}{dt} = \omega(t) \tag{4.3}$$

With the definition of the electrical angle, θ, flux linkages in the phases and the field winding are given by

$$\lambda_a(t) = L_{aa}i_a(t) + L_{ab}i_b(t) + L_{ac}i_c(t) + L_{af}(\theta)i_f(t) \tag{4.4}$$

$$\lambda_b(t) = L_{ba}i_a(t) + L_{bb}i_b(t) + L_{bc}i_c(t) + L_{bf}(\theta)i_f(t) \tag{4.5}$$

$$\lambda_c(t) = L_{ca}i_a(t) + L_{cb}i_b(t) + L_{cc}i_c(t) + L_{cf}(\theta)i_f(t) \tag{4.6}$$

$$\lambda_f(t) = L_{fa}(\theta)i_a(t) + L_{fb}(\theta)i_b(t) + L_{fc}(\theta)i_c(t) + L_{ff}i_f(t) \tag{4.7}$$

The time variation of rotor electrical angle θ is not indicated in the above equations (and in the rest of the chapter) for notational simplicity. In the flux linkage equations (4.4)-(4.7), there are three types of inductances: (1) self-inductances of the stator phases (L_{aa}, L_{bb}, L_{cc}) and rotor (L_{ff}), (2) phase-to-phase mutual inductances (L_{ab}, L_{ac}, L_{ba}, L_{bc}, L_{ca}, L_{cb}) and (3) stator-to-rotor angle-dependent mutual inductances ($L_{af}(\theta)$, $L_{bf}(\theta)$, $L_{cf}(\theta)$, $L_{fa}(\theta)$, $L_{fb}(\theta)$, $L_{fc}(\theta)$). Since the rotor is cylindrical, the self-inductance of the phases are angle-independent and can be expressed as

$$L_{aa} = L_{bb} = L_{cc} = L_{ls} + L_{ms} \tag{4.8}$$

where L_{ms} is the portion of the self-inductance due to the space-fundamental air-gap flux and L_{ls} is due to the stator leakage flux. In a similar fashion, the self-inductance of the field winding can be expressed as

$$L_{ff} = L_{lf} + L_{mf} \tag{4.9}$$

where L_{mf} is the portion of the self-inductance due to the space-fundamental air-gap flux and L_{lf} is due to the field winding leakage flux. Assuming that the phase-to-phase mutual inductances are only due to the space-fundamental air gap flux results in

$$L_{ab} = L_{ac} = L_{ba} = L_{bc} = L_{ca} = L_{cb} = L_{ms}\cos\frac{2\pi}{3} = -\frac{1}{2}L_{ms} \tag{4.10}$$

The angle-dependent stator-to-rotor mutual inductances are given by

$$L_{af}(\theta) = L_{fa}(\theta) = M\cos(\theta) + M_3\cos(3\theta) \tag{4.11}$$

$$L_{bf}(\theta) = L_{fb}(\theta) = M\cos\left(\theta - \frac{2\pi}{3}\right) + M_3\cos\left(3\left(\theta - \frac{2\pi}{3}\right)\right) \tag{4.12}$$

$$L_{cf}(\theta) = L_{fc}(\theta) = M\cos\left(\theta + \frac{2\pi}{3}\right) + M_3\cos\left(3\left(\theta + \frac{2\pi}{3}\right)\right) \tag{4.13}$$

where M is the peak stator-to-rotor mutual inductance given by

$$M = \sqrt{L_{ms}L_{mf}} \tag{4.14}$$

and M_3 represents the peak value of the third harmonic of the stator-to-rotor mutual inductance and is included to take into account pole saliency. The effects of the third harmonic modeled by M_3 are often ignored in other analyses but must be taken into account if the influence of the booster diodes needs to be considered. Unless otherwise noted, we will consider the third harmonic magnitude of the stator-to-rotor mutual inductance to be 1/10 of the fundamental (i.e., $M_3 = M/10$). The flux linkage equations (4.4)-(4.7) may now be expressed in compact matrix form as

$$\begin{bmatrix} \lambda_a(t) \\ \lambda_b(t) \\ \lambda_c(t) \\ \lambda_f(t) \end{bmatrix} = \begin{bmatrix} L_{ls} + L_{ms} & -\frac{1}{2}L_{ms} & -\frac{1}{2}L_{ms} & L_{af}(\theta) \\ -\frac{1}{2}L_{ms} & L_{ls} + L_{ms} & -\frac{1}{2}L_{ms} & L_{bf}(\theta) \\ -\frac{1}{2}L_{ms} & -\frac{1}{2}L_{ms} & L_{ls} + L_{ms} & L_{cf}(\theta) \\ L_{fa}(\theta) & L_{fb}(\theta) & L_{fc}(\theta) & L_{lf} + L_{mf} \end{bmatrix} \begin{bmatrix} i_a(t) \\ i_b(t) \\ i_c(t) \\ i_f(t) \end{bmatrix} \tag{4.15}$$

The square matrix of inductances is referred to as the *inductance matrix* of the machine and denoted $\mathbf{L}(\theta)$. The matrix expression (4.15) is used as the mathematical basis for several alternator models in Saber. The computer code for these models is given in Appendix D. In the following section, we develop a model for the field current regulator which will be used to help simulate the entire alternator system.

4.3 Field Current Regulator

A field current regulator is an integral part of an automotive alternator as shown in Figure 4.2. The dc output voltage of the alternator is controlled by regulating the current flowing through the field winding. The model for a typical regulator is shown in Figure 4.4. The terminals labeled p and m are connected to the field winding of the machine. The regulation of the output voltage is accomplished by switching a power transistor between terminal m and ground. The on duration of the power transistor is derived by comparing a compensated error signal to a sawtooth as shown

in the figure. For the purposes of our simulations, it is sufficient to model the power transistor as a voltage-controlled switch; however, more detailed models may be used if needed. It should be noted that the reference voltage V_{ref} is temperature compensated and therefore the nominal output voltage of the alternator varies with temperature as well. A typical value for the reference voltage V_{ref} at 25°C is 14.2 V with a linear temperature coefficient of -7 mV/°C. In practice, the frequency of the sawtooth is in the range 120-160 Hz and the compensator structure can vary depending on the manufacturers. Many of the compensators are simple proportional controllers although PI controllers are also common. For our system, we use a lag controller with transfer function:

$$H(s) = \frac{K}{1 + s/\omega_c} \tag{4.16}$$

where K is the dc gain and ω_c is the cutoff frequency. The field current regulator system of Figure 4.4 is implemented in Saber to be used in conjunction with the synchronous generator model. The code for the regulator Saber model is given in Appendix D.
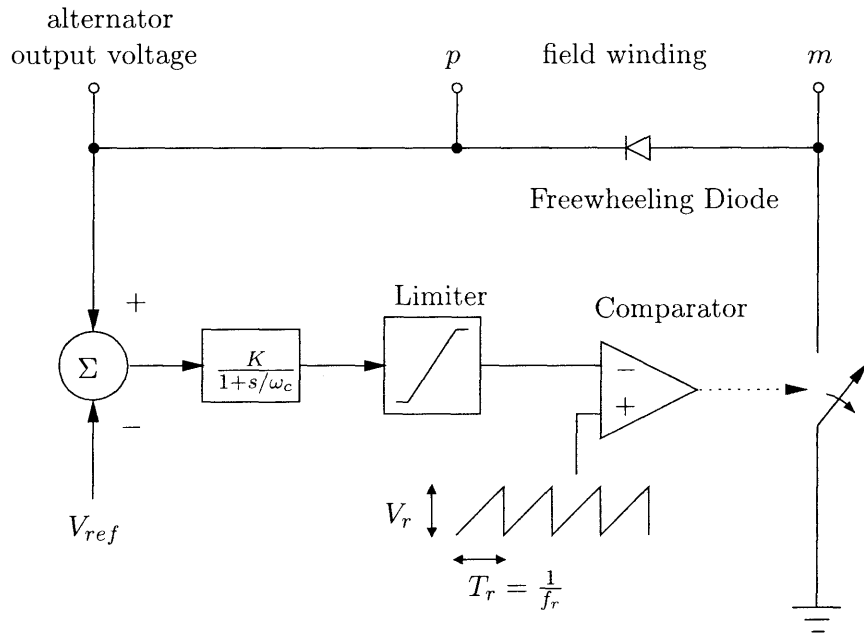
Figure 4.4: Switching alternator voltage regulator.
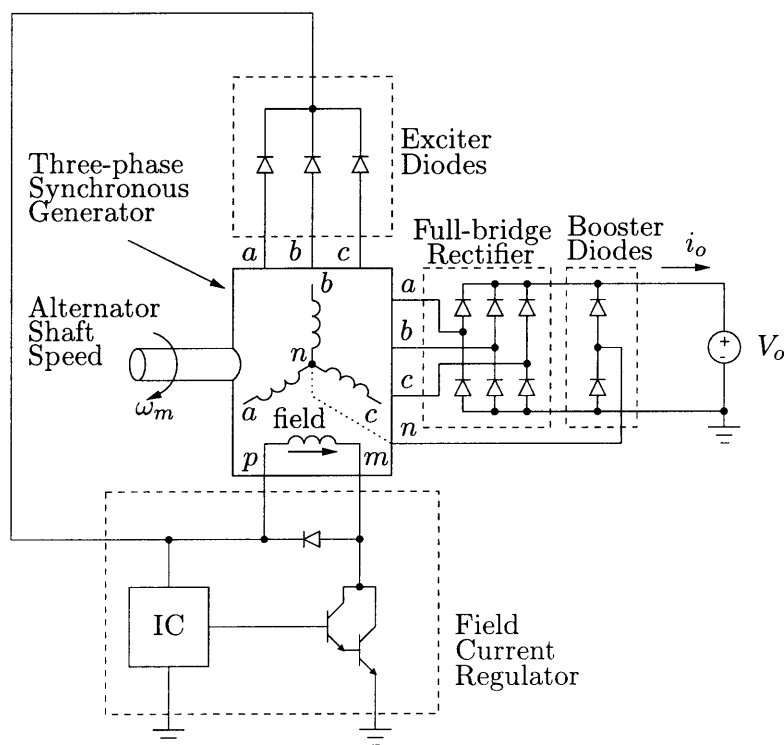
Figure 4.5: Automotive alternator system for simulation.

4.4 Alternator Simulation

In this section, we evaluate/validate the generator and regulator models developed in the last two sections by performing simulations and comparing them with experimental data. The performance characteristics of automotive alternators are usually specified by the current output capability of the system versus shaft speed at a prescribed output voltage. For our comparison, we will use data from a typical 14 V automotive alternator (Bosch NC 14V 60-120A) which is capable of delivering at 60 A at idle speed (1800 rpm) and 120 A at cruising speed (6000 rpm). The system being simulated is shown in Figure 4.5. To exercise the model, we will set the output voltage V_o equal to 13.5 V and measure the output current i_o (and its average value) over alternator shaft speeds ranging from 1800 to 18000 rpm. This is precisely the procedure used by the manufacturer to obtain the experimental data. Typical parameter values for the synchronous machine and the regulator are given in Tables 4.1 and 4.2. Unless otherwise specified, these are the values used in the simulations.

Since the alternator output voltage is set to 13.5 V and the desired output voltage is V_{ref} (= 14.2 V), the compensator within the regulator will force the power transistor to always be on.

Table 4.1: Synchronous machine parameters.

Parameter	Description	Typical Value
R_s	stator winding resistance	33 mΩ
L_{ls}	stator leakage inductance	15 μH
L_{ms}	stator magnetizing inductance	105 μH
R_f	rotor winding resistance	3.44 Ω
L_{lf}	rotor leakage inductance	300 mH
L_{mf}	rotor magnetizing inductance	150 mH
p	number of poles	12

Table 4.2: Field current regulator parameters.

Parameter	Description	Typical Value
V_{ref}	Alternator output voltage reference	14.2 V
K	Compensator dc gain	20
ω_c	Compensator cutoff frequency	1000 rad/s
f_r	Sawtooth frequency	140 Hz
V_r	Sawtooth voltage magnitude	5 V

With the power transistor on, the field current in the steady state will be given approximately by V_o/R_f.

Typical waveforms for a simulation at 1800 rpm are shown in Figure 4.6. The top waveform is the current in phase a of the machine and bottom waveform is the output (rectified) current. From the simulated waveform, the average value of the output current is calculated as 60.4 A. This simulation is performed at several values of alternator shaft speed. Each simulation is run long enough to reach steady state, then the output current is examined and its average value calculated as in Figure 4.6. The results of simulations over the speed range from 1800 rpm to 18000 rpm are shown in Figure 4.7. The dashed line in the figure represents manufacturer's experimental data. The simulation results are marked with a $\times$ and show excellent agreement with the experimental data. It should be noted that if the booster diodes at the alternator output are removed, the current output capability (data marked with $\circ$) above 3000 rpm is somewhat reduced. This reduction in output current ranges from 5–20 A in the speed range from 4000–18000 rpm and has been reported recently [43, 45]. Most alternators produced today do use the booster diode arrangement – especially those with rated output currents of 90 A or above.
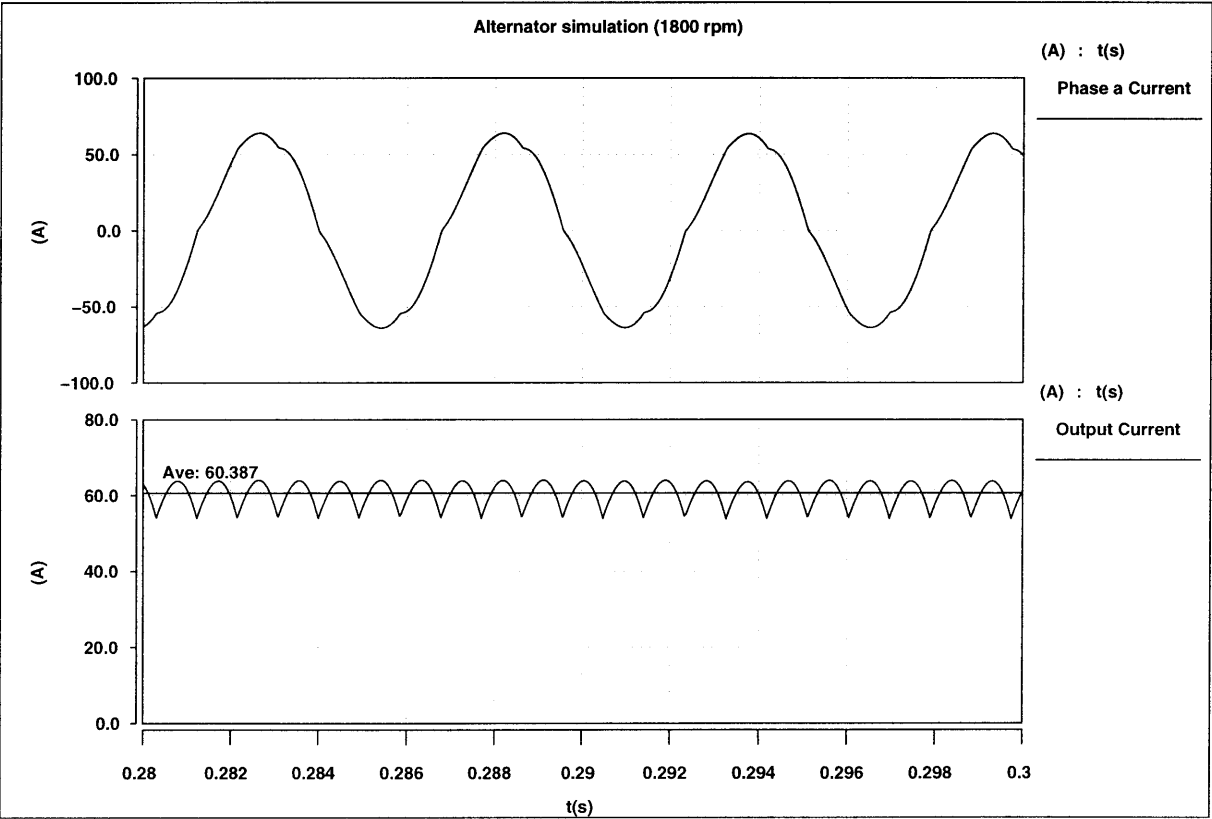
Figure 4.6: Simulation of alternator system at 1800 rpm: Phase a current (top) and alternator output current (bottom). The average value of the output current is approximately 60.4 A.
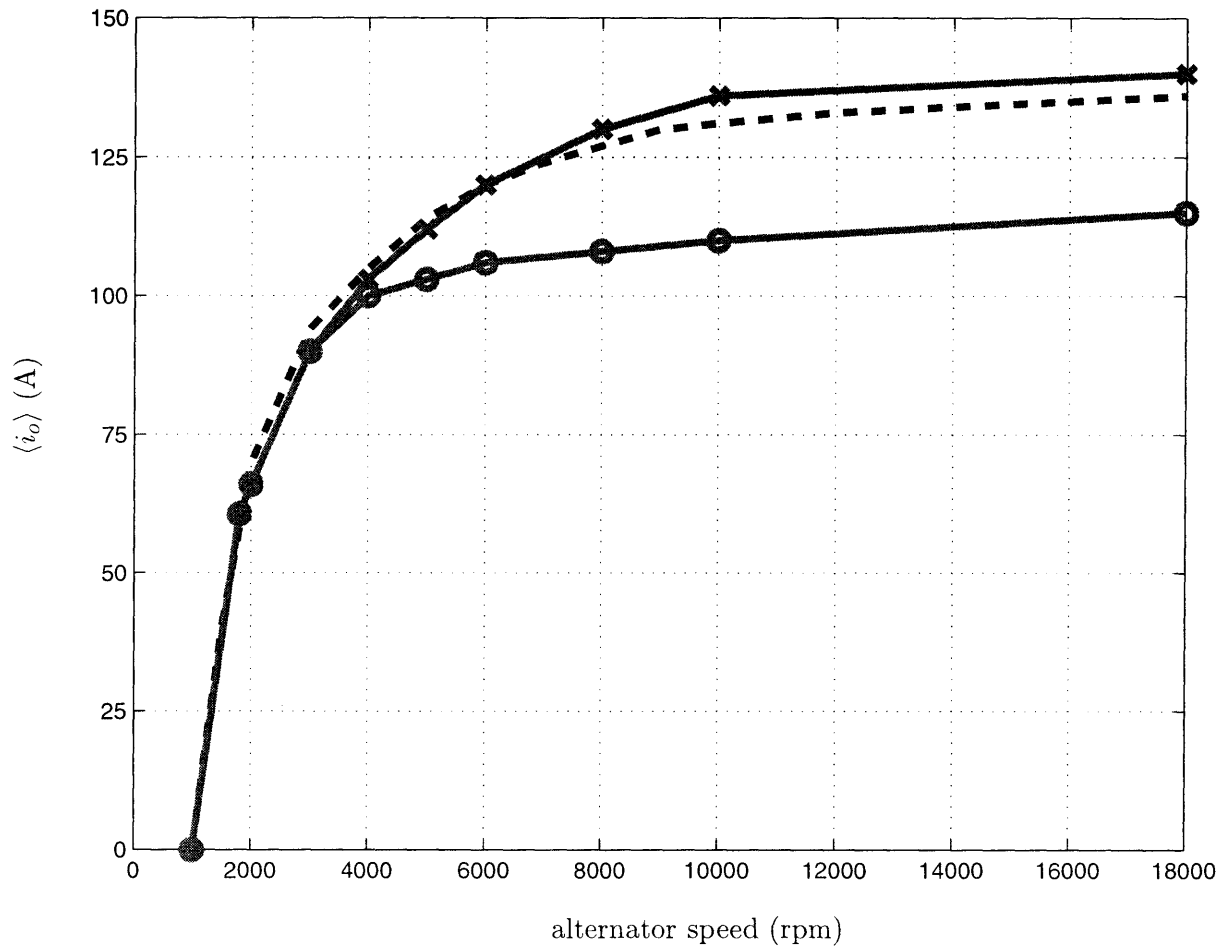
Figure 4.7: Comparison of alternator average output curent versus speed. Dashed line represents the experimental data from the manufacturer. The solid lines are constructed from simulation of the alternator with ($\times$) and without ($\circ$) the presence of booster diodes.

The model for the system consisting of the machine, regulator and rectifier can be used to study the steady-state and dynamic characteristics of alternator-based power systems - our focus here is automotive electrical systems. While the simulation results give excellent correlation with experimental data, the simulations are computationally intensive and therefore time consuming. This is especially true when the alternator system is embedded in a larger system with numerous other subsystems. For example, in load-dump transient simulations, the use of the full models that were developed in Section 4.2 are unavoidable. On the other hand, if one is interested in low frequency or steady-state behavior of the alternator system, it would be beneficial to have simplified models that are structurally simple yet computationally accurate. The next section addresses this question by developing averaged models for the alternator system.

4.5   Averaged Alternator Model

To derive an averaged model for the alternator, one can use a number of common assumptions to simplify the synchronous machine model described by (4.15). The most significant of these assumptions is to neglect the presence of third and higher harmonics in the averaged analysis. This is due to neglecting the third harmonic rectification by the booster diodes as described in Sections 4.1 and 4.4. This assumption substantially simplifies the analysis but does introduce errors of 5-20 A over the speed range from 1,800–18,000 rpm. However, the alternator speed is normally between 1800 rpm (idle) and 6,000 rpm (cruising) and the maximum error in the current over this range is about 10 A (9% error). Assuming a balanced system with balanced three-phase stator currents, we have

$$i_a + i_b + i_c = 0 \tag{4.17}$$

Using (4.17) in (4.15) results in the simplified version of the flux linkage equations given by

$$
\begin{bmatrix} \lambda_a(t) \\ \lambda_b(t) \\ \lambda_c(t) \\ \lambda_f(t) \end{bmatrix} = \begin{bmatrix} L_s & 0 & 0 & L_{af}(\theta) \\ 0 & L_s & 0 & L_{bf}(\theta) \\ 0 & 0 & L_s & L_{cf}(\theta) \\ L_{fa}(\theta) & L_{fb}(\theta) & L_{fc}(\theta) & L_{ff} \end{bmatrix} \begin{bmatrix} i_a(t) \\ i_b(t) \\ i_c(t) \\ i_f(t) \end{bmatrix} \tag{4.18}
$$

where $L_s \overset{\triangle}{=} L_{ls} + \frac{3}{2}L_{ms}$ is referred to as the stator synchronous inductance. In addition to balanced operation, if one further assumes that the stator currents are a three-phase set with constant

amplitude, the expression for the field flux linkage in (4.18) simplifies to

$$\lambda_f(t) = \Lambda_f + L_{ff}i_f(t) \tag{4.19}$$

where Λ_f is time-independent. The detailed derivation of (4.19) is presented in Appendix B. Based on this simplified expression for the field flux linkage, the matrix expression in (4.18) can be rewritten as

$$
\begin{bmatrix} \lambda_a(t) \\ \lambda_b(t) \\ \lambda_c(t) \\ \lambda_f(t) \end{bmatrix}
=
\begin{bmatrix}
L_s & 0 & 0 & M\cos(\theta) \\
0 & L_s & 0 & M\cos(\theta - \frac{2\pi}{3}) \\
0 & 0 & L_s & M\cos(\theta + \frac{2\pi}{3}) \\
0 & 0 & 0 & L_{ff}
\end{bmatrix}
\begin{bmatrix} i_a(t) \\ i_b(t) \\ i_c(t) \\ i_f(t) \end{bmatrix}
+
\begin{bmatrix} 0 \\ 0 \\ 0 \\ \Lambda_f \end{bmatrix}
\tag{4.20}
$$

The induced voltages of the phase and field windings may be found by taking the derivatives of the flux linkages in (4.20) and are given by

$$\frac{d\lambda_a(t)}{dt} = L_s \frac{di_a(t)}{dt} + M\cos(\theta)\frac{di_f(t)}{dt} - \omega M \sin(\theta)i_f(t) \tag{4.21}$$

$$\frac{d\lambda_b(t)}{dt} = L_s \frac{di_b(t)}{dt} + M\cos\left(\theta - \frac{2\pi}{3}\right)\frac{di_f(t)}{dt} - \omega M \sin\left(\theta - \frac{2\pi}{3}\right)i_f(t) \tag{4.22}$$

$$\frac{d\lambda_c(t)}{dt} = L_s \frac{di_b(t)}{dt} + M\cos\left(\theta + \frac{2\pi}{3}\right)\frac{di_f(t)}{dt} - \omega M \sin\left(\theta + \frac{2\pi}{3}\right)i_f(t) \tag{4.23}$$

$$\frac{d\lambda_f(t)}{dt} = L_{ff}\frac{di_f(t)}{dt} \tag{4.24}$$

where ω is the electrical angular frequency as defined in (4.3). A simplified schematic of a Y-connected three-phase synchronous machine based on the induced winding voltages of (4.21)-(4.24), is shown in Figure 4.8. The phase winding resistances (R_s) and the field winding resistance (R_f) are also explictly shown. Writing a KVL equation for each of the windings yields

$$v_a(t) = R_s i_a(t) + L_s \frac{di_a(t)}{dt} + M\cos(\theta)\frac{di_f(t)}{dt} - \omega M \sin(\theta)i_f(t) \tag{4.25}$$

$$v_b(t) = R_s i_b(t) + L_s \frac{di_b(t)}{dt} + M\cos\left(\theta - \frac{2\pi}{3}\right)\frac{di_f(t)}{dt} - \omega M \sin\left(\theta - \frac{2\pi}{3}\right)i_f(t) \tag{4.26}$$

$$v_c(t) = R_s i_c(t) + L_s \frac{di_b(t)}{dt} + M\cos\left(\theta + \frac{2\pi}{3}\right)\frac{di_f(t)}{dt} - \omega M \sin\left(\theta + \frac{2\pi}{3}\right)i_f(t) \tag{4.27}$$

$$v_f(t) = R_f i_f(t) + L_{ff}\frac{di_f(t)}{dt} \tag{4.28}$$

The phase terminal voltages v_a, v_b and v_c indicated in Figure 4.8 and given in (4.25)-(4.27) are measured with respect to the neutral terminal and the phase currents i_a, i_b and i_c are chosen in the *motoring* direction. In an automotive alternator, the positive (top) field terminal is normally

connected to the alternator output voltage whereas the negative (lower) field terminal is connected to the field current (voltage) regulator. The voltage regulator controls the field current i_f in order to regulate the alternator output voltage.
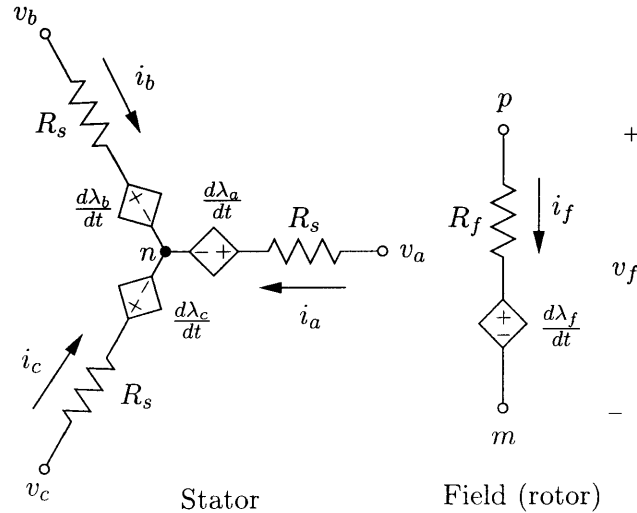
Figure 4.8: Simplified diagram showing each of the phases and the field winding of the synchronous machine.

One can construct an equivalent circuit of the synchronous machine which corresponds to the voltage equations (4.25)-(4.28). Such an equivalent circuit is shown in Figure 4.9 where the phase currents are shown in the *generating* direction. This equivalent circuit can be further simplified under certain special situations. For instance, the field current (with time constant $\frac{L_f}{R_f}$) usually varies much more slowly than the phase currents; therefore, one may neglect the dependent voltage sources that are proportional to $\frac{di_f(t)}{dt}$. In many instances, the field current is assumed to be constant which results in the same simplification. As a consequence of the preceding simplifications, the synchronous machine can be reduced to the classic three-phase set of voltages each with a corresponding synchronous inductance and winding resistance which is illustrated in Figure 4.10.

The three-phase synchronous generator connected to a diode bridge rectifier with a constant voltage-source is shown in Figure 4.11. The averaged modeling of this rectifier system was one of the subjects of Chapter 3 where we developed an approximate expression for the average output current $\langle i_o \rangle$. In this section, we develop an averaged equivalent circuit for this system. As in Chapter 3, we begin with the assumption that v_{sa}, v_{sb} and v_{sc} are a three phase set of voltages
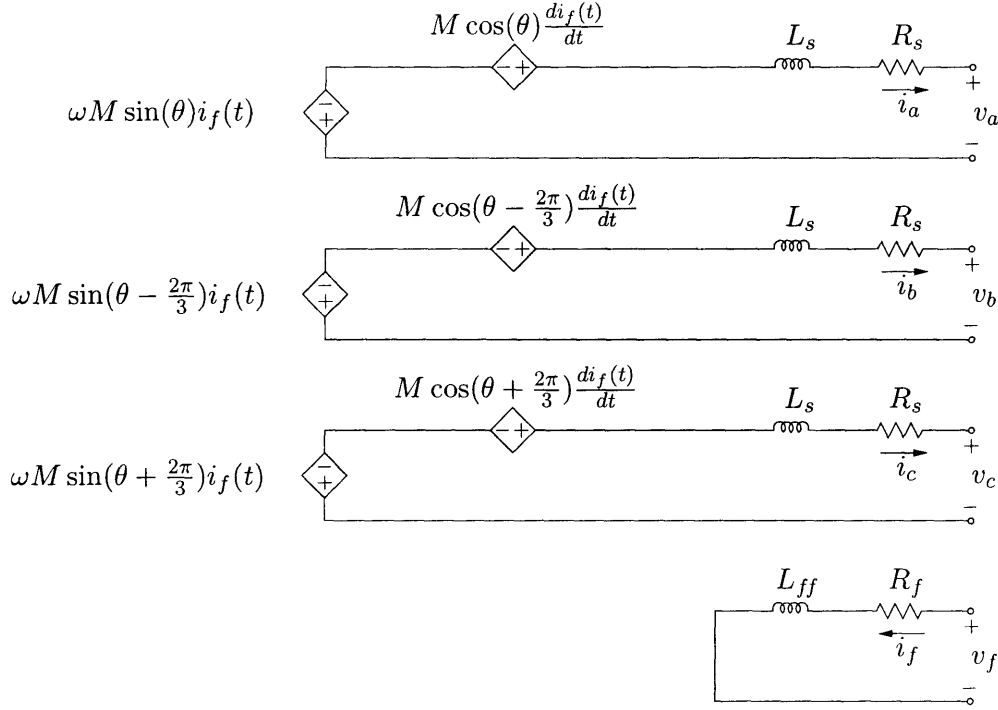
Figure 4.9: Equivalent circuit of the simplified three-phase synchronous generator.

with magnitude V_s and angular frequency ω:

$$v_{sa} = V_s \sin(\omega t) \tag{4.29}$$

$$v_{sb} = V_s \sin(\omega t - 2\pi/3) \tag{4.30}$$

$$v_{sc} = V_s \sin(\omega t + 2\pi/3) \tag{4.31}$$

The magnitudes V_s of the voltage sources can be calculated by using the analysis of last section and are given by $\omega M I_f$. The diodes in the full bridge rectifier are assumed ideal except for a finite on-voltage, V_d. In developing this model we follow the assumptions and notation of Section 3.2. We repeat here some of the assumptions for convenience. We start our analysis by assuming (as in Chapter 3) that phase currents i_a, i_b and i_c are continuous and can be well approximated by their fundamental components

$$i_a \approx i_{a1} = I_{s1} \sin(\omega t - \phi) \tag{4.32}$$

$$i_b \approx i_{b1} = I_{s1} \sin(\omega t - \phi - 2\pi/3) \tag{4.33}$$

$$i_c \approx i_{c1} = I_{s1} \sin(\omega t - \phi + 2\pi/3) \tag{4.34}$$

where I_{s1} is the magnitude of the fundamental phase current ϕ is the phase angle between the voltage
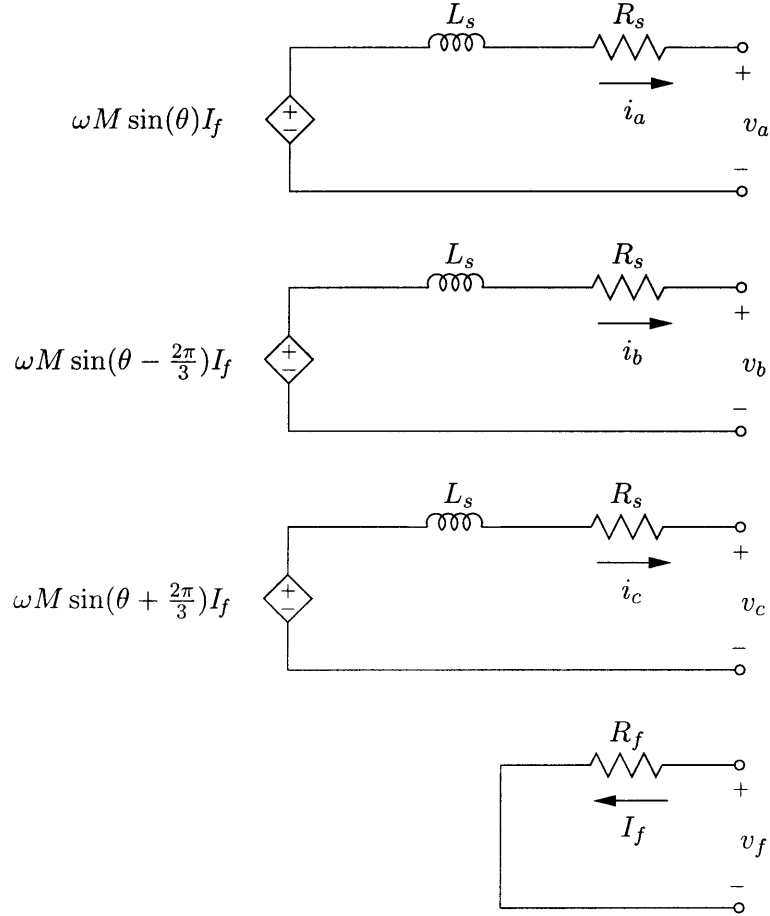
Figure 4.10: Equivalent circuit of the simplified three-phase synchronous generator assuming constant or slowly varying field current denoted as I_f. The phase angles for the source voltages have been shifted, without loss of generality, to reflect the three-phase set based on sine waves.

source and the corresponding current in each phase. Note that I_{s1} and ϕ could be computed using the methods developed in Section 3.2; however, our purpose here is to derive an equivalent circuit model based on an averaged analysis. Based on the above assumptions, it can be shown that there are six conduction intervals within each operating period. During each of the six intervals, three of the six diodes in the bridge conduct. It is sufficient to consider one of these intervals for the averaging process. For example, consider the time interval when diodes 1, 2 and 6 are conducting. This conduction pattern corresponds to the case where $i_a > 0$, $i_b < 0$ and $i_c < 0$ and is illustrated in Figure 4.12. Writing a KVL equation around the loop with phases a and c, diodes D_1 and D_2 and the voltage source V_o gives:

$$v_{sa} - v_{sc} = L_s \frac{di_a}{dt} + R_s i_a - L_s \frac{di_c}{dt} - R_s i_c + 2V_d + V_o \qquad (4.35)$$
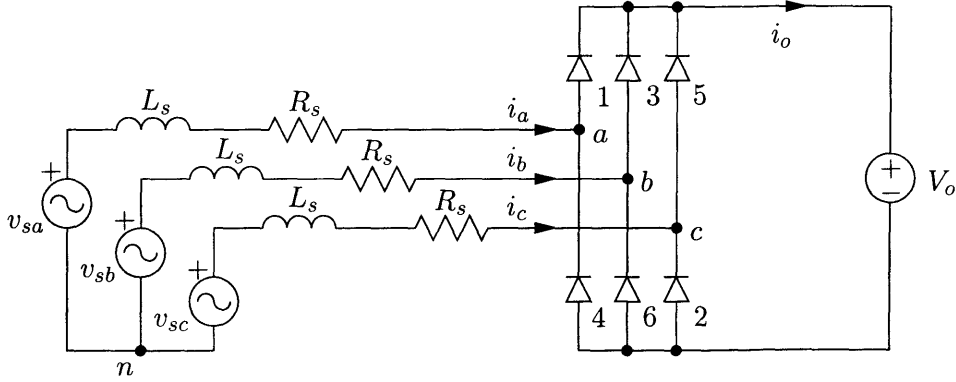
Figure 4.11: Three-phase diode bridge rectifier including phase synchronous inductance and winding resistance.
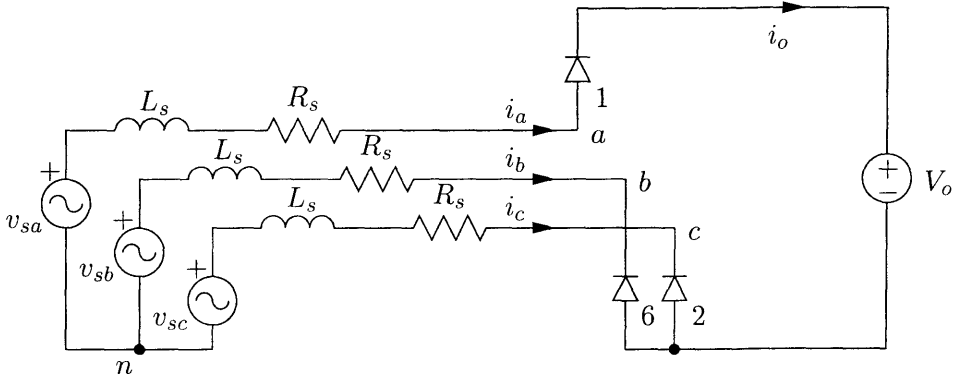
Figure 4.12: Three-phase diode bridge rectifier equivalent circuit during the interval when diodes 1, 2 and 6 are conducting.

Substituting (4.31) and (4.34) in (4.35) and simplifying yields:

$$\sqrt{3}V_s \sin\left(\omega t - \frac{\pi}{6}\right) = ZI_{s1}\cos(\omega t - \phi - \alpha) - ZI_{s1}\cos\left(\omega t - \phi + \frac{2\pi}{3} - \alpha\right) + 2V_d + V_o \quad (4.36)$$

where $Z = \sqrt{R_s^2 + (\omega L_s)^2}$ and $\alpha = \tan^{-1}(\frac{R_s}{\omega L_s})$. A sketch of the phase a current over the interval of interest is illustrated in Figure 4.13. As can be seen from this figure, phase a current i_a is identical to the output current during the interval $\phi + \frac{\pi}{3} \leq \omega t \leq \phi + \frac{2\pi}{3}$. Averaging (4.36) over a conduction angle of $\frac{\pi}{3}$ yields the following expression:

$$\sqrt{3}V_s\left(\frac{3}{2\pi}\left[\sqrt{3}\cos\phi + \sin\phi\right]\right) = ZI_{s1}\left(\frac{3}{\pi}\sin\alpha\right) - ZI_{s1}\left(-\frac{3}{2\pi}\left[\sqrt{3}\cos\alpha + \sin\alpha\right]\right) + 2V_d + V_o$$

$$(4.37)$$

Using trigonometric identitites for angles ϕ and α, the expression in (4.37) can be further simplified

to

$$\underbrace{\frac{3\sqrt{3}}{\pi} V_s \cos\left(\phi - \frac{\pi}{6}\right)}_{V_e} = \underbrace{\left[\frac{3R_s}{2} + \frac{\sqrt{3}\omega L_s}{2}\right]}_{Z_e(\omega)} \underbrace{\frac{3}{\pi} I_{s1}}_{\triangleq \langle i_o \rangle} + 2V_d + V_o \qquad (4.38)$$

Now let us examine each of the components of the above expression. The left hand side of (4.38) represents an effective dc source voltage V_e reflected from the ac-side to the dc-side. We note that given component values, angle ϕ is a constant; therefore, $\cos\left(\phi - \frac{\pi}{6}\right)$ can be evaluated using (3.23) as shown in Chapter 3. The expression for $Z_e(\omega)$ in square brackets on the right hand side of (4.38) represents the effective dc-side impedance of the stator winding. The term multiplying the effective impedance is simply the average value of output current $\langle i_o \rangle$ which was defined in (3.19) in Chapter 3. Figure 4.14 shows an averaged equivalent circuit based on the expression in (4.38). The details of the Saber implementation of the averaged alternator including an integrated voltage regulator are given in Appendix C while the computer code is given in Appendix D.
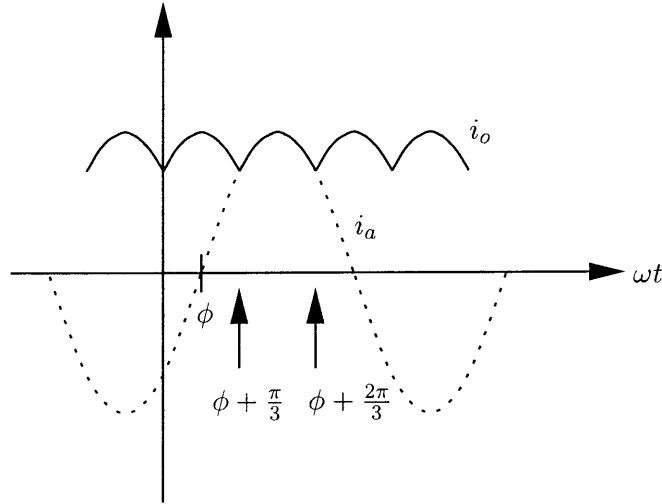
Figure 4.13: Phase a current i_a and output current i_o. During the interval when diodes 1, 2 and 6 are conducting $(\phi + \frac{\pi}{3} \le \omega t \le \phi + \frac{2\pi}{3})$ i_a is identical to i_o.

4.6 Averaged Alternator Simulation

In this section, we simulate the averaged alternator model and compare it to the manufacturer's data. The system structure is identical to that of Figure 4.5 except for the synchronous generator and rectifier systems which are replaced by our averaged model. The use of the averaged model
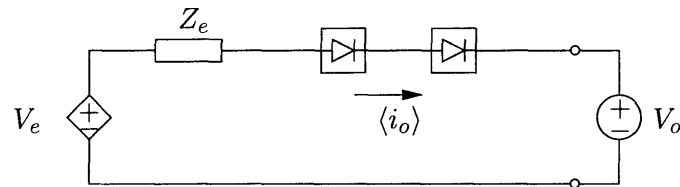
Figure 4.14: Averaged equivalent circuit for synchronous generator with a bridge rectifier driving a constant-voltage load. V_e and Z_e are effective voltage and impedance of the machine reflected to the dc-side.

reduces computational complexity and leads to shorter simulation times. However, since we are neglecting higher harmonics and the presence of booster diodes, we know our results will be less accurate than the full model presented earlier in the chapter.

The simulations are shown in Figure 4.15 and use the parameters given in Tables 4.1 and 4.2. Looking at the figure, we see that there is good agreement between the simulation (solid line) and the manufacturer's data (dashed line). There is about a 10-15% error in our predictions due to our simplifications. However, the averaged model does display the correct trend in the output current and its accuracy can be improved, e.g., by including the effect of the third harmonic in the averaged model. Another method to improve the simulation would be to adjust the effective voltage V_e to take into account the presence of third and higher harmonics in the phase voltages.

4.7   Summary

In this chapter, the mathematical modeling of the Lundell alternator was investigated. After a brief overview of the automotive power generation system, analytical models for the alternator system were developed based on flux linkage equations of a three-phase synchronous machine. An alternator regulator model was also developed and used in the simulation of the alternator system. Simplifying assumptions were used to derive an averaged model which reduces the computational complexity at the cost of accuracy. The averaged model for a three-phase rectifier with constant-voltage load developed in Chapter 3 and the averaged alternator model developed in Section 4.5 can be both used to answer questions about the power output capabilities of an alternator. The averaged model in Chapter 3 is better for hand calculations whereas the averaged model developed in this chapter is circuit-based and is more appropriate for averaged circuit simulations. For example, the circuit-based averaged model is ideal for vehicle electrical load-flow simulations where the simulation is run over drive cycles which model hours of actual driving. Since load-flow simulations are more concerned with power flow and not the details of alternator operation, the use of the averaged model is justified and substantially reduces simulation time [46].
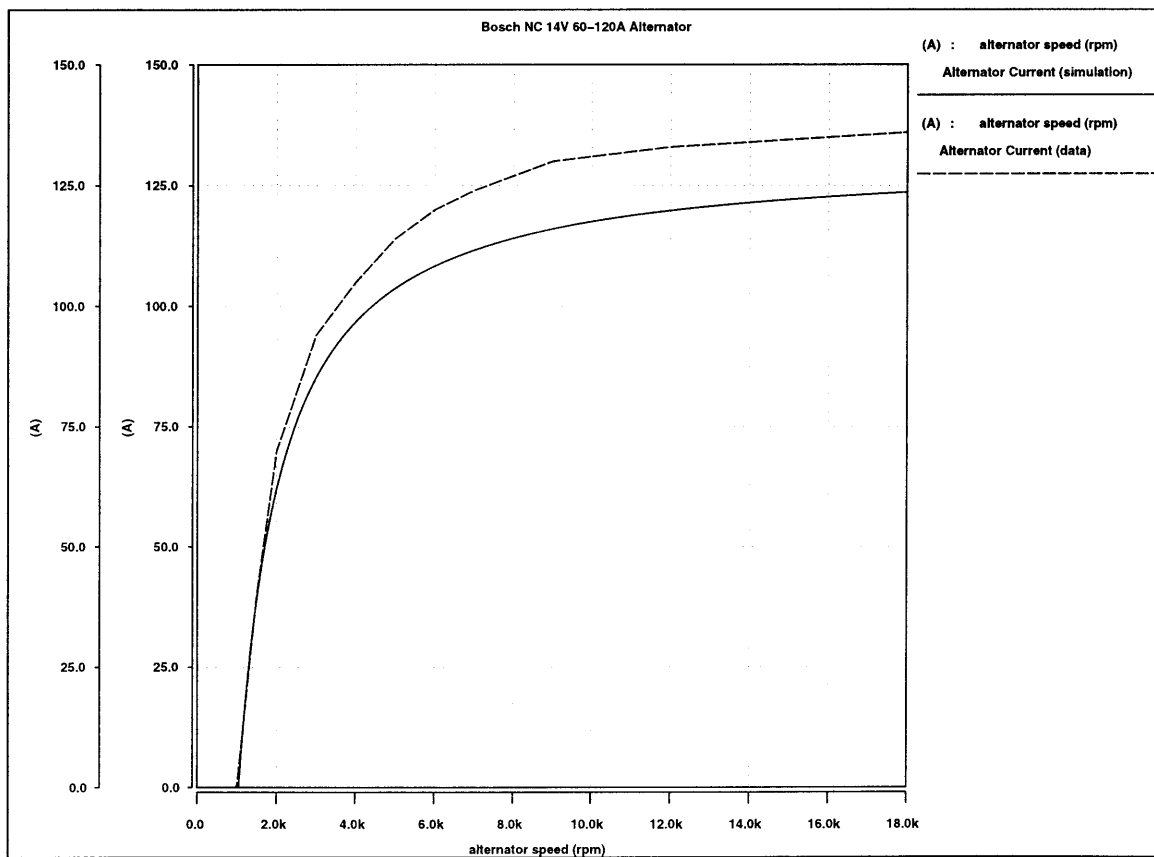
Figure 4.15: Comparison of the averaged alternator model with the data for the Bosch NC 14 V 60-120 A alternator. The dashed line is manufacturer's data and the solid line is the result of the Saber simulation of the averaged model.

Chapter 5

Dual-Controlled Alternator

This chapter describes some new developments in the application of power electronics to automotive power generation and control. A new load-matching technique is introduced that allows substantial increases in the output power capability and efficiency of automotive alternators to be achieved through the use of a simple switched-mode rectifier. Using the models developed in Chapters 3 and 4, analysis and implementation of the proposed technique are addressed and analytical control laws for the approach are established. Experimental results are provided that demonstrate large increases in peak and average power output capability from a conventional Lundell alternator, along with commensurate improvements in efficiency. Additional performance and functionality improvements of particular value in high voltage (e.g., 42 V) alternators are also demonstrated. We show that tight load dump transient suppression can be achieved using this new architecture. It is also shown that the alternator system can be used to implement jump charging (the charging of the high-voltage system battery from a low-voltage source). Experimental results from a prototype system are provided that demonstrate the transient suppression and jump charging features of the proposed architecture.

5.1   Introduction

Here we consider a new technology suitable for automotive alternators. The new approach allows much higher levels of output power and efficiency to be achieved as compared to conventional systems while retaining low cost and simplicity of structure and control. Section 5.2 of the chapter describes the behavior of conventional wound-field automotive alternators (i.e., Lundell alternators) and develops simple analytical models for the alternator system. Section 5.3 of the chapter introduces a new alternator design and control technique which uses both field control and a simple switched-mode rectifier. A load-matching control technique is introduced which allows the system to achieve very high levels of output power and efficiency. Section 5.4 shows experimental results from a prototype system that demonstrate the high performance of the system and validates the analytical predictions.

We also show how the proposed approach can be used to provide two functional improvements of great importance in dual- and high-voltage electrical systems. Section 5.5 of the chapter demonstrates that tight load-dump transient suppression can be achieved using the proposed alternator system. Section 5.6 introduces a new technique by which the proposed alternator system can be used to jump charge a high-voltage battery from a low-voltage source. In each case, experimental results from a prototype system are used to validate the proposed operating technique. Finally Section 5.7 presents a summary and assessment of the new developments.

5.2   The Lundell Alternator

The Lundell, or claw-pole, alternator is a wound-field synchronous machine in which the rotor comprises a pair of stamped pole pieces ("claw poles") secured around a cylindrical field winding. The field winding is driven from the stator via a pair of slip rings. The stator is wound in a three-phase configuration and a full-bridge diode rectifier is traditionally used at the machine output. Alternator system output voltage (or current) is controlled by regulating the field current. A relatively long field time constant and a high armature leakage reactance are characteristic of this type of alternator, and tend to dominate its electrical performance.

5.2.1   A Simple Alternator Electrical Model

Figure 5.1 shows a simple electrical model for a Lundell alternator system. The field current i_f of the machine is determined by the field current regulator which applies a pulse-width modulated voltage across the field winding. Average field current is determined by the field winding resistance and the average voltage applied by the regulator. Changes in field current occur with an L/R field-winding time constant that is typically on the order of 100 ms or more.

The armature is modeled as a Y-connected set of sinusoidal three-phase back emf voltages v_{sa}, v_{sb}, and v_{sc} and leakage inductances L_s. The electrical frequency ω of the back emf voltages is proportional to the alternator mechanical speed ω_m and the number of machine poles p ($\omega = \frac{p}{2}\omega_m$). The magnitude of the back emf voltages is proportional to both frequency and field current:

$$V_s = k\omega i_f \tag{5.1}$$

A diode bridge rectifies the ac machine outputs into a constant voltage V_o representing the battery and associated loads. As will be seen, this simple model captures many of the important characteristics of alternators while remaining analytically tractable. Other effects, such as stator
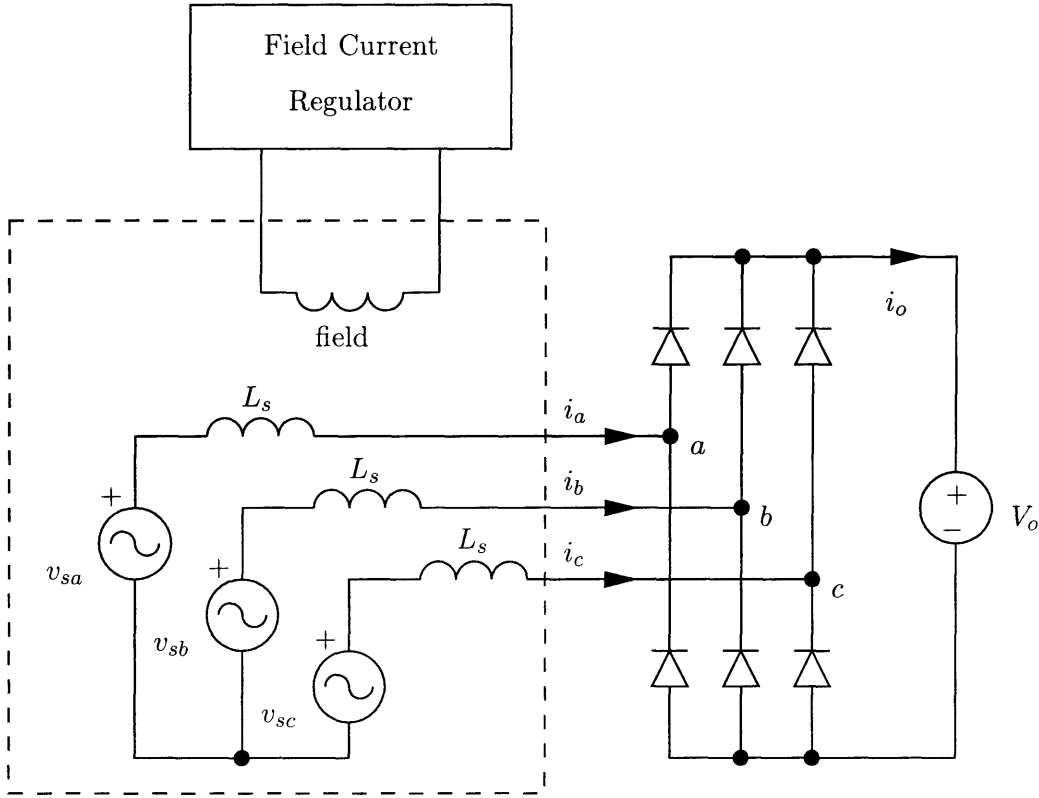
Figure 5.1: Simple Lundell alternator model.

resistance and mutual coupling, magnetic saturation, waveform harmonic content, etc., can also be incorporated into the model at the expense of simplicity.

5.2.2 Alternator Electrical Behavior

To characterize alternator electrical behavior we turn to the simple electrical model of Figure 5.1. The constant-voltage load of the rectifier makes the analysis of the system different from the classic case of a rectifier system with a current-source (or inductive) load [40]. Nevertheless, with reasonable approximations the behavior of this system can be described analytically, as shown in Chapter 3. For example, alternator output power vs. operating point can be calculated as:

$$P_{out} = \frac{3V_o}{\pi} \frac{V_s{}^2 - V_{o1}^2}{V_{o1}R_s + \sqrt{(\omega L_s)^2 \left(V_s{}^2 - V_{o1}^2\right) + R_s^2 V_s^2}} \tag{5.2}$$

where $V_{o1} = \frac{4}{\pi}(V_o/2 + V_d)$, V_o is the output voltage, V_d is the on-voltage of the bridge diodes, V_s is the back emf magnitude, ω is the electrical frequency, R_s stator winding resistance and L_s is the

stator synchronous inductance.

Figure 5.2 shows the calculated output power versus output voltage of a conventional 14 V automotive alternator at constant (full) field current, parameterized by the speed of the alternator. The accuracy of these curves in capturing the behavior of a real alternator are demonstrated in Sec 5.4. As can be seen, for any given speed there is a substantial variation in output power capability with output voltage. At each speed there is an output voltage above which the output current (and hence output power) becomes zero. This voltage corresponds to the peak of the line-to-line back emf voltage, above which the diodes in Figure 5.1 will not conduct. At each speed there is also a single output voltage at which maximum output power is achieved, and this output voltage is substantially below the line-to-line back emf voltage magnitude. This behavior can be traced to the large armature leakage inductances of the Lundell machine. Significant voltage drops occur across the leakage inductances when current is drawn from the machine, and these drops increase with increasing output current and operating speed. Consequently, the Lundell alternator exhibits heavy load regulation when used with a diode rectifier. For example, in a typical automotive alternator, back voltages in excess of 80 V may be needed to source rated current into a 14 V output at high speed. An appropriate dc-side model for the system is a large open circuit voltage in series with a large speed- and current-dependent output impedance. The output power vs. output voltage characteristics of Figure 5.2 may then be understood in terms of the maximum power transfer theorem for a source with output impedance. In short, the high armature leakage reactance of the Lundell machine results in a large dc-side output impedance, and necessitates the use of large back-emf voltages to source rated current. This high alternator output impedance results in the power deliverable by the alternator at a given speed to be maximized only at a single "load matched" output voltage.

Consider the operational characteristics of the automotive alternator system described by Figure 5.2. The output power vs. output voltage curves of Figure 5.2 are calculated for constant (full) field current and parameterized by the speed of the alternator, with 1800 rpm corresponding to idle speed and 6000 rpm corresponding to cruising speed. At any given speed and output voltage, output power can be reduced below the value shown by reducing the field current, which in turn reduces the back-emf voltage and output current. If the alternator is used at the designed output voltage of 14 V, then the output power capability across speed is represented by the vertical 14 V locus intersecting the curves of Figure 5.3. The alternator delivers its maximum idle speed power near the 14 V design voltage. At higher speeds and 14 V output, the alternator delivers more power (up to about 1500 W at 6000 rpm), but does not achieve the maximum power possible across voltage because of the way the voltage-power curve changes with engine speed. At 42 V output and 6000 rpm, for example, the alternator can deliver over 3500 W. Nevertheless, this alternator could not usually be used for a 42 V system, because at 42 V output and lower speeds the output power drops

P_{alt} vs. V_x for various alternator speeds
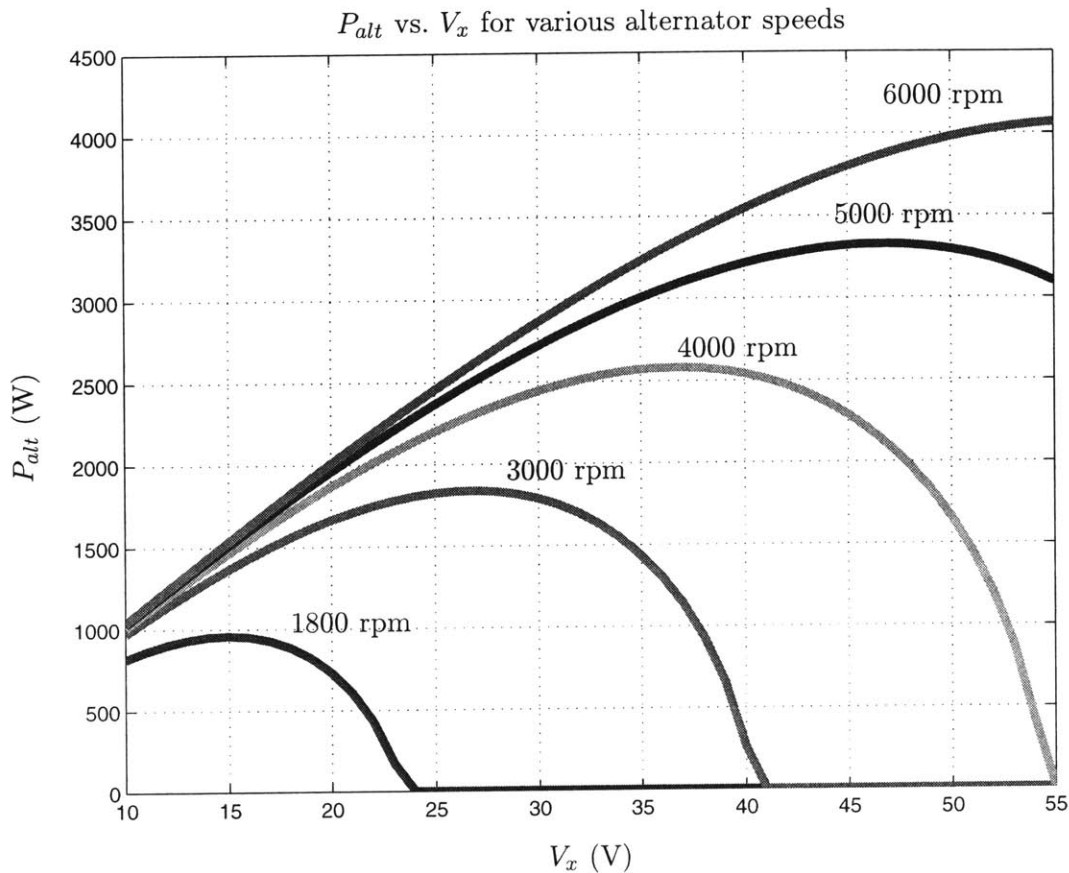
Figure 5.2: Calculated alternator output power vs. rectifier output voltage for several speeds.

off rapidly, with no power generation at idle speed. Thus, the need to generate sufficient power at the low speed means that the peak power capability of the machine across voltage is not achieved at higher speeds.

It should be also noted how the alternator characteristics change with the winding of the stator. As described above, the output power vs. output voltage curves of Figure 5.2 are well-suited to an output voltage of 14 V, but not suitable for use at a higher voltage such as 42 V. If one wanted to operate at 42 V, one could rewind the stator with three times as many turns of wire having about 1/3 the cross-sectional area. Based on the simplified models of Chapter 3, this would have the effect of stretching the horizontal axis in Figure 5.2 such that the all the curves would peak with the same output power at 3 times the output voltage (e.g. with the 1800 rpm curve peaking near 42 V). Thus, to first order, the output power capability of an alternator of a given size does not depend on the output voltage for which it is designed, since the stator may be rewound to provide the same power characteristics vs. speed at any other fixed output voltage.

Alternator output power vs. V_x
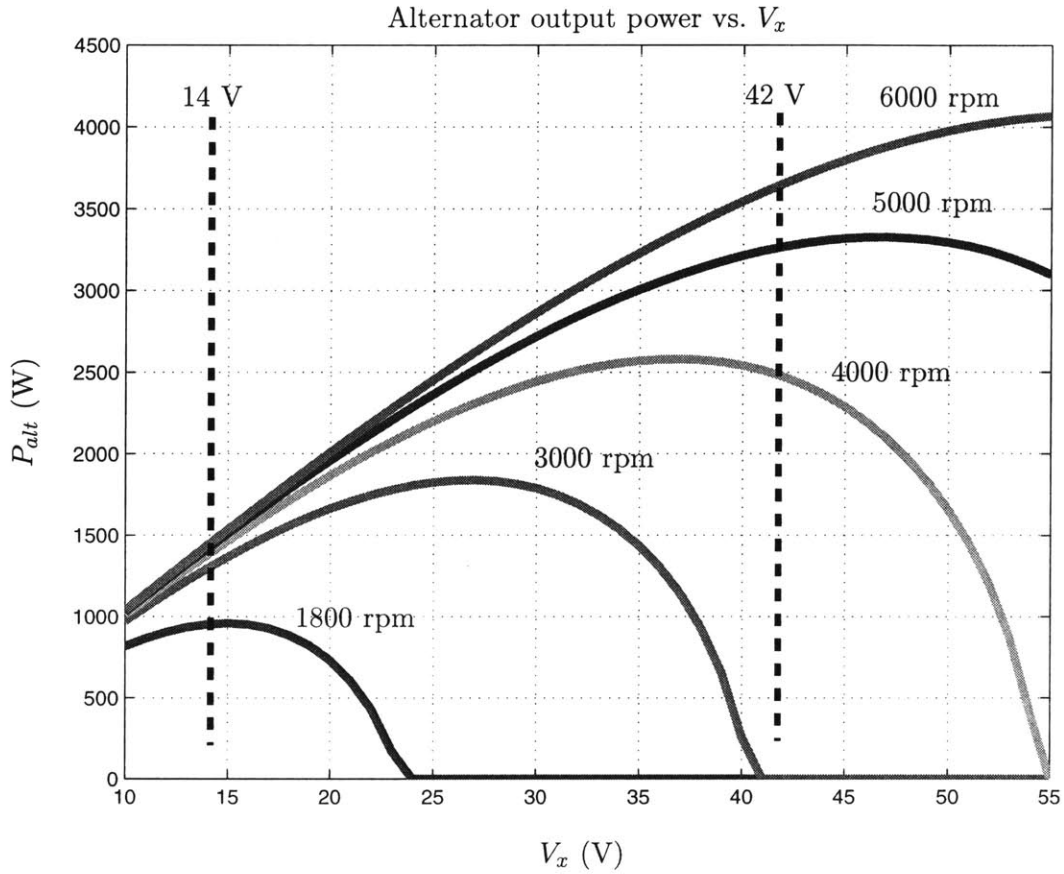
Figure 5.3: Alternator operating loci for 14 V and 42 V operation.

5.3 The Load Matching Concept

We now introduce a new design and control approach for automotive alternators. The new alternator system uses both field control and a simple switched-mode rectifier (SMR) with a conventional claw-pole alternator to achieve substantially higher levels of power and performance [47]. High power is achieved by using the switched-mode rectifier as a second control handle to properly match the constant-voltage load to the alternator.

5.3.1 SMR Load Matching

Consider the alternator and switched-mode rectifier shown in Figure 5.4. In this system, a diode bridge is followed by a "boost switch set" comprising a controlled switch (such as a MOSFET) Q_x and a diode D_x. The switch Q_x is turned on and off at high frequency in a Pulse-Width

Modulation (PWM) fashion with duty ratio d. The diode bridge operates in continuous conduction mode (CCM), so that the diode D_x is on when Q_x is off. The PWM operation of Q_x and D_x causes the voltage v_x to be a pulsating waveform with an average value dependent on the output voltage v_o and the duty ratio d. Neglecting device drops, and assuming v_o is relatively constant over a PWM cycle, we may calculate the local average value of v_x as:

$$\langle v_x \rangle = (1-d)v_o. \tag{5.3}$$

Similarly, assuming the diode bridge output current i_x is approximately constant over a switching cycle, we may calculate the local average output current, i_o, of the alternator system as:

$$\langle i_o \rangle = (1-d)i_x. \tag{5.4}$$

In an averaged sense, the boost switch set acts as a dc transformer with a turns ratio controlled by the PWM duty ratio d. Because the PWM frequency is much higher than the ac frequency and the machine inductances L_s are relatively large, the alternator machine and diode bridge react to the average value of v_x almost exactly as they would to the output voltage in a conventional diode-rectified alternator. As a result, by controlling the duty ratio d, one has control over the average voltage at the output of the bridge, v_x, to any value below the true output voltage of the alternator system, v_o. The switched-mode rectifier can thus be used as an additional control handle to extract much higher levels of performance from the alternator. For example, consider that in the present system, the maximum possible output power of the alternator at a given speed and field current is determined by the average of v_x, not by the output voltage v_o. By adjusting the duty ratio d, and hence v_x the alternator can generate up to its maximum power as speed varies, while supplying a constant output voltage, v_o, (of 50 V, for example). As illustrated in Figure 5.5, this operating mode allows much more power to be drawn from the machine at most speeds than is achievable with a diode rectifier supplying a fixed output voltage (Figure 5.3). What makes this possible is that the switched-mode rectifier provides the necessary controlled voltage transformation to match the constant-voltage load to the alternator. This load matching is most simply achieved by appropriately controlling the SMR duty ratio as a function of alternator speed. The output power can be efficiently regulated to any value below the achievable maximum with field control.

Examining the output power vs. output voltage curves of Figures 5.2, 5.3 and 5.5, we see that while this particular machine is suited for use at 14 V output with a diode rectifier, with the new SMR load-matching technique and the boost-type rectifier of Figure 5.4, it is better suited to a higher output voltage (e.g., 50-55 V). Figure 5.6 shows the output power capability (at full field) for this (theoretical) machine as a function of alternator speed for different operating conditions. Used with a diode rectifier at its optimized voltage of 14 V, the machine is capable of generating
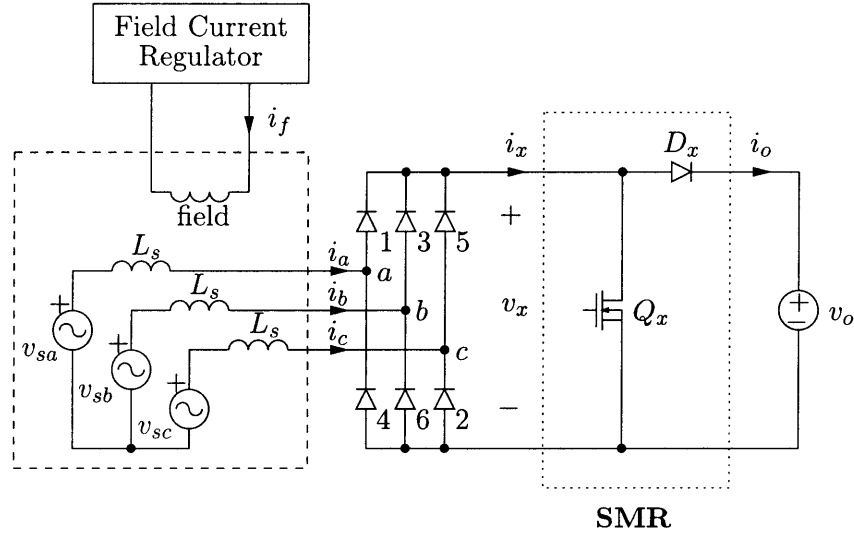
(a)
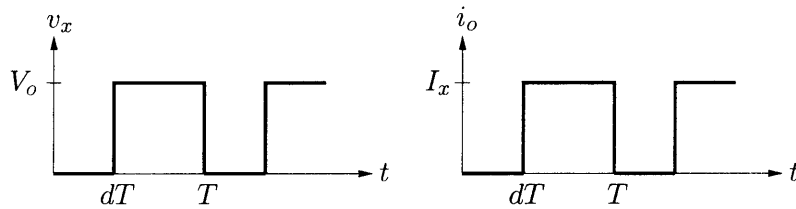
(b)

Figure 5.4: Switched-mode rectifier: (a) load matching stage inserted in an alternator, (b) representative waveforms.

approximately 1 kW at idle (1800 rpm), increasing up to approximately 1.5 kW at cruising speed (6000 rpm). Operating with the new load-matching SMR at its (approximately optimal) voltage of 50 V output, the machine is capable of similar performance at idle, but its power capability increases to 4 kW at cruising speed! *This improvement in power capability is not fundamentally due to the change in output voltage, since to first order the machine can be rewound to operate at any voltage with the same power capability.* Rather, the improvement results from using an additional degree of control freedom to achieve load matching over the alternator speed range.

It should also be pointed out that a machine suitable for diode rectification at 14 V may also be directly employed at 42 V (without rewinding) by using a switched-mode rectifier and

Alternator output power vs. V_x
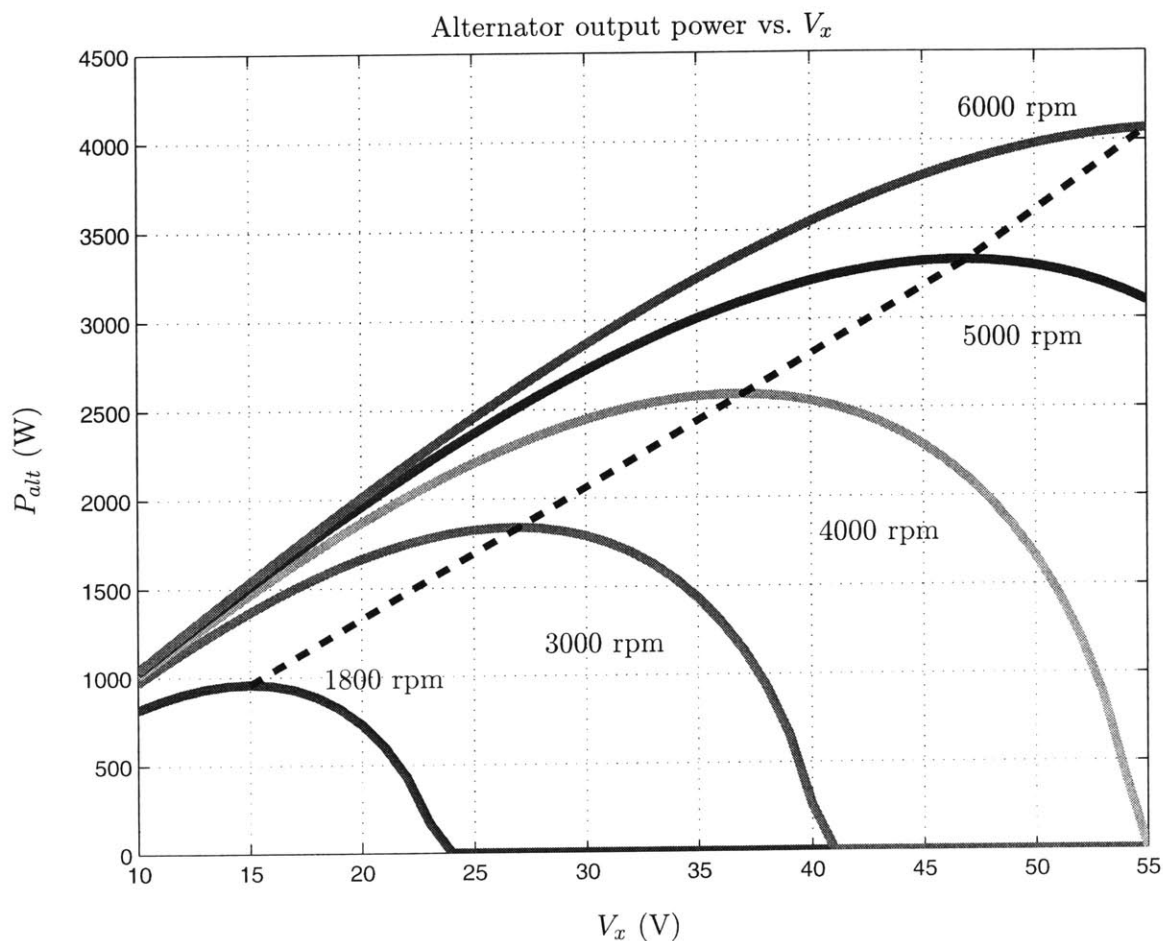
Figure 5.5: Alternator operating locus for load-matched operation. The alternator operates at the peak of the alternator power/voltage curve at every speed.

the new load-matching technique. This is relevant due to the imminent introduction of 42 V automotive electrical systems which will require 42 V alternators. Operation under this condition is also illustrated in Figure 5.6. For much of the speed range, load matching can be achieved at full field, and the maximum load-matched power can be obtained. Above a certain speed, the SMR duty ratio goes to zero and load matching can no longer be maintained. The machine again sees the actual (fixed) output voltage, which results in high-power operation but not as high as could be achieved under load-matched conditions. With the new approach, even present 14 V alternator designs are suitable for high-power operation at 42 V output; only the rectifier stage and controls need to be changed, and one could even conceive of manufacturing both 42 V and 14 V machines on the same production line. Thus, the load-matching approach is timely for meeting the demands of higher power and higher voltage alternators in the automotive industry.
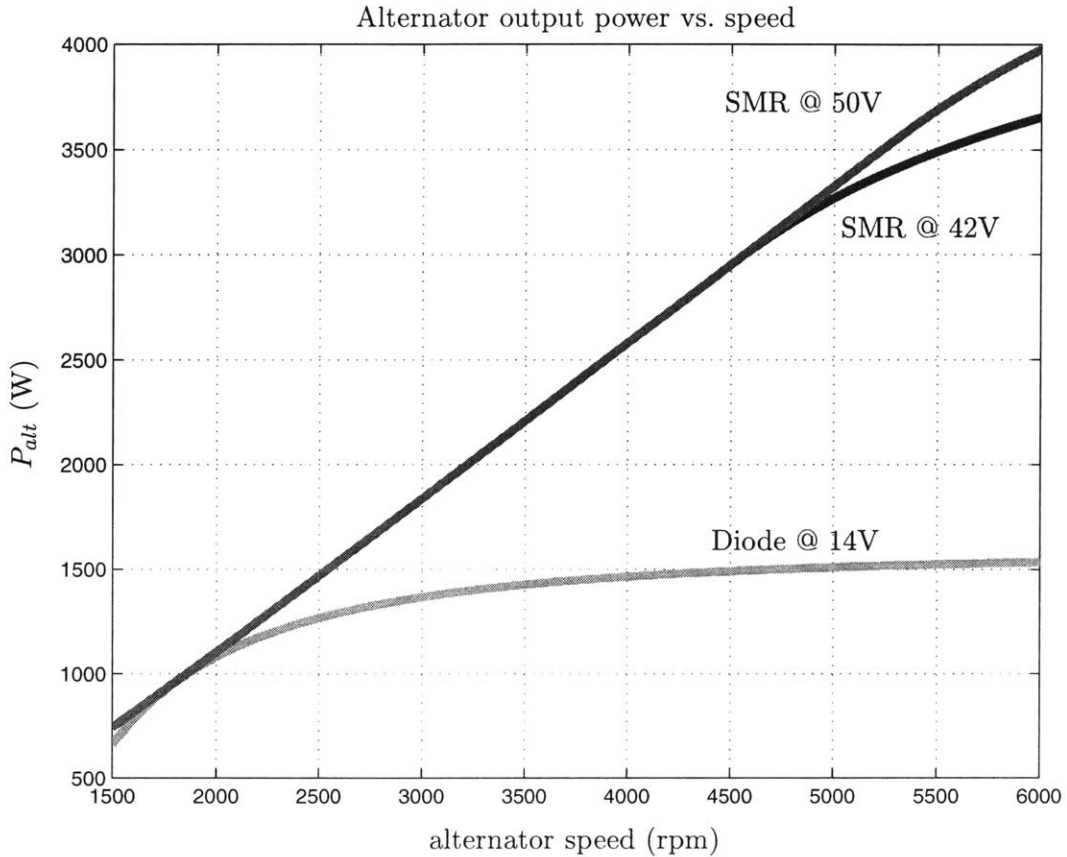
Figure 5.6: Analytical prediction of alternator output power vs. speed at full field current for different operating conditions.

5.3.2 Average Power Improvement

With the new SMR load-matching technique, substantial increases in alternator output power can be achieved, particularly at speeds above idle. The curves of Figure 5.6 indicate that, using the load-matching technique, the alternator power capability increases almost linearly with speed between idle and cruising speed. This contrasts with the case of a conventional diode-rectified alternator in which the available output power is relatively flat over much of the speed range. The behavior of power with speed for the SMR-alternator design is ideally suited to some anticipated loads. For example, the power requirement of electromechanical engine valves (a future automotive electrical load) increases almost linearly with speed, from a small value at idle to a large value (as much as 2 kW) at cruising speed. Other types of high-power loads (e.g., heated windscreens) do not have a speed-dependent power requirement, and thus do not fully benefit from the increased power output capability at higher speeds.

To better characterize the average power improvement provided by the load-matching technique, we have examined the alternator power output over a Federal Test Procedure (FTP) drive cycle. A commonly-used form of the FTP drive cycle, illustrated in Figure 5.7, is the FTP72 which contains idling time, city driving, and a small amount of highway-speed driving. Based on the maximum power vs. speed characteristics of Figure 5.6, it was found that the average power capability of a properly wound load-matched machine is approximately a factor of 1.9 higher than that of a conventional diode-rectified machine of the same size. Also, using a conventional 14 V machine (not rewound) with SMR load matching at 42 V also provides an average power capability improvement of about 1.9. These results, summarized in Table 5.1, indicate that a given size machine is capable of almost twice the average power output capability over a drive cycle when the new SMR load-matching technique is employed! It also means that the alternator size required to achieve a given output power requirement is roughly halved using the new technique. This represents a substantial savings in alternator size, mass, and cost.
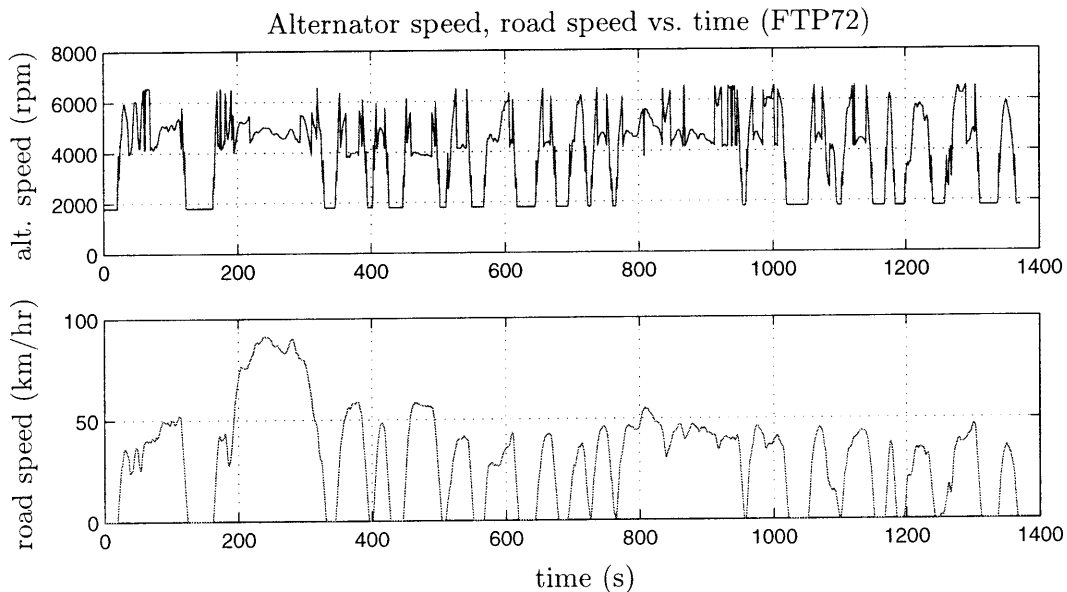
Figure 5.7: The FTP72 drive cycle: alternator shaft speed (top) and road speed (bottom).

System	Average Power	Normalized Power
Diode rectified (14V)	1.31 kW	1.0
SMR matched (42V)	2.51 kW	1.9
SMR matched (50V)	2.54 kW	1.9

Table 5.1: Available output power over the FTP72 drive cycle for different rectifier systems.

5.3.3 Other SMR Structures

The switched-mode rectifier of Figure 5.4 has been used in both continuous and discontinuous conduction modes in other contexts (see [48]–[50] for example). As applied here, this simple boost-type rectifier allows the output power capability of the alternator system to be increased by properly matching the fixed output voltage to that required by the alternator for maximum output power.

Many other simple switched-mode rectifiers can be used to achieve the desired load-matching effect (Figure 5.8) [50]. For example, the SEPIC-based rectifier of Figure 5.8(b) can provide an effective transformation ratio of greater or less than one by varying the duty ratio. The Cuk-based rectifier (Figure 5.8(c)) also allows this, and provides both smoothed output current and natural voltage inversion in cases where that is desirable. The push-pull-based rectifier of Figure 5.8(a) provides natural isolation and additional degrees of design freedom through incorporation of a high-frequency transformer, as do the isolated versions of SEPIC and Cuk converters (Figure 5.8(d)). Note that while all of these rectifier topologies have been proposed previously [50], they have not been employed in the manner described here.

One boost-type switched-mode rectifier that is of particular advantage in automotive applications is shown in Figure 5.8(e); repeated as Figure 5.9. In this switched-mode rectifier, the boost stage has been incorporated into the bridge, saving a device drop as compared to the circuit of Figure 5.4; in other regards the operational characteristics are the same. The three ground-referenced switches Q_x, Q_y, and Q_z may be gated on and off together with duty ratio d, resulting in the same operating characteristics as the system of Figure 5.4. With a slight degree of additional control the active devices can also be used to provide synchronous rectification, further reducing conduction losses. This topology is particularly simple and inexpensive to implement, and represents only a slight structural change from the diode rectifier in use today. While the fundamental design and control techniques we describe here work with a wide range of SMR topologies, for simplicity we will focus on the topology of Figure 5.8(e) (or Figure 5.9) in the remainder of the chapter.

5.3.4 Alternator Control

The static control goal for the alternator system is to regulate the output voltage for load requirements from zero up to the maximum achievable power. In the proposed design this is accomplished by properly selecting the alternator field current (or field regulator duty ratio) and SMR duty ratio as a function of output voltage and alternator speed. A unique control command exists which will produce maximum power at a given speed (i.e., full field current at the proper SMR duty ratio for load matching). For many operating points (when less than full power is required) there are
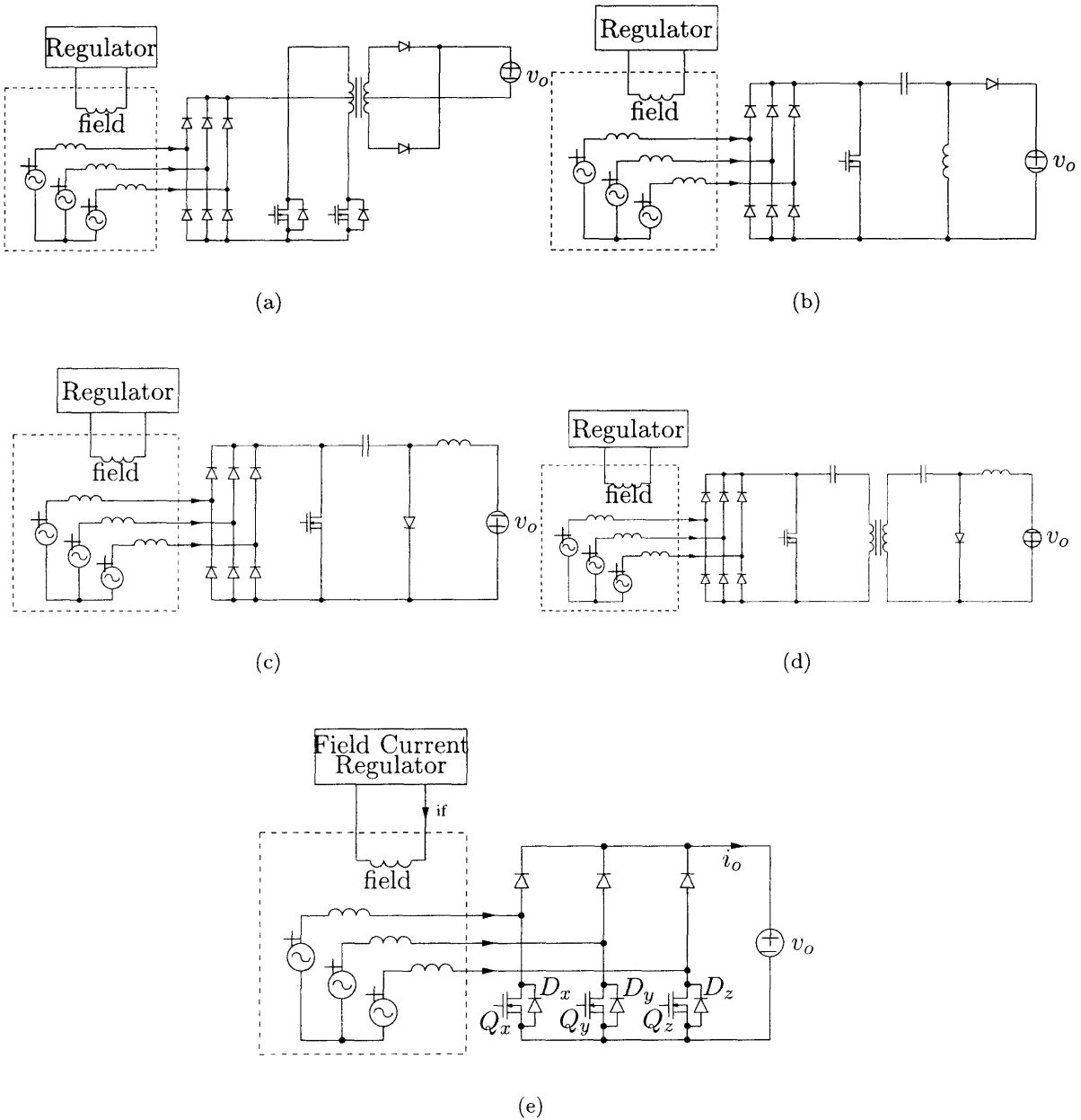
Figure 5.8: Various switched-mode rectifier implementations: (a) Push-pull, (b) SEPIC and (c) Cuk, (d) Isolated Cuk and (e) boost semi-bridge.
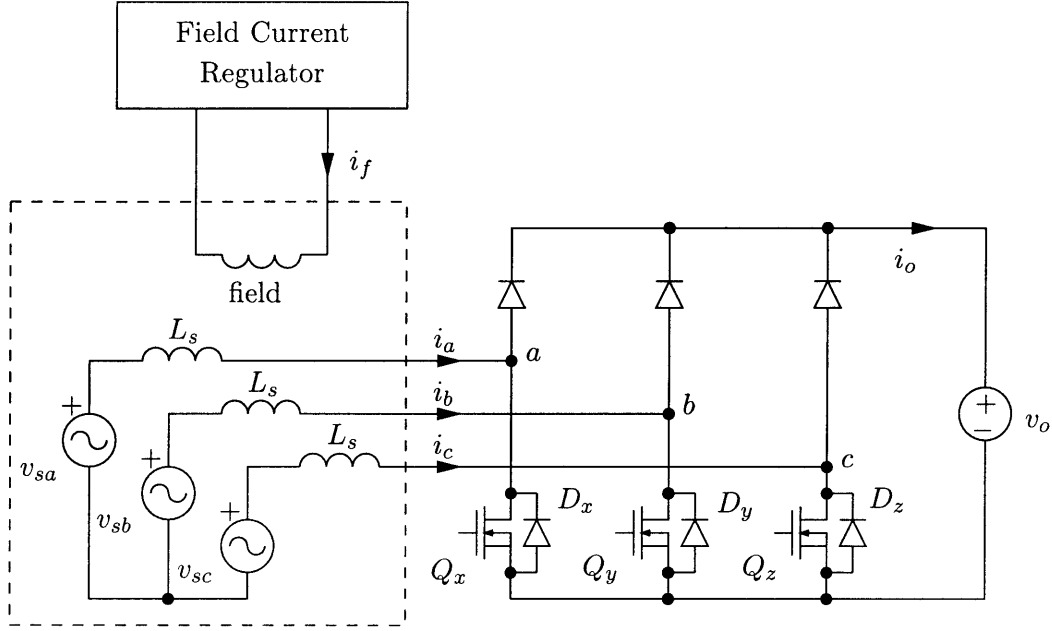
Figure 5.9: Simple boost rectifier implementation.

multiple control combinations which will yield the desired output voltage. As a result, there is some freedom to achieve objectives in addition to increased output power capability (e.g., maximizing efficiency) in selecting a control law. It is a straightforward task to derive the SMR duty ratio control law for achieving load matching with a boost converter. Neglecting the effects of the diode forward voltage V_d and the phase resistance R_s, the alternator output power P_{out} is given by

$$P_{out} = V_o \langle i_o \rangle = \frac{3 d' V_o}{\pi \omega L_s} \sqrt{(k \omega i_f)^2 - \left(\frac{2 d' V_o}{\pi} \right)^2} \tag{5.5}$$

where we have defined $d' \triangleq 1 - d$ and have explicitly used the fact that $V_s = k \omega i_f$. The alternator system delivers maximum power to the output under the load-matched condition which occurs when

$$\frac{\partial P_{out}}{\partial d'} = 0 \tag{5.6}$$

Evaluating the partial derivative and solving for d' yields the control law for the SMR

$$d' = 1 - d = \left(\frac{\sqrt{2} \pi k}{4 V_o} \right) \omega i_f \tag{5.7}$$

where i_f is the field current, ω is the alternator angular speed, k is the machine back-emf constant, and V_o is the output voltage. To achieve load matching, one thus controls the complement of the SMR duty ratio to be proportional to the field current and the alternator speed. In general, the alternator angular speed is available (from the tachometer) while the field current is easily measurable at the field regulator if desired. (Note that unlike other machine control techniques, such as field-oriented control, there is no need for position or stator current information and the control law can be implemented with simple, inexpensive circuitry.)

The simplest control design is to use conventional field control to regulate the output voltage and select the SMR duty ratio as

$$1 - d = \left(\frac{\sqrt{2}\pi k i_{f,max}}{4V_o} \right) \omega = C\omega \tag{5.8}$$

where $i_{f,max}$ is the full field current and C is a net proportionality constant between duty ratio complement and angular speed. With this simple control law, the output voltage can be controlled from zero power up to the maximum load-matched power as a function of speed.

A more sophisticated control approach is to again use field control to regulate the output voltage, but to set the SMR duty ratio (or its complement) using the actual instantaneous field current (which can be easily measured at the field regulator) as per (5.7). In addition to allowing the output voltage to be properly regulated over the full power range, this control law also ensures that load matching is achieved at all operating points. It can be shown that this guarantees that the minimum possible machine excitation is always being used by the controller to achieve the necessary level of output power. In machines where excitation losses dominate, this becomes a desirable control method. Note that with this control law, the SMR duty ratio complement is proportional to the product of field current, alternator speed, and the back-emf constant of the machine.

In conventional automotive alternators, the conduction losses in the stator windings and the semiconductor devices dominate the alternator losses. In this case, if one wants to maximize the alternator efficiency over all load conditions, one should choose the alternator control law such that the alternator system always generates the needed output power at the lowest stator and device currents possible. This is done by controlling the SMR so that the alternator always sees the largest effective voltage v_x that can be used for that level of output power. For a boost-type SMR, this is done by ensuring that the lowest duty ratio possible (for the required level of output power) is always used. One simple controller structure which achieves this is illustrated in Figure 5.10. This controller structure ensures that the duty ratio will only be raised above zero when maximum field current at zero duty ratio is not sufficient to provide the needed output power. In this case

the duty ratio will only be raised by an amount necessary to provide the needed output power or to reach the load-matched condition, whichever is lower. The fault protection controller shown in Figure 5.10 overrides the optimized control strategy described above and is only activated when a large output voltage is detected. The control method thus allows very high efficiency control of the system while providing a simple, inexpensive control structure.

A variety of other control laws also exist. In general, the field current (or field regulator duty ratio) and SMR duty ratio are jointly selected as a function of output voltage and speed to regulate the output voltage, achieve high-power operation (when needed), and achieve other goals at partial load (such as maximizing efficiency). What all such controllers share is the regulation of the SMR for the load-matched condition when maximum output power is needed.

5.4 Experimental Demonstration of Load Matching

In this section, we provide experimental results of the load matching technique that support the analytical results presented in the earlier sections.

5.4.1 Description of Experimental Setup

The experimental setup consists of a standard Lundell automotive alternator (with a rated current of 130 A at 14 V) driven by a computer-controlled variable speed drive. Also included in the test stand is a torque meter which is used to measure the mechanical power into the alternator. For the purposes of our experiments, the internal alternator field current regulator is disabled and a constant field current is supplied to the alternator by using an external power supply ($i_{f,max} = 3.6$ A). The full-bridge three-phase rectifier that is a part of the original alternator assembly is disabled in order to connect the phases directly to the SMR. The alternator is loaded by the parallel combination of an electronic load (HP6050A) and a resistor bank. The electronic load is also used to set the output voltage level. Figure 5.11 shows the prototype switched-mode rectifier that was constructed to demonstrate the load-matching technique. The experimental setup that was used to obtain the data presented in this chapter is shown in Figure 5.12.

5.4.2 Output power versus speed

To verify the analytical results presented Section 5.2, a number of tests were performed at several alternator speeds. At a given constant speed, the alternator system output voltage, V_o, was
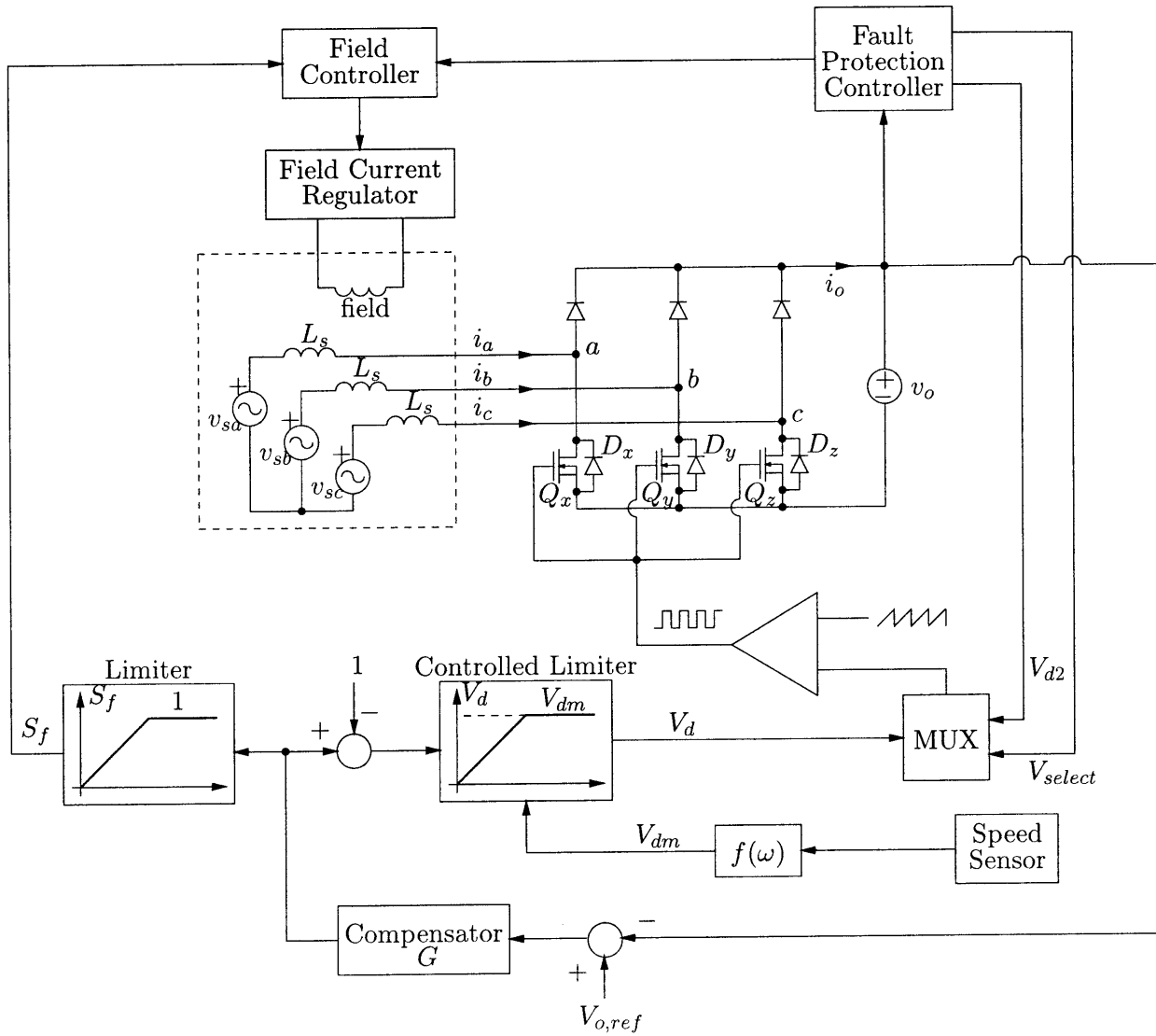
Figure 5.10: Alternator with switched-mode rectifier and efficiency optimizing controller.
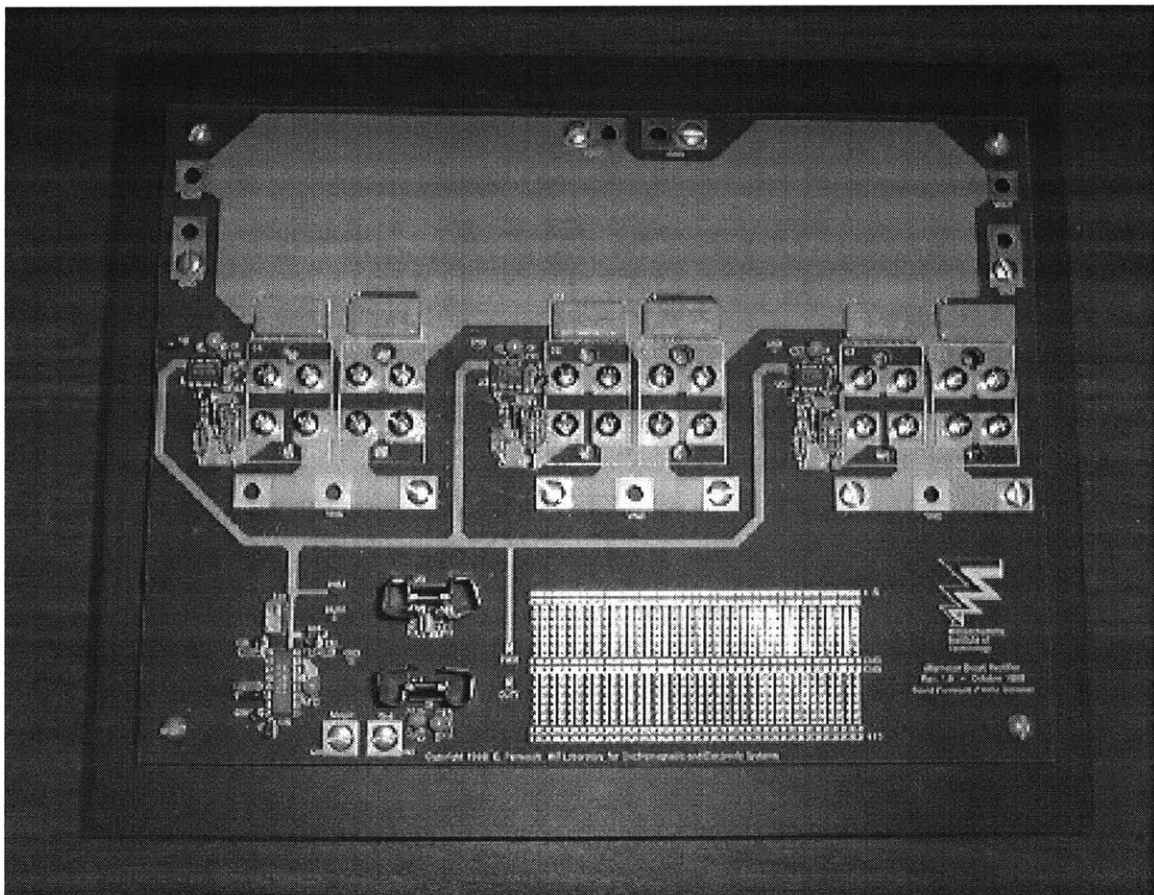
Figure 5.11: Prototype switched-mode rectifier.
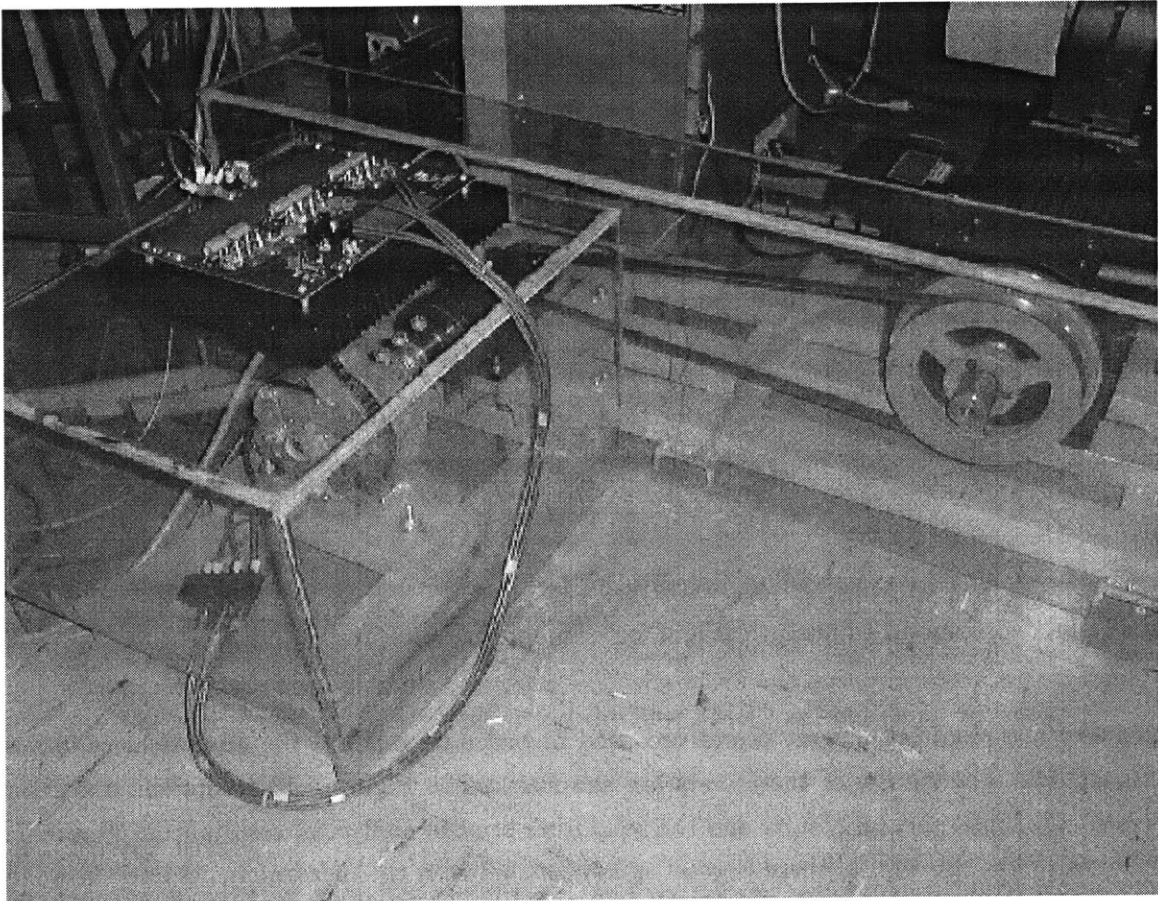
Figure 5.12: Experimental setup for the switched-mode rectifier.
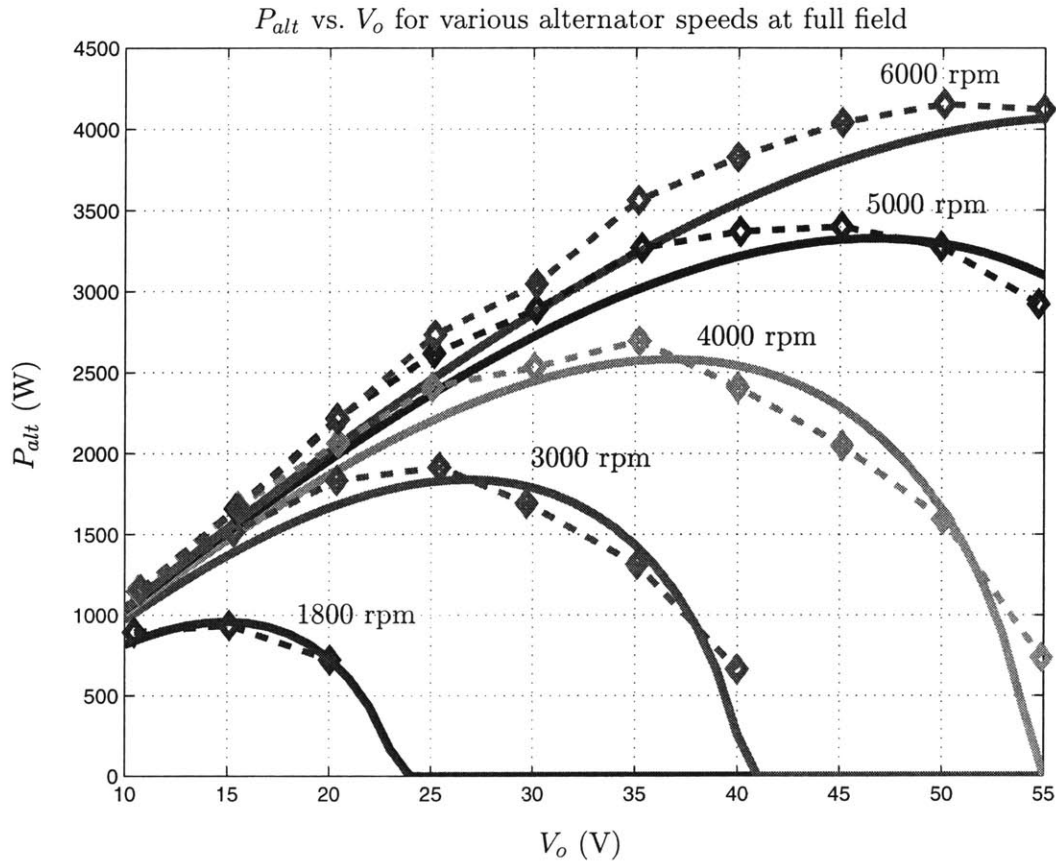
Figure 5.13: Alternator output power vs. alternator output voltage for several speeds. Solid and dashed plots correspond to analytical and experimental results, respectively.

varied and the resulting output power recorded in order to validate the analytical results shown in Figure 5.2. The results of these tests are summarized in Figure 5.13 where the dashed curves represent the experimental results and the solid lines are the analytical results from Figure 5.2. As can be seen from this figure, there is good agreement between the measurements and the analytical results. The agreement between the experimental and analytical results show the validity of our simplified analytical models despite the approximations that were used in their derivation.

To validate the analytical results of Figure 5.6, the alternator and switched-mode rectifier were tested across a range of speeds and output voltages with both diode rectification ($d = 0$) and under the load-matched condition of (5.7). The dashed curves in Figure 5.14 shows the measured maximum power output of the alternator system for three cases: diode rectification at 14 V and switched-mode rectification at 42 V and 50 V. The solid lines in the figure are identical to the curves of Figure 5.6 and are repeated for the sake of comparison. Once again, the experimental results validate the analytical results derived earlier in the chapter. Clearly, tremendous increases
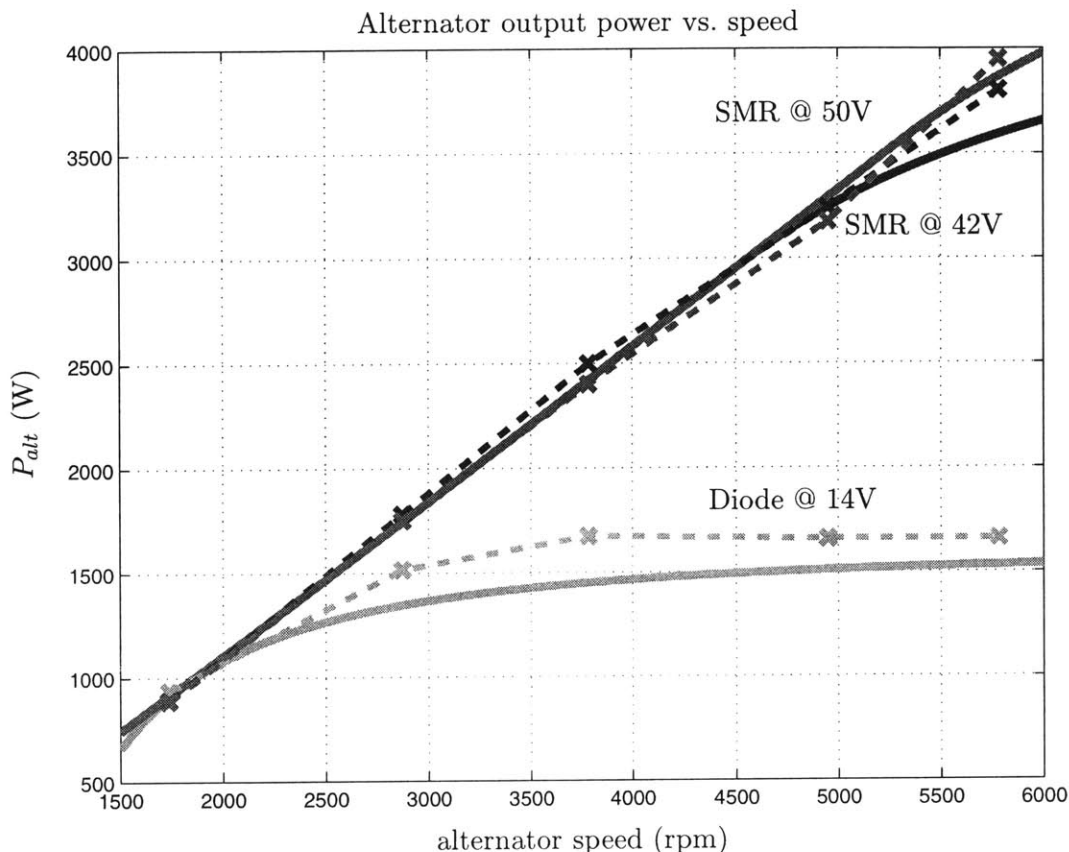
Figure 5.14: Alternator output power vs. speed for different operating conditions: comparison of analytical (solid) and experimental (dashed) results.

in output power with speed are achievable using the new SMR load-matching technique.

5.4.3   Power losses

As described earlier in this section, the experimental test stand includes a dynamometer which allowed the measurement of mechanical input power to the alternator system. Using the measurements of electrical output power and mechanical input power, one can plot the power loss in the alternator system. Shown in Figure 5.15 are the measured power losses versus speed at full field for the alternator system using a diode rectifier at 14 V and a switched-mode rectifier at 50 V. (Again, these voltages represent the optimal output voltages of the two operating modes for the alternator used in the experiments. Similar results are obtainable in each mode at other output voltages merely by rewinding the machine stator appropriately.) This figure shows that the power losses associated with the alternator system using switched-mode rectifier load-matching are less
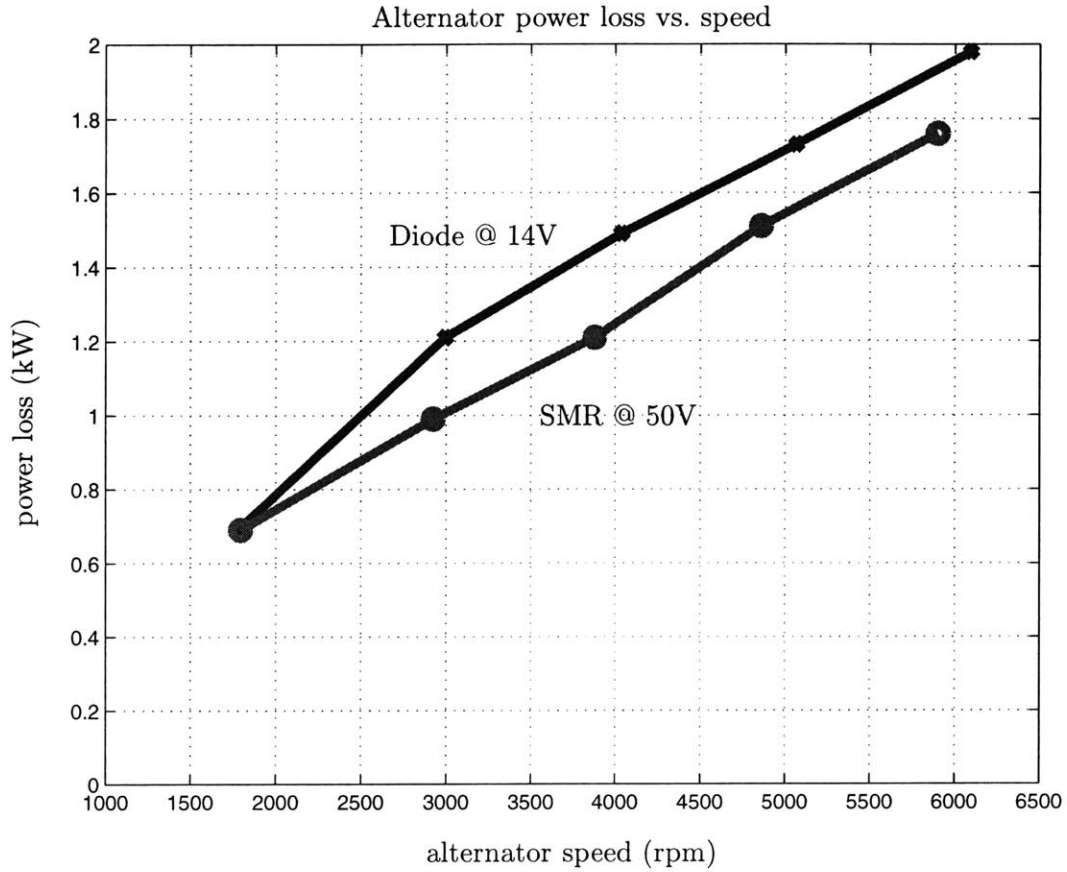
Figure 5.15: Experimentally-determined alternator loss at full field as a function of speed for different operating modes. The SMR load-matching technique (at its optimal output voltage) yields the same or lower losses than diode rectification at its optimal output voltage.

than or equal to the ones with diode rectification over the range of operating speeds. This results primarily from the fact that the new operating technique uses the same or lower stator and device currents than the conventional diode rectifier at all operating speeds. Thus, we can conclude that the proposed load-matched operating technique may be advantageous from a thermal design point of view.

5.4.4   Efficiency improvement

Since the proposed system achieves both lower losses and increased power output, the efficiency of the overall system is improved. The experimentally-measured mechanical input to electrical output efficiency at full field is plotted in Figure 5.16 for the alternator system using conventional diode rectification at 14 V and SMR load-matching at 50 V. With the conventional diode rectified system,

Alternator efficiency vs. speed
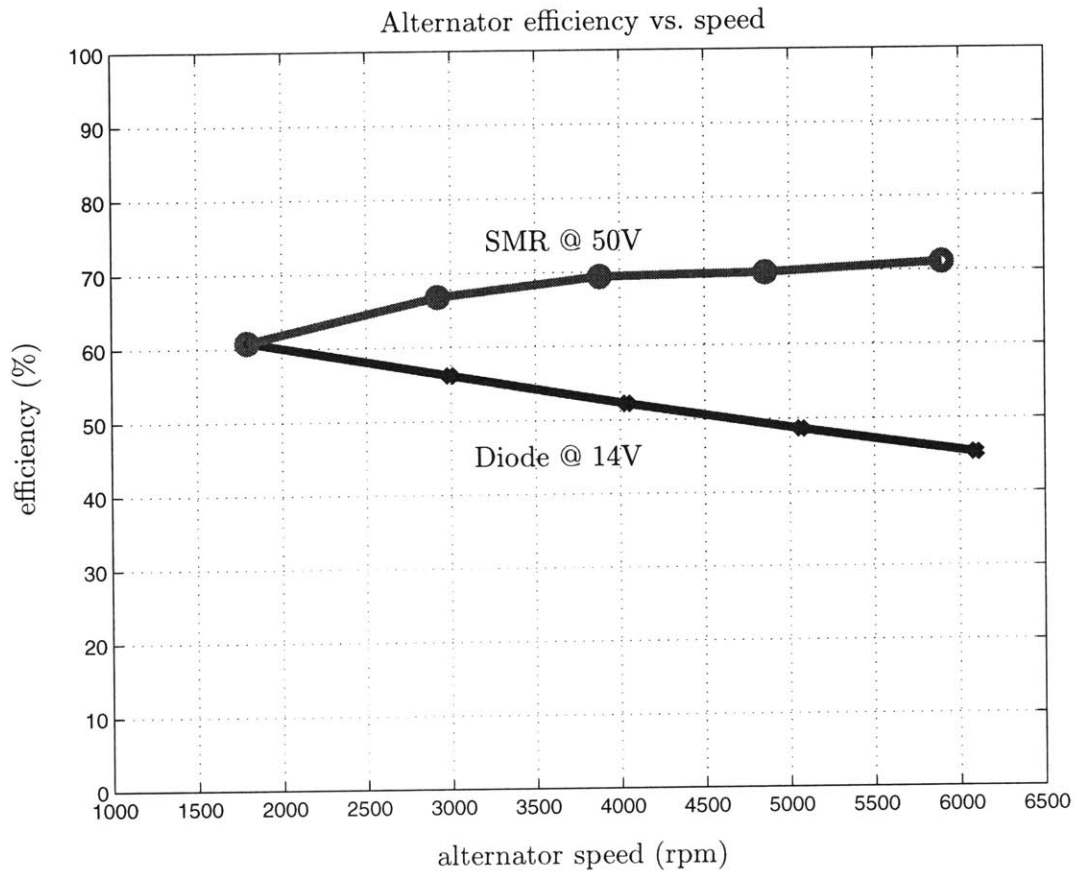
Figure 5.16: Experimentally-determined alternator efficiency at full field as a function of speed for different operating modes.

the efficiency starts at around 61% at idle speed of around 1800 rpm and declines to about 45% near the cruising speed of 6000 rpm. With the switched-mode rectified system, the efficiency also starts near 61% at idle speed but *increases* to about 71% at cruising speed. The improved efficiency provided by the new SMR load-matching is valuable from a fuel economy and environmental point of view and will become even more so as the average electrical loads in vehicles continue to increase.

5.5 Load Dump Protection

As discussed in earlier sections, the Lundell alternator has large stator leakage reactances which in turn have large reactive voltage drops during normal operation. As a result, very large machine back-emf voltage magnitudes are needed to source the rated machine current. If a large current

consuming load is suddenly removed from the alternator, the reactive drops become smaller and a larger fraction of the back-emf voltage appears at the alternator output while the field current is being reduced by the regulator. The resulting transient is commonly referred to as a *load dump* transient. In today's 14 V alternators, the load dump transient can have peak voltages of 80 V and last hundreds of milliseconds. In 42 V machines, the transient peak may reach hundreds of volts. This is unlikely to be acceptable in practice, motivating the search for effective, inexpensive transient suppression techniques. In this section, we show that load dump transient suppression can be achieved through proper control of the switched-mode rectifier.

5.5.1 Use of the SMR for Load Dump Protection

Load dump transient fault protection can easily be implemented within the framework of the new system. A fault protection controller is used to detect and manage load dump transients in the system through appropriate control of the field current and SMR duty ratio. When a significant overvoltage is detected at the output terminals of the alternator system, the fault protection controller acts to decrease the field current and adjust the SMR duty ratio to limit the load dump transient at the alternator output.

In the simplest version of the approach, the boost switch(es) of the SMR can be turned on continuously (crowbar operation) and the field current regulator can be adjusted for deexcitation of the field until the field current and machine currents are at an acceptable level. A more sophisticated version of the approach would adjust the pulse-width modulation of the switched-mode rectifier in concert with the field current regulator to regulate the output voltage and suppress the transient.

5.5.2 Experimental Results

Figure 5.17 shows the experimental results of a load dump transient test on an SMR-based system with an output voltage of 50 V. The output current of the system is suddenly reduced from 50 A to 30 A (2.5 kW to 1.5 kW), thus inducing a load dump transient. When the overvoltage is detected, the fault protection controller adjusts the duty ratio (in this case to zero) to match the new loading demand. Using active transient suppression control via the switched-mode rectifier, a transient having a peak overvoltage of 25 V and lasting about 100 μs occurs. In a conventional diode rectified system the overvoltage would exceed 100 V and last hundreds of milliseconds. It should be noted that the short, low-energy transient in the new system can be further clamped using a transient voltage suppressor (TVS). This is much less practical with the long, high-voltage transients in conventional systems. It may be concluded that rapid transient suppression can be
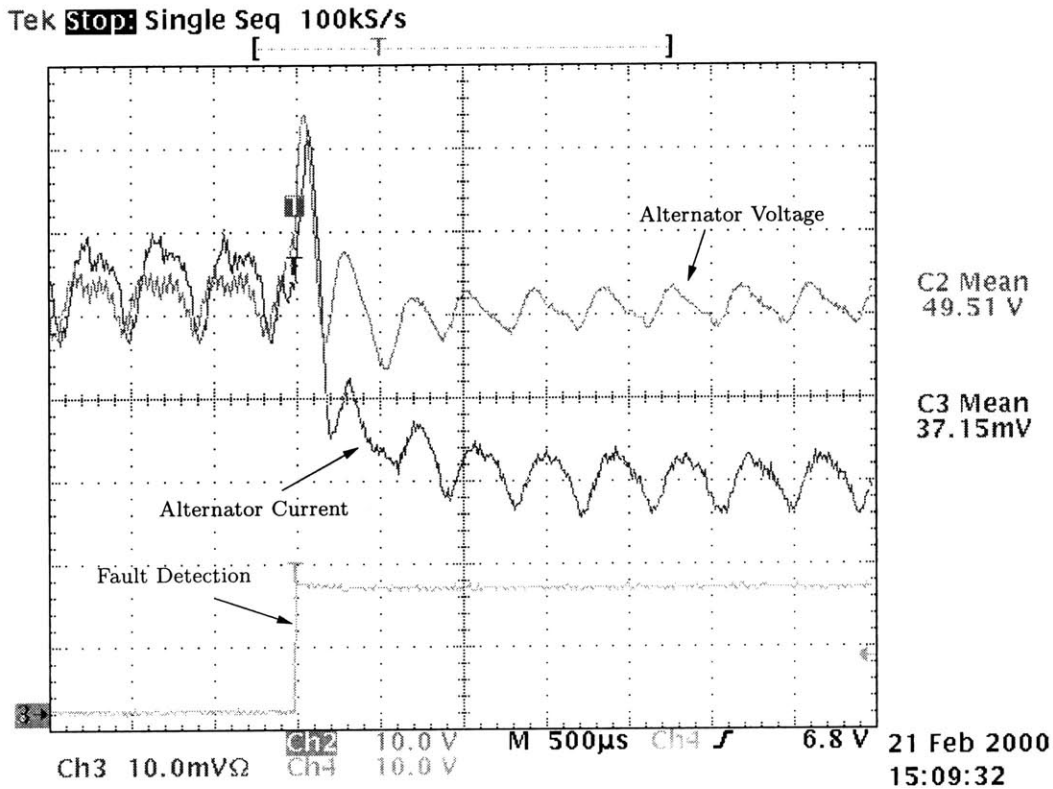
Figure 5.17: Experimental demonstration of load dump transient suppression using the switched-mode rectifier (horizontal: 500 μs/div; vertical: 10 A/div, 10 V/div).

achieved within the framework of the new system. This is valuable in present-day 14 V alternators, and of central importance for future high-voltage alternator systems.

5.6 Jump Start Technique

There is a desire to introduce 42 V and dual 42/14 V automotive electrical systems in the near future. Providing jump start capability for 42 V systems from 14 V or 28 V is a major deployment issue. To solve the jump-start problem, expensive dc/dc converter solutions have been proposed. In this section, we show that jump start can be implemented using the alternator and the switched mode rectifier. It is shown that a low voltage charging source connected between the machine neutral and system ground can be used to charge the 42 V bus by using the alternator leakage inductances and SMR as a dc/dc converter [51].
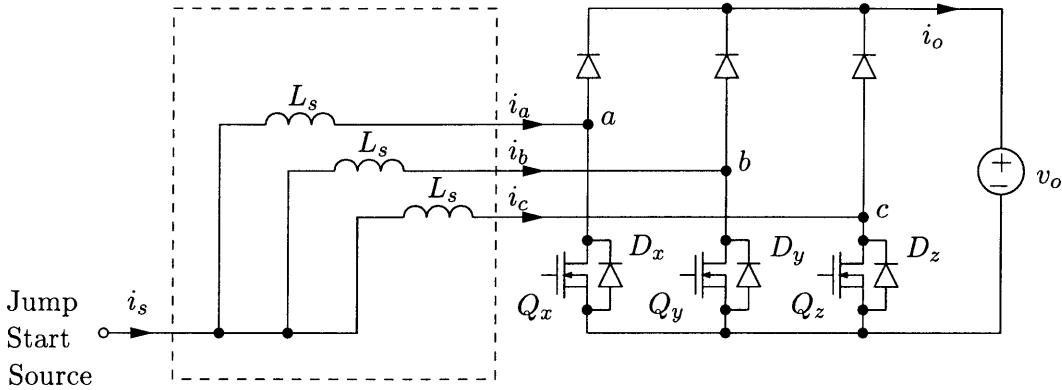
Figure 5.18: 42 V jump start charging technique using the SMR.

5.6.1 Motivation

A dual- or high-voltage system having a starter motor coupled to a high-voltage bus requires a charged high-voltage battery to start. In cases where the high-voltage battery is not fully charged or is depleted, it is desirable to be able to charge the depleted high-voltage battery from a low-voltage source (such as a 14 V or 28 V system) in order to provide jump-start capability for dual/high voltage systems. In an automobile which includes only a single high-voltage system, one may desire to transfer energy from a low-voltage power source, battery or alternator of a different vehicle to the high-voltage system. In a dual-voltage system, one may desire to transfer energy from the low-voltage battery of the dual-voltage system to the high voltage battery of the dual-voltage system or from the low-voltage battery or alternator of a different vehicle to the high-voltage battery of the dual-voltage system.

5.6.2 Jump-Charging Implementation

Here we show that the alternator and switched-mode rectifier can be used to implement jump charging in dual/high voltage systems (e.g., 42 V or 42/14 V systems.) In one possible implementation, a mechanism is provided for connecting the positive terminal of a charging source to the machine neutral point (Figure 5.18). This enables the switched-mode rectifier to be used in conjunction with the alternator machine inductances as a dc/dc converter to charge the battery at the output of the switched-mode rectifier from the charging source. The inclusion of these elements provides an important improvement in the alternator system functionality over what is achieved in conventional systems.

It should be recognized that this approach may be used in dual-voltage systems as well. In

the case of a dual-voltage system, the charging source may be the low-voltage battery of the same vehicle, or it may be supplied from a different vehicle or source. Again, a mechanism is provided for selectively connecting the neutral of the ac machine to the desired charging source. In a dual-voltage system charging from its own low-voltage battery, this connection may be conveniently provided by a relay connecting the machine neutral to the positive terminal of the low-voltage battery, for example.

5.6.3 Experimental Results

One possible way to implement jump-charging within the framework of the new alternator system is shown in Figure 5.18. In this scheme, the positive terminal of the charging source is connected to the machine neutral while the negative terminal of the charging source is connected to system ground. (Note that the machine back-emf voltage sources are not present since the engine/alternator in the vehicle to be jump-charged is not running.) This scheme enables the switched-mode rectifier to be used in conjunction with the alternator machine inductances as a dc/dc converter to charge the battery at the output of the switched-mode rectifier from the charging source. This represents an important improvement in the alternator system functionality over what is achieved in conventional systems.

Figure 5.19 presents experimental results from a jump-charging test using a low voltage (14 V) source connected to the machine neutral to deliver energy at the high-voltage alternator output. The results of Figure 5.19 show a prototype alternator jump-charging system delivering approximately 920 W at 43 V output from a 14 V source, with an overall efficiency of about 87%. This capability substantially exceeds the minimum necessary in practice, and is achieved at little incremental system cost. We note here that this approach may be used in dual-voltage systems where the charging source may be internal (low-voltage battery of the same vehicle) or external (from a different vehicle or source).

5.7 Summary

Rapid growth in automobile electrical power requirements is pushing the limits of conventional automotive alternators and is motivating the development of high-power and high-voltage automotive electrical systems and components. This chapter introduces a set of new design and control techniques for automotive alternators which yield dramatic improvements in performance and functionality as compared to conventional systems.
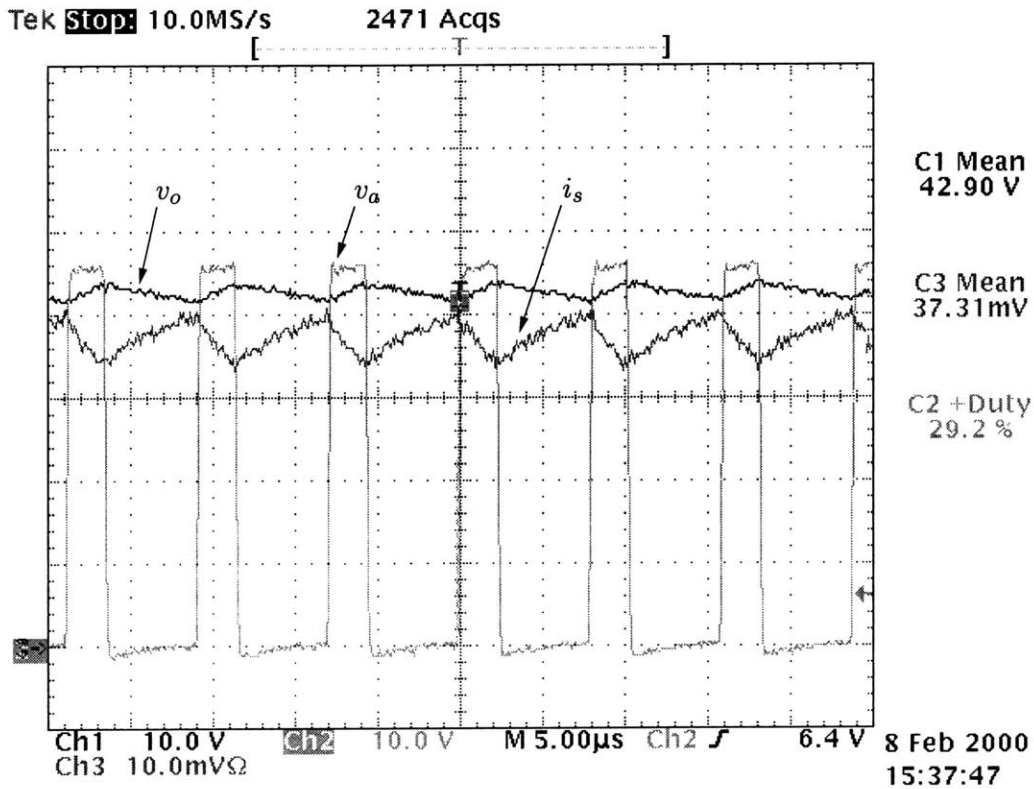
Figure 5.19: Experimental results demonstrating the alternator/SMR-based jump charging technique. A 14 V jump charging source is used. The illustrated results represent a delivered output power of about 920 W at 87% efficiency (horizontal: 5 μs/div; vertical: 20 A/div, 10 V/div).

A new load-matching technique is introduced that allows substantial increases in alternator output power and efficiency to be achieved through the use of a simple switched-mode rectifier. Only minimal, inexpensive modifications to existing alternators are required to implement the new technique, and simple control laws based on readily-available signals can be used. Analysis and implementation of the proposed technique are addressed, and simple analytical control laws for the approach are established. Experimental results demonstrating output power increases of factors of 2.5 (peak) and 1.9 (average) along with substantial increases in efficiency are provided. This new technique overcomes the power limitations of present-day Lundell alternators, and allows significant improvement in vehicle fuel economy (and commensurate reduction in environmental impact) to be achieved.

Two major challenges to the introduction of high-voltage (42 V) electrical systems are the need to achieve much greater transient control (particularly for alternator load dump) and the need to provide a mechanism for recharging the high-voltage battery from a low-voltage source (jump

charging). It is shown that both of these functions can be readily implemented within the proposed framework. Tight load dump transient suppression can be achieved by joint control of the alternator field current and switched-mode rectifier duty ratio. Jump charging can be implemented by using the switched-mode rectifier and alternator leakage inductances together as a dc/dc converter to charge the high-voltage battery from a low-voltage source. Experimental results from a prototype system are provided to demonstrate the transient suppression and jump charging features of the proposed architecture.

The developments described here address some of the major present challenges in automotive power generation and control. It is expected that the further development and adoption of these techniques will facilitate the rapid introduction of high-power and high-voltage electrical systems in automobiles.

Extensions of the proposed technology for dual-output (e.g. 42/14 V) alternator systems will be described in Chapter 8. In addition to providing the benefits that result in single-output alternators (e.g. improved output power and efficiency, transient suppression, and jump charging), it will be shown that one can achieve tremendous improvements in control bandwidth and reductions in filter size as compared to conventional implementations.

Dc/Dc Converter Architecture

6.1 Introduction

This chapter describes the design, modeling and control of the dc/dc converter system. The dc/dc converter based dual-voltage architecture is shown in Figure 6.1. The architecture consists of a high-voltage alternator to supply a 42 V bus which is down-converted to 14 V by the use of the dc/dc converter. The high-voltage alternator is likely to be a modified version of today's Lundell alternator although other machines are also being considered. The switched-mode rectifier based Lundell alternator system presented in Chapter 5 is an excellent candidate for the high-voltage alternator in this architecture. The dc/dc converter architecture in Figure 6.1 is shown with batteries on both buses, but there have been proposals to remove one of the batteries to reduce system weight and complexity. However, the removal of a battery does alter the dynamics of operation and requires resizing of components.
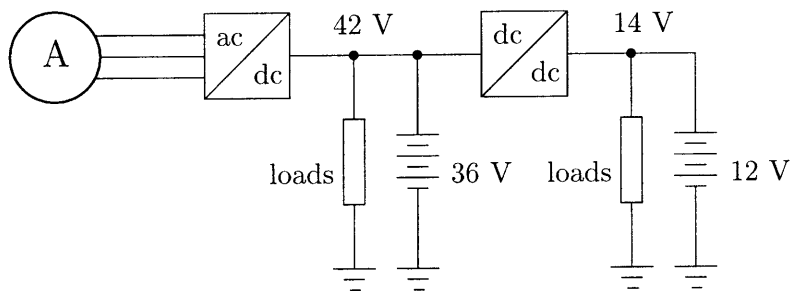
Figure 6.1: Dc/Dc converter architecture.

6.2 Dc/Dc Converter System

There are a number of ways one can implement and optimize the dc/dc converter system. One of the main issues in the implementation of such a system is the relative benefits of centralized versus distributed power conversion approaches (Figure 6.2). The operational characteristics and benefits of using a paralleled converter system must also be taken into consideration. The design space for
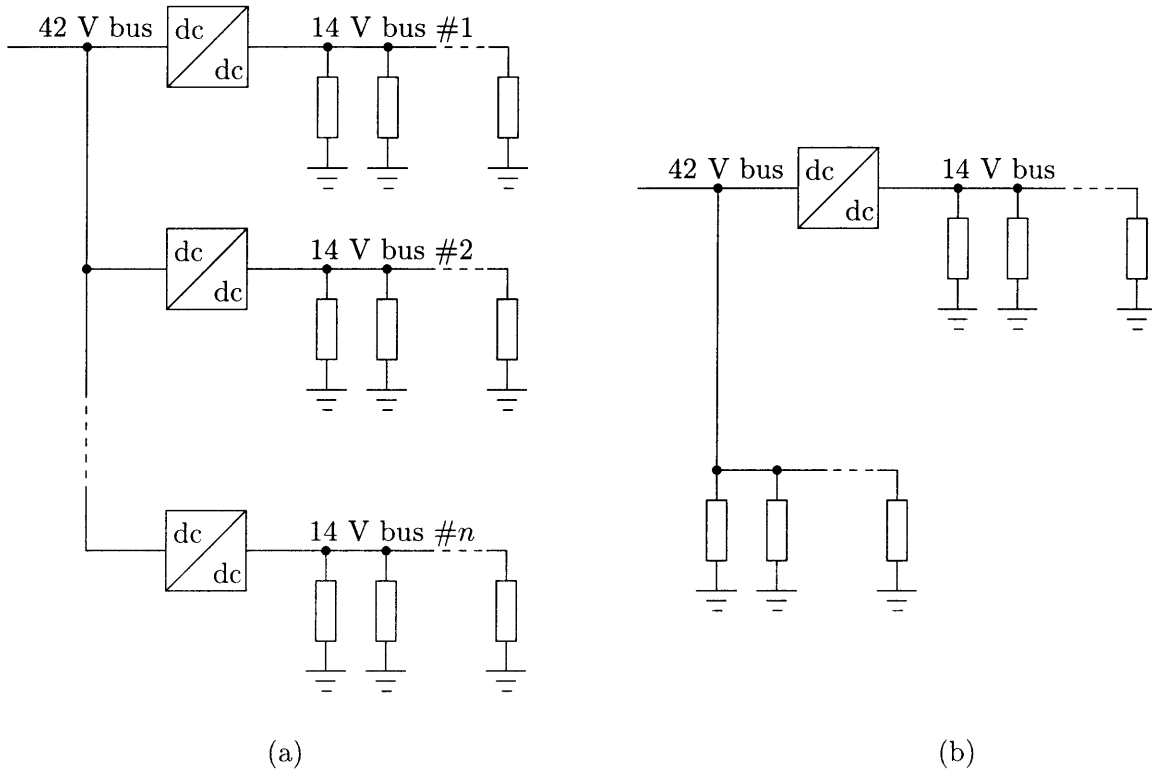
Figure 6.2: Dc/Dc converter system implementations: (a) distributed and (b) centralized.

such a converter system, given specifications and numerous options for power stage topologies, is quite large. We will not discuss the details of these design space explorations and tradeoffs, but refer the reader to some recent work on computer-aided optimization of dc/dc converters [16] and dc/dc conversion architectures for dual-voltage automotive electrical systems [52].

As a result of these cited investigations, it was concluded that a centralized dc/dc converter system has a number of advantages over a distributed system. A centralized converter system results in lower converter power rating, reduced EMI filtration requirements and a lower cost per kVA of conversion hardware. It was also concluded that the presence of a storage battery on the 14 V bus was preferable to a larger converter system. The average power output requirement for a dc/dc converter in a dual-voltage automotive electrical system depends on the extent to which loads are converted to the 42 V bus but may be on the order of 1 kW. The peak power demand on the 14 V bus is typically 3-4 times the average power requirements. This implies that, without energy storage, the converter power rating must be increased by at least a factor of three.

Due to the relatively high power levels and high operating temperatures, either paralleled components or paralleled converters are needed for practical implementation of the dc/dc converter

(a)

(b)
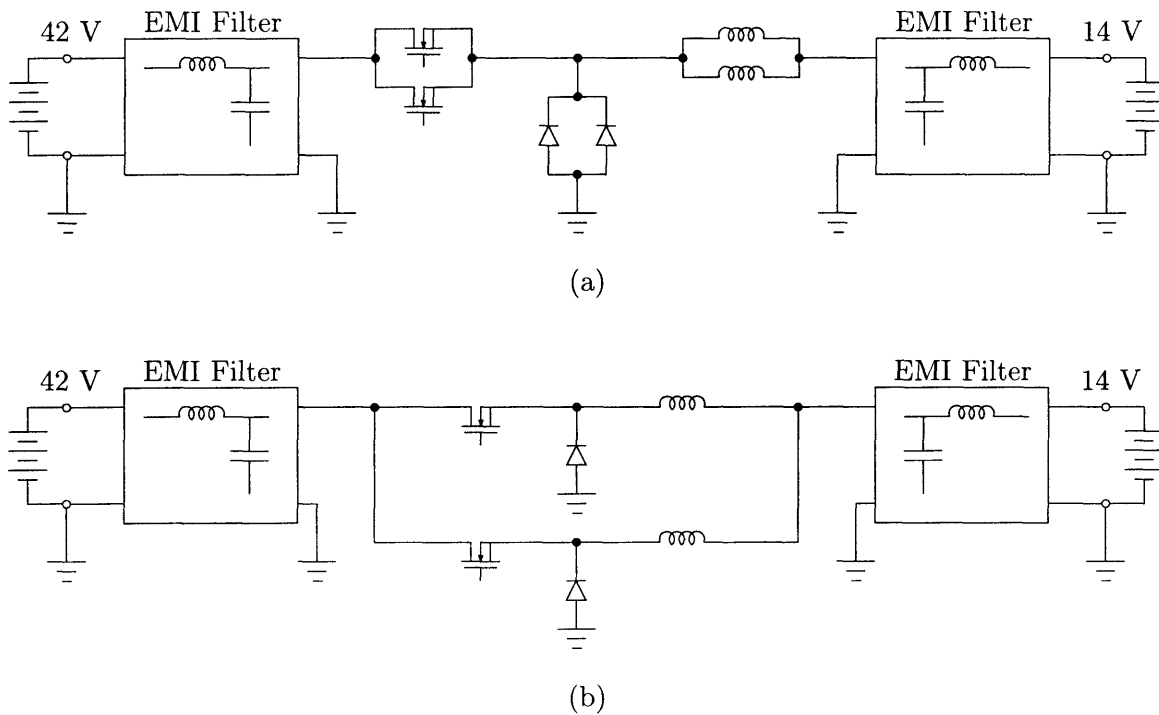
Figure 6.3: Dc/Dc converter topology implementations: (a) paralleled components and (b) paralleled power stages.

system (Figure 6.3). The paralleling of the devices is necessary in order to use presently-available single-die MOSFET and diode packages. It was concluded that paralleled converter power stages employing interleaved clocking which reduce output current ripple have substantial advantages [52]. The number of cells and switching frequency of the cells are design variables that must be traded off to arrive at an optimized design. In the next three sections, we discuss the interleaved dc/dc converter topology chosen for the application along with an appropriate control strategy.

6.3 Dc/Dc Converter System Specifications

As part of the work of the MIT/Industry Consortium [52], a dc/dc converter has been constructed using paralleled power stages. The major specifications for the converter system are shown in Table 6.1 and are a result of automobile industry concensus. The rated output current of 68 A at a nominal output voltage of 14 V produces approximately 1 kW of output power. The input and output voltage ranges reflect variations around nominal voltages of 14 V and 42 V, respectively. The presence of storage batteries on both buses and their operating voltage and temperature ranges influences these voltage ranges. The EMI limits imposed by SAE J1113/41 are quite stringent and

Rated Output Current (at 14 V)	68 A
Energy Storage	12 V battery on 14 V bus
Input/Output Voltage Ranges	$33V < V_{in} < 52V$, $11V < V_o < 16V$
EMI Limits	SAE J1113/41, Class 1
Operating Temperature	105 °C

Table 6.1: Specifications for the dc/dc converter system.

do not directly apply to dc/dc conversion equipment. The specifications for Class 1 equipment leads to significant design penalties for the EMI filter [15]. The operating temperature of 105 °C reflects the underhood environment of the vehicle and generally results in oversizing of components which increases weight and cost.

Given these specifications, a multi-cell interleaved buck converter system was chosen for the design. A two cell example of this system is illustrated in Figure 6.3(b). Paralleled stages with interleaving lead to reduced magnetic storage requirements and/or current ripple at the converter output which can reduce EMI filter sizing. Each of the converter cells operates in discontinuous conduction mode which results in a simplified control design model for the system. The discontinuous mode operation also improves the transient response of the system because it results in a mimimum stored energy requirement for the ripple filters [52]. Typical steady-state operation of a five cell interleaved buck converter system has been simulated in Saber and is shown in Figure 6.4. The interleaved clocking of the cells is apparent from the relative time delay of the current waveforms, which in the case of five cells is 72°. There are also two points worth mentioning related to the current ripple. The first is that the peak-peak ripple in the total output current (top trace in Figure 6.4) is lower than in the individual cell currents. The second is the fact that the total output current ripple frequency is five times that of the cell currents. Both of these points, which are features of interleaved parallel converters, result in reduced magnetics and filter component sizes.

6.4 Buck Converter in Discontinuous Conduction Mode

The basic building block for the multi-cell interleaved converter system is the buck dc/dc converter which is shown in Figure 6.5(a). To analyze the converter system and proceed with control design requires development of appropriate averaged and small-signal models. This section will provide the averaged and small-signal models for a single buck-converter cell in discontinuous conduction

mode.   Referring to Figure 6.5(a), the duty ratio of the MOSFET Q is normally used as the control variable to provide a regulated output voltage in the presence of input voltage and load variations. In most dc/dc converters, the input and output voltages vary slowly as compared to the switching period [41]. This assumption is quite appropriate in our system since under normal operating conditions both input and the output of the converter system will be connected to storage batteries. With these assumptions, one can sketch the inductor current i_L and the input current i_{in} as shown in Figure 6.5(b) and Figure 6.5(c), respectively. These waveforms assume that the converter cell inductance L is chosen appropriately to result in discontinuous conduction mode operation. Figure 6.5(d) shows the gate drive signal (in binary representation) with duty ratio d. We consider the duty ratio signal to be a local average of the binary gate drive signal $q(t)$ defined by the moving average [41]:

$$d(t) \stackrel{\triangle}{=} \bar{q}(t) = \frac{1}{T_s} \int_{t-T_s}^{t} q(\tau) d\tau \qquad (6.1)$$

Since the input and output voltages are slowly varying, they can be well approximated by their local averages:

$$v_{in}(t) \approx \bar{v}_{in}(t) = \frac{1}{T_s} \int_{t-T_s}^{t} v_{in}(\tau) d\tau \qquad (6.2)$$

$$v_o(t) \approx \bar{v}_o(t) = \frac{1}{T_s} \int_{t-T_s}^{t} v_o(\tau) d\tau \qquad (6.3)$$

With the duty ratio defined, the peak inductor current is given by

$$i_{L,max} = \frac{\bar{v}_{in} - \bar{v}_o}{L} dT_s \qquad (6.4)$$

An averaged model for the buck converter cell can be developed by evaluating the local average for the inductor and input current. The local averages for the currents can be expressed as functions of the local averages for the input and output voltages and the duty ratio:

$$\bar{i}_L = \frac{\bar{v}_{in} \left(\bar{v}_{in} - \bar{v}_o \right) d^2 T_s}{2L\bar{v}_o} \stackrel{\triangle}{=} f(\bar{v}_{in}, \bar{v}_o, d) \qquad (6.5)$$

$$\bar{i}_{in} = \frac{\left(\bar{v}_{in} - \bar{v}_o \right) d^2 T_s}{2L} \stackrel{\triangle}{=} g(\bar{v}_{in}, \bar{v}_o, d) \qquad (6.6)$$

An equivalent circuit representing the averaged buck converter in discontinuous conduction mode is shown in Figure 6.6. The switching action of the MOSFET-diode combination has been averaged and replaced by the controlled current source pair. The current source $\bar{i}_e$ models a large signal disturbance at the output of the converter such as a step change in load current. This model
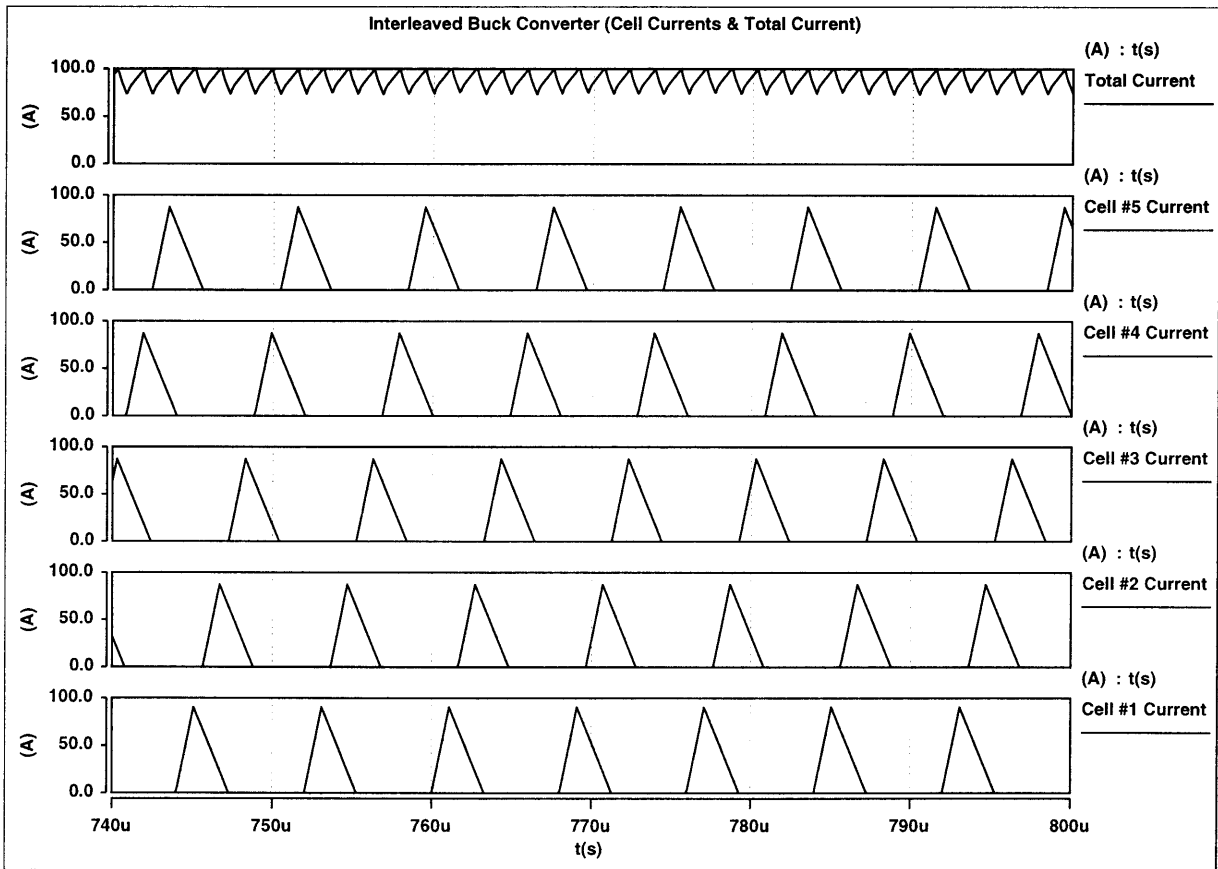
Figure 6.4: Currents in an interleaved five-cell dc/dc converter system. Bottom five traces are the individual cell currents and the top trace is the total output current which is just the sum of the individual cell currents.
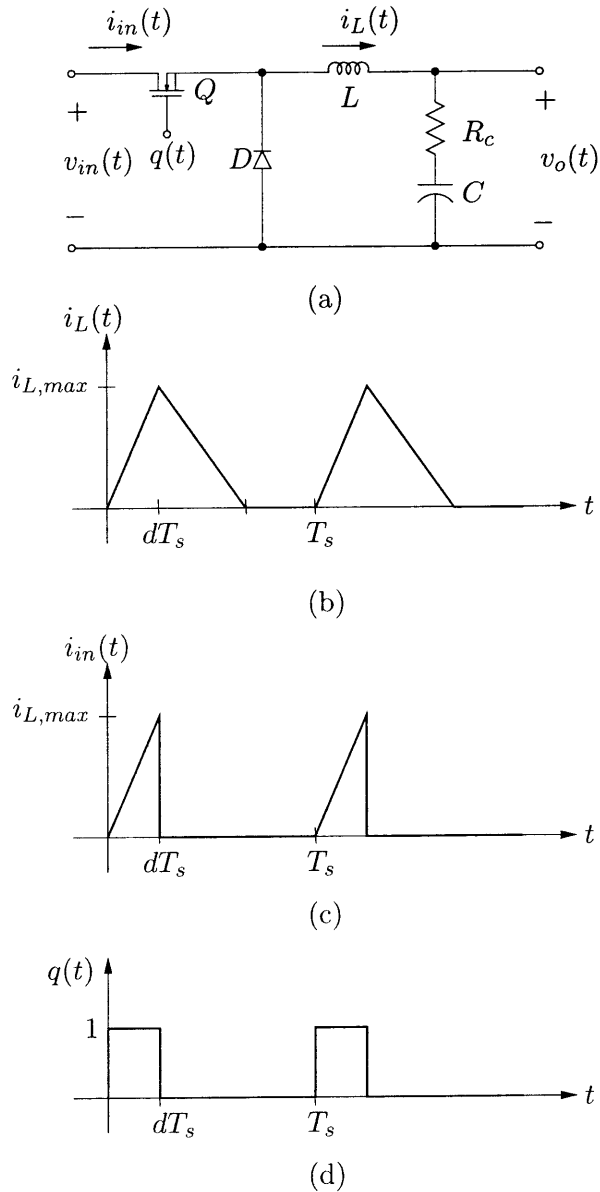
Figure 6.5: Buck converter: (a) simplified schematic, (b) inductor current and (c) input current waveforms in discontinuous conduction mode, (d) binary gate drive (switching) signal.
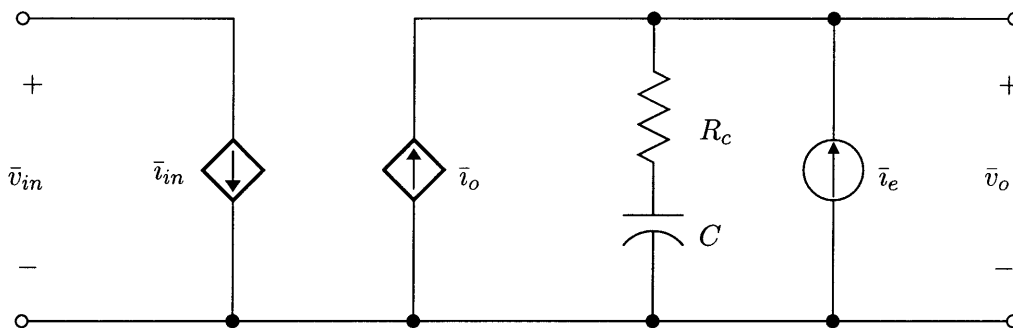
Figure 6.6: Averaged model for a buck converter in discontinuous conduction mode. The current source $\tilde{\imath}_e$ models a large signal disturbance at the output of the converter.

is extremely useful in modeling and simulating the averaged dynamic behavior of the converter; however, it still is not in a form suitable for control design. For control design purposes, a small-signal model based on linearizing the system in Figure 6.6 has to be developed. The small-signal model can be derived by linearizing (6.5) and (6.6) about the operating point. Mathematically, we have

$$\tilde{\imath}_L = \frac{\partial f}{\partial \bar{v}_{in}}\, \tilde{v}_{in} + \frac{\partial f}{\partial \bar{v}_o}\, \tilde{v}_o + \frac{\partial f}{\partial d}\, \tilde{d} \stackrel{\triangle}{=} A_o\, \tilde{v}_{in} - B_o\, \tilde{v}_o + G_o\, \tilde{d} \qquad (6.7)$$

$$\tilde{\imath}_{in} = \frac{\partial g}{\partial \bar{v}_{in}}\, \tilde{v}_{in} + \frac{\partial g}{\partial \bar{v}_o}\, \tilde{v}_o + \frac{\partial g}{\partial d}\, \tilde{d} \stackrel{\triangle}{=} A_{in}\, \tilde{v}_{in} - B_{in}\, \tilde{v}_o + G_{in}\, \tilde{d} \qquad (6.8)$$

where the variable $\tilde{x}$ represents the small-signal portion of signal $\bar{x}$ $(= X + \tilde{x})$ and all partial derivatives are evaluated at the operating point (at $\bar{x} = X$). A block diagram representing the small-signal model is shown in Figure 6.7 and expressions used to characterize the block parameters are listed in Table 6.2. This block diagram has been derived by taking the Laplace transform of (6.7) and (6.8) and recognizing that $\tilde{v}_o(s) = Z(s)\tilde{\imath}_o(s)$. By using this block diagram, one can derive any transfer function of interest. It is important to realize that, in Figure 6.7, signals $\tilde{v}_{in}$, $\tilde{d}$ and $\tilde{\imath}_e$ are excitations ("inputs") whereas $\tilde{v}_o$ and $\tilde{\imath}_{in}$ are responses ("outputs"). The only block with frequency dependent characteristics is the impedance $Z(s)$. This impedance is the parallel combination of the converter cell capacitance C with equivalent series resistance (ESR) R_c and resistance R which models the current demand of the battery and the associated loads in a vehicle.

The averaged and small-signal models developed in this section form the basis of models used for simulation models for a buck converter cell implemented in Saber. With the development of generalized models, it is a straightforward task to put any number of cell models in parallel to simulate a multi-converter system. The dc/dc converter system that is discussed in the remainder of the chapter is a four cell interleaved system with each cell operating at 125 kHz [16].
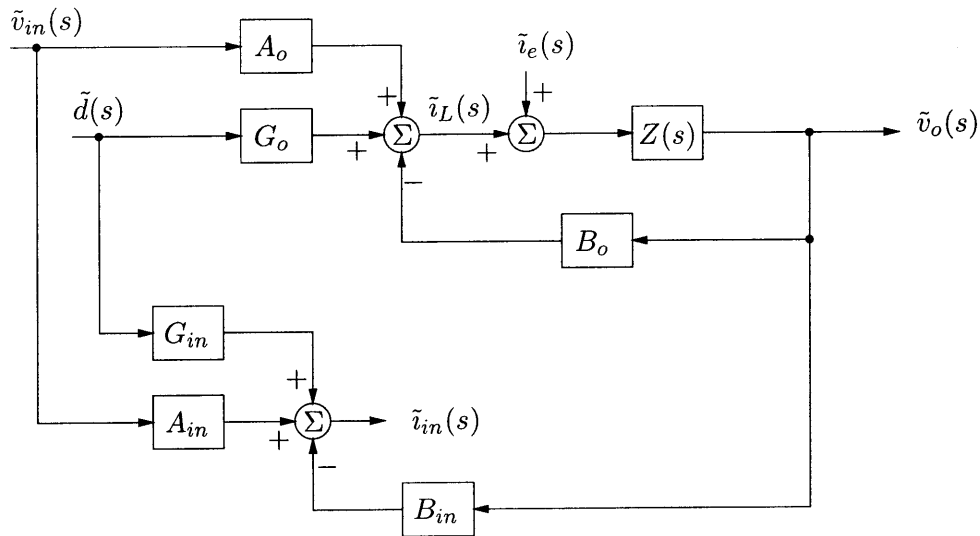
Figure 6.7: Block diagram representing the small-signal model of a buck converter in discontinuous conduction mode.

Parameter	Expression	Parameter	Expression
A_o	$\frac{(2V_{in}-V_o)D^2T_s}{2LV_o}$	A_{in}	$\frac{D^2T_s}{2L}$
B_o	$\frac{V_{in}{}^2D^2T_s}{2LV_o{}^2}$	B_{in}	$\frac{D^2T_s}{2L}$
G_o	$\frac{V_{in}(V_{in}-V_o)DT_s}{LV_o}$	G_{in}	$\frac{(V_{in}-V_o)DT_s}{L}$
$Z(s)$	$R\frac{1+sCR_c}{1+sC(R+R_c)}$		

Table 6.2: Buck converter small-signal model parameters.

6.5   Control Strategy and Design

In order to control the buck converter we use the well-known multi-loop control method commonly referred to as average current-mode control [53, 54]. A schematic of a single buck converter using average current-mode control is shown in Figure 6.8. The inductor current is sensed (with a transresistance gain R_t) and fed to a current error amplifier to establish an inner control loop. There is also an outer voltage loop which involves the output voltage and a voltage error amplifier. The voltage error amplifier output is used as the reference current (current command) for the faster inner current loop. Using this method, we have fast control of the output current which delivers power to the battery and the loads. This lends itself well to energy management methods
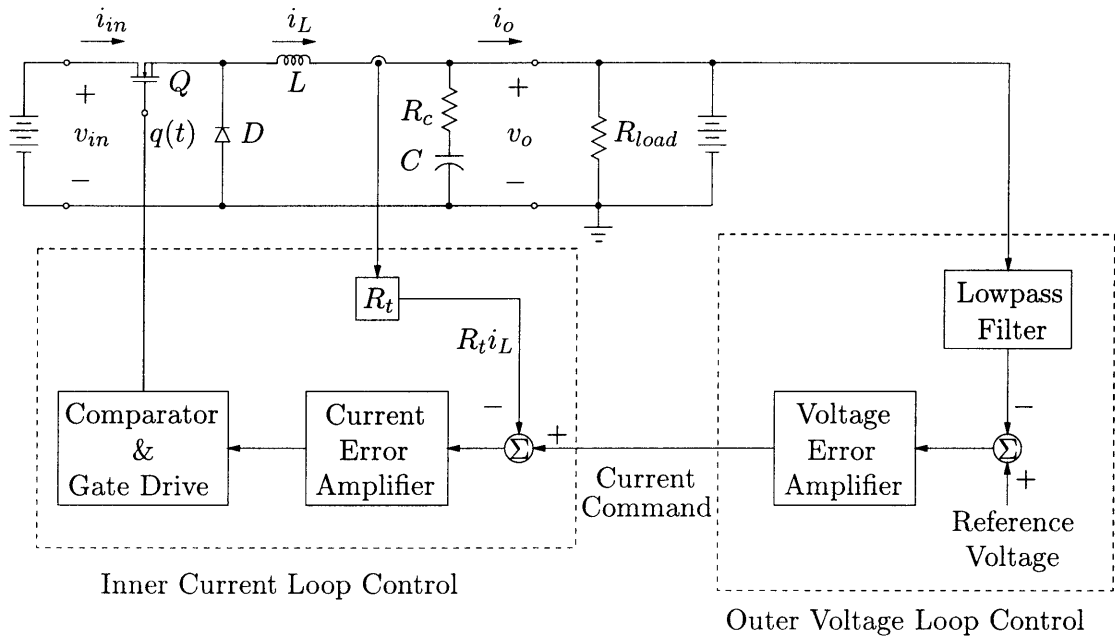
Figure 6.8: Simplified schematic of a single buck converter using average current-mode control.

which must be allowed to dynamically adjust the power delivery characteristics of the generating system depending on system parameters such as temperature, battery state-of-charge and load power demand.

The output voltage of today's alternator is controlled by a field current regulator as described in Chapter 4. When the output voltage drops below the temperature-compensated reference value, the field current is increased which in turn raises the machine back-emf voltage magnitude to drive more current out of the alternator and increase the output voltage. The output of the converter system is designed to operate in a similar manner but with higher bandwidth and accuracy than the present alternator system. Figure 6.9 shows the output current versus output voltage characteristics of the converter system. The converter system provides an output current that is proportional to the error in the output voltage up to a maximum of I_{max}. The maximum current output is 17 A/cell or 68 A for the entire four cell converter system. The reference voltage V_{ref} is set at 14.2 V at 25 °C and has a linear temperature coefficient of -7 mV/°C to match the lead-acid battery charging characteristics.

The voltage and current loops of the converter can be designed with the help of small-signal model shown in Figure 6.7. The transfer function of interest to us is the duty-ratio to output voltage transfer function $\tilde{v}_o(s)/\tilde{d}(s)$; therefore, we need that portion of the model involving blocks B_o, G_o and $Z(s)$. The small-signal model used for control design is illustrated in Figure 6.10. In this figure, the components that are a part of the control design for the current and voltage
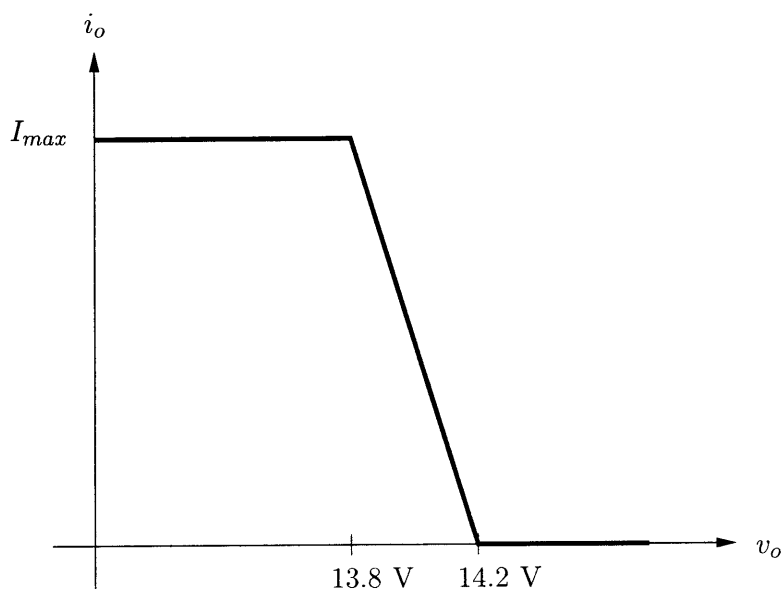
Figure 6.9: Buck converter output current-voltage characteristics. The maximum current I_{max} is 17 A per cell (68 A for the four-cell system) and can be reduced by an external signal from an energy management system. The output voltage v_o is regulated from 13.8 V to 14.2 V corresponding to $V_{o,min}$ and V_{ref}, respectively.

loops are indicated inside dashed boxes. The inner control loop consists of transfer functions for the transresistance R_t, current error amplifier $H_{ca}(s)$ and comparator (modulator) H_{comp}. The outer voltage loop consists of transfer functions for the lowpass filter $H_{lp}(s)$ and the voltage error amplifier $H_{va}(s)$. Next, we look more closely at the the design of current and voltage loops based on our small signal models.

6.5.1 Inner Current Loop

The purpose of the inner current loop is to force the average inductor current (which is equal to the average converter output current) to follow the command current set by the outer voltage loop. As mentioned earlier, this is accomplished by using average current-mode control. The inductor current is sensed indirectly by measuring the voltage across a resistor R_s which is in series with the cell inductor. The sensed voltage is amplified by a differential amplifier with a gain G_{da}. This results in a voltage $R_t i_L$ that is proportional to the cell inductor current with the constant of proportionality being the transresistance R_t $(= R_s G_{da})$. The entire sensing/amplification process is modeled by the transresistance and is represented by a block marked R_t in Figures 6.8 and 6.10. The purpose of the error amplifier is to establish a large current loop gain at low frequencies to reduce steady state tracking error and have large enough attenuation at higher frequencies to suppress noise. In
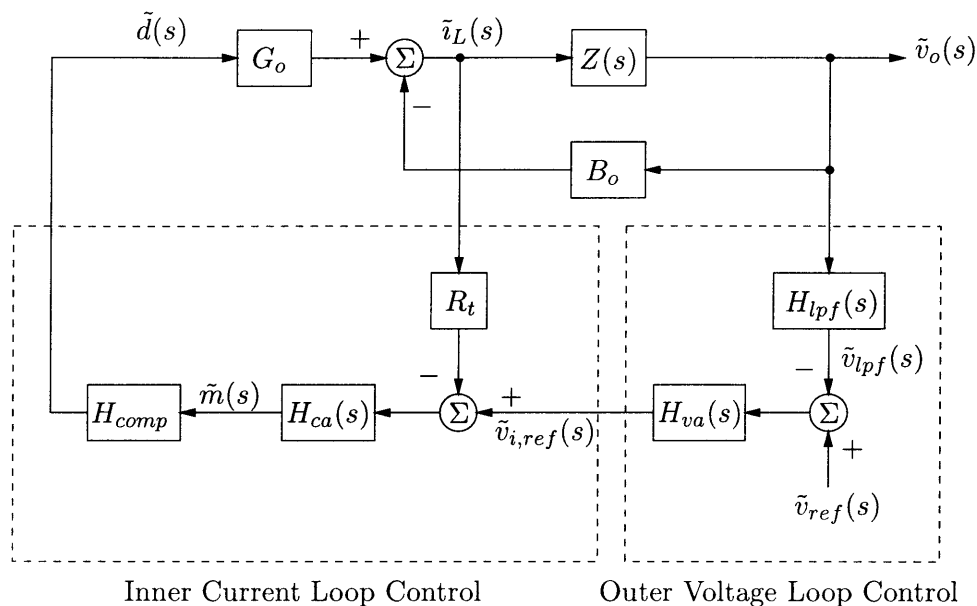
Figure 6.10: Control design for the buck converter.

practice, the bandwidth of the current loop is typically 1/6 to 1/8 of the switching frequency which in our case is 125 kHz [54]. We will design our current loop gain to be in the vicinity of 20 kHz which is a little less than 1/6 of our switching frequency.

6.5.2 Outer Voltage Loop

The outer voltage loop indirectly controls the output voltage of the converter by producing a current reference (for the inner current loop) that is proportional to the error in the output voltage. A lowpass filtered and attenuated version of the output voltage is sensed and compared to a temperature-compensated reference voltage to produce the error voltage. The error voltage drives the voltage error amplifier to produce the current reference signal $v_{i,ref}$. The voltage loop dynamics are typically slower than the current loop and are usually 1/10 of the switching frequency [54]. In our implementation, we have chosen a voltage loop bandwidth of 10 kHz. The overall bandwidth of the system is usually on the order of the outer loop bandwidth which in our case will be around 5-10 kHz.

6.5.3 Control Implementation

A single buck converter employing average current-mode control is shown in Figure 6.11. The figure also shows component values that yield the desired steady-state and transient characteristics.
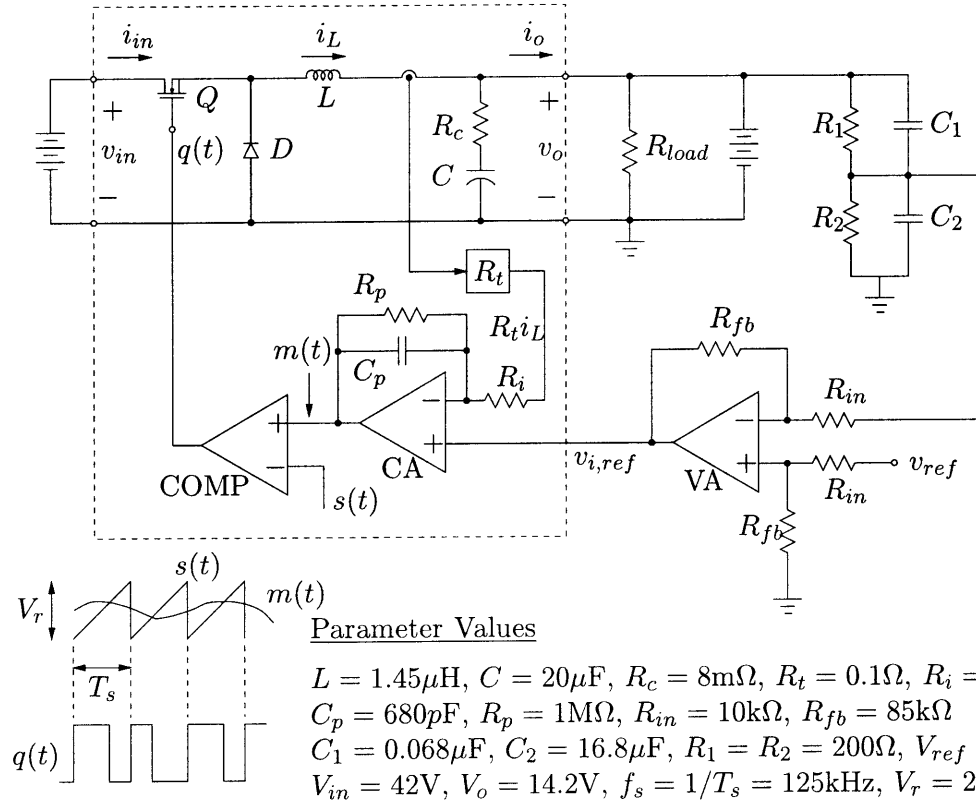
Figure 6.11: Schematic of a single buck converter using average current-mode control. To implement a parallel converter system, only the system inside the dashed region needs to be replicated.

This system was designed using the simulation models that were based on the analytical models of Figures 6.7 and 6.8. Detailed simulation results will be presented in the next section. To implement a parallel converter system based on the average current-mode control, one needs to replicate the system inside the dashed region of Figure 6.11. With the paralleling technique, each converter cell would have an associated inner control loop that is fed by a common current reference signal $v_{i,ref}$ established by a single outer voltage loop. Each transfer function appearing in the small signal model of Figure 6.10 has been implemented in Figure 6.11. As mentioned earlier, a current sensing resistor in combination with a differential amplifier has been used to implement the transresistance R_t to produce a voltage proportional to the cell resistor. This has been implemented with a series resistor R_s of 5 mΩ and a differential amplifier with gain G_{da} of 20. The transresistance R_t is then equal to $R_s G_{da}$ or 0.1 Ω. The lowpass filter $H_{lp}(s)$ is the resistor/capacitor voltage divider R_1, C_1, R_2, C_2. The transfer function of the filter is

$$H_{lp}(s) = \frac{R_2}{R_1 + R_2} \frac{1 + sC_1R_1}{1 + s\left(C_1 + C_2\right)\left(R_1 \parallel R_2\right)} \tag{6.9}$$

The designed values yield a voltage divider ratio of 1/2 at low frequencies which is compared to the nominal reference voltage 7.1 V (corresponding to an output voltage of 14.2 V). The voltage amplifier is a simple differential amplifier with transfer function:

$$H_{va} = \frac{R_{fb}}{R_{in}} \left(v_{ref} - v_o \right) \tag{6.10}$$

The output of the differential amplifier is the current command reference signal $v_{i,ref}$ which drives the inner current loop. The current amplifier tries to drive the sensed cell current $R_t i_L$ ($=0.1\ i_L$) to equal to the current reference which is at most 1.7 V. This voltage range corresponds to the scaled version of the current output range for a converter cell which has a maximum value of 17 A. The current error amplifier is basically a lossy integrator with inherently large gain at low frequencies that improves tracking of average cell current. The transfer function of the current amplifier is given by

$$H_{ca}(s) = -\frac{R_p}{R_i} \frac{1}{1 + sC_pR_p} \tag{6.11}$$

The output of the current amplifier is a modulation signal $m(t)$ which is compared to a ramp signal with magnitude V_r and frequency f_s to generate the switching signal $q(t)$ with the proper duty ratio. The transfer function of the comparator is given by

$$H_{comp} \triangleq \frac{\tilde{d}(s)}{\tilde{m}(s)} = \frac{1}{V_r} \tag{6.12}$$

This control system was developed using the simulation models and analytical expressions derived earlier in this chapter. The next section describes the simulation model that was developed in Saber to design and verify the operation of the converter and control system. Several simulations are performed to verify the operation of the system, including current and voltage loop gains and load transient response.

6.6   Simulation and Experimental Results

The Saber simulation model for a buck converter with average current-mode control is shown in Figure 6.12. This is an averaged model of the system shown in Figure 6.11 and follows the block diagram structure given in Figure 6.10. This model is versatile in that both averaged transient and small-signal simulations can be performed using the same simulation diagram. One can also run full switched (non-averaged) simulations if the block for the averaged buck cell is replaced by a switching cell and the comparator gain is replaced by an actual comparator with a ramp input. The
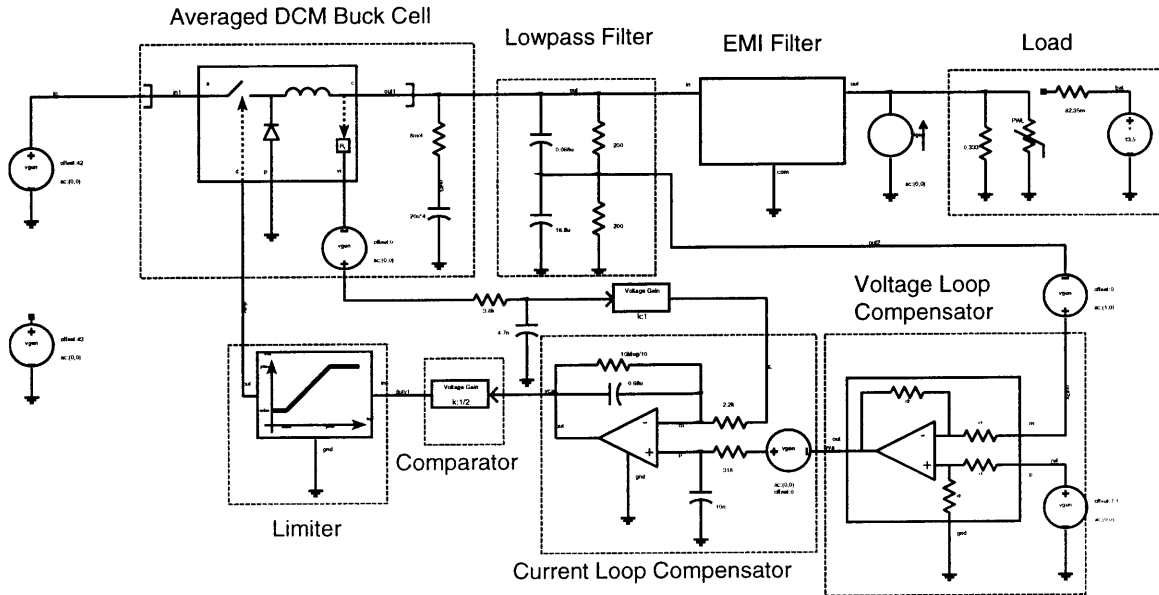
Figure 6.12: Saber simulation model for a buck converter with average current-mode control. This model is versatile in that both averaged transient and small-signal simulations can be performed using the same system.

switching-cell based model has also been developed but is not shown since the simulation diagrams are essentially identical. Note that the model in Figure 6.12 also includes the EMI filter which was not discussed in the chapter but must be considered as part of the practical implementation [15, 16]. Also note the presence of RC lowpass filters that are at the inputs of the current error amplifier. These filters were used in the experimental prototype to attenuate high frequency noise and were added to the simulation model for the sake of completeness. The addition of the EMI and the RC filters do not significantly change the analytical results presented earlier.

6.6.1 Loop Gains

In order to verify the frequency response associated with the control design, the small-signal loop gains of the converter system shown in Figure 6.12 were simulated. The loop gain measurements can be performed by placing a small-signal voltage source in series with either the current control loop or the voltage control loop and measuring the voltage gain across the source. It should be noted that breaking the loop and inserting a small-signal source between the break point and ground and measuring the returned signal is also theoretically correct. However, this method of signal injection leads to erroneous measurements since the operating point is disturbed.

From a control viewpoint, the worst case (lowest phase margin) loop gains are encountered when the battery is absent from the output of the converter system. The worst case minimum nominal load is 4.25 A/cell, that is, 25% of the full current. The current loop gain under this worst case condition for a single buck converter is illustrated in Figure 6.13. The crossover frequency is approximately 20 kHz with a phase margin of 45°. The voltage loop gain is given in Figure 6.14 and shows the crossover frequency to be approximately 10 kHz with a phase margin of 79°. The phase margin and bandwidth are both acceptable for the worst case scenario and verify the desired small-signal frequency response of the control design.

6.6.2   Transient Response

With the control loop design in place, we can now exercise the converter model by running a number of transient tests. As mentioned earlier, the averaged simulation model presented in Figure 6.12 is a rather accurate representation of the actual switched converter cell and is computationally more efficient. Figures 6.15 and 6.16 show the switched and averaged simulations of a load transient response of a single cell buck converter with average current-mode control. The nominal current of the converter cell is 4.25 A which is 25% of the full current for the cell. The current demand at the output is changed according to the identical current profiles shown as the top traces in Figures 6.15 and 6.16. As can be seen from the figures, the resulting voltage traces match quite well. The averaged model does not have the switching ripple information, but this information is not necessary for the design of the control system which itself is designed to regulate average values. The full switched simulation is still useful if stresses for the switching elements, namely the peak currents and voltages for the semiconductor devices, are to be determined.

Figure 6.17 shows a transient response due to sudden changes in the input voltage of the converter system which is nominally at 42 V. Once again, the system is simulated in the absence of a battery and 25% of full load. The top trace in the figure shows the input voltage which is stepped to 52 V and down to 33 V before returning to the nominal value of 42 V. The stepped values 33 V and 52 V correspond to the minimum and maximum of the input voltage given in the converter design specifications in Table 6.1. As can be seen from the output voltage response (bottom trace) in Figure 6.17, the maximum transient is 16 V, the system recovers in 150 μs to the nominal system voltage of 14 V even without the aid of a stiff voltage source as would be presented by a battery.

The simulation results so far have only considered a single cell converter with average current-mode control. The modeling and simulation of a multi-cell system is also straightforward using the models presented earlier. In fact, the simulation model in Figure 6.12 has been designed such that one only needs to supply the number of cells in order to re-evaluate the results above for
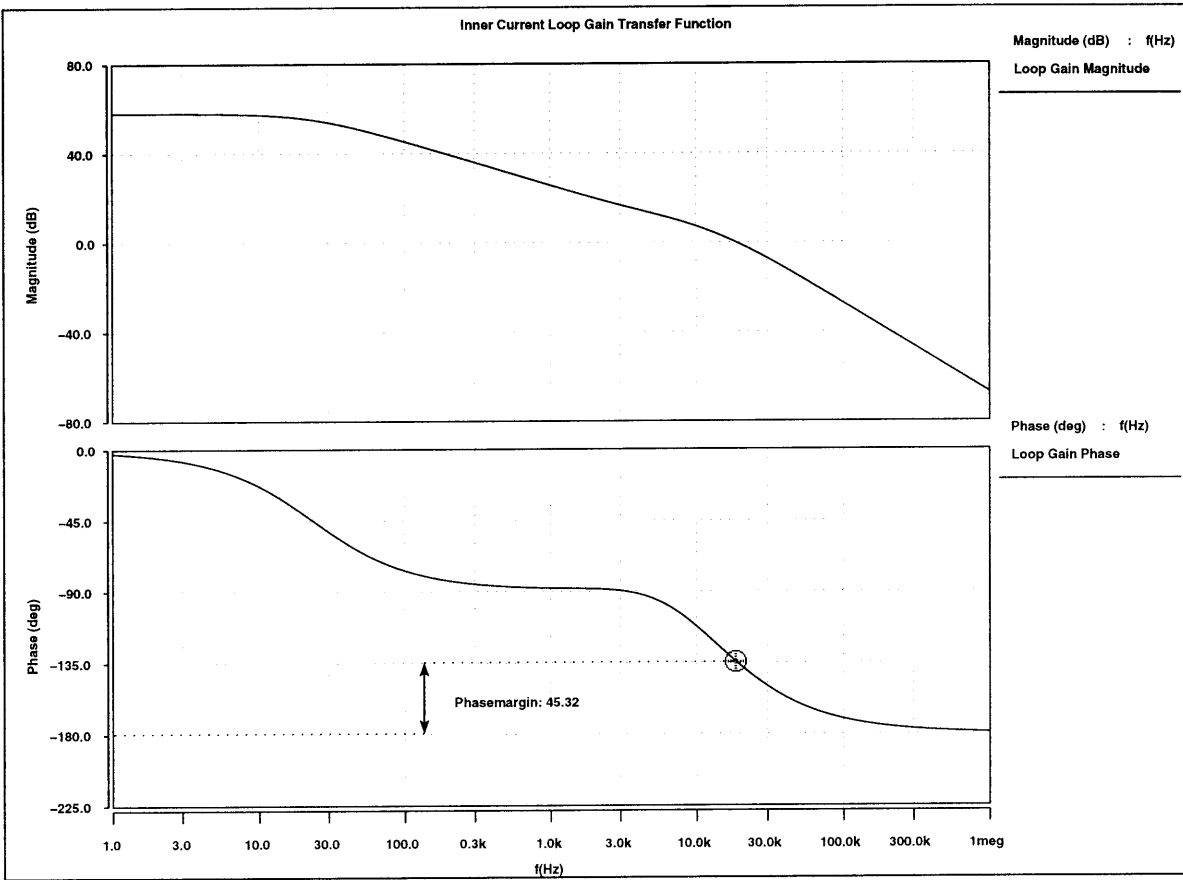
Figure 6.13: Simulation of inner current loop gain transfer function for a single buck converter under average current-mode control. The crossover frequency is approximately 20 kHz with a phase margin of 45°.
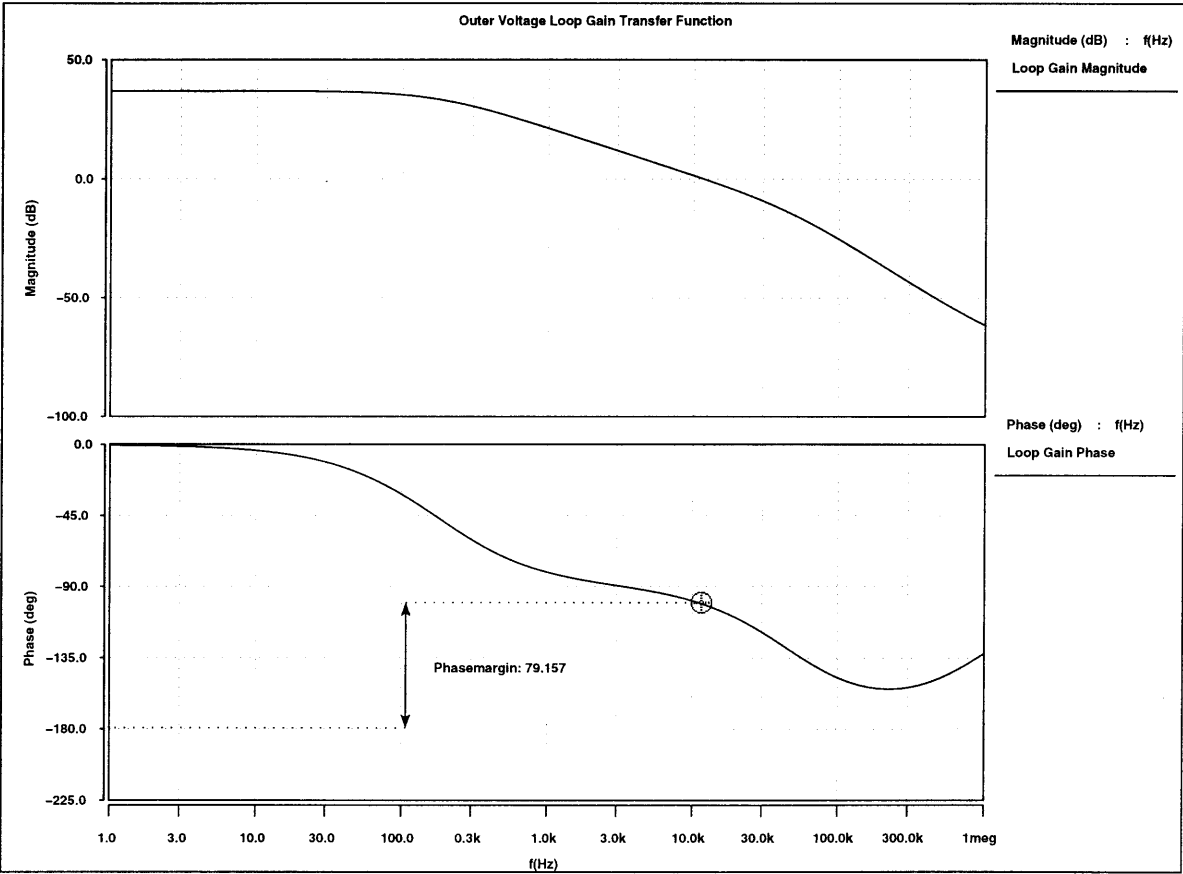
Figure 6.14: Simulation of outer voltage loop gain transfer function for a single buck converter under average current-mode control. The crossover frequency is approximately 10 kHz with a phase margin of 79°.
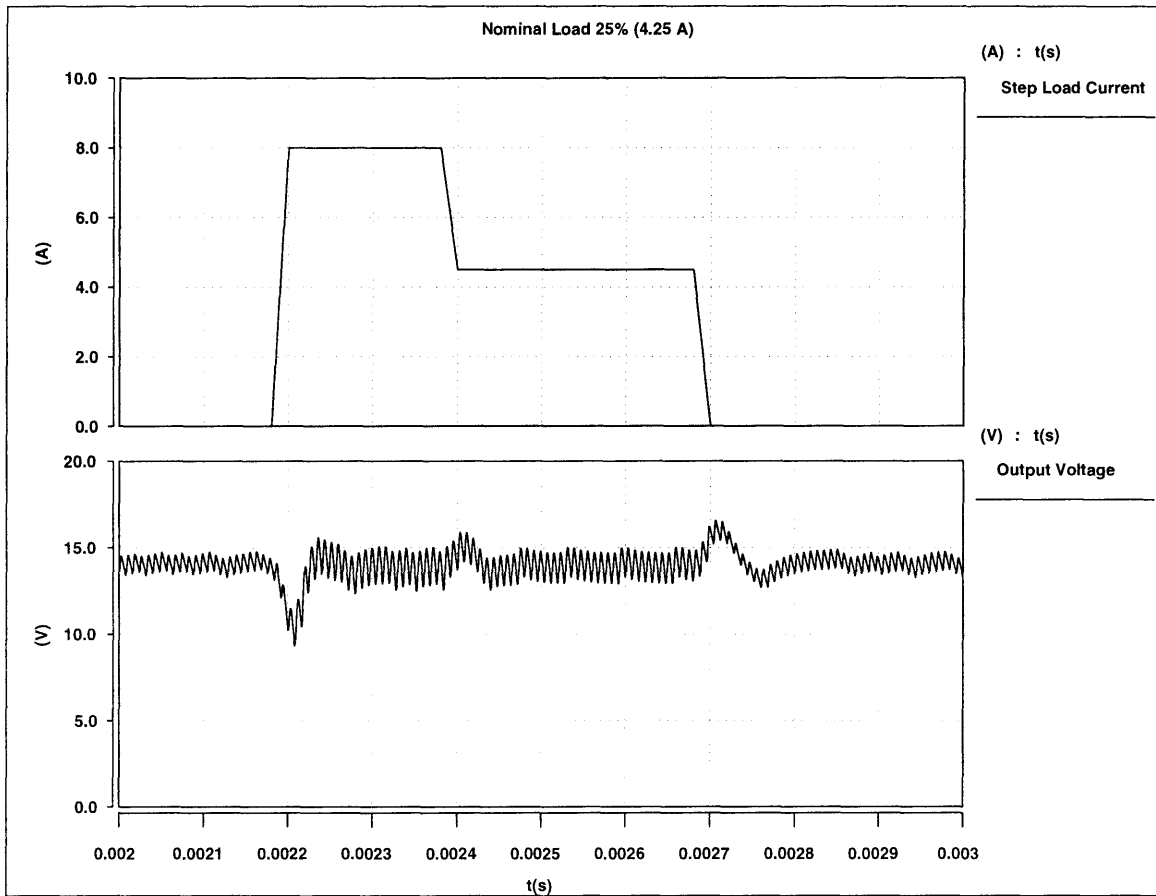
Figure 6.15: Simulation, using a switched model, of load current switching transient response for a buck converter cell with average current-mode control at 4.25 A (25% of full current). The top trace is the additional current demand at the output of the converter while the bottom trace is the resulting output voltage.

any number of cells. To illustrate this feature, we have simulated a load transient for a four cell converter system. Once again, the simulation considers the worst case condition when the battery is disconnected from the output of the system. To induce the transient, the load at the output of the converter system is suddenly changed from 80% of full current to 50% then back up to 80%. The results of the simulation are presented by the dashed line in Figure 6.18 which shows the overshoot (undershoot) of the output voltage as the load current demand is reduced (increased). As can be seen from the figure, the voltage deviations do remain within the specifications in Table 6.1. The analytical results and simulations presented have been used to support the design and implementation of an experimental prototype of the dc/dc converter discussed. The solid line in Figure 6.18 shows experimental results from the four cell interleaved converter subjected to the same load transient as the simulation. As can be seen from Figure 6.18, the experimental results
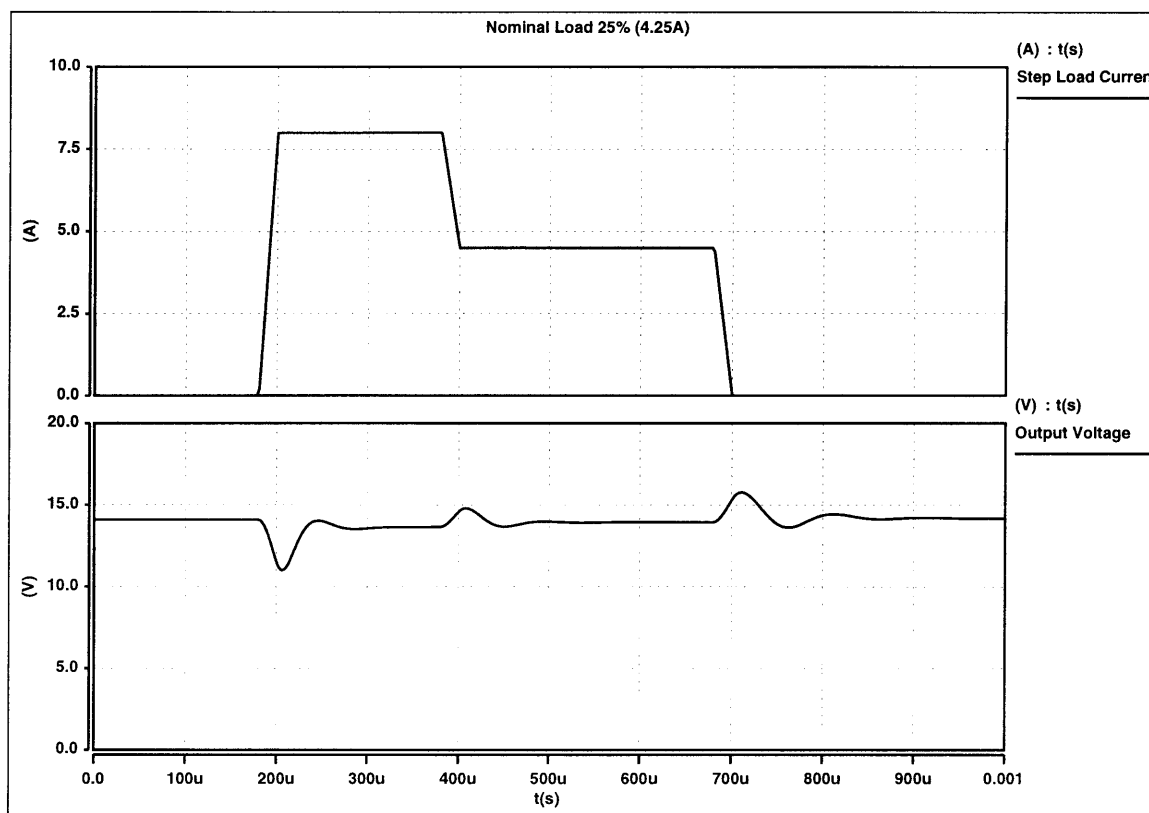
Figure 6.16: Simulation of load current average transient response for buck converter cell with average current-mode control at 4.25 A (25% of full current). The top trace is the additional current demand at the output of the converter while the bottom trace is the resulting output voltage.

closely match the simulation results. The transients observed on the prototype are also within the desired specifications of Table 6.1. Figure 6.19 shows the picture of the prototype four cell converter from which the experimental results were obtained.

6.7 Summary

In this chapter, analysis and design of an interleaved dc/dc converter system was presented. This system is at the heart of the dual-voltage architecture shown in Figure 6.1. The dc/dc converter system provides a number of features that do not exist in today's electrical systems. Among these features is a well-regulated 14 V bus with a high control bandwidth. The regulation of the 14 V is retained under load transients even in the absence of a storage battery. The improved performance, however, results in a large cost penalty when compared to the present generation system. In order
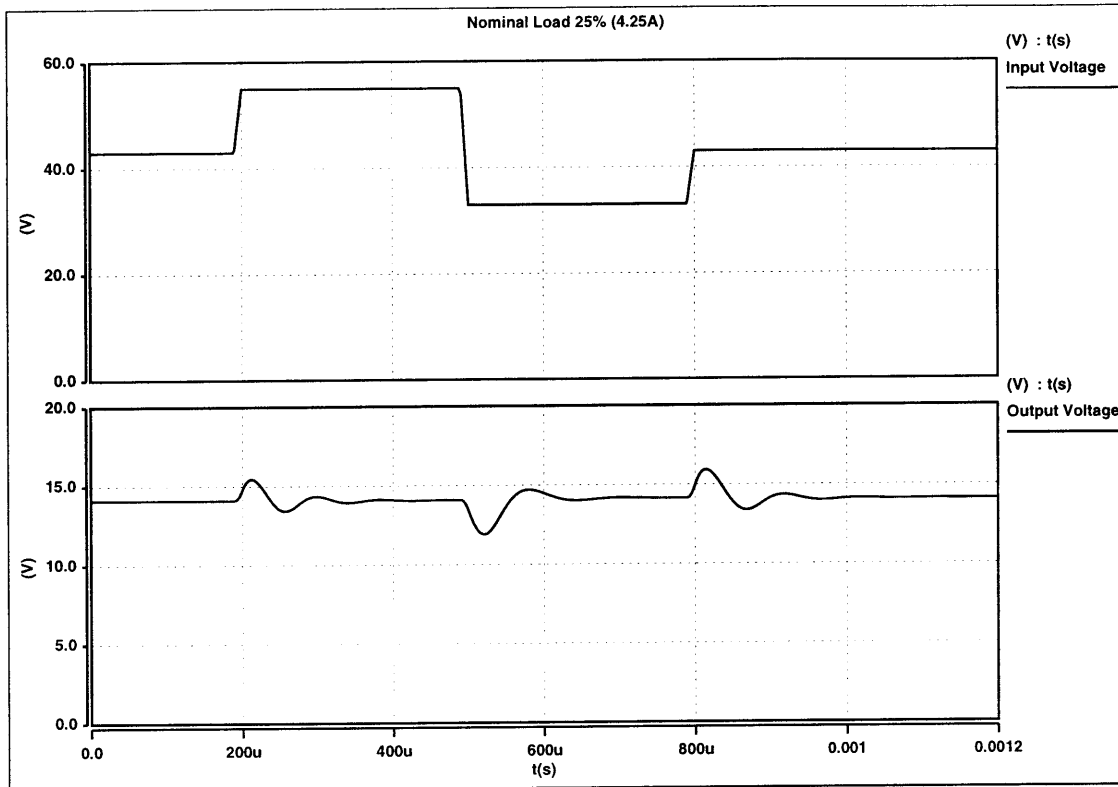
Figure 6.17: Simulation of the transient response of the buck converter cell to sudden changes in the input voltage at 25% of full load. The input voltage (top trace) which is initially at the nominal value of 42 V is increased to 52 V and then down to 33 V before returning to the nominal value. The output voltage is shown in the bottom figure.

to make the case for the dc/dc converter system, one must consider system costs and present the additional benefits the converter system provides besides the power output. For example, based on the performance of the dc/dc converter, it is apparent that little or no transient suppression is necessary at the 14 V output. The improved transient response may lead to the elimination or redesign of protection circuitry for electronics connected to the 14 V bus. While the transient response of the 14 V bus is improved, the transients on the high voltage bus (42 V) remain. Since a high voltage Lundell alternator is the most likely generator to be used in this architecture, the load dump transient will be the dominating transient to be considered and suppressed. The peak transients on the high voltage bus can easily reach several hundreds of volts during a load dump. The dc/dc converter may be used to absorb this transient; however, this will add to the cost and complexity of the converter system which is already high. An attractive alternative is the combination of the new alternator system (Chapter 5) and the dc/dc converter. This complete dc/dc converter system (further described in Chapter 8) offers fast load-dump control of both buses and has the additional benefits associated with the alternator system described in Chapter 5.
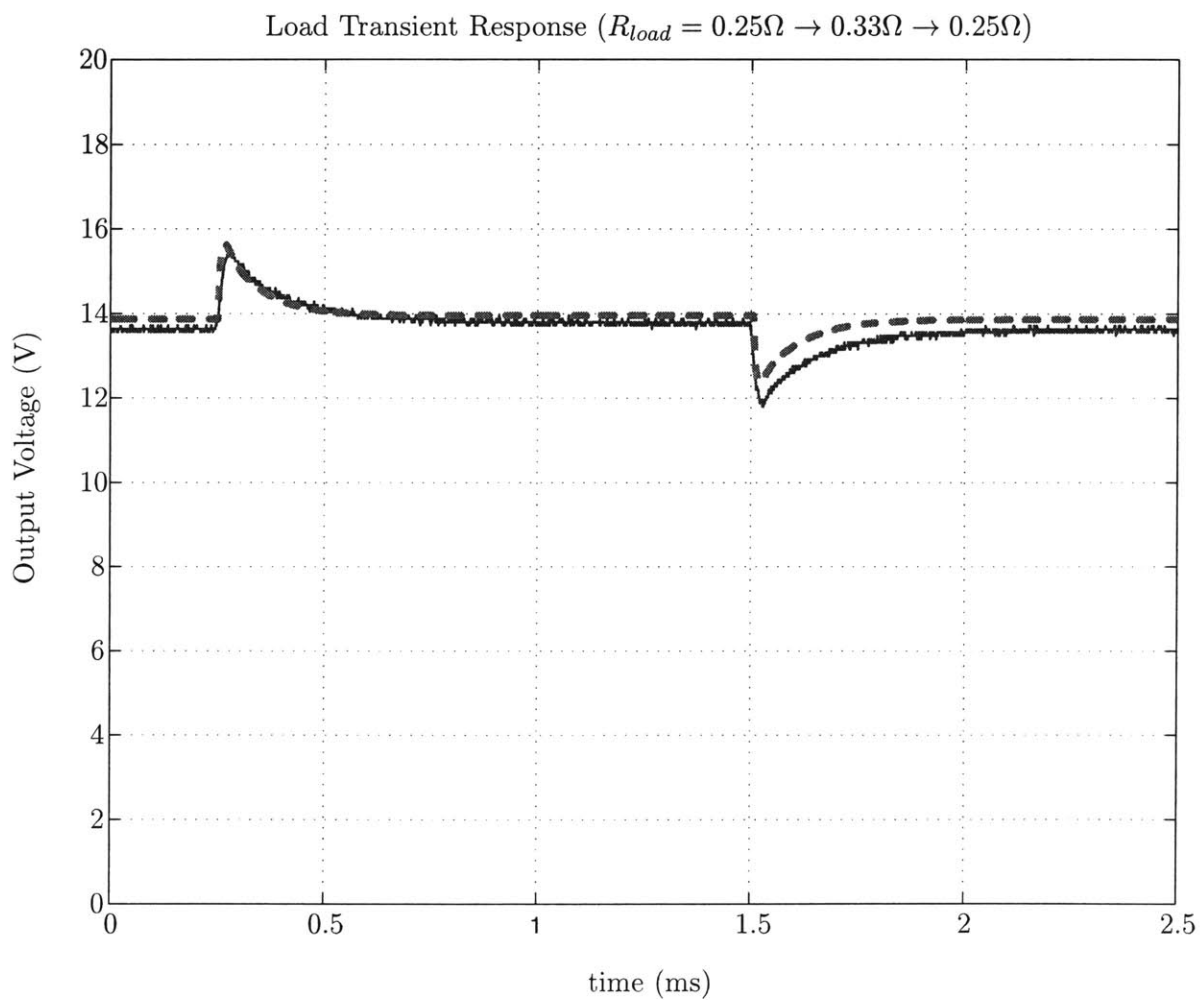
Figure 6.18: Load transient response of the four cell interleaved converter system with a disconnected battery: experimental (solid) and simulation (dashed). The load is suddenly changed from 80% of full current to 50% then back up to 80%.

Figure 6.19: Experimental prototype of the four cell interleaved buck converter using average current-mode control. The electronics for the cells are primarily located near heat sinks on which the power MOSFET and diode for each stage are mounted. The wound coils at the top and bottom are a part of the input and output EMI filters, respectively.

Dual-Stator Alternator Architecture

7.1 Introduction

The dual-stator alternator architecture is shown in Figure 7.1 and is based on a dual winding synchronous machine providing both high and low voltage three phase outputs. Each winding of the machine is followed by a rectifier to produce the desired dc voltage level. One possible way to control the dc bus voltages is to regulate the alternator field current for the 42 V bus and use a phase-controlled rectifier with firing angle control to regulate the 14 V bus. This is the method of control that will be described here.

In this chapter, we first develop a mathematical model for the dual-stator alternator in terms of inductance and resistance matrices for the two sets of three-phase stator windings plus the field winding. A simulation model for the dual-stator alternator is then implemented in Saber by using the analytical description. The model for the machine is used to simulate the dual-stator alternator architecture system and determine the average output current of each rectifier as a function of the control variables (field current and firing angle). Averaging techniques developed in Chapter 4 are used to predict system limitations. In addition to their use in investigating the steady-state characteristics of the architecture, the simulation models are also used to investigate the dynamics of the architecture and illustrate passive transient protection.

7.2 Dual-Stator Alternator Model

The dual-stator alternator architecture has recently received attention as a candidate dual-voltage automotive electrical system. This architecture offers a dual-voltage system based on rectifiers and a two stator version of the Lundell alternator and is considered to be a viable lower-cost alternative to the dc/dc converter based system discussed in Chapter 6. In order to determine the steady-state and transient characteristics, a model for the dual-stator alternator is needed. This section describes the development of a dual-stator alternator model suitable for simulation in Saber.
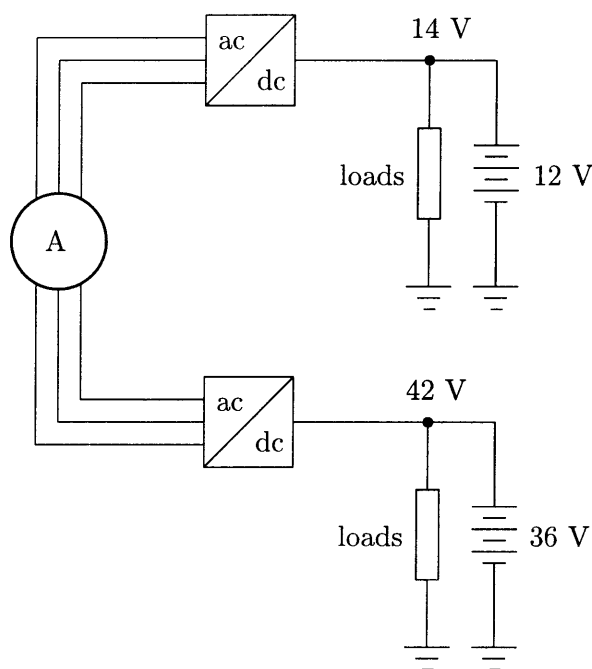
Figure 7.1: Dual-stator alternator architecture.

The dual-stator alternator that we consider in this chapter is a two stator version of the Lundell alternator that was discussed in Chapter 4. The presentation in this chapter will follow the development and the nomenclature introduced in Chapter 4 with slight modifications to distinguish between the two stators. The particular geometry that we are considering is shown schematically in Figure 7.2 where the windings are geometrically offset by $0°$. The similarly-named phase windings for each stator share the same slots (e.g., phases a_1 and a_2). Machines with stator offsets other than $0°$ are also possible; however, the present geometry was chosen since it will maximize the magnetic coupling between the two stators, thus presenting a worst-case upper bound on expected adverse cross-regulation effects.

In order to proceed with the analysis, we make some common simplifying assumptions such as neglecting saturation and hysteresis and treating the machine as a lumped parameter system as was done for the synchronous machine in Chapter 4. The schematic diagram of a dual-stator synchronous machine showing the two sets of stators geometrically offset by $0°$ is shown in Figure 7.3. The coils indicated by $a_1 a_1'$, $b_1 b_1'$, $c_1 c_1'$ represent the distributed windings for the low voltage stator (14 V) and coils indicated by $a_2 a_2'$, $b_2 b_2'$, $c_2 c_2'$ represent the ones for the high voltage stator (42 V). The magnetic axes of the phases are displaced from each other by $120°$.

Using the conventions and terminology introduced in Chapter 4, the flux linkages in the

Low Voltage Winding   High Voltage Winding   Field Winding
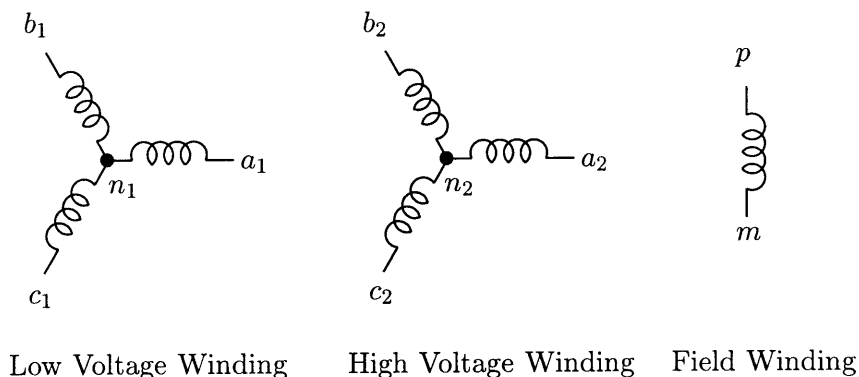
Figure 7.2: Definitions of windings and terminals for the dual-stator alternator.

phases and the field winding are given by

$$
\underbrace{\begin{bmatrix} \lambda_{a_1} \\ \lambda_{b_1} \\ \lambda_{c_1} \\ \hline \lambda_{a_2} \\ \lambda_{b_2} \\ \lambda_{c_2} \\ \hline \lambda_f \end{bmatrix}}_{\underline{\lambda}(t)} = \underbrace{\left[\begin{array}{ccc|ccc|c} L_{a_1a_1} & L_{a_1b_1} & L_{a_1c_1} & L_{a_1a_2} & L_{a_1b_2} & L_{a_1c_2} & L_{a_1f} \\ L_{b_1a_1} & L_{b_1b_1} & L_{b_1c_1} & L_{b_1a_2} & L_{b_1b_2} & L_{b_1c_2} & L_{b_1f} \\ L_{c_1a_1} & L_{c_1b_1} & L_{c_1c_1} & L_{c_1a_2} & L_{c_1b_2} & L_{c_1c_2} & L_{c_1f} \\ \hline L_{a_2a_1} & L_{a_2b_1} & L_{a_2c_1} & L_{a_2a_2} & L_{a_2b_2} & L_{a_2c_2} & L_{a_2f} \\ L_{b_2a_1} & L_{b_2b_1} & L_{b_2c_1} & L_{b_2a_2} & L_{b_2b_2} & L_{b_2c_2} & L_{b_2f} \\ L_{c_2a_1} & L_{c_2b_1} & L_{c_2c_1} & L_{c_2a_2} & L_{c_2b_2} & L_{c_2c_2} & L_{c_2f} \\ \hline L_{fa_1} & L_{fb_1} & L_{fc_1} & L_{fa_2} & L_{fb_2} & L_{fc_2} & L_{ff} \end{array} \right]}_{\mathbf{L}(\theta(t))} \underbrace{\begin{bmatrix} i_{a_1} \\ i_{b_1} \\ i_{c_1} \\ \hline i_{a_2} \\ i_{b_2} \\ i_{c_2} \\ \hline i_f \end{bmatrix}}_{\underline{i}(t)}
\tag{7.1}
$$

The matrix expression (7.1) can also be expressed in compact form as

$$
\underline{\lambda}(t) = \mathbf{L}\left(\theta(t)\right)\underline{i}(t)
\tag{7.2}
$$

where $\mathbf{L}(\theta)$ is the inductance matrix of the machine, $\underline{\lambda}$ is the flux linkage vector and $\underline{i}$ is the current vector (the explicit time variation has been dropped to reduce notational complexity). The elements of the inductance matrix characterize the machine and are in general functions of the rotor electrical angle θ. As in the single stator machine discussed in Chapter 4, there are three types of inductances that are appear in $\mathbf{L}(\theta)$: (1) stator and rotor self inductances (7 terms), (2) stator-stator mutual inductances (30 terms) and (3) stator-rotor mutual inductances (12 terms). These inductances are expressed in Tables 7.1, 7.2 and 7.3 and include the effects of space-fundamental air gap flux (L_{ms1}, L_{ms2}, L_{mf}), slot mutual flux (L_{ss1}, L_{ss2}), leakage flux (L_{ls1}, L_{ls2}, L_{lf}) and rotor saliency (L_{g1}, L_{g2}). The subscripts 1 and 2 refer to stator 1 and stator 2, respectively. Table 7.4 defines some of the inductance variables introduced in Tables 7.2 and 7.3.
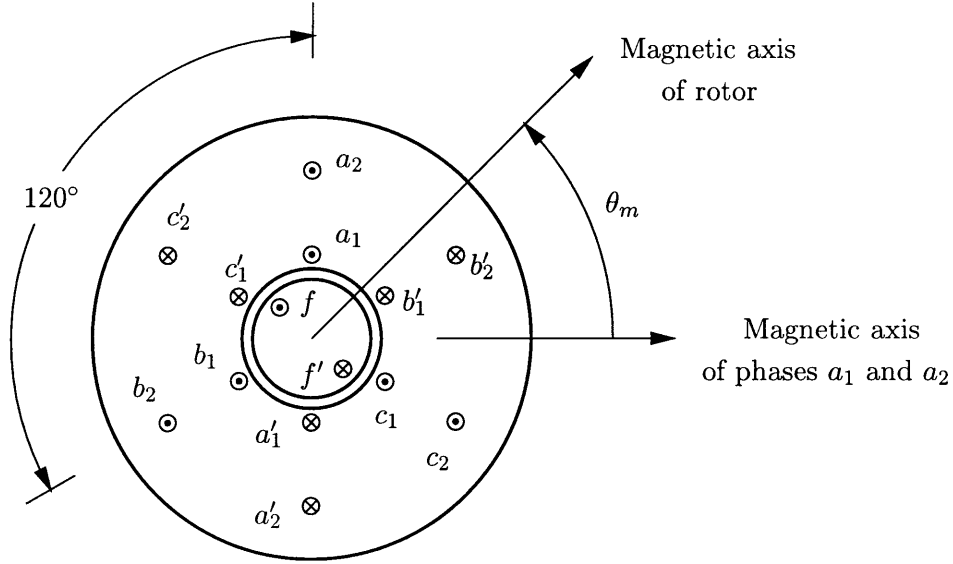
Figure 7.3: Schematic diagram of a dual-stator synchronous machine showing the two sets of stators geometrically offset by 0°.

Referring to Figure 7.3 and Table 7.1, it can be seen that the self inductance of each phase is maximum when the rotor magnetic axis is aligned with the magnetic axis of that phase. On the other hand, stator-stator mutual inductances given in Table 7.2 are maximum when the rotor magnetic axis is aligned with the midpoint of the magnetic axes of the two phases [44]. With the inductance matrix completely specified, the terminal voltages of the machine are given by

$$\underline{v} = \mathbf{R}\underline{i} + \frac{d\underline{\lambda}}{dt} \tag{7.3}$$

In the matrix expression of (7.3) variables $\underline{v}$ and $\mathbf{R}$ represent the terminal voltage vector and the machine resistance matrix, respectively, and are given by

$$\underline{v} = [v_{a_1} \ v_{b_1} \ v_{c_1} \ v_{a_2} \ v_{b_2} \ v_{c_2} \ v_f]^T \tag{7.4}$$

$$\mathbf{R} = \mathrm{diag}\,[R_{s1} \ R_{s1} \ R_{s1} \ R_{s2} \ R_{s2} \ R_{s2} \ R_f] \tag{7.5}$$

In the voltage vector given in (7.4), phase terminal voltages v_{a_1}, v_{b_1} and v_{c_1} are measured with respect to neutral terminal n_1 while v_{a_2}, v_{b_2} and v_{c_2} are measured with respect to neutral terminal n_2. The variables R_{s1}, R_{s2} and R_f in (7.5) are the resistances for stator 1, stator 2 and the field windings, respectively. A simplified schematic corresponding to (7.3) is shown in Figure 7.4. Expression (7.3) for the dual-stator machine forms the basis of a computer model that is implemented in Saber. The next section uses this model to derive the steady-state and transient characteristics of the dual-stator alternator.

Table 7.1: Dual-stator synchronous machine stator and rotor self inductances.

Inductance	Expression
$L_{a_1 a_1}$	$L_{ls1} + L_{ms1} + L_{g1} \cos (2\theta)$
$L_{a_2 a_2}$	$L_{ls2} + L_{ms2} + L_{g2} \cos (2\theta)$
$L_{b_1 b_1}$	$L_{ls1} + L_{ms1} + L_{g1} \cos \left(2\theta + \frac{2\pi}{3}\right)$
$L_{b_2 b_2}$	$L_{ls2} + L_{ms2} + L_{g2} \cos \left(2\theta + \frac{2\pi}{3}\right)$
$L_{c_1 c_1}$	$L_{ls1} + L_{ms1} + L_{g1} \cos \left(2\theta - \frac{2\pi}{3}\right)$
$L_{c_2 c_2}$	$L_{ls2} + L_{ms2} + L_{g2} \cos \left(2\theta - \frac{2\pi}{3}\right)$
L_{ff}	$L_{lf} + L_{mf}$

7.3 Dual-Stator Alternator Architecture Characteristics

The dual-stator alternator architecture that we will consider is shown in Figure 7.5. This figure presents a particular implementation of the more generic system which was shown in Figure 7.1. As in the single stator alternator, a field current regulator is used to control the field current for the machine. The back-emf produced in each of the two stators are proportional to the field current and the machine speed. The two three-phase stator outputs are then rectified to produce the bus voltages. The high voltage stator outputs are fed into a diode bridge rectifier while the low voltage stator outputs are connected to a phase-controlled rectifier. Each bus is connected to a battery and associated loads.

We will use the dual-stator alternator parameters given in Table 7.5 for our simulations. Referring to this table, we note that the low voltage stator parameters (subscript 1) are identical to those presented in Chapter 4 while the high voltage stator (subscript 2) and the field winding parameters have been voltage scaled by a factor of three. For the purposes of our analysis, we will neglect the effect of the slot magnetizing inductances L_{ss1} and L_{ss2} and approximate the mutual inductance L_{ms12} (Table 7.4) as $\sqrt{L_{ms1} L_{ms2}}$. The dual-stator alternator has approximately the same output power capability ($\approx$ 1.8 kW) as the one presented in Chapter 4 except that the power is evenly distributed between the two stators. As a result, the low voltage and high voltage stators can each deliver approximately 900 W at average output currents of 65 A and 22 A, respectively, Figure 7.7 shows the Saber schematic which illustrates the implementation of

Table 7.2: Dual-stator synchronous machine stator-stator mutual inductances.

Inductance	Expression
$L_{a_1b_1}, L_{b_1a_1}$	$L_{ms11} + L_{g1} \cos\left(2\theta - \frac{2\pi}{3}\right)$
$L_{a_2b_2}, L_{b_2a_2}$	$L_{ms22} + L_{g2} \cos\left(2\theta - \frac{2\pi}{3}\right)$
$L_{a_1c_1}, L_{c_1a_1}$	$L_{ms11} + L_{g1} \cos\left(2\theta + \frac{2\pi}{3}\right)$
$L_{a_2c_2}, L_{c_2a_2}$	$L_{ms22} + L_{g2} \cos\left(2\theta + \frac{2\pi}{3}\right)$
$L_{b_1c_1}, L_{c_1b_1}$	$L_{ms11} + L_{g1} \cos\left(2\theta\right)$
$L_{b_2c_2}, L_{c_2b_2}$	$L_{ms22} + L_{g2} \cos\left(2\theta\right)$
$L_{a_1a_2}, L_{a_2a_1}$	$L_{ms12} + L_{g12} \cos\left(2\theta\right)$
$L_{b_1b_2}, L_{b_2b_1}$	$L_{ms12} + L_{g12} \cos\left(2\theta + \frac{2\pi}{3}\right)$
$L_{c_1c_2}, L_{c_2c_1}$	$L_{ms12} + L_{g12} \cos\left(2\theta - \frac{2\pi}{3}\right)$
$L_{a_1b_2}, L_{b_2a_1}, L_{a_2b_1}, L_{b_1a_2}$	$-\frac{1}{2}L_{ms12} + L_{g12} \cos\left(2\theta - \frac{2\pi}{3}\right)$
$L_{c_2a_1}, L_{a_1c_2}, L_{c_1a_2}, L_{a_2c_1}$	$-\frac{1}{2}L_{ms12} + L_{g12} \cos\left(2\theta + \frac{2\pi}{3}\right)$
$L_{b_1c_2}, L_{c_2b_1}, L_{b_2c_1}, L_{c_1b_2}$	$-\frac{1}{2}L_{ms12} + L_{g12} \cos\left(2\theta\right)$

the dual-stator alternator architecture including the field current and firing angle controllers.

7.3.1 Steady-State Characteristics

Steady-state current vs. alternator speed for the two outputs of the dual-stator alternator at full field are shown in Figure 7.6 and are parameterized by the firing angle α of the thyristors. The results are generated by simulating the dual-stator alternator architecture in Saber (Figure 7.7) at a constant speed with constant-voltage loads until steady-state is reached. The waveforms are then analyzed to determine the average values for each bus current. For our rectifier system with a constant-voltage load, the firing angle α is defined relative to the forward voltage that appears across the thyristor. With the firing angle set to zero, the phase-controlled rectifier behaves as

Table 7.3: Dual-stator synchronous machine stator-rotor mutual inductances.

Inductance	Expression	Inductance	Expression
L_{fa_1}, L_{a_1f}	$M_1 \cos(\theta)$	L_{fa_2}, L_{a_2f}	$M_2 \cos(\theta)$
L_{fb_1}, L_{b_1f}	$M_1 \cos\left(\theta - \frac{2\pi}{3}\right)$	L_{fb_2}, L_{b_2f}	$M_2 \cos\left(\theta - \frac{2\pi}{3}\right)$
L_{fc_1}, L_{c_1f}	$M_1 \cos\left(\theta + \frac{2\pi}{3}\right)$	L_{fc_2}, L_{c_2f}	$M_2 \cos\left(\theta + \frac{2\pi}{3}\right)$

Table 7.4: Dual-stator synchronous machine mutual inductances.

Parameter	Description	Expression
L_{ms11}	average stator 1 – stator 1 mutual inductance	$-\frac{1}{2}L_{ms1}$
L_{ms22}	average stator 2 – stator 2 mutual inductance	$-\frac{1}{2}L_{ms2}$
L_{ms12}	stator 1 – stator 2 mutual inductance	$\sqrt{L_{ms1}L_{ms2}} + \sqrt{L_{ss1}L_{ss2}}$
L_{g12}	stator 1 – stator 2 saliency inductance	$\sqrt{L_{g1}L_{g2}}$
M_1	peak stator 1 – rotor mutual inductance	$\sqrt{L_{mf}L_{ms1}}$
M_2	peak stator 2 – rotor mutual inductance	$\sqrt{L_{mf}L_{ms2}}$

a conventional bridge rectifier and the power output of each bus is roughly equal (with the 42 V bus generating one-third the current of the 14 V bus). As the firing angle of the phase-controlled rectifier is increased, the amount of current delivered to the 14 V bus is reduced and becomes available to the 42 V bus. As can be seen from these characteristics, the firing angle provides a second control handle by which power flow to the dual voltage system can be regulated.

7.3.2 Transient Characteristics

In this subsection, we present the dynamics of the dual-stator architecture, that is, the behavior of the system due to transients. The transient voltage variations on each bus have a strong impact on our ability to use low cost semiconductors as switches in the architecture. We will concentrate on the load dump since it tends to be the worst of the transients in the electrical system. The Saber
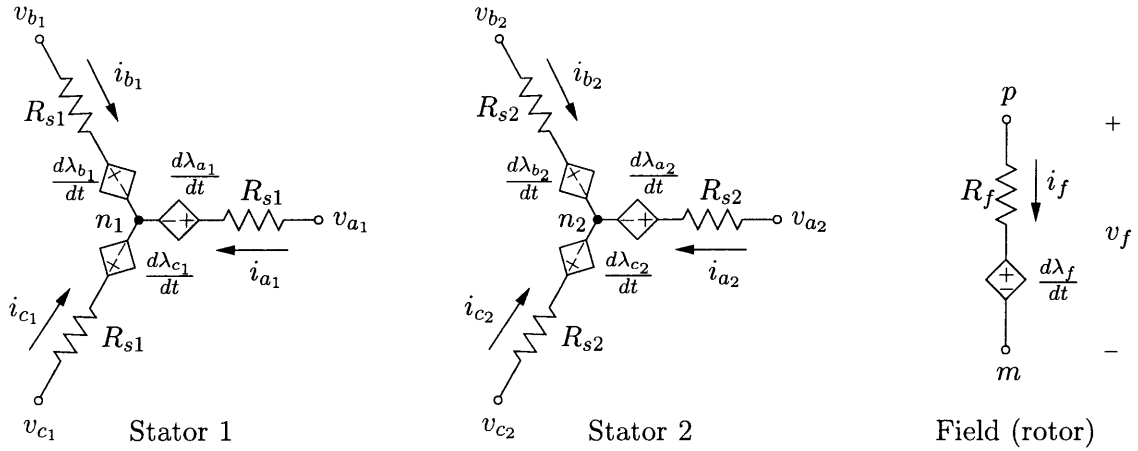
Figure 7.4: Simplified diagram showing the stator phases and the field winding of the dual-stator synchronous machine.

Table 7.5: Dual-stator synchronous machine parameters and typical values for high voltage to low voltage turns ratio of 3:1.

Parameter	Description	Typical Values
R_{s1}, R_{s2}	stator winding resistances	33 mΩ, 297 mΩ
L_{ls1}, L_{ls2}	stator leakage inductances	15 μH, 135 μH
L_{ms1}, L_{ms2}	stator magnetizing inductances	105 μH, 945 μH
L_{ss1}, L_{ss2}	slot magnetizing inductances	see text
L_{g1}, L_{g2}	stator saliency inductances	10 μH, 90 μH
R_f	rotor winding resistance	31 Ω
L_{lf}	rotor leakage inductance	2700 mH
L_{mf}	rotor magnetizing inductance	1350 mH

model of the dual-stator architecture (Figure 7.7) that was used to determine the steady-state characteristics is very generic in its structure; therefore, it will be also used to simulate the load dump transients.

Figure 7.8 shows the transient response of the bus voltages to a load dump on the 14 V bus at 6000 rpm (cruising speed). The transient is induced by a sudden change of the 14 V bus load from its nominal value of 45 A to 10 A at 50 ms. The loading on the 42 V bus remains at its nominal value of 25 A. The voltage on the 42 V bus deviates from its nominal by approximately 1 V but recovers within 50 ms to its nominal value of 42.6 V. The voltage on the 14 V bus also deviates by about 5 V but recovers within 10 ms as the firing angle is increased by the controller. The transient voltage deviations observed in this simulation are within the preliminary voltage limits
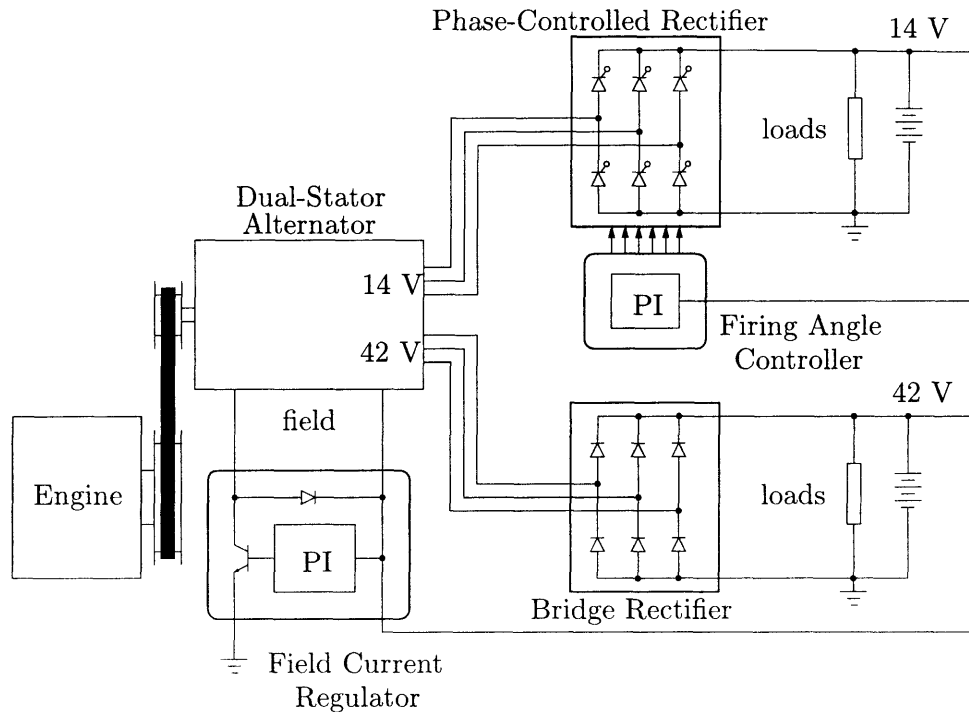
Figure 7.5: A particular implementation of the dual-stator architecture. Field current is used to control the 42 V bus while firing angle control is used for the 14 V bus.

specifications that were given in Table 2.1 and can be further suppressed by the use of transient voltage suppressors. Figure 7.9 shows the transient response of the bus voltages to a load dump on the 42 V bus at 6000 rpm. The transient is induced by a sudden change of the 42 V bus load from its nominal value of 30 A to 5 A at 50 ms. The loading on the 14 V bus remains at the its nominal value of 30 A. The peak transient voltage on the 14 V bus is approximately 16 V and decreases as the firing angle is adjusted. This deviation is within the allowed deviations and can be further suppressed if necessary.

The simulation results in Figure 7.9 illustrate two key limitations of the dual-stator architecture. First is the large peak voltage that is observed on the high voltage bus which reaches 97 V. This overshoot, while quite high, is not surprising since 14 V Lundell machines are known to be susceptible to load dumps and rewinding the machine for 42 V worsens the results. This overshoot alone makes this machine unusable in a dual-voltage system unless voltage suppression circuits and/or techniques are employed.

A second limitation is the voltage regulation of the 14 V bus when the 42 V bus is lightly loaded. This limitation is not due to the transient characteristics of the architecture but was revealed as the steady-state voltages of the system after a load dump were examined. The effects
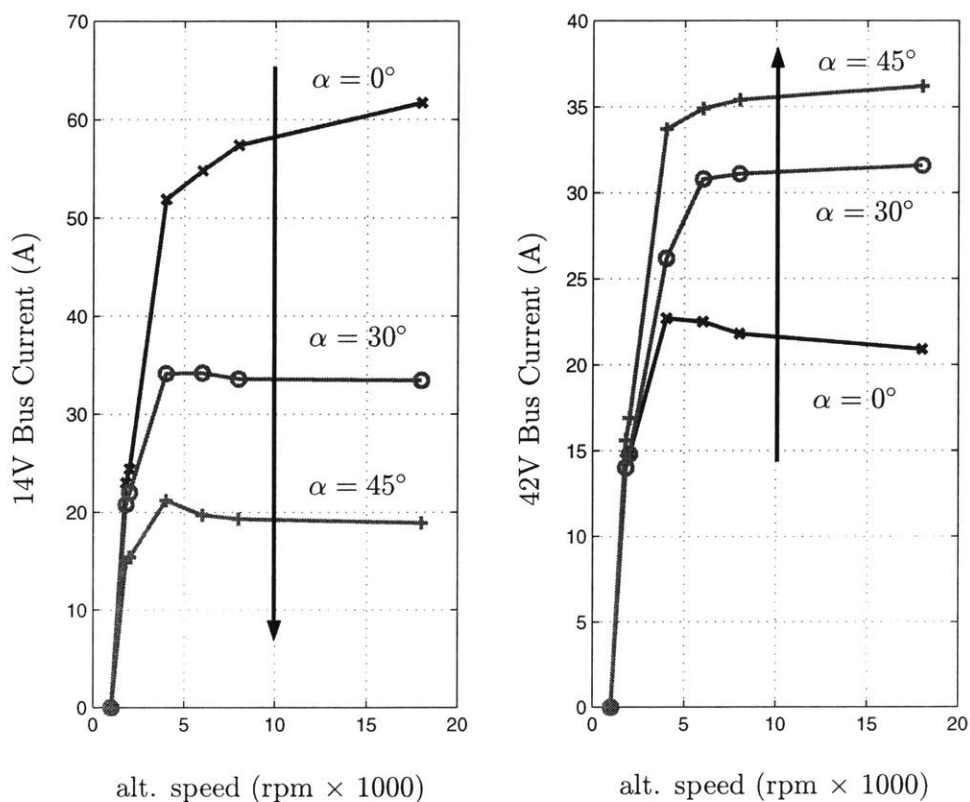
Figure 7.6: Steady-state output current vs. alternator speed of the dual-stator alternator at full field. The curves are parameterized by the firing angle α of the thyristors.

of voltage regulation of the low voltage bus can be seen in Figure 7.9 from the inability of the 14 V bus voltage to recover to its nominal voltage of 14.2 V. Instead it ends up at approximately 13 V.

The cause of the voltage regulation can be understood by examining the simulation results shown in Figure 7.10 which includes the control variables (firing angle, field current) in addition to the voltages from Figure 7.9. Figure 7.10 shows that as the load on the high voltage bus is reduced from 30 A to 5 A, the field current decreases in order to regulate the high voltage bus at 42.6 V. The decrease in the field current results in the reduction of the back-emf voltages for both of the stators. Since there is still a large amount of current demand on the low voltage side, the firing angle decreases in order to regulate the voltage at 14.2 V; however, the voltage drops below the nominal value even though the firing angle is at its minimum. With the firing angle at its minimum, the back-emf that is available to the 14 V stator is not sufficient to maintain an output voltage of 14.2 V at 30 A.

The voltage regulation that is observed in Figure 7.10 can also be understood by examining Figures 7.11(a) and (b) which show sketches of voltage vs. current characteristics for the high and
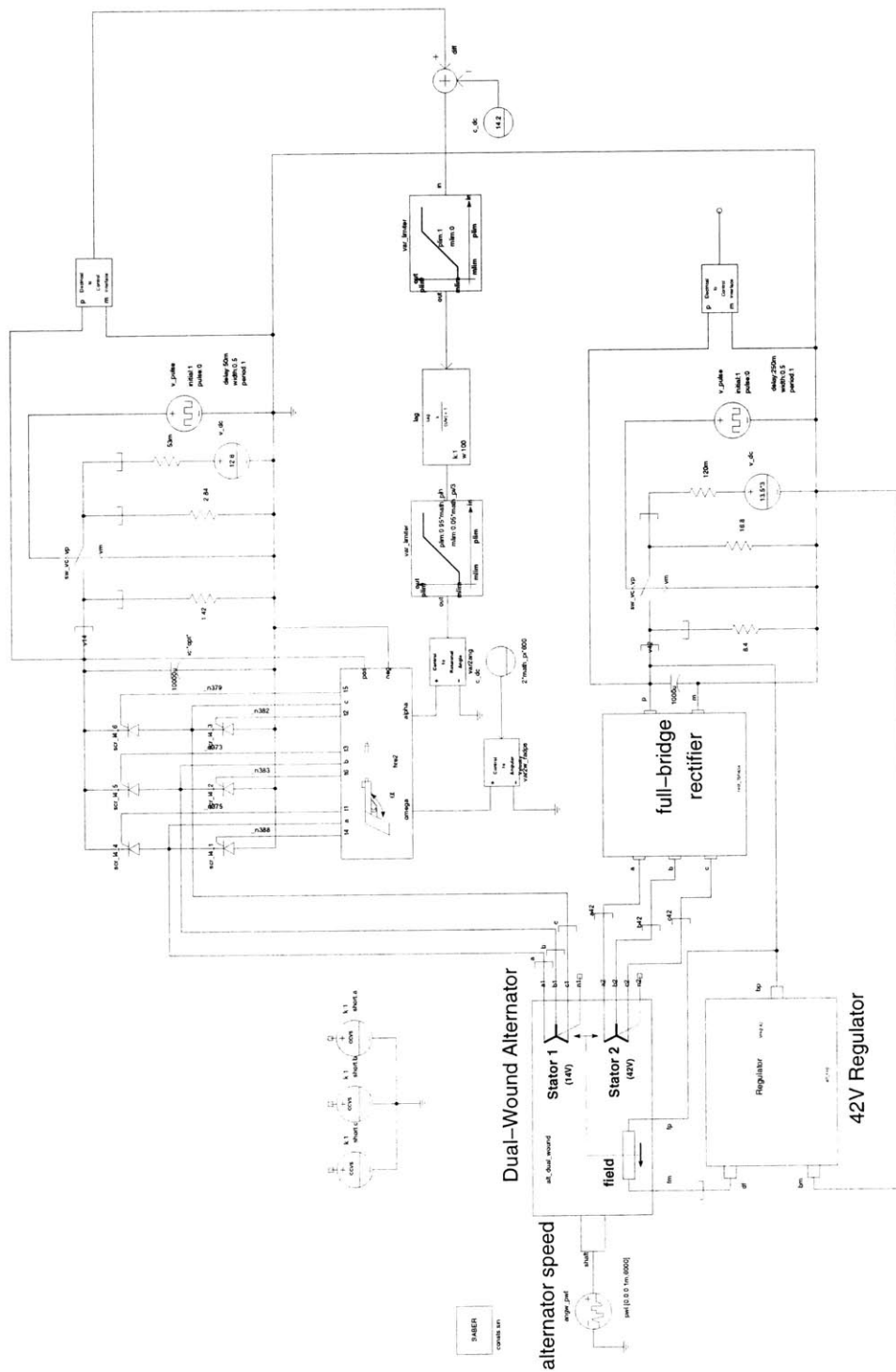
Figure 7.7: Saber schematic illustrating the implementation of the dual-stator alternator architecture including the field current and firing angle controllers.
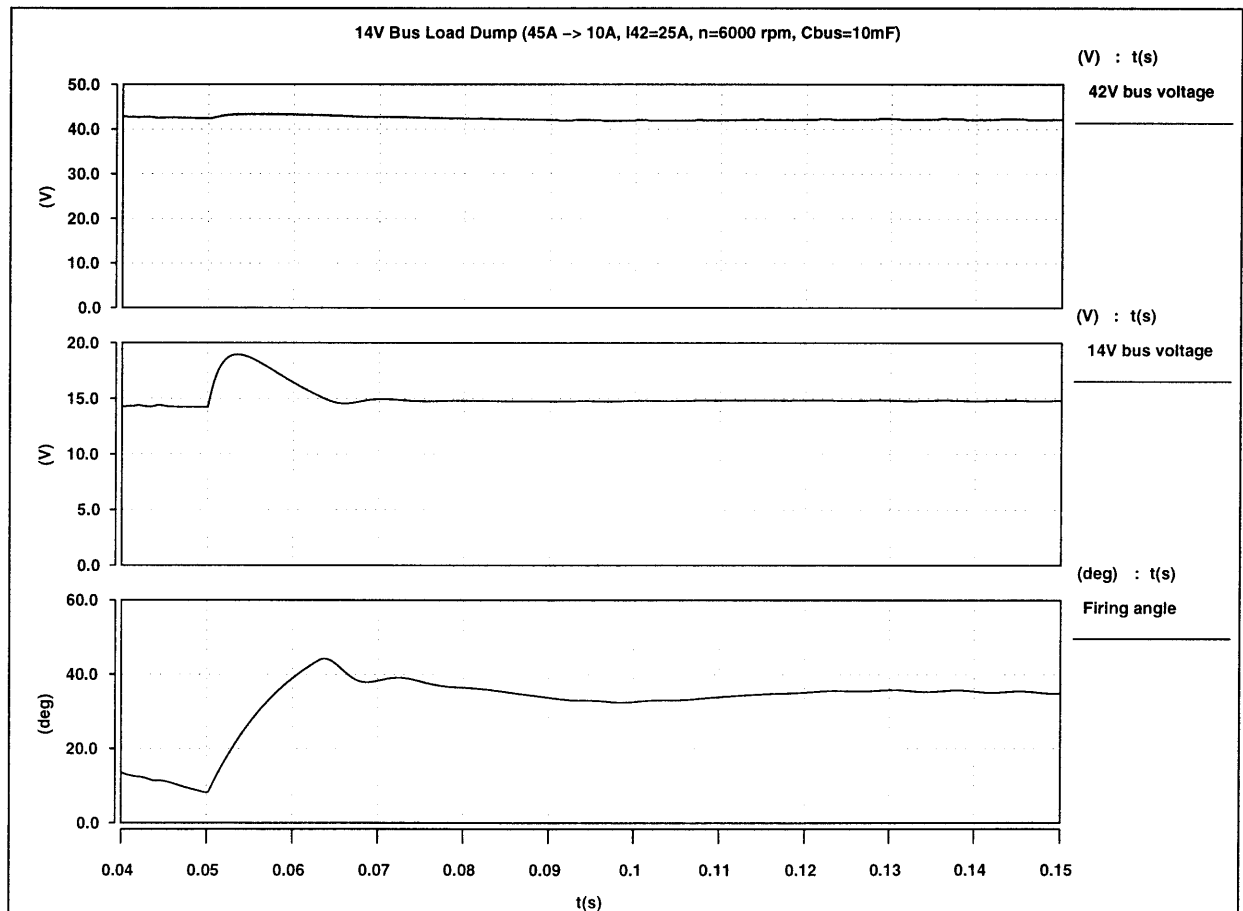
Figure 7.8: Dual-stator architecture bus voltage waveforms due to a load dump on the 14 V bus: 42 V bus voltage (top), 14 V bus voltage (middle) and firing angle α (bottom).
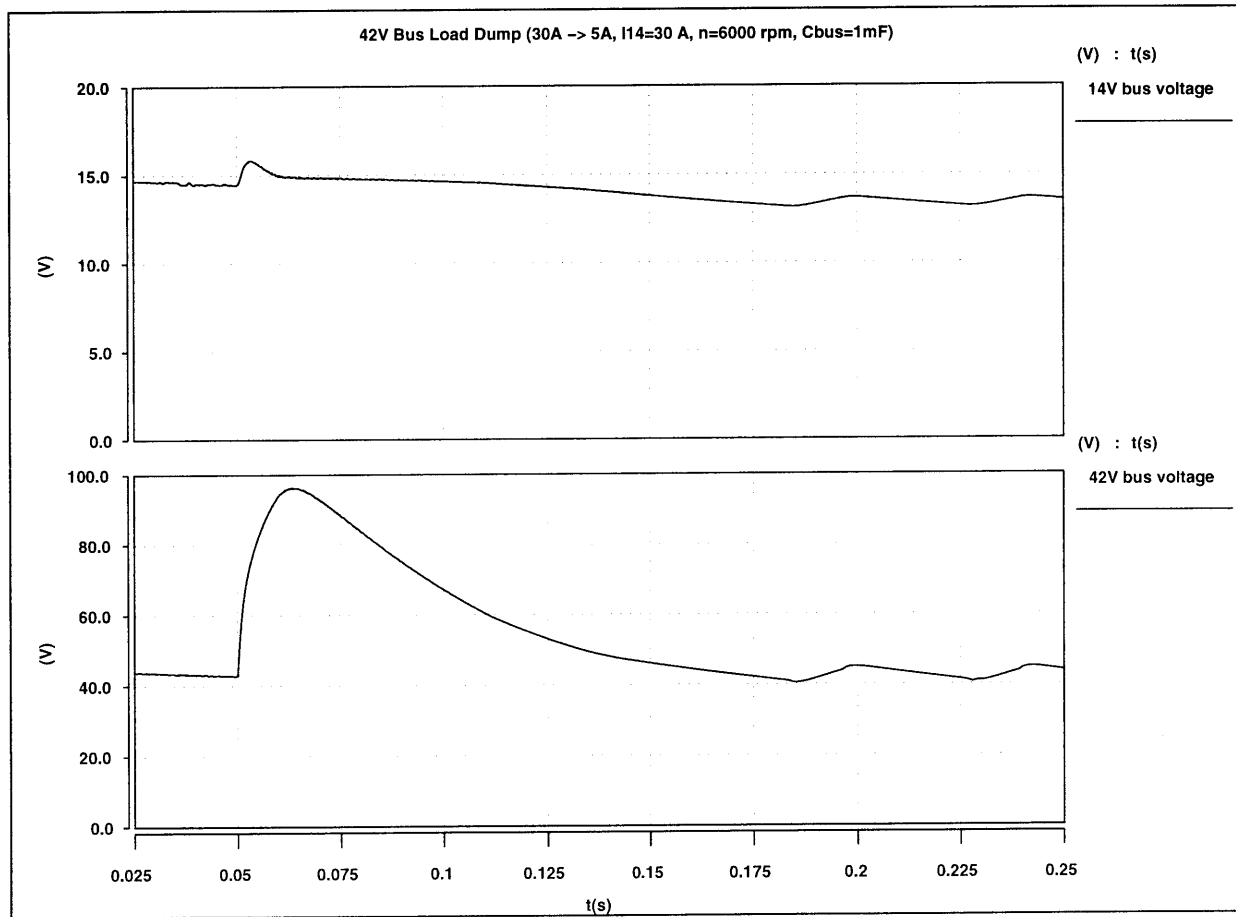
Figure 7.9: Dual-stator architecture bus voltage waveforms due to a load dump on the 42 V bus: 14 V bus voltage (top) and 42 V bus voltage (bottom).
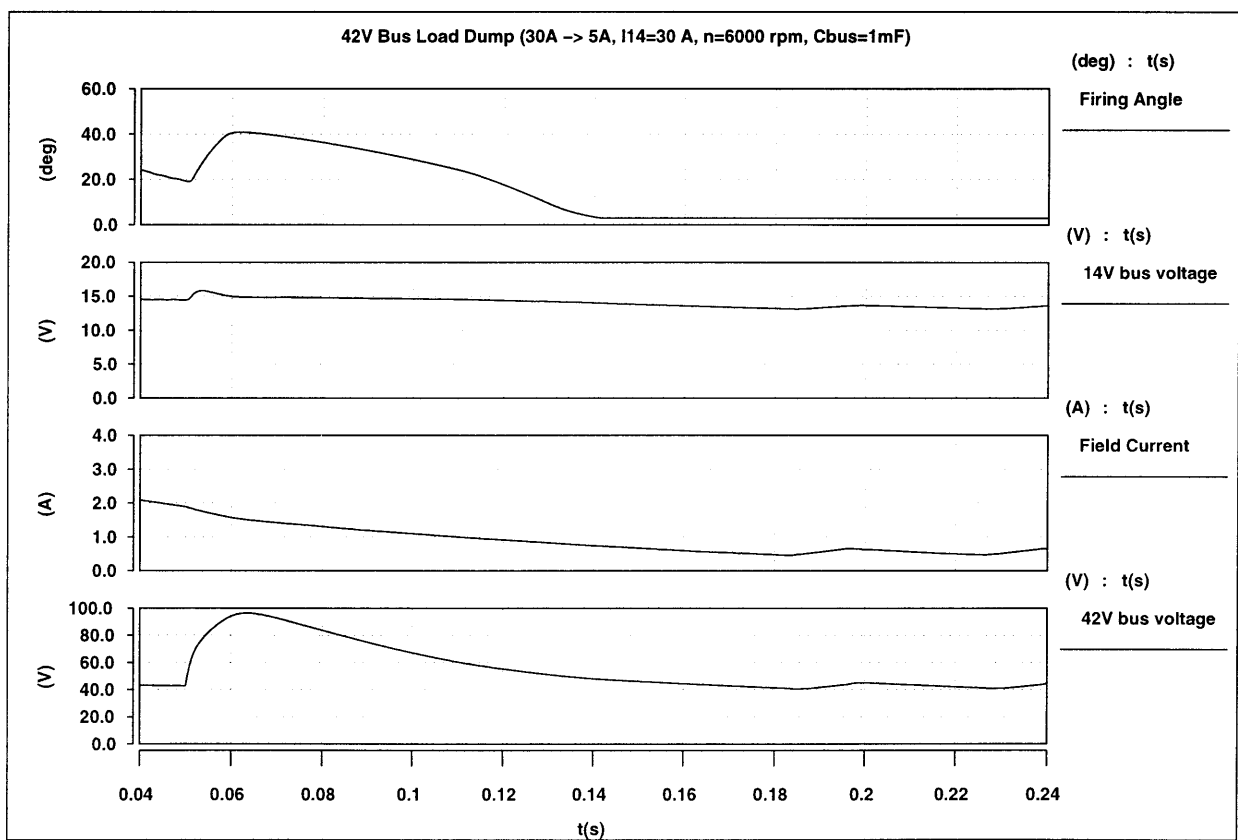
Figure 7.10: Dual-stator architecture bus voltage responses to a load dump on the 42 V bus.
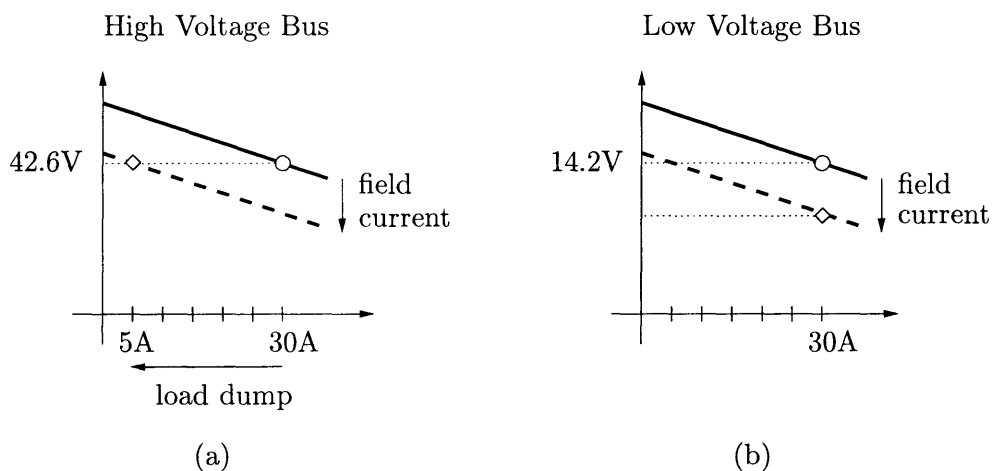
Figure 7.11: Voltage vs. current plots for the high and low voltage buses ((a) and (b), respectively) for the dual-stator alternator architecture. The figure illustrates voltage regulation on the 14 V bus when the 42 V bus is heavily (solid lines) and lightly (dashed lines) loaded.

low voltage buses, respectively. The slope of the curves are due to the high ac side reactance of the machine. Before the load dump is initiated, both buses are at their nominal voltages and are each delivering 30 A (marked by 'o' on the solid curves). When the load on the high voltage bus is suddenly changed from 30 A to 5 A, the field current decreases and the regulation curves for both buses are lowered to keep the high voltage bus regulated at 42.6 V while delivering 5 A (marked by a '⬦' in Figure 7.11(a)). With the reduction in the field current, the low voltage bus cannot be regulated at 14.2 V and drops to 13 V to supply the 30 A load.

It should be noted that the results that we have presented so far have been based on a 3:1 turns ratio (stator 2: stator 1) for the machine with stator 1 parameters based on a conventional Lundell machine. The simulation results show that the 3:1 turns ratio is not optimal when the high voltage bus is lightly loaded and the low voltage is heavily loaded. To be able to select a proper turns ratio, simplified models for bus current output characteristics are necessary. In the next section, we develop an averaged model for the dual-stator alternator architecture under this worst-case loading condition. The worst-case scenario corresponds to the case where the phase-controlled rectifier firing angle α is cut back to its minimum.

7.4 Simplified Model

Here we develop a simplified model for the dual-stator alternator under the worst-case loading condition that was discussed in the preceding section. In this case, the phase-controlled rectifier is

operated at minimum or zero firing angle; therefore, it can be treated as if it were a diode bridge rectifier. A number of common simplifying assumptions will be made to arrive at a model that is analytically tractable. We proceed with the analysis by starting with the flux-linkage equation of the machine (7.1) and use the notation and variables introduced earlier in the chapter. Consider the flux linkage of phase a of stator 1 given by

$$\lambda_{a_1} = L_{a_1 a_1} i_{a_1} + L_{a_1 b_1} i_{b_1} + L_{a_1 c_1} i_{c_1} + L_{a_1 a_2} i_{a_2} + L_{a_1 b_2} i_{b_2} + L_{a_1 c_2} i_{c_2} + L_{a_1 f} i_f \tag{7.6}$$

where the currents are given in the motoring direction. Neglecting saliency (i.e., $L_{g1} = 0$, $L_{g2} = 0$), flux linkage expression of (7.6) may be written as

$$\lambda_{a_1} = (L_{ls1} + L_{ms1}) i_{a_1} - \frac{1}{2} L_{ms1} (i_{b_1} + i_{c_1}) + L_{ms12} \left(i_{a_2} - \frac{1}{2} [i_{b_2} + i_{c_2}] \right) + L_{a_1 f} i_f \tag{7.7}$$

Under balanced steady-state operation with balanced three-phase currents for each stator, we have

$$i_{a1} + i_{b1} + i_{c1} = 0 \tag{7.8}$$

$$i_{a2} + i_{b2} + i_{c2} = 0 \tag{7.9}$$

Using (7.8) and (7.9) in (7.7) and assuming that the field current i_f varies slowly (and can be well approximated by a constant I_f) gives a simplified expression for λ_{a_1}

$$\lambda_{a_1} = \underbrace{\left(L_{ls1} + \frac{3}{2} L_{ms1} \right)}_{\triangleq L_{s1}} i_{a_1} + \underbrace{\frac{3}{2} L_{ms12}}_{\triangleq L_m} i_{a_2} + M_1 \cos(\theta) I_f \tag{7.10}$$

The flux linkage expression for phase a of stator 2 can be derived in a similar fashion and is given by

$$\lambda_{a_2} = \underbrace{\left(L_{ls2} + \frac{3}{2} L_{ms2} \right)}_{\triangleq L_{s2}} i_{a_2} + \frac{3}{2} L_{ms12} i_{a_1} + M_2 \cos(\theta) I_f \tag{7.11}$$

The terminal voltages for phases a_1 and a_2 are evaluated using (7.3) and are given by

$$v_{a_1} = R_{s1} i_{a_1} + L_{s1} i_{a_1} + L_m i_{a_2} + v_{s1} \tag{7.12}$$

$$v_{a_2} = R_{s2} i_{a_2} + L_{s2} i_{a_2} + L_m i_{a_1} + v_{s2} \tag{7.13}$$

where $v_{s1} = -M_1 \omega I_f \sin(\omega t)$, $v_{s2} = -M_2 \omega I_f \sin(\omega t)$ and v_{a_1}, v_{a_2} are line-neutral voltages measured with respect to n_1 and n_2, respectively. For the loading case under consideration, the system can be
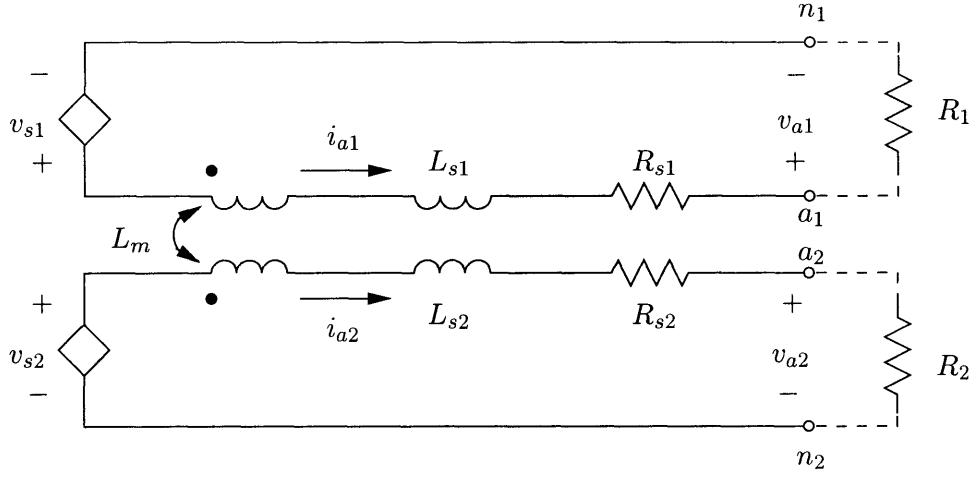
Figure 7.12: Simplified model of the dual-stator architecture in steady-state with firing angle $\alpha = 0$. Resistances R_1 and R_2 are used to replace the effects of the rectifier and load on each stator.

treated as two full bridge diode rectifiers connected to constant-voltage loads. Assuming that the phase currents can be well approximated by their fundamental components, the technique presented in Chapter 3 can be used in the analysis to replace the rectifier and the constant-voltage loads by resistances which are functions of the circuit parameters. An equivalent circuit presenting this simplification is shown in Figure 7.12 and can be used to determine the fundamental components of the phase current magnitudes which are proportional to the average bus currents. Applying complex phasor analysis and writing KVL equations for the equivalent circuit in Figure 7.12 yields

$$\begin{bmatrix} R_1 + R_{s1} + j\omega L_{s1} & j\omega L_m \\ j\omega L_m & R_2 + R_{s2} + j\omega L_{s2} \end{bmatrix} \begin{bmatrix} \bar{I}_{a_1} \\ \bar{I}_{a_2} \end{bmatrix} = \begin{bmatrix} \bar{V}_{s_1} \\ \bar{V}_{s_2} \end{bmatrix} \tag{7.14}$$

where $\bar{I}_{a_1}$, $\bar{I}_{a_2}$, $\bar{V}_{s_1}$ and $\bar{V}_{s_2}$ are the complex magnitudes of the phase currents i_{a_1} and i_{a2} and source voltages v_{s1} and v_{s2}, respectively. The matrix expression (7.14) can be solved to determine the magnitudes $\left|\bar{I}_{a_1}\right|$ and $\left|\bar{I}_{a_2}\right|$ of the phase currents in terms of the equivalent resistances R_1 and R_2. Based on the analysis presented in Chapter 3, each equivalent resistance can be written in terms of its corresponding phase current magnitude, the bridge device forward voltages and the constant-voltage connected to each bus. The equivalent resistance may be expressed as

$$R_1 = \frac{4\left(\frac{V_{o,14}}{2} + V_t\right)}{\pi \left|\bar{I}_{a_1}\right|} \tag{7.15}$$

$$R_2 = \frac{4\left(\frac{V_{o,42}}{2} + V_d\right)}{\pi \left|\bar{I}_{a_2}\right|} \tag{7.16}$$

where $V_{o,14}$ and $V_{o,42}$ are the constant-voltage loads at the rectifier outputs for the 14 V and 42 V buses, respectively. Voltages V_t and V_d represent the forward voltages of the thyristors and the diodes in the bridges, respectively. The phase current magnitudes can be evaluated by solving for $|\bar{I}_{a_1}|$ and $|\bar{I}_{a_2}|$ in (7.14) subject to (7.15) and (7.16). The average output current for each bus can then be determined by the following expressions:

$$\langle i_{o,14} \rangle = \frac{3}{\pi} |\bar{I}_{a_1}| \tag{7.17}$$

$$\langle i_{o,42} \rangle = \frac{3}{\pi} |\bar{I}_{a_2}| \tag{7.18}$$

The procedure has been carried out using the parameter values presented earlier in the chapter. The results of the analytical results developed in this section are shown by the solid curves in Figure 7.13 and compared to the simulation results (for $\alpha = 0$ and full field) of the full model that were presented in Figure 7.6. As can be seen from Figure 7.13 there is excellent agreement between the full simulation and the analytical results obtained from the simplified model developed here. The analytical results given in Figure 7.13 are for maximum (full) field current; however, the procedure described above can be used to evaluate the current output capability at other field currents. For example, the results of Figure 7.10 show that when the 42 V bus is lightly loaded (5 A), field current decreases to 0.5 A ($I_{f,max} = 1.4$A) which leads to voltage regulation of the 14 V bus. Using $I_f = 0.5$A in our calculations yields average currents of 12 A and 10 A for the 14 V and 42 V bus, respectively. These currents are delivered at bus voltages regulated at 14.2 V and 42.6 V with a combined power output of 596 W. This means that at 6000 rpm we can draw up to 12 A and 10 A from the low and high voltage buses, respectively, without sacrificing voltage regulation. In the situation illustrated by Figure 7.10, the 42 V bus load is only 5 A; thus, the low voltage bus can deliver 27 A which results in the same combined power output. However, the load on the low voltage bus is 30 A which leads to the low voltage bus dropping to 13 V to meet the power demand.

A proper turns ratio of the low and high voltage stators of the dual-stator machine has important consequences for voltage regulation and has been considered in a recent thesis [18]. The reader is referred to this work for more detailed discussion of this issue. Given a turns ratio for the high voltage to low voltage stator windings, it has been shown that reducing the 42 V turns gives more favorable to increasing the 14 V turns [18]. This is because increasing the 14 V turns by a factor N increases the back-emf by a factor of N and the impedance by N^2; therefore, the resulting current on the 14 V bus is reduced by N [18]. By using the above models, we can show that reduction the turns ratio from 3:1 to 2.5:1 results in improved voltage regulation. With a 2.5:1 turns ratio and 5 A load on the 42 V bus, the 14 V bus can deliver up to 41.7 A while the voltage is regulated at 14.2 V.
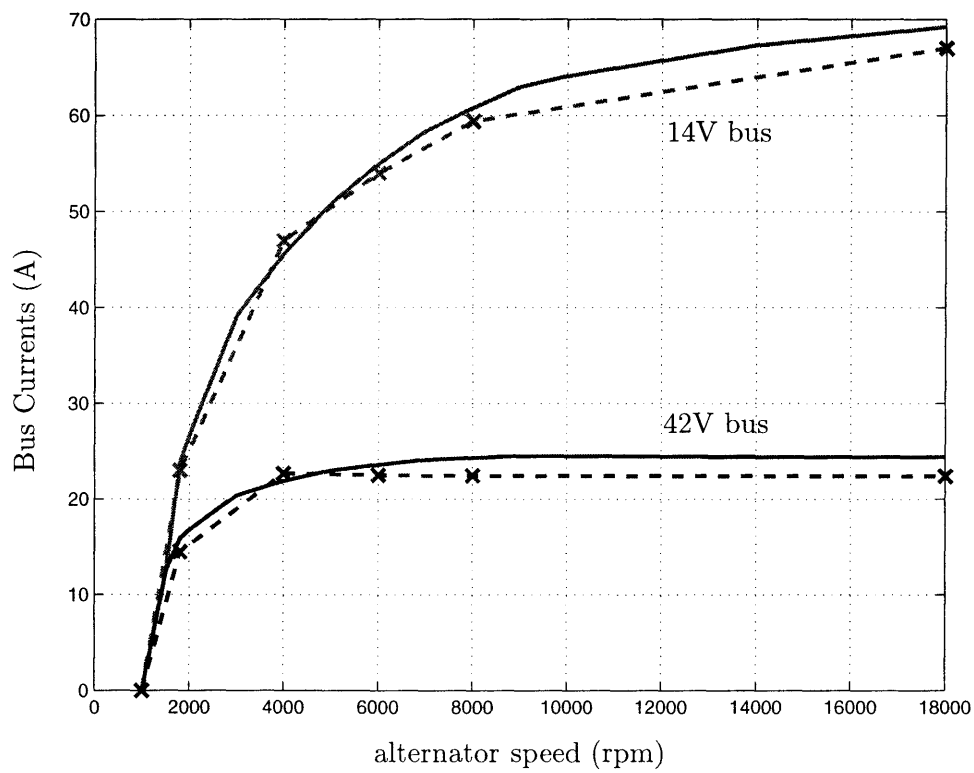
Figure 7.13: Average bus currents for the dual-stator architecture in steady-state with firing angle $\alpha = 0$ and full field. The dashed lines (marked with ×) are the simulation results for $\alpha = 0$ presented in Figure 7.6. The solid lines are the analytical results from the simplified analysis.
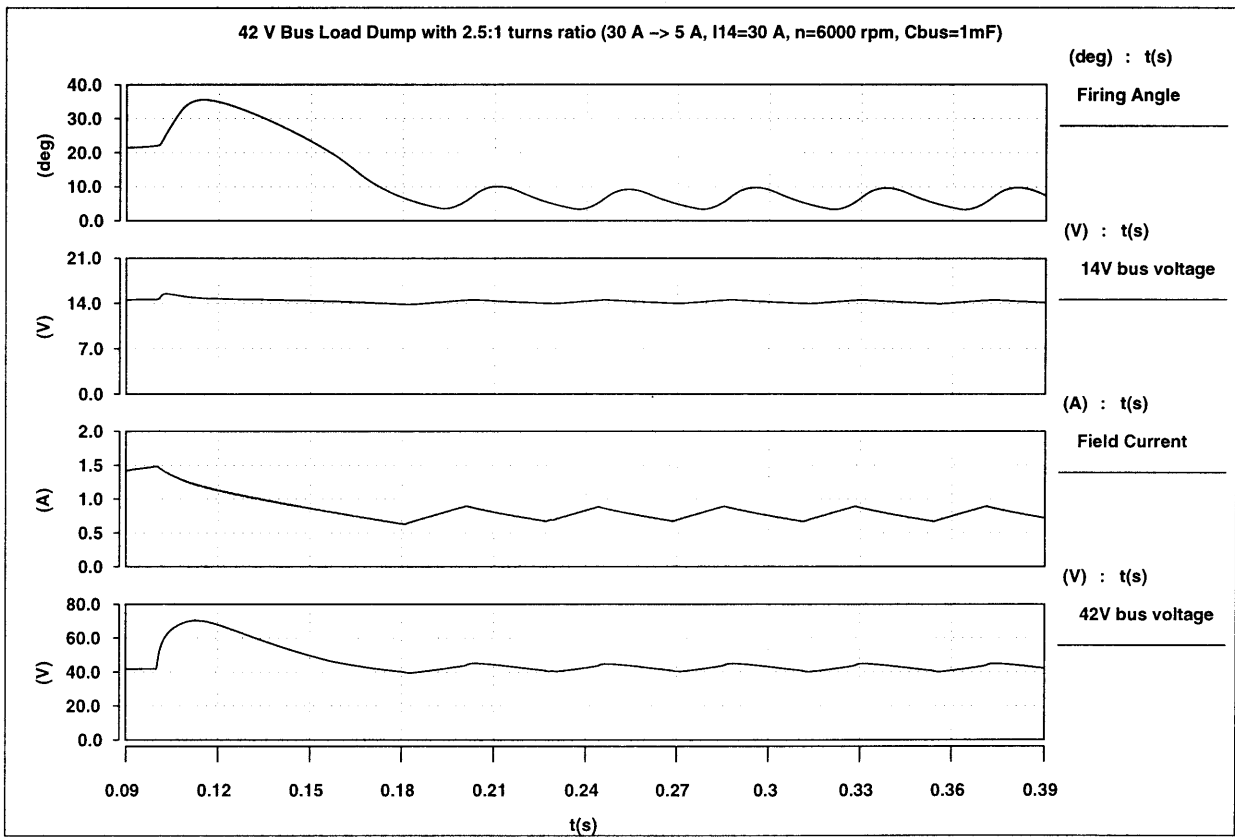
Figure 7.14: Dual-stator architecture bus responses to a load dump on the 42 V bus with stator turns ratio of 2.5:1.

Figure 7.14 shows the transient response of the system to a load dump on the 42 V bus at 6000 rpm with a 2.5:1 turns ratio. As in Section 7.3, the transient is induced by a sudden change of the 42 V bus load from its nominal value of 30 A to 5 A at 50 ms and the load on the 14 V bus is 30 A. Comparing Figure 7.14 to Figure 7.9 (3:1 turns ratio), we see that the 14 V is properly regulated at around 14.2 V when the 42 V bus is lightly loaded. Also note that the peak voltage of the 42 V has been reduced to 72 V as compared to Figure 7.9 where it is 97 V. This is due in part to the reduction of the back-emf which results from the reduction in the turns ratio. Figure 7.14 shows that when the field current decreases after the load dump, the firing angle adjusts to regulate the voltage at 14.2 V without saturating. The steady-state oscillations observed in the responses shown in Figure 7.14 are due to the absence of the buffering action provided by the battery which is disconnected to initiate the load dump transient.

7.5   Transient Suppression

As illustrated in the simulation results in Figures 7.9, 7.10 and 7.14, large peak voltages can occur on the high voltage bus in a dual-stator alternator architecture. It is not uncommon to expect voltages in excess of two hundred volts at high alternator speeds when large current consuming loads are disconnected from the high voltage bus. The large transient voltages present a severe limitation and must be suppressed in order for the dual-stator architecture to be a viable candidate for a dual-voltage electrical system.

The most common technique to suppress transient voltages is to use transient voltage suppressors (TVS). Metal-oxide varistors (MOV) and zener diodes are the types of transient suppressors that are most often encountered in the automotive electrical system [55, 56]. Metal-oxide varistors are voltage-dependent, nonlinear devices whose electrical behavior is similar to back-to-back zener diodes. For a given nominal voltage, zener diodes have low peak energy absorption capability while the MOVs have higher clamping voltages [55]. The transients generated by an alternator are normally suppressed by connecting a single TVS across the output terminals or connecting three smaller TVSs across each pair of three phase outputs (line-line) before the rectifiers. It should be noted that the lead-acid storage battery is an excellent transient suppressor; however, the disconnection of the battery itself can be the cause of the transient in the case of the load dump, and the voltage must be controlled in this event.

In anticipation of the introduction of higher voltage electrical systems and its associated transients, a number of automotive suppliers have begun to manufacture TVSs to handle the voltage and the energy absorption capabilities required from such devices in the 42 V electrical

system (see for example [57]). We will now demonstrate transient suppression by using zener power diodes that have been specifically designed for the 42 V system. The simulation model for the zener diode that we use in the simulation has been developed by the manufacturer [57] and is based on preliminary specifications for the 42 V bus given in Table 2.1.

Figure 7.15 shows a comparison of the load dump transient on the 42 V bus with and without the presence of a TVS. The dashed lines for the voltages correspond to the ones from Figure 7.14 in which no transient suppression was used. The solid lines in Figure 7.15 are due to the addition of a single zener diode across the output terminals.

As can be seen from the figure, the zener diode is able to clamp the output voltage at around 51 V which is well within the voltage levels presented in Table 2.1. The voltage on the 14 V bus is not significantly reduced by the addition of the zener diode but was not large to begin with. Figure 7.15 also shows the junction temperature of the zener diode during the transient with an initial (ambient) temperature of 85 °C. The maximum junction temperature during the simulation is 113 °C which is well below the peak operating junction temperature of 280 °C reported by the manufacturer [57]. A number of simulations were run over the designed speed range of the alternator (1,800 rpm – 18,000 rpm) and higher ambient temperatures (105 °C and 125 °C) to confirm the operation of the zener diode suppression. The clamping voltages ranged from 44–51 V while the temperature rose 30–50 °C.

Transient suppression can also be achieved by implementing the bridge rectifier with zener diodes. Figure 7.16 shows the results of a load dump simulation where zener power diodes have been used to construct such a bridge rectifier. The simulation results possess the same general response as those shown in Figure 7.15 with minor differences. The 42 V bus voltage is clamped to 49 V during the transient while the 14 V bus voltage is not significantly effected. The maximum junction temperature during the simulation is 92 °C which is 11 °C less than what was observed for a single zener diode. This reduction in temperature rise is due to the lower device current stresses in the bridge rectifier. One disadvantage of using zener diodes for clamping is the variation of the clamping voltage with temperature. The avalanche breakdown voltage of a zener diode decreases with decreasing temperature while the alternator output voltage set by the regulator increases, indicating a possible discrepancy. This situation results in very tight design tolerances for the zener diodes which may impact manufacturability and cost.
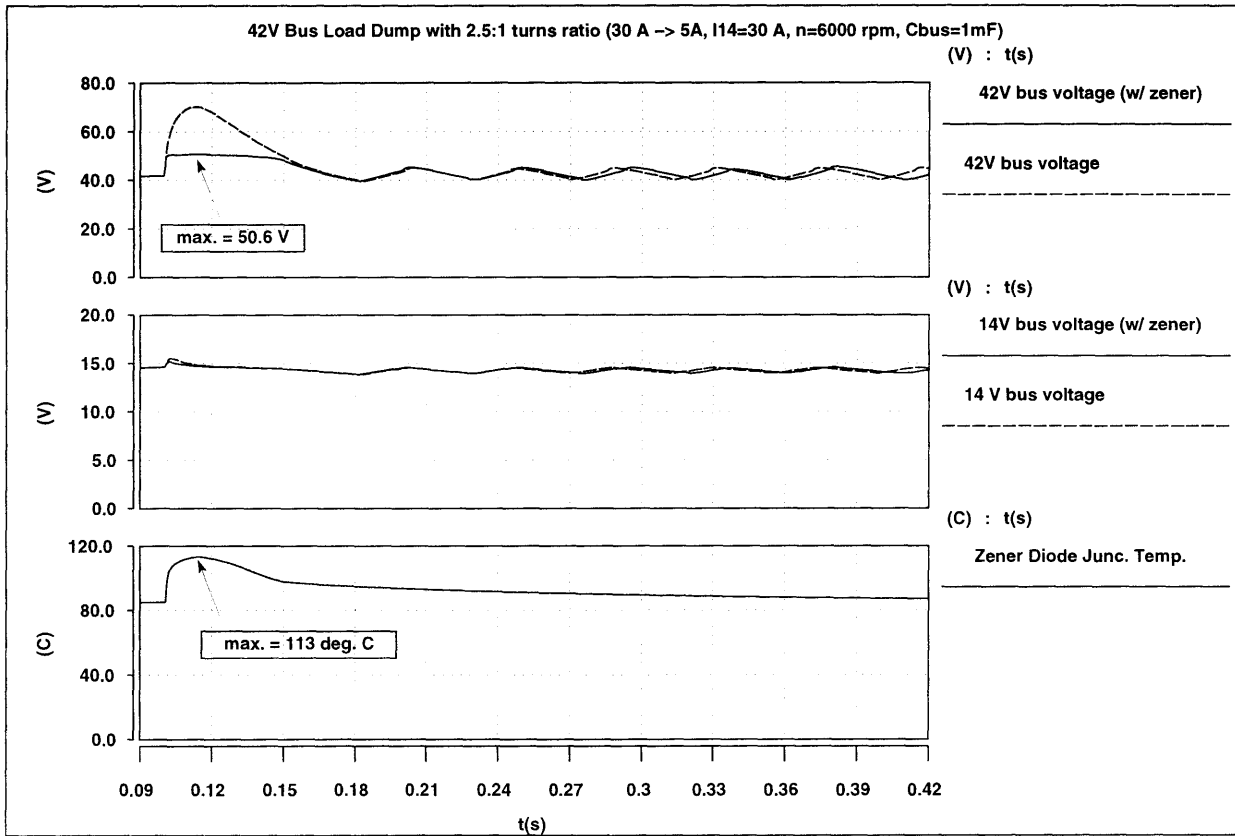
Figure 7.15: Load dump transient suppression using a single zener diode across the 42 V bus output terminals: 42 V bus voltage (top), 14 V bus voltage (middle) and zener diode temperature (bottom). Dashed lines show the results of the load dump without transient suppression from Figure 7.14.
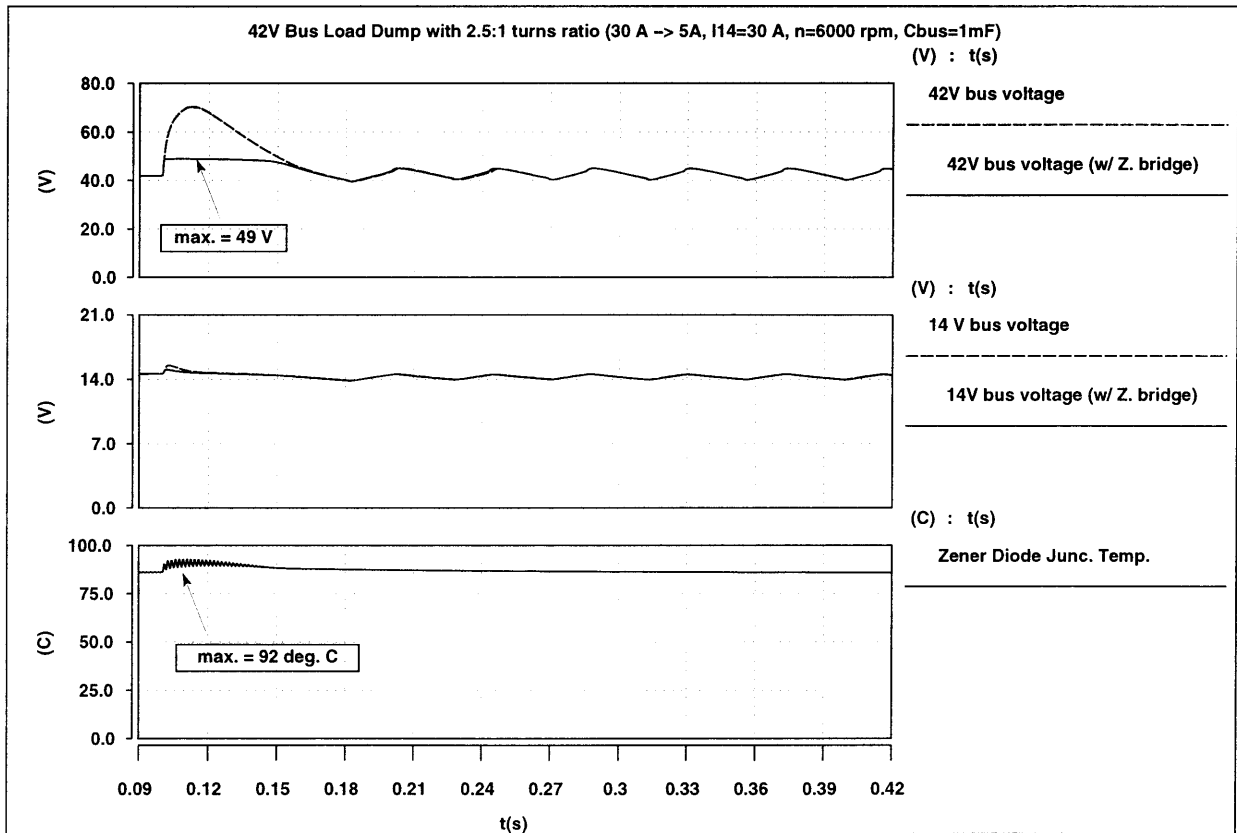
Figure 7.16: Load dump transient suppression of the 42 V bus using bridge zener diodes: 42 V bus voltage (top), 14 V bus voltage (middle) and zener diode temperature (bottom). Dashed lines for the voltages show the results of the load dump without transient suppression from Figure 7.14.

7.6   Summary

In this chapter, the modeling, analysis and simulation of a dual-stator alternator electrical system was presented.   A mathematical model for the dual-stator alternator based on inductance and resistance matrices was developed.   A simulation model for the dual-stator alternator was then implemented in Saber and used throughout the chapter to answer a variety of questions including the steady-state output current capabilities and transient behavior due to load dump on each of the buses. The simulation results revealed that the 42 V bus voltage is unacceptably high during the load dump and must be suppressed by external means.   The 14 V bus voltage peak did not increase to unacceptable levels during the load dump; however, voltage regulation problems were observed under extreme loading conditions. Simplified analytical models were developed and used to predict system output capabilities and choose the turns ratio of the stator windings to improve the voltage regulation of the 14 V bus under light loading conditions.   Zener power diodes were used to limit the peak voltages on the 42 V bus thus demonstrating passive transient protection.

Comparison of Dual/High Voltage Automotive Electrical Systems

In this chapter, we present a summary of the characteristics and features of candidate dual-voltage architectures. Extensions of the dual-controlled alternator (Chapter 5) to dual-voltage systems are also discussed.

8.1 Characteristics of Dual-Voltage Architectures

In recent years, dual-voltage electrical systems have received much attention in the context of modern automotive power generation systems and there is a strong international effort to introduce dual 42/14 V automotive electrical systems in the near future. The most widely considered systems employ expensive dc/dc converter-based architectures that have the basic structure shown in Figure 8.1(a). The dc/dc converter-based systems feature high bandwidth control of the low-voltage bus and jump-start charging. Other dual-voltage candidate architectures under consideration are the dual-stator alternator architecture and the dual-rectified alternator architecture which are illustrated in Figure 8.1(b) and Figure 8.1(c), respectively. The dual-stator and dual-rectified alternator architectures are considered to be lower cost alternatives to the dc-dc converter architecture but with lower performance characteristics. In the following subsections, we will outline the features and drawbacks of these architectures.

8.1.1 Dc/Dc Converter Architecture

The dc/dc converter based dual-voltage architecture is shown in Figure 8.1(a). Issues related to the modeling, simulation, control and implementation of this architecture are discussed in detail in Chapter 6. The architecture consists of a high-voltage Lundell alternator to supply a 42 V bus which is down-converted to 14 V by the use of the dc/dc converter. Batteries are shown on both buses since this particular arrangement leads to the smallest converter volume for a given power rating [52]. The system batteries can be optimized based on the type of loads placed on each bus.
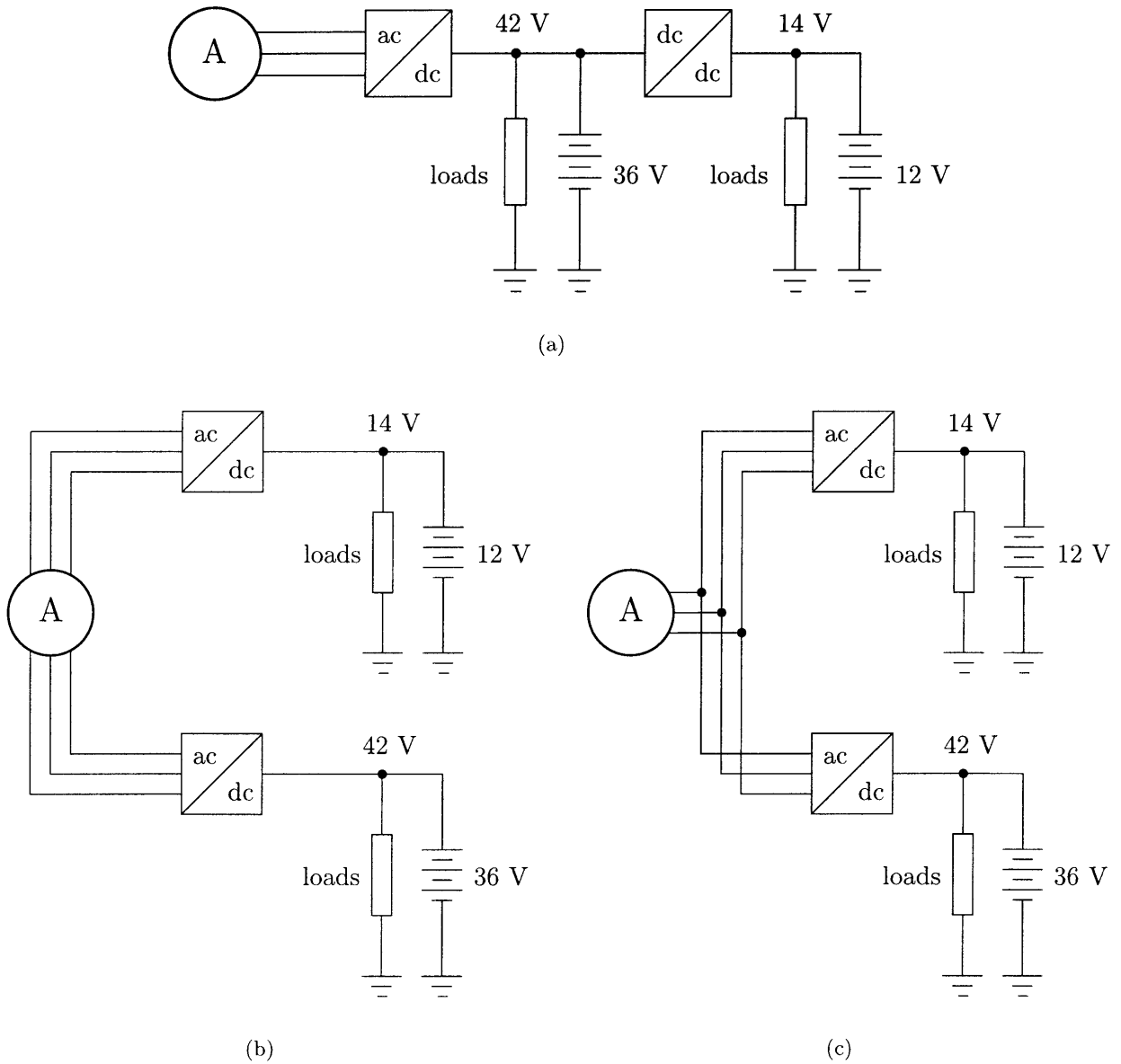
Figure 8.1: Candidate dual-voltage architectures: (a) dc/dc converter architecture, (b) dual-stator alternator architecture and (c) dual-rectified alternator architecture.

It is common to place the starter motor and high power loads on the high voltage bus and the key-off, lighting and ECU loads on the low voltage bus. Given this arrangement, the battery on the high voltage bus is optimized for high power delivery for engine cranking at low temperatures. On the other hand, the battery on the low voltage bus is optimized for energy density to deliver power to the key-off loads [58]. The optimization of battery functions results in reduction of mass so that the weight of the high voltage battery is not simply three times that of the low voltage battery. The present automotive battery designs are a compromise between the power delivery and the energy density features and are not optimal for either function.

As described in Chapter 6, the dc/dc converter system provides a number of features that do not exist in today's automotive electrical system. Among these features is a well-regulated 14 V bus with a relatively high bandwidth. The regulation of the 14 V bus is retained under load transients even in the absence of a storage battery. Charging of the high voltage battery from the low voltage battery and jump charging are also possible if a bidirectional dc/dc converter system is used. The high performance features of the dc/dc converter architecture result in a large cost penalty when compared to the present generation system. In order for the dc/dc converter system to be economically feasible, the additional benefits of the converter system and its effects on system cost must be considered. Based on the performance results of the dc/dc converter presented in Chapter 6, it is apparent that little or no transient suppression is necessary at the 14 V output. The improved transient response may lead to the elimination or redesign of protection circuitry for electronics connected to the 14 V bus. While the transient response of the 14 V bus is improved, the transients on the high voltage bus (42 V) remain due to the presence of the high voltage Lundell alternator. The peak transients on the high voltage bus can easily reach several hundreds of volts during a load dump and must be suppressed. The dc/dc converter itself may be used to absorb this transient; however, this will increase the peak power rating of the converter and add to the cost and complexity of the converter system which is already very high.

8.1.2 Dual-Stator Alternator Architecture

The dual-stator alternator architecture is shown in Figure 8.1(b) where the generator is a Lundell alternator with both high and low voltage three phase outputs. Each winding of the machine is followed by a rectifier to produce the desired dc voltage level at each bus. Detailed analysis of this architecture is presented in Chapter 7 where field current is used to regulate the 42 V bus while a phase-controlled rectifier with firing angle control is used for the 14 V bus.

The results of the analysis of Chapter 7 show that the 42 V bus voltage is unacceptably high during the load dump transient and must be suppressed to keep the voltage to acceptable levels. On

the other hand, the 14 V bus transient voltage peaks are within an acceptable range; however, there are voltage regulation problems when the buses are under extreme loading conditions. Simplified analytical models were developed and used to predict system output capabilities and choose the turns ratio of the stators to improve the voltage regulation of the 14 V bus under light loading conditions. Zener power diodes were used in the bridge rectifier to limit the peak voltages on the 42 V bus.

8.1.3 Dual-Rectified Alternator Architecture

The dual-rectified alternator architecture is shown in Figure 8.1(c) where a high voltage Lundell alternator is followed by two rectifiers to produce the high and low voltage levels. Since the rectifiers are sharing a common three-phase input, the current that is generated by the machine will alternately flow in one or the other rectifier. This alternating flow of current in the rectifiers results in very large current ripples at each rectifier output. Reducing the current ripples requires substantial filtering and adds to the size and weight of the system which makes this architecture less attractive than alternatives. Load dump transient voltages in this architecture are comparable to those observed in the dual-stator alternator in that they require some form of suppression. Due to these disadvantages, this architecture was not considered in this thesis; however, a modified version of this architecture that overcomes the above disadvantages will be presented later in the chapter. The modified dual-rectified alternator architecture will make use of the switched-mode rectifier and load-matching concepts developed in Chapter 5.

8.1.4 Comparison of Dual-Voltage Architectures

There have been many dual-voltage electrical systems that have been considered as replacements for the present automotive electrical system. Cost is the main drawback of the dc/dc converter-based systems which becomes worse if they are bidirectional. The dual-stator and dual-rectifier architectures are lower in cost but have poor steady-state and transient characteristics which results in larger and heavier systems.

Since each dual-voltage architecture is based on a Lundell alternator, it inherits the features and also the drawbacks of such a system as described in Chapter 5. There are three major drawbacks that are common to all of the dual-voltage architectures shown in Figure 8.1:

1. *Limited alternator power output/low alternator efficiency* – As presented in Section 5.2 a Lundell alternator exhibits heavy load regulation when used with a rectifier and constant-

voltage load. This results in low output power and efficiencies for a given machine independent of the rated output voltage of the machine (to first order).

2. *Large peak transient voltages due to load dump on the high voltage bus* – Because of its construction, a Lundell machine has large stator leakage inductances which require large back-emf voltages in order to source the rated machine current (Section 5.5). When a large load is suddenly removed from the alternator, a large fraction of the back-emf appears at the alternator output. The transient peak voltages get higher as higher voltage Lundell machines are used, and require the use of additional circuitry and techniques for suppression.

3. *Expensive jump start implementation* – As mentioned in Section 5.6, the inclusion of the jump start function is essential to the introduction of dual-voltage automotive electrical systems and is a major deployment issue. None of the dual-voltage architectures shown in Figure 8.1 feature simple and cost-effective solutions to the jump start problem.

In Section 8.2 we will show that each of these drawbacks can be alleviated by extending and applying the concepts based on the load-matched switched-mode rectifier (SMR) discussed in Chapter 5.

8.2 Dual-Voltage Application of Switched-Mode Rectifiers

In this section, we will describe dual-voltage extensions to the switched-mode rectifier (SMR) load-matching approach that was introduced in Chapter 5, and highlight advantageous features of these systems [59].

8.2.1 Dc/Dc Converter Architecture with SMR Load-Matching

An implementation of the dc/dc converter dual-voltage architecture (Figure 8.1(a)) that includes a load-matching SMR is shown in Figure 8.2. By controlling the field current of the alternator and the duty ratio of the MOSFETs, the high voltage bus can be regulated to 42 V while maximizing the output power of the alternator. The duty ratio of the dc/dc converter can be independently controlled to regulate the 14 V bus. Load dump transient protection of the 42 V bus is easily implemented by the techniques of Chapter 5. The transient protection of the low voltage bus is handled by the dc/dc converter itself as described in Chapter 6. Jump-start charging is also. easily implemented without additional circuitry by using the SMR and the machine neutral with an internal or external source. This particular implementation of the dc/dc converter system overcomes the major drawbacks of the conventional dc/dc converter system shown Figure 8.1(a).
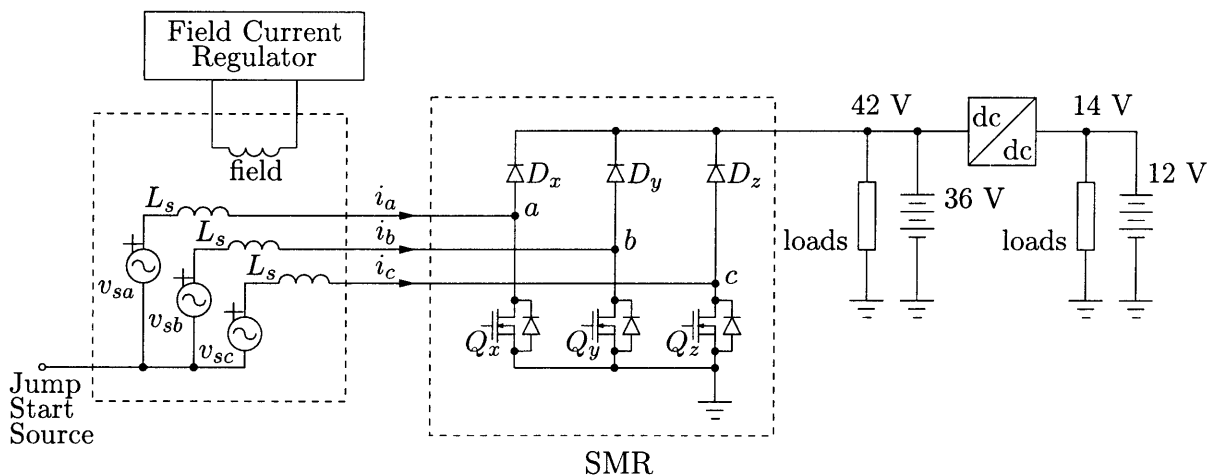
Figure 8.2: Dc/dc converter architecture implementation using the switched-mode rectifier structure.

The use of the SMR structure allows the introduction of essential features such as jump-start charging with little additional cost.

8.2.2 Dual-Stator Alternator Architecture with SMR Load-Matching

A typical implementation of dual-stator alternator architecture (Figure 8.1(b)) is illustrated in Figure 8.3 where V_{o1} and V_{o2} represent the low and high voltage buses, respectively. This is the particular implementation that is analyzed in Chapter 7. In this system, field current control is used to regulate the full bridge rectifier output voltage V_{o2} to 42 V while the firing angle of the thyristors is used to regulate V_{o1} to 14 V. The results presented in Chapter 7 show that the 42 V bus voltage is unacceptably high during the load dump and must be suppressed to keep it within accepted levels. The 14 V bus voltage does not deviate from the nominal levels but experiences voltage regulation problems under extreme loading conditions, particularly when the high voltage bus is lightly loaded. Appropriate choice of the stator turns ratio is used to improve the 14 V bus voltage regulation while zener power diodes are used as bridge rectifier diodes to limit the peak voltages on the 42 V bus. Implementing transient suppression by the use of passive zener diodes brings forth the issue of repeatability of the clamping voltages which will change with temperature and manufacturing process. Furthermore, as with the other dual-voltage architectures, there is no simple mechanism to implement jump-start charging in the system shown in Figure 8.3.

One possible implementation of a dual-stator alternator system using the SMR is shown in Figure 8.4. where SMR based rectifiers are substituted for the diode and thyristor bridge rectifiers. By controlling the field current of the alternator and the duty ratio of each set of three MOSFETs
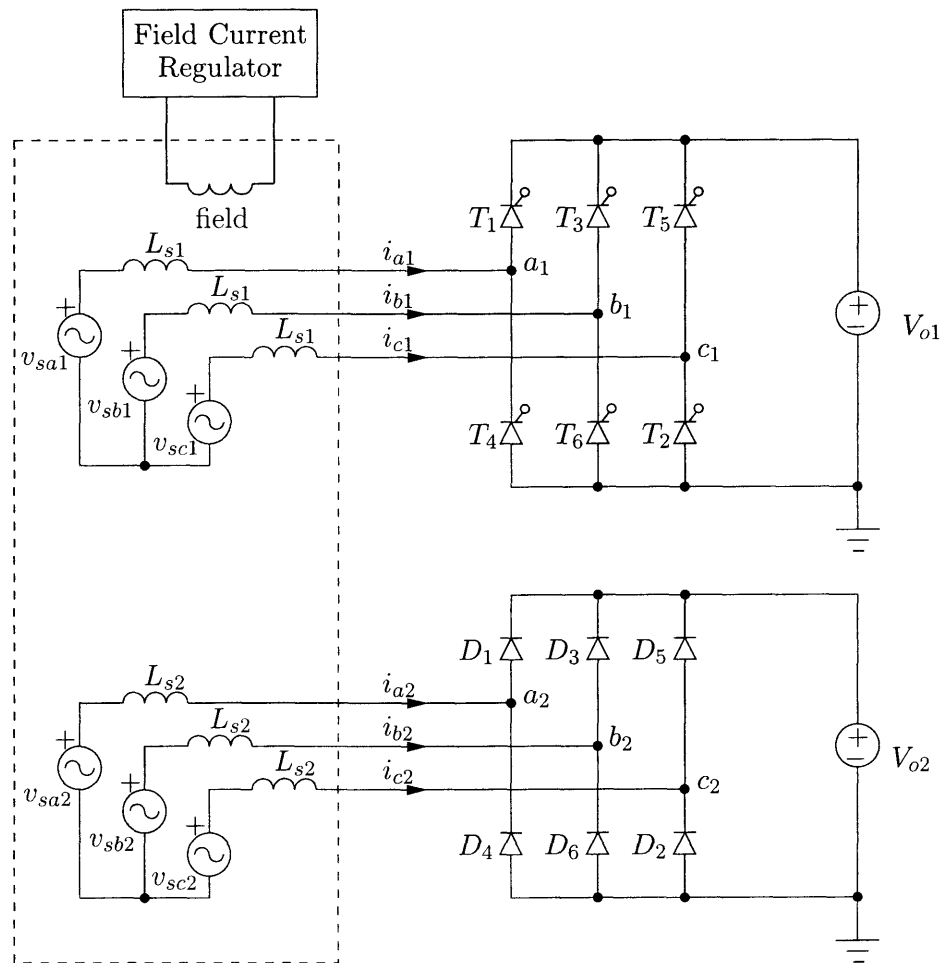
Figure 8.3: A particular implementation of the dual-stator alternator architecture. The coupling between the two stators is not shown for the sake of simplicity.

both bus voltages can be regulated while maximizing the power output of the dual-stator alternator (Section 5.3). It is shown in Chapter 7 that when the 42 V bus is lightly loaded the 14 V bus drops below its nominal value even when the firing angle is cut back to its minimum. This is because the back-emf of the machine is low due to a reduction in the field current (which is the control variable for the 42 V bus). With the additional control handle provided by the MOSFET duty ratio of each SMR, we can regulate the 14 V bus to its nominal value under this light loading condition. Load dump transient protection and jump-start charging can also be implemented without additional circuitry within the same framework. As shown in Figure 8.4, the neutral of the high voltage stator can be used with external or internal sources to provide jump-start charging. For example, the low voltage bus can be connected to the high voltage stator neutral and used to charge the high voltage battery with duty ratio of the lower set of MOSFETs as the control. The SMR-based dual-stator alternator system shown in Figure 8.4 provides simple and inexpensive solutions to the drawbacks associated with a conventional dual-stator architecture, and has additional benefits such as increased output power and jump-start charging.

8.2.3   Conventional Dual-Rectifier Alternator Architecture

An often-considered implementation of the dual-rectified alternator architecture (Figure 8.1(c)) is illustrated in Figure 8.5 where V_{o1} and V_{o2} represent the low and high voltage buses, respectively. In this system, field current control is used to regulate the full bridge rectifier output voltage V_{o2} to 42 V while phase angle control is used to regulate V_{o1} to 14 V. Voltage sources V_{o1} and V_{o2} represent the combination of a battery and associated loads. One of the disadvantages of this system is that the full current of the alternator is chopped back and forth between the two outputs at a low multiple of the alternator electrical frequency. The large, low frequency ripple in the output necessitate the use of large filters for both buses. The addition of the filter circuits increases the cost, size and weight of the rectifier system. Another major disadvantage of the system of Figure 8.5 is the low control bandwidth of the system. The bandwidth is dominated by the large field time constant of the machine and the slow phase control of the thyristors. In addition to these shortcomings, the dual-rectified system of Figure 8.5 offers no simple mechanism for jump-start charging or load dump transient suppression. Also, if rated alternator power is to be supplied to both buses, machine is oversized.

8.2.4   Dual-Rectifier Alternator Architecture with SMR Load-Matching

One possible implementation of a dual-rectified alternator system using the SMR is shown in Figure 8.6. In this system, the switched-mode rectifier of Figure 5.9 is used in place of the uncontrolled
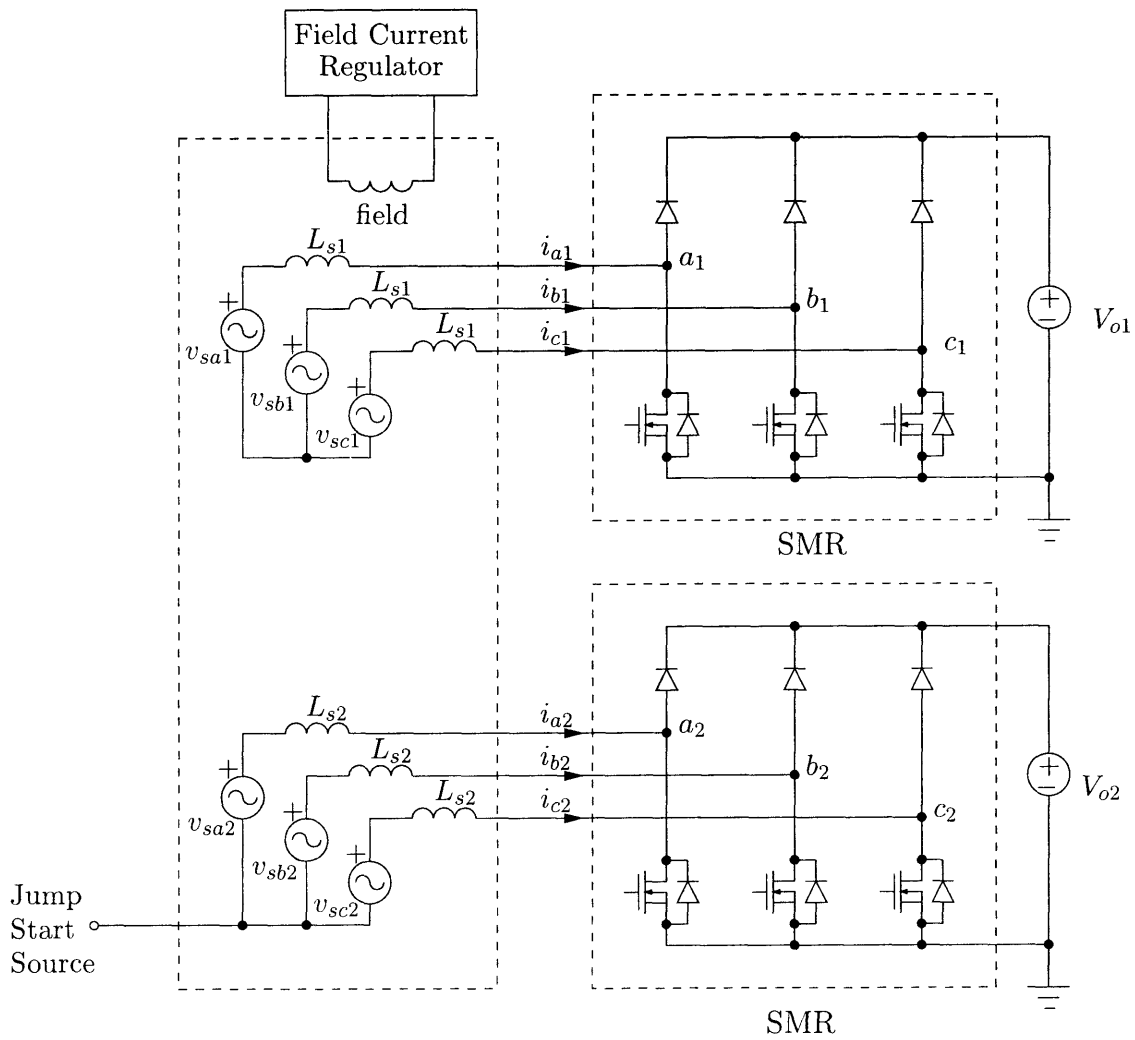
Figure 8.4: Implementation of the dual-stator alternator architecture incorporating a SMR.
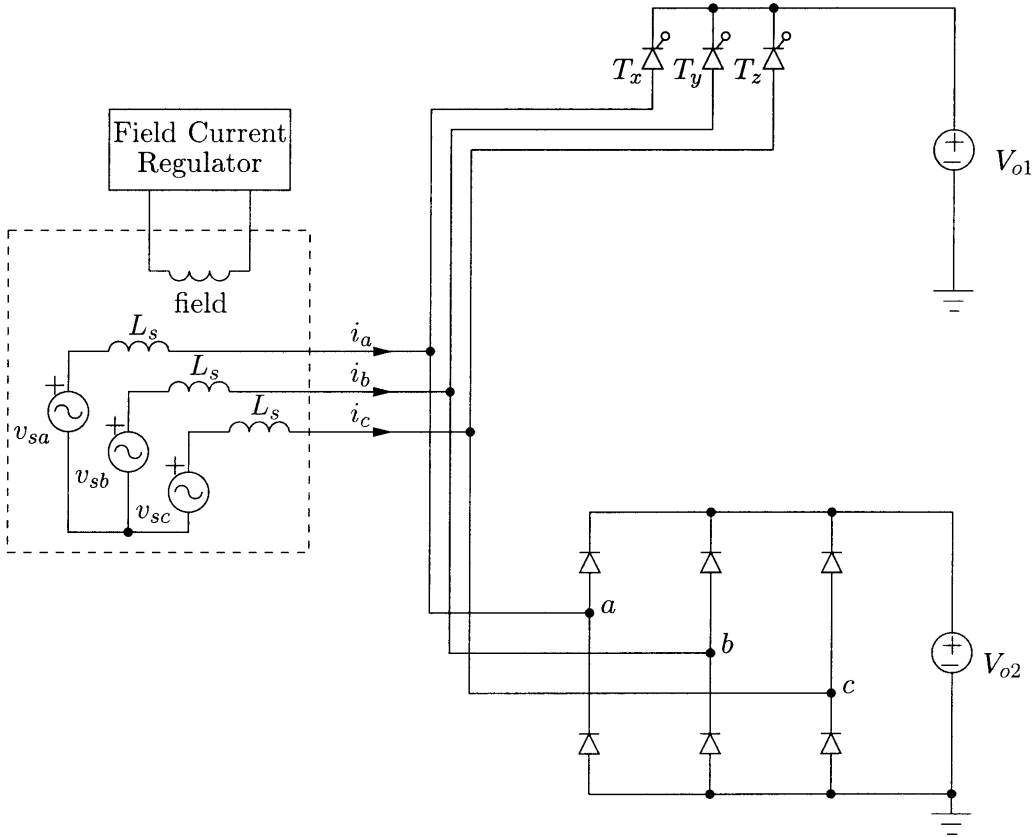
Figure 8.5: A particular implementation of the dual-rectifier alternator architecture.
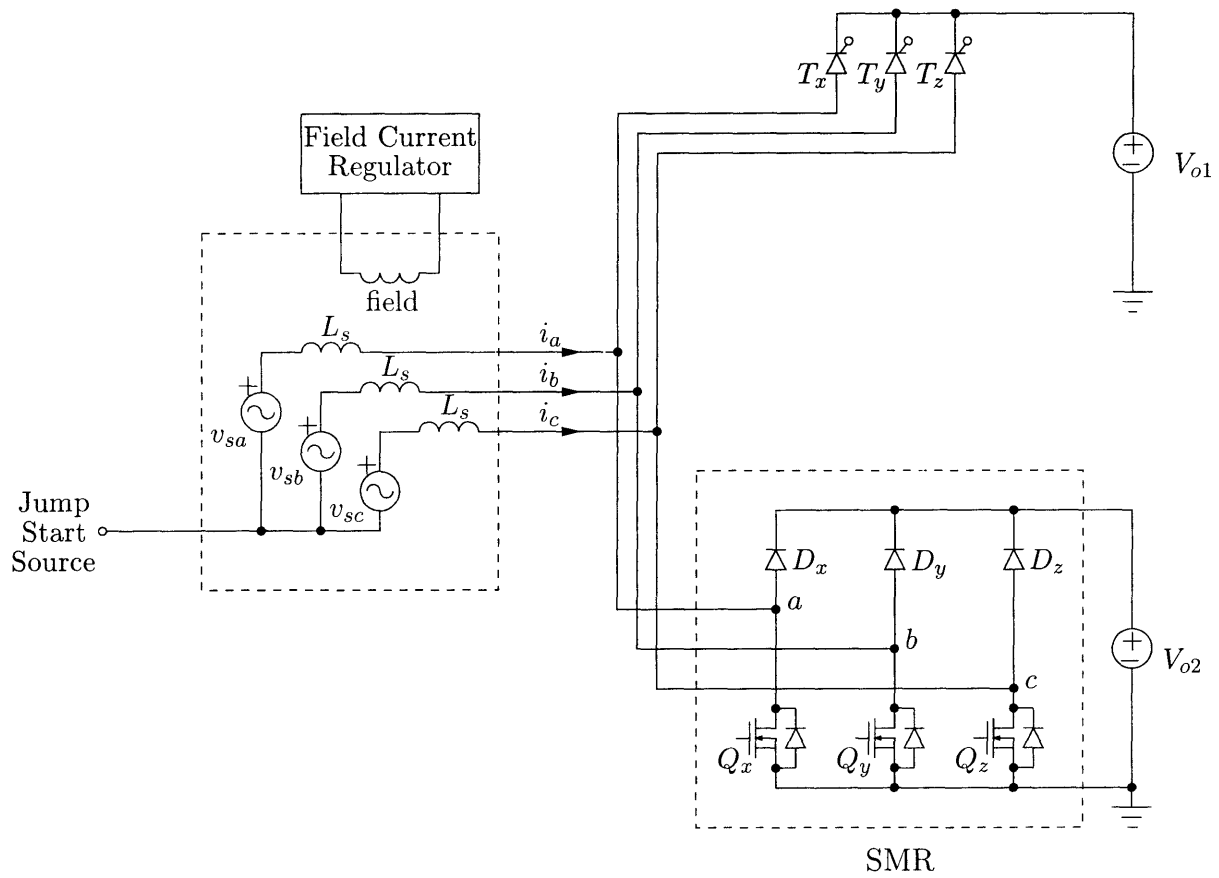
Figure 8.6: Dual-rectified alternator architecture implementation using the switched-mode rectifier structure.

full-bridge diode rectifier. This system offers substantial improvements over the conventional system of Figure 8.5. In particular, the introduction of the SMR for the high voltage bus (V_{o2}) allows high frequency modulation of the thyristors that regulate the low voltage bus (V_{o1}). By using the SMR the power output capability of the system is increased without oversizing the machine. One possible method of control is as follows: at the beginning of an operating cycle all MOSFETs $(Q_x,$ $Q_y,$ $Q_z)$ are turned on and stay on for a specified time. When the MOSFETs are turned off a subset of diodes $(D_x,$ $D_y,$ $D_z)$ turns on. After a pre-specified diode conduction period, thyristors $(T_x,$ $T_y,$ $T_z)$ are fired and machine phase currents are directed through a subset of the thyristors for the remainder of the operating cycle. With this scheme, current is chopped back and forth between the two output at the switching frequency. The upper limit on the switching frequency for the thyristors in the system is largely determined by the *turn-off time* t_q of the devices. Due to the high frequency operation of the thyristors, the control bandwidth for regulating the 14 V bus is improved. The higher operating frequency also results in substantial reduction in filter cost, size and weight. One disadvantage of this design is the cost and availability of low-t_q thyristors.

By controlling the field current of the alternator and the duty ratio of the MOSFETs and thyristors, it is possible to regulate both voltage buses while simultaneously maximizing the power output of the system (as shown in Section 5.3). In other words, by using the three control handles (MOSFET duty ratio, field current, thyristor duty ratio), one can regulate the two output voltages and simultaneously meet the load matching condition of the alternator. Furthermore, load dump transient protection and jump-start charging can be implemented using the techniques illustrated in Sections 5.5 and 5.6, respectively. In the dual-rectified system of Figure 8.6, the jump-start source can either be external (as was shown in Section 5.6) or internal. For example, the battery connected to the low voltage bus (V_{o1}) can be connected to the machine neutral and used as the jump-start source to charge a battery connected to the high voltage bus. In conclusion the SMR-based dual-rectified alternator shown in Figure 8.6 overcomes the disadvantages associated with the conventional dual-rectified alternators and has great potential for inexpensive implementation. The bandwidth of the 14 V bus may be further increased by replacing the thyristors $T_x,$ $T_y,$ T_z with diodes and placing a MOSFET between the cathodes of the diodes and voltage source $V_{o1}.$ Controlling the duty ratio of the MOSFET at a high switching frequency allows fast regulation of the 14 V bus while simplifying the control.

8.2.5 Push-Pull Dual-Rectifier Architecture with SMR Load-Matching

Another SMR-based dual-rectified alternator system is shown in Figure 8.7. This dual-voltage system is based on the push-pull rectifier that was introduced in Section 5.3 and illustrated in Figure 5.8(a). As in the dual-rectified system of Figure 8.6, thyristors in this system can also
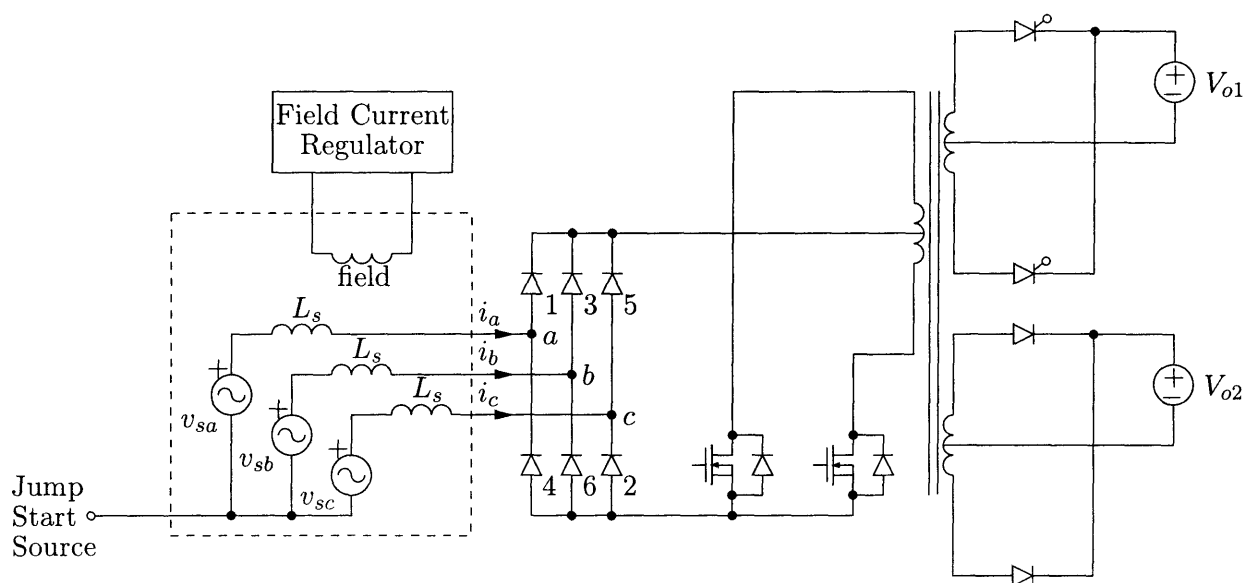
Figure 8.7: Dual-rectified alternator architecture implementation using a push-pull switched-mode rectifier structure.

operate at relatively high frequencies which results in high regulation bandwidth for the low voltage bus (V_{o1}). Voltage regulation of both buses and load-matching can be simultaneously achieved as in the previous SMR based dual-rectified system. The turns ratio of the transformer provides an extra degree of freedom for the machine/rectifier system. Load dump suppression and jump-start charging can also be implemented within the same framework for little cost. The push-pull converter based dual-voltage system shown in Figure 8.7 also allows the jump-start source to be either internal or external to the system.

8.3 Summary

In this chapter, we have higlighted the characteristics of dual-voltage automotive electrical systems (Figure 8.1). These architectures possess attractive features which have resulted in further investigation of their viability as replacements for the present automotive electrical system. Since each of these architectures is based on a Lundell-type alternator, they share some disadvantages: (1) limited alternator power output/low alternator efficiency, (2) large peak transient voltages due to load dump on the high voltage bus and (3) expensive jump start implementation. It is essential to provide cost-effective solutions to each of these issues to facilitate the introduction of these system into automobiles. In this chapter we presented extensions of the switched-mode rectifier (SMR) load-matching approach introduced in Chapter 5. Given a three-phase generator, the application

of the load-matching SMR structure increases the power output capabilities of each dual-voltage architecture. The SMR-based system also allows cost-effective implementation of load dump suppression and jump-start charging. It is expected that the developments described here will facilitate the rapid introduction of high-power and high-voltage electrical systems in automobiles.

Conclusions and Recommendations for Future Work

In this chapter we summarize the material presented in this thesis and highlight its major conclusions. Recommendations for further work in the area of automotive electrical systems is also outlined.

9.1   Thesis Summary and Conclusions

Chapter 1 provided a motivation for the study of dual/high voltage automotive electrical systems. New loads anticipated to be introduced with the next ten years cannot be powered effectively with the present 14 V system. It was concluded that a power supply architecture with a single high-voltage bus will be the most effective option in the long term, while dual-voltage architectures will be necessary in the short term for a smooth transition to the single-voltage system. We concluded the chapter by proposing to investigate a promising set of architectures through analysis, modeling and simulation and provide their operational characteristics and limitations.

Chapter 2 discussed how the introduction of new automotive loads and the restrictions of the present 14 V elecrical system led automakers to consider alternative architectures. It was shown that a high voltage (42 V) system is needed to support the features required and envisioned for the future automobile. It also become evident that the automotive industry cannot suddenly make the transition to the high-voltage electrical system due to the present 14 V infrastructure. We concluded that in the near term a Lundell or claw-pole alternator will likely be the generator that will power any candidate architectures due to its compact size and low cost. We pointed out that the low efficiency and high transient voltages that are inherent in this type of alternator will present serious limitations to its use as a high-voltage high-power generator. We proposed to develop analytical models for the alternator (including rectifiers) to be used in investigation of high and dual voltage electrical systems.

Chapter 3 presented an analysis of the operating characteristics of three-phase bridge recti-

fiers with ac-side reactance and constant-voltage loads operating in continuous conduction mode. We concluded that constant-voltage loading of a rectifier presents quite a different load than the often-considered constant-current loads. It was showen that classical models based on constant-current loads are not very accurate for constant-voltage loaded systems. We derived analytical expressions for the output current characteristics and power factor of three-phase diode and thyristor bridge rectifiers with constant-voltage loads. The analytical expressions were compared to computer simulations and shown to be quite accurate.

Chapter 4 investigated the mathematical modeling of the Lundell alternator. Analytical models for the alternator system were developed based on flux linkage equations of a three-phase synchronous machine. We also developed an alternator regulator model and used it in the simulation of the alternator system. Simplifying assumptions were used to derive an averaged equivalent circuit model for the alternator system. The circuit-based averaged model developed in this chapter was used to investigate the output current characteristics of a Lundell machine and also served as the basis for approximations of the dual-stator alternator model studied in Chapter 7.

Chapter 5 introduced a new design and control technique (based on a switched-mode rectifier) for automotive alternators which produced dramatic improvements in performance and functionality as compared to conventional systems. Based on the analytical and circuit-based alternator models developed in Chapters 3 and 4, respectively, a new load-matching technique was introduced which resulted in substantial increases in alternator output power and efficiency. The implementation of the technique was shown to require minimal and inexpensive modifications to existing alternators. We addressed the implementation of the proposed technique and provided simple analytical control laws. Experimental results demonstrated that output power increases of factors of 2.5 (peak) and 1.9 (average) along with substantial increases in efficiency are achievable. We concluded that this technique will allow us to overcome the power limitations imposed by today's Lundell alternators and provide significant improvement in vehicle fuel economy. We also showed that both transient suppression and jump-start charging functions can be implemented within the proposed framework. Experimental results from a prototype system demonstrated the transient suppression and jump charging features of the proposed architecture.

Two candidate dual-voltage architectures were analyzed in the thesis. In Chapter 6 the analysis and design of an interleaved dc/dc converter system was presented. We presented a detailed analysis, simulation and control of the converter system and used the results to aid in the construction of an experimental prototype. It was shown that the output voltage (14 V) of the system is well-regulated and has a relatively high bandwidth. The regulation of the 14 V bus was shown to perform well under load transients even in the absence of a storage battery. The improved performance comes with a large cost penalty when compared to the present generation system, and

the transients on the high voltage bus (42 V) remain since a high voltage Lundell alternator is the most likely generator to be used in this architecture.

In Chapter 7 the modeling, analysis and simulation of a dual-stator alternator electrical system was presented. A mathematical model for the dual-stator alternator based on inductance and resistance matrices was developed and used to predict steady-state output current capabilities and transient behavior due to load dump on each of the buses. The simulation results showed that the high transient voltages on the 42 V bus must be suppressed to keep it within accepted levels. Voltage regulation problems were shown to occur on the 14 V bus under extreme loading conditions. Simplified analytical models were developed and used to predict system output capabilities and choose a turns ratio of the stators to improve the voltage regulation of the 14 V bus under light loading conditions. Zener power diodes were used to limit the peak voltages on the 42 V bus thus demonstrating passive transient protection.

Chapter 8 presented a summary of dual-voltage electrical system characteristics for several architectures. We showed that all of the architectures have major drawbacks since they are likely to be powered by a Lundell-type alternator. The drawbacks that are common among these systems include the limited output power and low efficiency of the alternator and the existence of large transient voltages on the high voltage bus. The large transient voltages require the use of transient suppression techniques to keep the bus voltages within desired levels and add to the cost and complexity of the overall system. To overcome the drawbacks of the dual-voltage architectures, we presented dual-voltage extensions of the switched-mode rectifier (SMR) load-matching approach (Chapter 5). In particular an attractive complete dual-voltage system, which incorporates the new alternator system (Chapter 5) and the dc/dc converter (Chapter 6), is introduced. This new dual-voltage system offers fast load-dump control of both buses and has the additional benefits associated with the load-matching alternator system described in Chapter 5.

9.2   Recommendations for Future Work

The purpose of this thesis has been to develop and investigate dual/high voltage automotive electrical systems. There are three items that represent the overall approach of the work presented in this thesis: (1) investigation and development of analytical system models to aid in the analysis of dual/high voltage automotive electrical systems, (2) implementation of computer simulation models based on the analytical results to predict and evaluate system performance and support the realization of such systems and (3) experimental demonstration of the performance of systems and subsystems and verification of the validity of the developed models. There are still many questions

to be answered in the area of dual/high voltage automotive electrical systems and the three-point approach mentioned above may be used as a guideline when addressing these. Below is a list of areas to explore along with suggestions for items to be investigated. The topics presented here are not meant be exaustive but are meant to give some direction for research based on the material presented in the thesis.

Power Electronics Applications in Automotive Power Generation and Control

The investigation of dual/high voltage electrical systems has shown that automotive applications promise to be a new market for power electronics [60]. The use of the switched-mode rectifier to improve and enhance the capabilities of a Lundell alternator in Chapter 5 is a good example of how power electronics can enable the timely introduction of high-voltage automotive electrical systems. The promising results obtained in Chapter 5 suggests that the design and control of alternators incorporating power electronics should be investigated further. The following are some topics that require further investigation:

- Use of switched-mode rectifiers with Lundell machines to achieve higher performance

- Impact of power electronics on the design, control and optimization of Lundell-type machines

- Investigation of alternative machines incorporating power electronic controls

Energy Management in Dual-Voltage Automotive Electrical Systems

The efficient use of electrical energy in the automobile has recently become an important issue due to increases in anticipated vehicle loads and higher fuel economy requirements. As a result, there is an urgent need to control energy flow and storage in dual/high voltage automobile electrical systems. The work presented in this thesis did not directly address issues in energy management; however, the systems and subsystems models that were developed are very generic and can be used to answer questions regarding the flow, utilization and storage of energy in vehicles. Here are some suggested topics for further investigation in the area of energy management:

- Development/Extension of Saber models incorporating the energy management features of the dc/dc converter

- Evaluation of energy management strategies/algorithms through the use of Saber models

- Implementation and experimental verification of energy management system

Appendices

Analysis of Single-Phase Diode Rectifier with Constant-Voltage Load

A single-phase rectifier with a voltage source load is illustrated in Figure A.1. Sinusoidal voltage source v_s $(=V_s\sin(\omega t))$ with the a series line inductance L_s drives the bridge. As in the three-phase rectifier, the diodes in the bridge rectifier are assumed ideal except for a finite on-voltage, V_d. Assuming that the source current i_s is continuous, voltage v_{ab} can be expressed as

$$v_{ab} = (V_o + 2V_d)\,\mathrm{sgn}(i_s) \tag{A.1}$$

where $\mathrm{sgn}(\bullet)$ is the signum function. We can approximate the voltage v_{ab} by its fundamental component, $v_{ab,1}$ since the fundamental component is the only one contributing to power transfer:

$$v_{ab} \approx v_{ab,1} = V_{o1}\sin(\omega t - \phi) \tag{A.2}$$

where $V_{o1} = \frac{4}{\pi}(V_o + 2V_d)$ and ϕ is the phase angle between v_{ab} and i_s. The line current i_s can also be approximated by its fundamental component i_{s1}.

$$i_s \approx i_{s1} = I_{s1}\sin(\omega t - \phi) \tag{A.3}$$

where I_{s1} is the magnitude of the fundamental component of the line current. As in the three-phase rectifier, the voltage sources $v_{ab,1}$ may be replaced by an equivalent resistor R_{ab} given by

$$R_{ab} = \frac{V_{o1}}{I_{s1}} \tag{A.4}$$

The equivalent circuit for our simplified single-phase full bridge rectifier is shown in Figure A.2. To determine an expression for the equivalent resistance, we first compute the phasor line current

$$\mathbf{I}_s \stackrel{\triangle}{=} I_{s1}e^{-j\phi} = \frac{V_s}{\sqrt{R_{ab}^2 + (\omega L_s)^2}}e^{-j\tan^{-1}(\omega L_s/R_{ab})} \tag{A.5}.$$
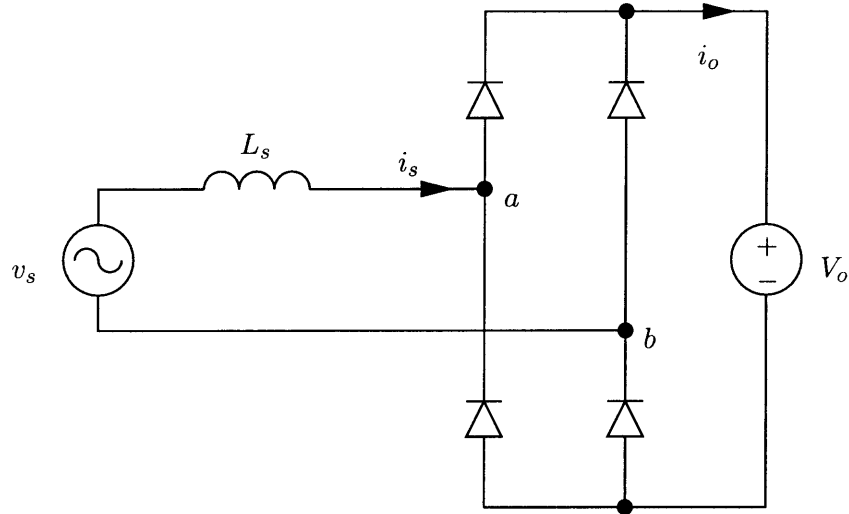
Figure A.1: Single-phase diode bridge rectifier.
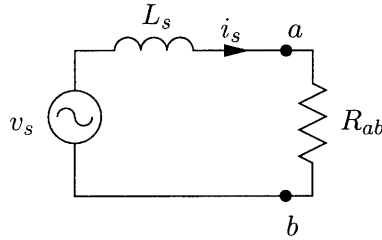
Figure A.2: Simplified model of the single-phase diode rectifier.

The equivalent resistance R_{ab} may now be written as

$$R_{ab} \stackrel{\triangle}{=} \frac{V_{o1}}{I_{s1}} = \frac{V_{o1}\sqrt{R_{ab}^2 + (\omega L_s)^2}}{V_s} \qquad \text{(A.6)}$$

Solving for R_{ab} in the above equation gives

$$R_{ab} = \frac{\omega L_s V_{o1}}{\sqrt{V_s^2 - V_{o1}^2}} \qquad \text{(A.7)}$$

Using the above expression for the equivalent resistance R_{ab}, the magnitude of the fundamental of the line current I_{s1} and the phase angle ϕ can be expressed as

$$I_{s1} = \frac{\sqrt{V_s^2 - V_{o1}^2}}{\omega L_s} \qquad \text{(A.8)}$$

$$\phi = \tan^{-1}\sqrt{(V_s/V_{o1})^2 - 1} \tag{A.9}$$

Note that the expressions for R_{ab}, I_{s1} and ϕ are identical in form to the ones given for the three-phase rectifier in Chapter 3. The only difference is the variable V_{o1} which is $\frac{4}{\pi}(V_o + 2V_d)$ for the single-phase rectifier and $\frac{4}{\pi}(V_o/2 + V_d)$ for the three-phase rectifier. The average output current delivered to the output voltage source load for the single-phase rectifier can be approximated as

$$\langle i_o \rangle \approx \frac{2}{\pi}I_{s1}. \tag{A.10}$$

Simplification of the Field Flux Linkage

Expression

In this appendix we present the details of the derivation of the simplified flux linkage equation (4.19). To derive this equation, we start with the field flux given in the matrix expression (4.18)

$$\lambda_f(t) = L_{fa}(\theta)i_a(t) + L_{fb}(\theta)i_b(t) + L_{fc}(\theta)i_c(t) + L_{ff}i_f(t) \tag{B.1}$$

Substituting the angle-dependent mutual inductances (4.11)-(4.13) into (B.1) gives

$$\lambda_f(t) = M\cos(\theta)\,i_a(t) + M\cos(\theta - 2\pi/3)\,i_b(t) + M\cos(\theta + 2\pi/3)\,i_c(t) + L_{ff}i_f(t) \tag{B.2}$$

where $\theta = \omega t$ and we have neglected the third harmonic of the mutual inductances (i.e., set $M_3 = 0$ in (4.11)-(4.13)). Next we assume that the phase currents can be well approximated by their fundamental components and are a three-phase set given by:

$$i_a(t) = I_{s1}\sin(\theta - \phi) \tag{B.3}$$

$$i_b(t) = I_{s1}\sin(\theta - \phi - 2\pi/3) \tag{B.4}$$

$$i_c(t) = I_{s1}\sin(\theta - \phi + 2\pi/3) \tag{B.5}$$

where I_{s1} is the magnitude of the fundamental component of the phase currents and ϕ is the angle between the phase current and the corresponding back-emf voltage yet to be determined. Note that the approximations for the phase currents in (B.3)-(B.5) are identical to the ones used in Chapter 3. Furthermore, the techniques developed in Chapter 3 can be used to determine the values for I_{s1} and ϕ. Substituting (B.3)-(B.5) into (B.2) yields

$$\lambda_f(t) = MI_{s1}[\cos(\theta)\sin(\theta - \phi) + \cos(\theta - 2\pi/3)\sin(\theta - \phi - 2\pi/3)$$
$$+ \cos(\theta + 2\pi/3)\sin(\theta - \phi + 2\pi/3)] + L_{ff}i_f(t) \tag{B.6}$$

.

Using trigonometric identities (B.6) becomes

$$\lambda_f(t) = MI_{s1}\left[-\frac{3}{2}\sin(\phi) + \frac{1}{2}\left\{\cos(\theta) + \cos(\theta - 2\pi/3) + \cos(\theta + 2\pi/3)\right\}\right] + L_{ff}i_f(t) \qquad (B.7)$$

We now recognize that the expression in the curly brackets of (B.7) is a three-phase set and is identically zero. Simplifying (B.7) results in a new expression for the field flux linkage

$$\lambda_f(t) = \underbrace{-\frac{3}{2}MI_{s1}\sin(\phi)}_{\stackrel{\triangle}{=}\Lambda_f} + L_{ff}i_f(t) \qquad (B.8)$$

$$= \Lambda_f + L_{ff}i_f(t) \qquad (B.9)$$

where Λ_f is a constant. The flux linkage equation given in (B.9) is the desired expression given in (4.18). The field winding voltage v_f is given by (4.28) and is repeated here for convenience

$$v_f(t) = R_f i_f(t) + L_{ff}\frac{di_f(t)}{dt} \qquad (B.10)$$

The expression in (B.10) shows that there is no voltage induced on the field winding due to the flux generated by armature (phase) currents. This is due to the fact that the field winding is stationary with respect to the resultant armature mmf wave.

Averaged Alternator Model Implementation

In this appendix we present the implementation of the averaged alternator model that was developed in Section 4.5. The equivalent circuit of the power stage of the alternator was given in Figure 4.14 but the details of the alternator regulator were not shown. The complete averaged alternator implementation in the form of an equivalent circuit is shown in Figure C.1. This figure shows three coupled circuits that are used to model the averaged behavior of the alternator: (1) the power stage, (2) the field winding and (3) the proportional controller.

The power stage of the averaged alternator model is shown at the top of Figure C.1 where the back-emf and the impedance are modeled by $V_e(\omega, i_f)$ and $Z_e(\omega)$, respectively. The back-emf and the impedance are functions of the electrical frequency ω of the alternator which is related to the alternator shaft speed by

$$\omega = \left(\frac{\pi p}{60}\right) n \tag{C.1}$$

where p is the number of poles and n is the alternator speed in rpm. We account for the dc voltage drop in the three phase rectifier by the including a series combination of a ideal diode and a constant voltage drop of $2V_d$, where V_d is the forward drop of a single power diode. In the figure, the use of ideal diodes is denoted by a *boxed* diode symbol.

The averaged model of the field winding and the proportional controller shown in Figure C.1 is based on the switching field current regulator that is described in Section 4.3 and illustrated in Figure 4.4. To derive the value of the field current, an amplified error signal is generated by subtracting the alternator output voltage v_o from the reference voltage V_{ref} and multiplying it by the proportional gain k_p. This error signal is modeled as a dependent current source $k_p(V_{ref} - v_o)$ shown on the bottom of Figure C.1 where the use of the ideal diode and the voltage source determines the relationship between the error signal and the regulator voltage v_{reg}:

$$v_{reg} = \begin{cases} k_p(V_{ref} - v_o) & \text{if } v_{reg} < V_{reg,min} \\ V_{reg,min} & \text{if } v_{reg} \geq V_{reg,min} \end{cases} \tag{C.2}$$

where voltage $V_{reg,min}$ is the minimum voltage of the regulator output from terminal m to ground
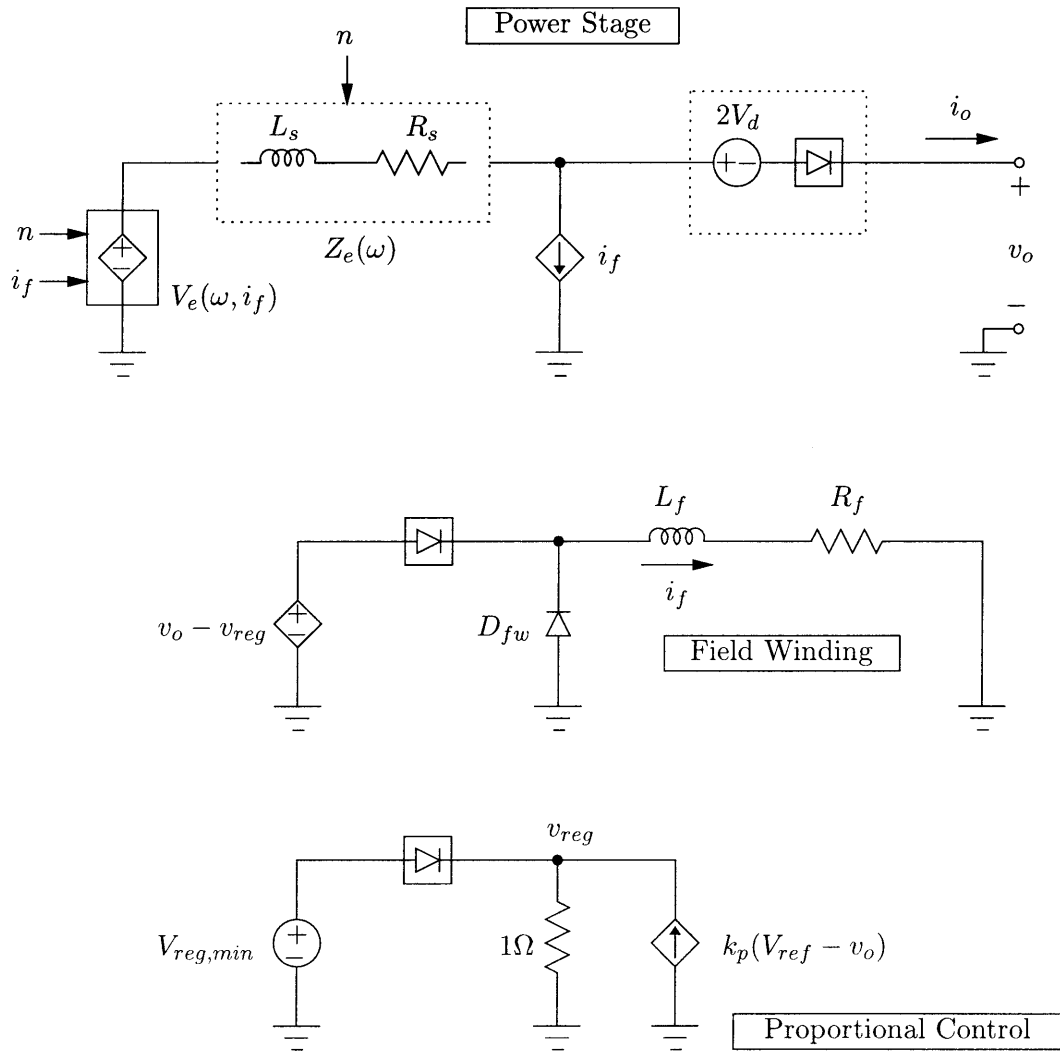
Figure C.1: Averaged model of an alternator showing the coupled electrical subcircuits for the power stage, field winding and proportional controller.

in Figure 4.4. The minimum regulator voltage $V_{reg,min}$ models the finite on-voltage of the switch in Figure 4.4 and corresponds to the collector-emitter saturation voltage of the Darlington transistor illustrated in Figure 4.2.

Once the regulator voltage v_{reg} is available, the voltage that is applied across field winding is simply $v_o - v_{reg}$ as illustrated by the dependent voltage source in the middle subcircuit of Figure C.1. Field current is generated by the application of the voltage $v_o - v_{reg}$ to the field RL circuit. The freewheeling diode D_{fw} shown in this subcircuit is used to circulate the field current. The output current io of the alternator is generated by subtracting the field current from the stator current i_s. This is due to the fact that the field winding current is drawn from the stator via the exciter diodes as shown in Figure 4.2. The code for the Saber implementation of the altnernator averaged model is given in Appendix D.

Saber MAST Templates for Various Systems

This appendix presents the Saber MAST templates that were used to run produce the simulation results given in this thesis. The templates have been tested (as part of simulations) and run successfully on two different hardware setups: (1) a Sun SparcStation 20 workstation with 192 MB of RAM running Solaris 2.4 and Saber version 4.3 (2) a Sun Ultra Sparc 10 workstation with 512 MB of RAM running Solaris 2.6 and Saber version 5.1.

In the remainder of this appendix, the code for the major MAST templates are given along with a front-end graphic that is used in conjunction with the template in constructing system schematics. The following are the list of the templates:

1. Three-Phase Lundell (Claw-Pole) Alternator Model

2. Improved Three-Phase Lundell Alternator Model

3. Dual-Stator Alternator Model

4. Averaged Alternator Model

5. Switched Alternator Regulator

6. Buck Cell Averaged Model (Continuous Conduction)

7. Buck Cell Averaged Model (Disontinuous Conduction)

8. Comparator

9. Comparator with Complementary Outputs

10. Differential Amplifier with Clipping

11. Firing Angle Driver

12. Limiting Function with Constant

13. Operational Amplifier with Clipping

14. Operational Amplifier with Clipping and Single-Pole Roloff

15. Three-Phase Full-Bridge Rectifier

16. Three-Phase Full-Bridge Rectifier with Booster Diodes

D.1   Three-Phase Lundell (Claw-Pole) Alternator Model
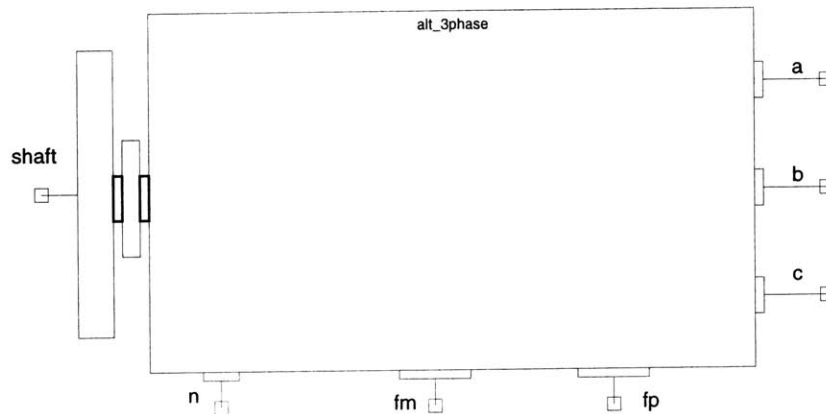

```
####################################################################
#       Three Phase Lundell Alternator Model
#
#       Vahe Caliskan, MIT
#       Created: November 2, 1997
#       Copying/electronic transfer of this code is strictly prohibited.
####################################################################


template alt_3phase shaft a b c n fp fm = rs, lls, lms, rr, llr, lmr, p, theta0

rotational_vel shaft    # rotor mechanical angular velocity connection

electrical      a,      # phase "a" voltage of the stator
                b,      # phase "b" voltage of the stator
                c,      # phase "c" voltage of the stator
                n,      # Neutral terminal of alternator
                fp,     # field "positive" terminal
                        # Usually connected to the bp terminal (of rectifier)
                fm      # field "minus" or "negative" terminal
                        # Usually connected to the bm terminal (of rectifier)


number          rs=  33m,     # Stator winding resistance
                lls= 18u,     # Stator leakage inductance
                lms= 180u,    # Stator magnetizing inductance
                rr=  3.44,    # Rotor winding resistance
                llr= 200m,    # Rotor leakage inductance
                lmr= 300m,    # Rotor magnetizing inductance
                p= 12,        # Number of poles
                theta0= 0     # Initial rotor angle.
```

```
{

<consts.sin

number      p2,         # Number of pole pairs
            phase,      # phase angle between stator windings (= 2*pi/3 = 120deg)
            ls,         # Stator winding self inductance (= lls + lms)
            lr,         # Rotor winding self inductance (= llr + lmr)
            lss,        # Stator-Stator mutual inductance (= lms * cos(phase))
            m           # Peak stator-rotor mutual inductance (= k * sqrt(lms*lmr))


val f       lambda_a,   # Flux linkage of "a" winding of stator.
            lambda_b,   # Flux linkage of "b" winding of stator.
            lambda_c,   # Flux linkage of "c" winding of stator.
            lambda_r    # Flux linkage of of rotor.


val l       lar,        # angle dependent mutual inductance between stator "a" and rotor
            lbr,        # angle dependent mutual inductance between stator "b" and rotor
            lcr,        # angle dependent mutual inductance between stator "c" and rotor
            lra,        # angle dependent mutual inductance between rotor and stator "a" (= lar)
            lrb,        # angle dependent mutual inductance between rotor and stator "b" (= lbr)
            lrc         # angle dependent mutual inductance between rotor and stator "c" (= lcr)


val w_radps omega_r     # rotor angular velocity

var ang_rad theta_r     # rotor angular position (variable)
val ang_rad theta_e     # rotor electrical angle (calculated)

# Branch current, voltage relationships for stator phases and rotor
branch ia=i(a->n),   va=v(a,n)
branch ib=i(b->n),   vb=v(b,n)
branch ic=i(c->n),   vc=v(c,n)
branch ir=i(fp->fm), vr=v(fp,fm)

# Define parameters
parameters  {
            p2 = p/2                # Number of pole pairs
            phase = 2*math_pi/3     # phase angle between stator windings
            ls = lls + lms          # Self inductance of the stator
            lr = llr + lmr          # Self inductance of the rotor
            lss = -0.5*lms          # Stator-stator mutual inductance
            m = sqrt(lmr*lms)       # Peak mutual inductance between stator and rotor
            }
```

```
values {
          # Evaluate rotor angular velocity and electrical angle
          omega_r = w_radps(shaft)    # rotor angular velocity
          theta_e = theta_r*p2        # rotor electrical angle

          # Evaluate angle−dependent mutual inductances
          lar = m*cos(theta_e)
          lbr = m*cos(theta_e − phase)
          lcr = m*cos(theta_e + phase)
          lra = lar
          lrb = lbr
          lrc = lcr

          # Evaluate flux linkages in the stator and rotor
          lambda_a =  ls*ia + lss*ib + lss*ic + lar*ir
          lambda_b = lss*ia +  ls*ib + lss*ic + lbr*ir
          lambda_c = lss*ia + lss*ib +  ls*ic + lcr*ir
          lambda_r = lra*ia + lrb*ib + lrc*ic +  lr*ir
    }

control_section {
          initial_condition(theta_r,theta0)
          }

equations     {
          va = rs*ia + d_by_dt(lambda_a)
          vb = rs*ib + d_by_dt(lambda_b)
          vc = rs*ic + d_by_dt(lambda_c)
          vr = rr*ir + d_by_dt(lambda_r)

          theta_r : d_by_dt(theta_r) = omega_r
          }
}
```

D.2   Improved Three-Phase Lundell Alternator Model
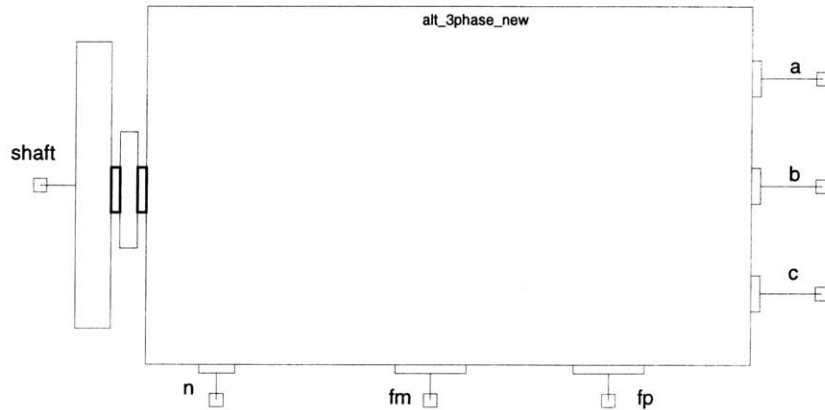

```
######################################################################
#       Three Phase Lundell Alternator Model (+ 3rd, 5th  Harmonics)
#
#       Vahe Caliskan, MIT
#       Created: May 14, 2000
#       Copying/electronic transfer of this code is strictly prohibited.
######################################################################


template alt_3phase_new shaft a b c n fp fm = rs, lls, lms, rr, llr, lmr, lg2, km3, km5, p, theta0


rotational_vel shaft   # rotor mechanical angular velocity connection


electrical      a,      # phase "a" voltage of the stator
                b,      # phase "b" voltage of the stator
                c,      # phase "c" voltage of the stator
                n,      # Neutral terminal of alternator
                fp,     # field "positive" terminal
                        # Usually connected to the bp terminal (of rectifier)
                fm      # field "minus" or "negative" terminal
                        # Usually connected to the bm terminal (of rectifier)


number      rs=  33m,    # Stator winding resistance
            lls= 18u,    # Stator leakage inductance
            lms= 180u,   # Stator magnetizing inductance
            rr=  3.44,   # Rotor winding resistance
            llr= 200m,   # Rotor leakage inductance
            lmr= 300m,   # Rotor magnetizing inductance
            lg2= 0,      # saliency inductance (added)
            km3 = 0,     # peak 3rd harm. mutual inductance between stator and rotor coefficient (added)
```

- 186 -

```
            km5 = 0,        # peak 5th harm. mutual inductance between stator and rotor coefficient (added)
            p= 12,          # Number of poles
            theta0= 0       # Initial rotor angle.


{


<consts.sin


number      p2,             # Number of pole pairs
            phase,          # phase angle between stator windings (= 2*pi/3 = 120deg)
            ls,             # Stator winding self inductance (= lls + lms)
            lr,             # Rotor winding self inductance (= llr + lmr)
            lss,            # Stator-Stator mutual inductance (= lms * cos(phase))
            m,              # Peak stator-rotor mutual inductance (= k * sqrt(lms*lmr))
            m3,             # peak 3rd harm. mutual inductance between stator and rotor (added) = km3*m
            m5              # peak 5th harm. mutual inductance between stator and rotor (added) = km5*m


val f       lambda_a,       # Flux linkage of "a" winding of stator.
            lambda_b,       # Flux linkage of "b" winding of stator.
            lambda_c,       # Flux linkage of "c" winding of stator.
            lambda_r        # Flux linkage of of rotor.


val l       lar,            # angle dependent mutual inductance between stator "a" and rotor
            lbr,            # angle dependent mutual inductance between stator "b" and rotor
            lcr,            # angle dependent mutual inductance between stator "c" and rotor
            lra,            # angle dependent mutual inductance between rotor and stator "a" (= lar)
            lrb,            # angle dependent mutual inductance between rotor and stator "b" (= lbr)
            lrc             # angle dependent mutual inductance between rotor and stator "c" (= lcr)


val w_radps omega_r         # rotor angular velocity


var ang_rad theta_r         # rotor angular position (variable)
val ang_rad theta_e         # rotor electrical angle (calculated)


# Branch current, voltage relationships for stator phases and rotor
branch ia=i(a->n),    va=v(a,n)
branch ib=i(b->n),    vb=v(b,n)
branch ic=i(c->n),    vc=v(c,n)
branch ir=i(fp->fm),  vr=v(fp,fm)


# Define parameters
parameters  {
            p2 = p/2                 # Number of pole pairs
            phase = 2*math_pi/3      # phase angle between stator windings
            ls = lls + lms           # Self inductance of the stator
```

```
              lr = llr + lmr              # Self inductance of the rotor
              lss = −0.5*lms             # Stator−stator mutual inductance
              m = sqrt(lmr*lms)          # Peak mutual inductance between stator and rotor
              m3 = km3*m                 # peak 3rd harm. mutual inductance between stator and rotor
              m5 = km5*m                 # peak 5th harm. mutual inductance between stator and rotor
              }


values {
              # Evaluate rotor angular velocity and electrical angle
              omega_r = w_radps(shaft)   # rotor angular velocity
              theta_e = theta_r*p2       # rotor electrical angle


              # Evaluate angle−dependent mutual inductances
              lar = m*cos(theta_e) + m3*cos(3*theta_e)  + m5*cos(5*theta_e)
              lbr = m*cos(theta_e − phase) + m3*cos(3*(theta_e − phase)) + m5*cos(5*(theta_e − phase))
              lcr = m*cos(theta_e + phase) + m3*cos(3*(theta_e + phase)) + m5*cos(5*(theta_e + phase))
              lra = lar
              lrb = lbr
              lrc = lcr


              # Evaluate flux linkages in the stator and rotor
              # modified for saliency
              lambda_a = (ls +lg2*cos(2*theta_e))*ia + (lss+lg2*cos(2*theta_e−phase))*ib
                           + (lss+lg2*cos(2*theta_e+phase))*ic + lar*ir
              lambda_b = (lss+lg2*cos(2*theta_e−phase))*ia + (ls +lg2*cos(2*theta_e + phase))*ib
                           + (lss+lg2*cos(2*theta_e))*ic + lbr*ir
              lambda_c = (lss+lg2*cos(2*theta_e+phase))*ia + (lss+lg2*cos(2*theta_e))*ib
                           + (ls +lg2*cos(2*theta_e − phase))*ic + lcr*ir
              lambda_r = lra*ia + lrb*ib + lrc*ic +  lr*ir
       }


control_section{
              initial_condition(theta_r,theta0)
              }


equations     {
              va = rs*ia + d_by_dt(lambda_a)
              vb = rs*ib + d_by_dt(lambda_b)
              vc = rs*ic + d_by_dt(lambda_c)
              vr = rr*ir + d_by_dt(lambda_r)

              theta_r : d_by_dt(theta_r) = omega_r
              }
}
```

D.3   Dual-Stator Alternator Model
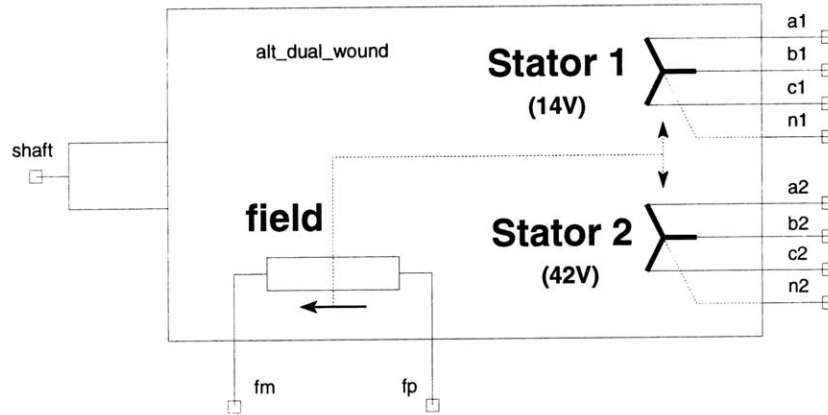

```
#######################################################################
#       Three Phase Dual Wound Alternator Model
#       Three phase sets offset by 0 degrees
#
#       Vahe Caliskan, MIT
#       Created: December 2, 1998
#       Copying/electronic transfer of this code is strictly prohibited.
#######################################################################


template alt_dual_wound shaft a1 b1 c1 a2 b2 c2 fp fm n1 n2 =
            rs1, rs2, lls1, lls2, lms1, lms2, lg1, lg2, rf, llf, lmf, p, theta0


rotational_vel shaft    # rotor mechanical angular velocity connection


electrical      a1,     # phase "a" voltage of the stator 1
                b1,     # phase "b" voltage of the stator 1
                c1,     # phase "c" voltage of the stator 1
                a2,     # phase "a" voltage of the stator 2
                b2,     # phase "b" voltage of the stator 2
                c2,     # phase "c" voltage of the stator 2
                fp,     # field "positive" terminal
                fm,     # field "minus" or "negative" terminal
                n1,     # neutral terminal of stator 1
                n2      # neutral terminal of stator 2


number      rs1   =     33m,      # Stator 1 winding resistance
            rs2   =   9*33m,      # Stator 2 winding resistance
            lls1  =     15u,      # Stator 1 leakage inductance
            lls2  =   9*15u,      # Stator 2 leakage inductance
            lms1  =    105u,      # Stator 1 magnetizing inductance
```

```
        lms2 = 9*105u,        # Stator 2 magnetizing inductance
        lg1  =    10u,        # Stator 1 saliency inductance magnitude
        lg2  =  9*10u,        # Stator 2 saliency inductance magnitude
        rf   = 9*3.44,        # Field (rotor) winding resistance
        llf  = 9*200m,        # Field (rotor) leakage inductance
        lmf  = 9*150m,        # field (rotor) magnetizing inductance
        p    =    12,         # Number of poles
        theta0 =    0         # Initial rotor angle


{


<consts.sin


number      p2,              # Number of pole pairs
            phase,           # phase angle between stator windings (= 2*pi/3 = 120deg)
            ls1,             # Stator 1 winding self inductance, ignoring saliency (= lls1 + lms1)
            ls2,             # Stator 2 winding self inductance, ignoring saliency (= lls2 + lms2)
            lf,              # Rotor winding self inductance (= llf + lmf)
            lms11,           # peak stator 1 - stator 1 mutual ind., w/o saliency (= lms1*cos(phase))
            lms22,           # peak stator 2 - stator 2 mutual ind., w/o saliency (= lms2*cos(phase))
            lms12,           # peak stator 1 - stator 2 mutual ind., w/o saliency (= k*sqrt(lms1*lms2))
            lms12p,          # peak stator 1 - stator 2 mutual ind., w/o saliency (= lms12*cos(phase))
            lg12,            # peak stator 1 - stator 2 saliency ind. magnitude (= sqrt(lg1*lg2))
            m1,              # Peak stator 1-rotor mutual inductance (= sqrt(lms1*lmf))
            m2               # Peak stator 2-rotor mutual inductance (= sqrt(lms2*lmf))


val f       lambda_a1,       # Flux linkage of "a" winding of stator 1.
            lambda_b1,       # Flux linkage of "b" winding of stator 1.
            lambda_c1,       # Flux linkage of "c" winding of stator 1.
            lambda_a2,       # Flux linkage of "a" winding of stator 2.
            lambda_b2,       # Flux linkage of "b" winding of stator 2.
            lambda_c2,       # Flux linkage of "c" winding of stator 2.
            lambda_f         # Flux linkage of of rotor.


val l       la1a1,           # stator a1-a1 self inductance
            la2a2,           # stator a2-a2 self inductance
            lb1b1,           # stator a1-a1 self inductance
            lb2b2,           # stator b2-b2 self inductance
            lc1c1,           # stator c1-c1 self inductance
            lc2c2,           # stator c2-c2 self inductance
            lff,             # rotor self inductance
            la1b1,           # stator a1-b1 mutual inductance (same winding)
            la2b2,           # stator a2-b2 mutual inductance (same winding)
            la1c1,           # stator a1-c1 mutual inductance (same winding)
            la2c2,           # stator a2-c2 mutual inductance (same winding)
```

```
       lb1c1,        # stator b1-c1 mutual inductance (same winding)
       lb2c2,        # stator b2-c2 mutual inductance (same winding)
       la1a2,        # stator a1-a2 mutual inductance
       lb1b2,        # stator b1-b2 mutual inductance
       lc1c2,        # stator c1-c2 mutual inductance
       la1b2,        # stator a1-b2 mutual inductance
       la2b1,        # stator a2-b1 mutual inductance
       lc2a1,        # stator c2-a1 mutual inductance
       lc1a2,        # stator c1-a2 mutual inductance
       lb1c2,        # stator b1-c2 mutual inductance
       lb2c1,        # stator b2-c1 mutual inductance
       lb1a1,        # lb1a1 = la1b1
       lb2a2,        # lb2a2 = la2b2
       lc1a1,        # lc1a1 = la1c1
       lc2a2,        # lc2a2 = la2c2
       lc1b1,        # lc1b1 = lb1c1
       lc2b2,        # lc2b2 = lb2c2
       la2a1,        # la2a1 = la1a2
       lb2b1,        # lb2b1 = lb1b2
       lc2c1,        # lc2c1 = lc1c2
       lb2a1,        # lb2a1 = la1b2
       lb1a2,        # lb1a2 = la2b1
       la1c2,        # la1c2 = lc2a1
       la2c1,        # la2c1 = lc1a2
       lc2b1,        # lc2b1 = lb1c2
       lc1b2,        # lc1b2 = lb2c1
       lfa1,         # rotor-stator winding a1 mutual inductance
       lfb1,         # rotor-stator winding b1 mutual inductance
       lfc1,         # rotor-stator winding c1 mutual inductance
       lfa2,         # rotor-stator winding a2 mutual inductance
       lfb2,         # rotor-stator winding b2 mutual inductance
       lfc2,         # rotor-stator winding c2 mutual inductance
       la1f,         # la1f = lfa1
       lb1f,         # lb1f = lfb1
       lc1f,         # lc1f = lfc1
       la2f,         # la2f = lfa2
       lb2f,         # lb2f = lfb2
       lc2f          # lc2f = lfc2


val w_radps  omega_r    # rotor angular velocity
var ang_rad  theta_r    # rotor angular position (variable)
val ang_rad  theta_e    # rotor electrical angle (calculated)


# Branch current, voltage relationships for stator phases and rotor
branch ia1=i(a1->n1),   va1=v(a1,n1)
```

```
branch ib1=i(b1->n1),    vb1=v(b1,n1)
branch ic1=i(c1->n1),    vc1=v(c1,n1)
branch ia2=i(a2->n2),    va2=v(a2,n2)
branch ib2=i(b2->n2),    vb2=v(b2,n2)
branch ic2=i(c2->n2),    vc2=v(c2,n2)
branch ifield=i(fp->fm), vf=v(fp,fm)
```

```
# Define parameters
parameters    {
              p2     = p/2                  # Number of pole pairs
              phase  = 2*math_pi/3          # phase angle between stator windings
              ls1    = lls1 + lms1          # Self inductance of stator 1, w/o saliency
              ls2    = lls2 + lms2          # Self inductance of stator 2, w/o saliency
              lf     = llf + lmf            # Self inductance of the rotor
              lms11  = lms1*cos(phase)      # peak stator 1 - stator 1 mutual ind., w/o saliency
              lms22  = lms2*cos(phase)      # peak stator 2 - stator 2 mutual ind., w/o saliency
              lms12  = sqrt(lms1*lms2)      # peak stator 1 - stator 2 mutual ind., w/o saliency
              lms12p = lms12*cos(phase)     # peak stator 1 - stator 2 mutual ind., w/o saliency
              lg12   = sqrt(lg1*lg2)        # peak stator 1 - stator 2 saliency ind. magnitude
              m1     = sqrt(lmf*lms1)       # Peak stator 1-rotor mutual inductance
              m2     = sqrt(lmf*lms2)       # Peak stator 2-rotor mutual inductance
              }
```

```
values  {
              # Evaluate rotor angular velocity and electrical angle
              omega_r = w_radps(shaft)    # rotor angular velocity
              theta_e = theta_r*p2        # rotor electrical angle

              # Evaluate angle-dependent stator and rotor self inductances
              la1a1 = ls1 + lg1*cos(2*theta_e)
              la2a2 = ls2 + lg2*cos(2*theta_e)
              lb1b1 = ls1 + lg1*cos(2*theta_e + phase)
              lb2b2 = ls2 + lg2*cos(2*theta_e + phase)
              lc1c1 = ls1 + lg1*cos(2*theta_e - phase)
              lc2c2 = ls2 + lg2*cos(2*theta_e - phase)
              lff   = lf

              # Evaluate angle dependent stator-stator mutual inductances
              la1b1 = lms11 + lg1*cos(2*theta_e - phase)
              la2b2 = lms22 + lg2*cos(2*theta_e - phase)
              la1c1 = lms11 + lg1*cos(2*theta_e + phase)
              la2c2 = lms22 + lg2*cos(2*theta_e + phase)
              lb1c1 = lms11 + lg1*cos(2*theta_e)
              lb2c2 = lms22 + lg2*cos(2*theta_e)
              la1a2 = lms12 + lg12*cos(2*theta_e)
```

```
lb1b2 = lms12 + lg12*cos(2*theta_e + phase)
lc1c2 = lms12 + lg12*cos(2*theta_e − phase)
la1b2 = lms12p + lg12*cos(2*theta_e − phase)
la2b1 = lms12p + lg12*cos(2*theta_e − phase)
lc2a1 = lms12p + lg12*cos(2*theta_e + phase)
lc1a2 = lms12p + lg12*cos(2*theta_e + phase)
lb1c2 = lms12p + lg12*cos(2*theta_e)
lb2c1 = lms12p + lg12*cos(2*theta_e)


lb1a1 = la1b1
lb2a2 = la2b2
lc1a1 = la1c1
lc2a2 = la2c2
lc1b1 = lb1c1
lc2b2 = lb2c2
la2a1 = la1a2
lb2b1 = lb1b2
lc2c1 = lc1c2
lb2a1 = la1b2
lb1a2 = la2b1
la1c2 = lc2a1
la2c1 = lc1a2
lc2b1 = lb1c2
lc1b2 = lb2c1


# Evaluate angle dependent rotor−stator mutual inductances
lfa1 = m1*cos(theta_e)
lfb1 = m1*cos(theta_e − phase)
lfc1 = m1*cos(theta_e + phase)
lfa2 = m2*cos(theta_e)
lfb2 = m2*cos(theta_e − phase)
lfc2 = m2*cos(theta_e + phase)
la1f = lfa1
lb1f = lfb1
lc1f = lfc1
la2f = lfa2
lb2f = lfb2
lc2f = lfc2


# Evaluate flux linkages in the stator and rotor
lambda_a1 = la1a1*ia1 + la1b1*ib1 + la1c1*ic1 + la1a2*ia2 + la1b2*ib2 + la1c2*ic2
            + la1f*ifield
lambda_b1 = lb1a1*ia1 + lb1b1*ib1 + lb1c1*ic1 + lb1a2*ia2 + lb1b2*ib2 + lb1c2*ic2
            + lb1f*ifield
```

lambda_c1 = lc1a1*ia1 + lc1b1*ib1 + lc1c1*ic1 + lc1a2*ia2 + lc1b2*ib2 + lc1c2*ic2
            + lc1f*ifield

lambda_a2 = la2a1*ia1 + la2b1*ib1 + la2c1*ic1 + la2a2*ia2 + la2b2*ib2 + la2c2*ic2
            + la2f*ifield

lambda_b2 = lb2a1*ia1 + lb2b1*ib1 + lb2c1*ic1 + lb2a2*ia2 + lb2b2*ib2 + lb2c2*ic2
            + lb2f*ifield

lambda_c2 = lc2a1*ia1 + lc2b1*ib1 + lc2c1*ic1 + lc2a2*ia2 + lc2b2*ib2 + lc2c2*ic2
            + lc2f*ifield

lambda_f = lfa1*ia1 + lfb1*ib1 + lfc1*ic1 + lfa2*ia2 + lfb2*ib2 + lfc2*ic2
            + lff*ifield

        }

control_section {
            initial_condition(theta_r,theta0)
            }

equations   {
            va1 = rs1*ia1   + d_by_dt(lambda_a1)
            vb1 = rs1*ib1   + d_by_dt(lambda_b1)
            vc1 = rs1*ic1   + d_by_dt(lambda_c1)
            va2 = rs2*ia2   + d_by_dt(lambda_a2)
            vb2 = rs2*ib2   + d_by_dt(lambda_b2)
            vc2 = rs2*ic2   + d_by_dt(lambda_c2)
            vf = rf*ifield + d_by_dt(lambda_f)

            theta_r : d_by_dt(theta_r) = omega_r
            }
}

D.4 Averaged Alternator Model


```
####################################################################
#       Alternator Averaged Model – 14 V – Level 0
#
#       Vahe Caliskan, MIT
#       Created: May 28, 1998
#       Copying/electronic transfer of this code is strictly prohibited.
####################################################################


template alt14v_avg_0 shaft bp bm data = k, rs, ls, rf, lf, p, kp, vd, vref, vregmin


rotational_vel shaft    # rotor mechanical angular velocity connection


electrical       bp,     # bp (battery +) terminal
                 bm      # negative terminal – ground


ref nu data              # data output (for comparison)


number       k=4.286769m, # Multiplier for speed voltage
                          # k = (vref+2*vd)/(n0 if)
                          # where if=(vconst−vregmin)/rf
                          # for NC 14V 60−120A, n0=1000
             rs = 33m,    # Stator winding resistance
             ls = 177u,   # Stator equivalent self−inductance
             rf = 3.44,   # Rotor (field) winding resistance
             lf = 800m,   # Rotor (field) self−inductance
             p  = 12,     # Number of poles
             kp = 20,     # Alternator regulator proportional gain
             vd = 1,      # diode drop in rectifier
             vref = 14.2, # alternator reference voltage
             vregmin=0.5  # min value of regulation voltage
```

```
{

<consts.sin


###############################################################
### Speed voltage
element template speedvolt n ifield pos neg = k
electrical      pos, neg
ref nu          n
number          k=1


ref      i      ifield


{

<consts.sin

branch i=i(pos,neg), v=v(pos,neg)
v=k*n*ifield


}
###############################################################
### Stator Impedance
element template zn n pos neg = rs, ls, p
electrical      pos, neg
ref nu          n

number rs = 33m,
       ls = 177u,
       p  = 12
{

<consts.sin

val nu  z

values {
#       z = sqrt( rs**2 + ( (math_pi/30)*(p/2)*n*ls )**2 )
        z = (3/math_pi)*( (3/2)*rs + (sqrt(3)/2)* (math_pi/30)*(p/2)*n*ls)
        }

branch i=i(pos,neg), v=v(pos,neg)
i=v/z


}
```

```
##################################################################
#### Netlist
# speed voltage k if n
rot_vel2var.1 shaft 0 n = units=ios
speedvolt.1 n i(l.lf) 1 bm = k=k      # v(1)=k*ifield*n
zn.1 n 1 2 = p=p, ls=ls, rs=rs        # stator impedance
#l.ls 20 2 = l=ls                     # stator inductance (for LD)
v.d2 2 3 = dc = 2*vd                  # two-diode drop
pwld.1 3 bp = von=1m                  # keeps i_stator >0
cccs.field i(l.lf) 2 bm = k=1         # pull ifield out of 2 node


v.ref ref bm = dc=vref                # v(ref) = vref
vsum.1 bp ref kerr = k1=kp, k2=-kp    # kerr = kp*(v(bp)-v(ref))


vccs.reg  kerr bm bm reg = k=1        # i(0->reg)=kp*(v(bp)-v(ref))=kerr
r.reg  reg bm = rnom=1                # v(reg)=kp*(v(bp)-v(ref))
pwld.clamp clamp reg = von=1m         #
v.clamp clamp bm = dc=vregmin         # min[v(reg)] = vregmin


vcvs.field bp reg field bm = k=1      # v(field) = (v(4) - v(reg))
r.rf bm1 bm2 = rnom=rf                # field resistance
l.lf bm2 bm3 = l=lf                   # field self inductance
v.if bm3 bm  = dc=0                   # i(field) = i(v.if)
d.flyback bm bm1                      # flyback diode
pwld.reg field bm1 = von=1m           # reg diode - pwl ideal


# data from Bosch NC 14V 60-120A alternator
map1d.1 n data = data=[(0, 0), (1k, 0), (1.5k, 40), (2k, 70), (3k, 94),
                (4k, 105), (5k, 114), (6k, 120), (7k, 124), (8k, 127),
                (9k, 130), (10k, 131), (11k, 132), (12k, 133),
                (13k, 133.5), (14k, 134), (15k, 134.5), (16k, 135),
                (17k, 135.5), (18k, 136)]


# data from Bosch KC 14V 45-90A alternator
#map1d.1 n data = data=[(0, 0), (1k, 0), (1239, 11.72), (1788, 50.81),
#                (2239, 65.89), (2740, 74.49), (2996, 77.12),
#                (3240, 79.19), (3497, 80.87), (4492, 85.36),
#                (6005, 88.75), (7995, 90.42), (10009, 90.61),
#                (12500, 90.58)]


}
```

D.5 Switched Alternator Regulator
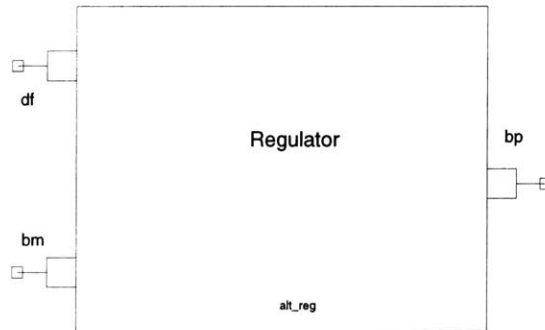

```
####################################################################
#      Alternator Regulator Model (Switched)
#      Parameters from Cherry Semiconductor CS-3341/51, CS-386-387, CS-3361
#
#      Vahe Caliskan, MIT
#      Created: September 9, 1997
#      Copying/electronic transfer of this code is strictly prohibited.
####################################################################


template alt_reg bp bm df = vreg, k, w

electrical      bp,          # alternator "plus" connection
                bm,          # alternator "minus" or ground connection
                df           # alternator field connection

number          vreg= 14.5,  # Regulator set-point.
                k= 10,       # Regulator low frequency gain
                w= 100       # Regulator pole frequency (rad/sec).
{


####################################################################
# limiting function with upper and lower limits as constant inputs
element template xlimit in out = plim, mlim

ref nu  in                   # Input (must refer to a "nu" var in another template).
var nu  out                  # Output.
number      plim=3,          # positive saturation limit
            mlim=1           # negative saturation limit


{
```

```
val nu output              # Value of the output.


values {
        if (in >= mlim & in <= plim) output = in
        else if (in > plim)  output =  plim
        else if (in < mlim)  output =  mlim
        }


equations      {
                out :  out = output
                }
}
```
##
```
# comparator (modulator) model used by alt_reg
element template modulator control ramp out


ref nu   control       # (−) terminal control signal
ref nu   ramp          # (+) terminal periodic ramp signal
var nu   out           # Output


{
val nu output          # Value of the output.


values {
        if (control >= ramp) output = 0
        else output =  1
        }


equations      {
                out :  out = output
                }
}
```
##
```
# Some of the netlist based on a Saber demo: Automotive Charging System
```
##
```
# netlist
# electrical filtering of the sense voltage
# r.r1 bp bp1 = rnom=100k # bp1 is attenuated and filtered bp
# r.r2 bp1 0  = rnom=50k   # dc voltage at bp1 is 1/3 of the dc
# c.c3 bp1 0  = c=0.47u     # voltage at bp  c=0.047u
elec2var.p bp 0 px
elec2var.m bm 0 mx
constant.vreg vregx = vreg  # due to the r.r1, r.r2 v. divider
sum.ref vregx mx ref
sum.error px ref error1 = k1 = 1, k2 = −1
```

```
xlimit.error error1 error = mlim=-5, plim=5
#gain.error error control1 = k=k                    # H(s) = k
lag.field error control1 = k = k, w = w            # H(s) = k/(1+s/w)
xlimit.control control1 control = mlim=0, plim=5


# 140 Hz ramp, rise/fall time ratio 17:1
#src.ramp ramp = tran =(ppwl= [0,1, 6.74m,3, 7.14m,1])
src.ramp ramp = tran =(ppwl= [0,1m, 6.74m,5, 7.14m,1m])
modulator.field control ramp out


# generate binary electrical control signal v(out1,bm)
var2elec.out out out1 bm


# voltage controlled switch between field (df) and gnd (bm)
# controlling signal is from out1 to bm
sw_vc.field df bm out1 bm = model=(vt=0.5, ron=1m, roff=10meg), ic=on


# freewheeling diode (circulates field current when switch is off)
pwld.f df bp


}
```

D.6   Buck Cell Averaged Model (Continuous Conduction)
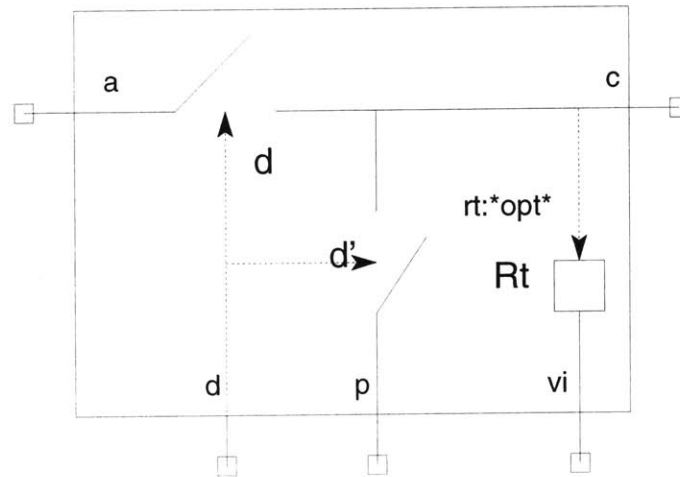

```
###################################################################
#      Buck Cell Averaged Model (Continuous Conduction Mode)
#
#      Vahe Caliskan, MIT
#      Created: November 5, 1999
#      Copying/electronic transfer of this code is strictly prohibited.
###################################################################


template buck_ccm a p c d vi = rt

electrical      a,      # PWM−switch active node.
                p,      # PWM−switch passive node.
                c,      # PWM−switch common node.
                vi,     # sensed inductor current vi=rt*iL
                d       # duty ratio (voltage) connection (0 < d < 1)

number      rt=0.1 # Transresistance

{

# Branch current, voltage relationships
branch iap=i(a−>p), vap=v(a,p)
branch icp=i(c−>p), vcp=v(c,p)
branch ivi=i(vi−>p), vvi=v(vi,p)

val nu vap1           # vap1 = v(a,p)
val nu vcp1
val nu iap1
```

```
val nu duty              # duty = v(d)
val nu vvi1

values {
        duty = v(d)
        vap1 = v(a) − v(p)
        vcp1 = duty*vap1
        iap1 = −duty*icp
        vvi1 = −rt*icp
        }

equations      {
               iap = iap1
               icp: vcp = vcp1
               ivi: vvi = vvi1
               }
}
```

D.7 Buck Cell Averaged Model (Disontinuous Conduction)
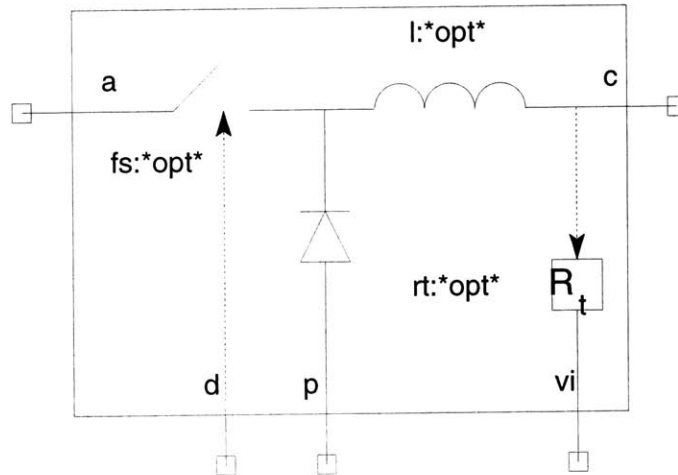

```
####################################################################
#      Buck Cell Averaged Model (Disontinuous Conduction Mode)
#
#      Vahe Caliskan, MIT
#      Created: April 4, 1998 Modified: May 19, 1998
#      Copying/electronic transfer of this code is strictly prohibited.
####################################################################

template buck_dcm a p c d vi = l, fs, rt

electrical       a,      # PWM−switch active node.
                 p,      # PWM−switch passive node.
                 c,      # PWM−switch common node.
                 vi,     # sensed inductor current vi=rt*iL
                 d       # duty ratio (voltage) connection (0 < d < 1)


number           l=1.72u,    # Buck cell inductance
                 fs=125k,    # switching frequency
                 rt=0.1      # Transresistance

{

# Branch current, voltage relationships
branch iap=i(a−>p), vap=v(a,p)
branch icp=i(c−>p), vcp=v(c,p)
branch ivi=i(vi−>p), vip=v(vi,p)
```

```
val nu vac1          # vac1 = v(a,p)−v(c,p)
val nu vac2          # limited vac1
val nu vap1          # vap1 = v(a,p)
val nu vcp1          # vcp1 = v(c,p)
val nu duty          # duty = v(d)
val nu iap1
val nu icp1
val nu icp2
val nu vil


values {
            # Evaluate vac = v(a,p)−v(c,p)
            vac1 = v(a) − v(c)
            vap1 = v(a) − v(p)
            vcp1 = v(c) − v(p)
            duty = v(d)


            if (vac1 >= 0.01 & vac1 <= 50) vac2 = vac1
            else if (vac1 > 50)  vac2 =  50
            else if (vac1 < 0.01)  vac2 =  0.01


            iap1 = vac2*duty*duty/(2*fs*l)
            icp1 = −vap1*vac2*duty*duty/(2*fs*l*vcp1 + 1u)


            if ( −icp1 >= 0.0 & −icp1 <= 500) icp2 = icp1
            else if (−icp1 > 500)  icp2 =  500
            else if (−icp1 < 0.0)  icp2 =  0.0


            vil = −rt*icp2
    }

equations {
            iap = iap1
            icp = icp2
            ivi: vip = vil
      }


}
```

D.8   Comparator
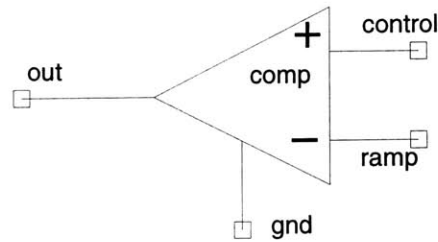

```
#####################################################################
#       Simple Comparator Model
#
#       Vahe Caliskan, MIT
#       Created:  May 22, 1998
#       Copying/electronic transfer of this code is strictly prohibited.
#####################################################################


element template comp control ramp out gnd

electrical      control,       # control (modulation) signal
                ramp,          # ramp (sawtooth) signal
                out,           # output voltage
                gnd            # ground (reference)
{
# Branch current, voltage relationships
branch iout=i(out->gnd), vout=v(out,gnd)

val nu vin                     # vin = v(control) - v(ramp)
val nu vout1                   # vout1=Heaviside(vin), [0,1]

values {
      vin = v(control) - v(ramp)
      if (vin >= 0) vout1 = 1
      else vout1 = 0
      }

equations      {
               iout : vout = vout1
               }
}
```

D.9 Comparator with Complementary Outputs
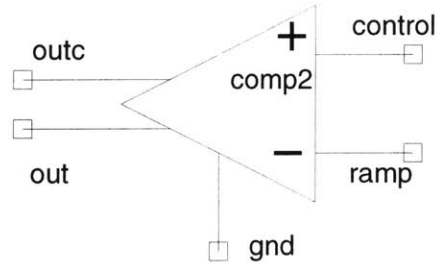

```
##########################################################################
#       Simple Comparator Model (with complementary outputs)
#
#       Vahe Caliskan, MIT
#       Created:  November 1, 1999
#       Copying/electronic transfer of this code is strictly prohibited.
##########################################################################


element template comp2 control ramp out outc gnd

electrical      control,        # control (modulation) signal
                ramp,           # ramp (sawtooth) signal
                out,            # output voltage
                outc,           # complement of output voltage
                gnd             # ground (reference)


{

# Branch current, voltage relationships
branch iout=i(out−>gnd), vout=v(out,gnd)
branch ioutc=i(outc−>gnd), voutc=v(outc,gnd)

val nu vin              # vin = v(control) − v(ramp)
val nu vout1            # vout1=Heaviside(vin), [0,1]
val nu vout1c           # complement of vout1

values {

        vin = v(control) − v(ramp)

        if (vin >= 0) vout1 = 1
        else vout1 = 0
```

```
        if (vout1 >= 1) vout1c=0
        else vout1c=1


        }

equations     {
            iout : vout = vout1
            ioutc : voutc = vout1c
            }
}
```

D.10 Differential Amplifier with Clipping
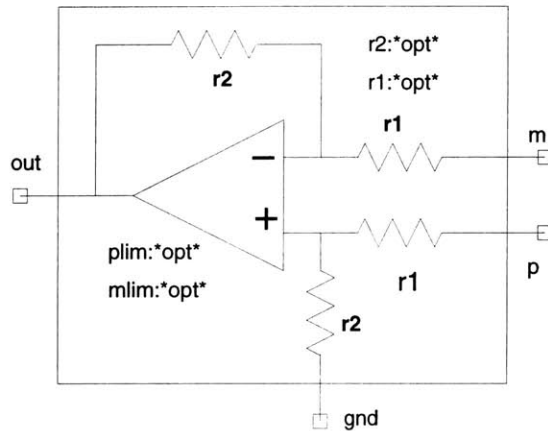

```
######################################################################
#      Differential Amplifier with clipping
#
#      Vahe Caliskan, MIT
#      Created:  May 19, 1998
#      Copying/electronic transfer of this code is strictly prohibited.
######################################################################


element template diffamp p m out gnd = plim, mlim, r2, r1

electrical      p,          # (+) voltage with respect to gnd
                m,          # (−) voltage with respect to gnd
                out,        # output voltage
                gnd         # ground (reference)

number          r2=85k,     # feedback resistance
                r1=10k,     # input resistance, vout=(r2/r1)*v(p,m)
                plim=1.7,   # positive saturation limit
                mlim=0      # negative saturation limit

{
# Branch current, voltage relationships
branch iout=i(out−>gnd), vout=v(out,gnd)

val nu vin              # vin = v(p) − v(m)
val nu vout1            # vout1 = (r2/r1)*vin
val nu vout2            # vout2 = limit(vout1,0,1.7)
```

```
values {
        vin = v(p) − v(m)
        vout1 = (r2/r1)*vin
        if (vout1 >= mlim & vout1 <= plim) vout2 = vout1
        else if (vout1 > plim)  vout2 =  plim
        else if (vout1 < mlim)  vout2 =  mlim
        }

equations     {
                iout : vout = vout2
                }
}
```

D.11   Firing Angle Driver
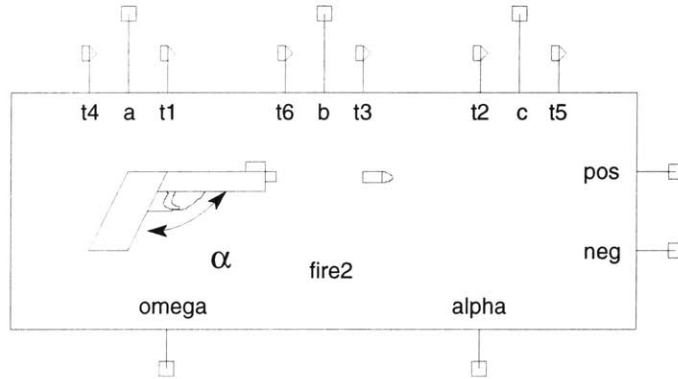

```
#######################################################################
#       Firing angle driver
#
#       Vahe Caliskan, MIT
#       Created:  December 24, 1998
#       Copying/electronic transfer of this code is strictly prohibited.
#######################################################################

template fire2 omega alpha a b c pos neg t1 t2 t3 t4 t5 t6

rotational_vel omega
rotational_ang alpha
electrical a,b,c,pos,neg
state logic_4 t1,t2,t3,t4,t5,t6

{
<consts.sin

number k1,k2,k3,k4,k5
val nu s0,s1,s2,s3,s4,s5,period,td
val rad alpha1,wt

state nu s0_b,s0_a
state nu s1_b,s1_a
state nu s2_b,s2_a
state nu s3_b,s3_a
state nu s4_b,s4_a
state nu s5_b,s5_a

parameters {
        k1=math_pi/3
```

```
        k2=2*k1
        k3=3*k1
        k4=4*k1
        k5=5*k1
        }

values {
        alpha1=ang_rad(alpha)
        wt=w_radps(omega)*time
        period=(2*math_pi)/(w_radps(omega)+1n)
        td=(alpha1/(2*math_pi))*period
        s0=v(a,pos)     # ref signal for t1 # s0=sin(wt)
        s1=v(neg,c)     # ref signal for t2 # s1=sin(wt−k1)
        s2=v(b,pos)     # ref signal for t3 # s2=sin(wt−k2)
        s3=v(neg,a)     # ref signal for t4 # s3=sin(wt−k3)
        s4=v(c,pos)     # ref signal for t5 # s4=sin(wt−k4)
        s5=v(neg,b)     # ref signal for t6 # s5=sin(wt−k5)
        }

when(dc_init) {
        schedule_event(time,t1,l4_0)
        schedule_event(time,t2,l4_0)
        schedule_event(time,t3,l4_0)
        schedule_event(time,t4,l4_0)
        schedule_event(time,t5,l4_0)
        schedule_event(time,t6,l4_0)
        }

when(threshold(s0,0,s0_b,s0_a)) {
        if (s0_b<0 & s0_a>0) {
                schedule_event(time,t5,l4_0)
                schedule_event(time,t6,l4_1)
                schedule_event(time+td,t1,l4_1)
                }
        }

when(threshold(s1,0,s1_b,s1_a)) {
        if (s1_b<0 & s1_a>0) {
                schedule_event(time,t6,l4_0)
                schedule_event(time,t1,l4_1)
                schedule_event(time+td,t2,l4_1)
                }
        }

when(threshold(s2,0,s2_b,s2_a)) {
```

```
        if (s2_b<0 & s2_a>0) {
                schedule_event(time,t1,l4_0)
                schedule_event(time,t2,l4_1)
                schedule_event(time+td,t3,l4_1)
                }
        }

when(threshold(s3,0,s3_b,s3_a)) {
        if (s3_b<0 & s3_a>0) {
                schedule_event(time,t2,l4_0)
                schedule_event(time,t3,l4_1)
                schedule_event(time+td,t4,l4_1)
                }
        }

when(threshold(s4,0,s4_b,s4_a)) {
        if (s4_b<0 & s4_a>0) {
                schedule_event(time,t3,l4_0)
                schedule_event(time,t4,l4_1)
                schedule_event(time+td,t5,l4_1)
                }
        }

when(threshold(s5,0,s5_b,s5_a)) {
        if (s5_b<0 & s5_a>0) {
                schedule_event(time,t4,l4_0)
                schedule_event(time,t5,l4_1)
                schedule_event(time+td,t6,l4_1)
                }
        }

}
```

D.12 Limiting Function with Constant
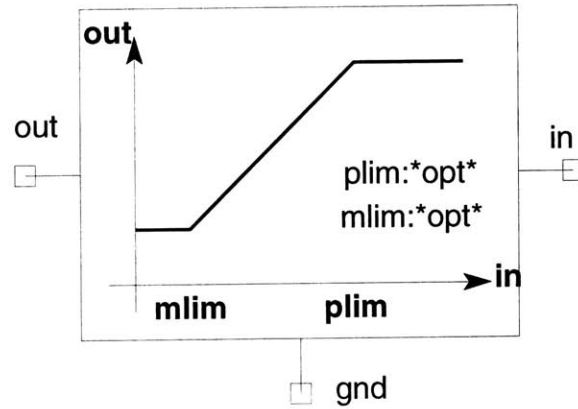

```
######################################################################
#       Limiting function with upper and lower limits as constants
#
#       Vahe Caliskan, MIT
#       Created:  May 19, 1998
#       Copying/electronic transfer of this code is strictly prohibited.
######################################################################


element template limiter in out gnd = plim, mlim


electrical       in,            # input voltage
                 out,           # output voltage
                 gnd            # ground (reference)



number           plim=0.99,     # positive saturation limit
                 mlim=0.01      # negative saturation limit



{

# Branch current, voltage relationships
branch iout=i(out->gnd), vout=v(out,gnd)


val nu vin1                     # vac1 = v(a,p)-v(c,p)
val nu vout1                    # vap1 = v(a,p)
```

```
values {

        vin1 = v(in) − v(gnd)
        if (vin1 >= mlim & vin1 <= plim) vout1 = vin1
        else if (vin1 > plim)  vout1 =  plim
        else if (vin1 < mlim)  vout1 =  mlim


        }

equations     {
              iout : vout = vout1
              }
}
```

D.13   Operational Amplifier with Clipping
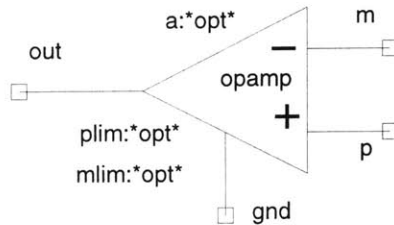

```
####################################################################
#      Operational Amplifier with clipping
#
#      Vahe Caliskan, MIT
#      Created:  May 21, 1998
#      Copying/electronic transfer of this code is strictly prohibited.
####################################################################


element template opamp p m out gnd = plim, mlim, a

electrical      p,             # (+) voltage with respect to gnd
                m,             # (−) voltage with respect to gnd
                out,           # output voltage
                gnd            # ground (reference)


number          a=2e5,         # dc gain
                plim=14,       # positive saturation limit
                mlim=−14       # negative saturation limit


{

# Branch current, voltage relationships
branch iout=i(out−>gnd), vout=v(out,gnd)

val nu vin             # vin = v(p) − v(m)
val nu vout1           # vout1 = a*vin
val nu vout2           # vout2 = limit(vout1,−14,14)

values {

        vin = v(p) − v(m)
        vout1 = a*vin
        if (vout1 >= mlim & vout1 <= plim) vout2 = vout1
```

```
        else if (vout1 > plim)  vout2 =  plim
        else if (vout1 < mlim)  vout2 =  mlim


    }



equations    {
             iout : vout = vout2
             }
}
```

D.14   Operational Amplifier with Clipping and Single-Pole Roloff
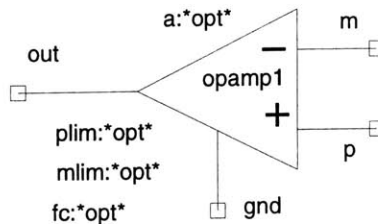

```
#####################################################################
#       Operational Amplifier with clipping & single pole roloff
#
#       Vahe Caliskan, MIT
#       Created:  May 22, 1998
#       Copying/electronic transfer of this code is strictly prohibited.
#####################################################################

element template opamp1 p m out gnd = plim, mlim, a, fc

electrical     p,            # (+) voltage with respect to gnd
               m,            # (−) voltage with respect to gnd
               out,          # output voltage
               gnd           # ground (reference)

number         a=2e5,        # dc gain
               plim=14,      # positive saturation limit
               mlim=−14,     # negative saturation limit
               fc=10         # corner frequency of gain (Hz)
{

<consts.sin

number         wc,           # corner frequency (rad/s)
               rc=10k,       # resistance for single pole roloff (arbitrary)
               cc,           # capacitance for single pole roloff
               vc0=0         # initial value of integrating capacitor

val nu  vin                  # vin = v(p) − v(m)
var nu  vc
val nu  vout1                # vout1 = limit(vc,−14,14)
```

Branch current, voltage relationships
branch iout=i(out−>gnd), vout=v(out,gnd)

```
parameters    {
              wc = 2*math_pi*fc
              cc = 1/(wc*rc)
              }
```

values {

```
        vin = v(p) − v(m)
        if (vc >= mlim & vc <= plim) vout1 = vc
        else if (vc > plim)   vout1 = plim
        else if (vc < mlim)   vout1 = mlim


        }
```

```
control_section {
              initial_condition(vc,vc0)
              }
```

```
equations     {
              iout : vout = vout1
              vc: d_by_dt(vc) = a*vin/(rc*cc) − vc/(rc*cc)
              }
}
```

D.15   Three-Phase Full-Bridge Rectifier
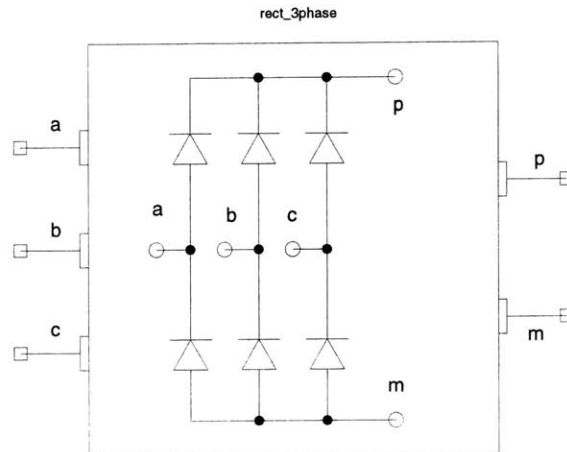

```
####################################################################
#       Three-phase full-bridge rectifier
#
#       Vahe Caliskan, MIT
#       Created:  November 2, 1997
#       Copying/electronic transfer of this code is strictly prohibited.
####################################################################


template rect_3phase a b c p m

electrical       a,      # phase a input
                 b,      # phase b input
                 c,      # phase c input
                 p,      # positive electrical terminal (alt bp) -> v(bp,bm)
                 m       # negative electrical terminal

{
d.ap a p  = model = (is=2e-15, rs=0.01m, cjo=2p, tt=1u)
d.am m a  = model = (is=2e-15, rs=0.01m, cjo=2p, tt=1u)
d.bp b p  = model = (is=2e-15, rs=0.01m, cjo=2p, tt=1u)
d.bm m b  = model = (is=2e-15, rs=0.01m, cjo=2p, tt=1u)
d.cp c p  = model = (is=2e-15, rs=0.01m, cjo=2p, tt=1u)
d.cm m c  = model = (is=2e-15, rs=0.01m, cjo=2p, tt=1u)
r.floata a 0 = rnom=1meg
r.floatb b 0 = rnom=1meg
r.floatc c 0 = rnom=1meg
}
```

D.16 Three-Phase Full-Bridge Rectifier with Booster Diodes

rect_3phase_neutral
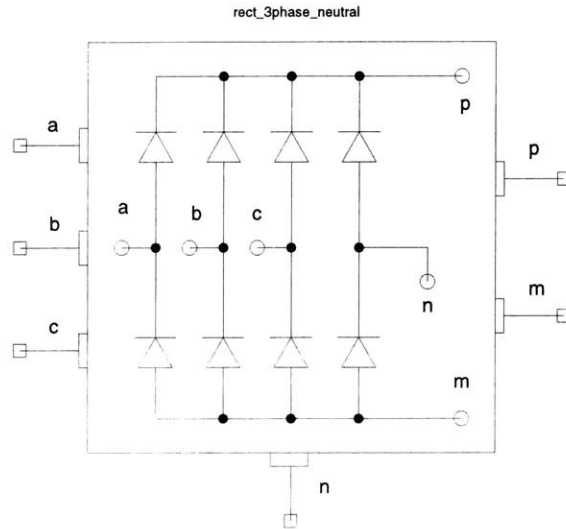
```
######################################################################
#       Three−phase full−bridge rectifier with booster diodes
#
#       Vahe Caliskan, MIT
#       Created:  May 18, 2000
#       Copying/electronic transfer of this code is strictly prohibited.
######################################################################


template rect_3phase_neutral a b c n p m


electrical      a,      # phase a input
                b,      # phase b input
                c,      # phase c input
                n,      # neutral
                p,      # positive electrical terminal (alt bp) −> v(bp,bm)
                m       # negative electrical terminal


{

# diode bridge
d.ap a p  = model = (is=2e−15, rs=0.01m, cjo=2p, tt=1u)
d.am m a  = model = (is=2e−15, rs=0.01m, cjo=2p, tt=1u)
d.bp b p  = model = (is=2e−15, rs=0.01m, cjo=2p, tt=1u)
d.bm m b  = model = (is=2e−15, rs=0.01m, cjo=2p, tt=1u)
d.cp c p  = model = (is=2e−15, rs=0.01m, cjo=2p, tt=1u)
d.cm m c  = model = (is=2e−15, rs=0.01m, cjo=2p, tt=1u)
```

```
# booster diodes
d.np n p  = model = (is=2e−15, rs=0.01m, cjo=2p, tt=1u)
d.mn m n  = model = (is=2e−15, rs=0.01m, cjo=2p, tt=1u)

# floating resistors for convergence
r.floata a 0 = rnom=1meg
r.floatb b 0 = rnom=1meg
r.floatc c 0 = rnom=1meg


}
```

Appendix E

Matlab Scripts

This appendix presents the Matlab scripts that were used to perform numerical calculations and generate plots. The scripts given here have been tested and are known to run successfully on a Sun Ultra Sparc 10 workstation with 512 MB of RAM running Solaris 2.6 and Matlab version 5.3.1.

The following is a list of the Matlab scripts given in this appendix:

1. Drive Cycle Simulation

2. Dual-Controlled Alternator Characteristics

3. Dual-Controlled Alternator Experimental Results

E.1   Drive Cycle Simulation

```
% Drive Cycle simulation (produces alternator rpm given drive cycle)
% Vahe Caliskan, MIT
% June 1, 1997


% Define some useful constants
% Constant          Units            Description
% —————            ———             ————————
Cd  = 0.3;     %    unitless         coefficient of air friction
Ac  = 1.85;    %    m^2              frontal cross-sectional area of vehicle
rho = 1.29;    %    kg/m^3           density of air
m   = 1300;    %    kg               mass of vehicle
Rr  = 0.012;   %    unitless         coefficient of static friction of tires
g   = 9.81;    %    m/s^2            acceleration due to gravity
d   = 0.65;    %    m                tire diameter
r   = d/2;     %    m                tire radius
g1  = 4.2;     %    unitless         first gear ratio
g2  = 2.4;     %    unitless         second gear ratio
g3  = 1.5;     %    unitless         third gear ratio
g4  = 1.0;     %    unitless         fourth gear ratio
g5  = 0.8;     %    unitless         fifth gear ratio
gd  = 2.8;     %    unitless         differential gear ratio
gea = 3.0;     %    unitless         engine-alternator gear ratio
eid = 600.0;   %    rpm (rev/min)    engine idle rpm


% Drive cycle: choose from ftp72, ftp75, 1_3mix, nefz (by uncommenting appropriate line)
% (time (s), velocity (km/hr)) data will be stored in variable named 'x'
% All of these drive cycles report velocity for delta_t = 1 second
%
% Drive Cycle  Description                        Duration (s)  v_avg (km/hr)  distance (m)
% —————        ——————————                        ————          ——————         ——————
ftp72          % FTP72 (Federal Test Procedure)   1371          31.4657        11992
% ftp75        % FTP75 (Federal Test Procedure)   2477          25.8193
% mix1_3       % Artificial Drive Cycle           1103          39.7009
% nefz         % New European Drive Cycle         1219          32.4979


% define time variable t (seconds) and the constant time increment delta_t (seconds)
t = x(:,1);
delta_t = 1.0;


% define velocity variable v (m/s) and define v_kmh and v_mph for later reference
v_kmh = x(:,2);
v_mph = v_kmh * 0.6212;
v = (10/36) * x(:,2);
```

```
% Calculate acceleration of vehicle a (m/s^2)
at(1) = 0;
        for i=2:size(v,1),
                at(i) = (v(i) - v(i-1)) / delta_t;
        end


% Make 'at' a column vector
a = at';


% Determine if car is accelerating (acc), decelerating (dec) at constant speed or at rest (rest)
for i=1:size(v,1),
        if a(i) > 0
                acc1(i) = 1;
                dec1(i) = 0;
                rest1(i) = 0;
        elseif a(i) < 0
                dec1(i) = 1;
                acc1(i) = 0;
                rest1(i) = 0;
        elseif a(i) == 0
                rest1(i) = 1;
                dec1(i) = 0;
                acc1(i) = 0;
        end
end


% create column vectors for acc, dec, and rest
acc = acc1'; dec = dec1'; rest = rest1';


% Force generated by static friction of tires (rolling resistance)
Froll = Rr * m * g * ones(size(v,1),1);


% Force due to air resistance (drag)
Fdrag = 0.5 * Cd * Ac * rho * v.^2;


% Force of moving vehicle due to acceleration
Facc  = m * a;


% Total force that is developed by the engine (Fe) at the wheels to accelerate the vehicle (Facc), overcome
% rolling resistance (Froll) and air drag (Fdrag)
Fe = Facc + Fdrag + Froll;


% Form a gear ratio vector g
g = [g1 g2 g3 g4 g5]';
```

```
% Calculate tire rpm (revolutions per minute) from road speed (v)
t_rpm = v * 60.0 / (pi*d) ;


% Calculate the transmission gear ratio 'gt' based on the current speed. This is a bit crude. gtt=gt'
for i=1:size(v,1),
        if v_kmh(i) >= 0 & v_kmh(i) < 15
                gtt(i) = g(1);
        elseif v_kmh(i) >= 15 & v_kmh(i) < 40
                gtt(i) = g(2);
        elseif v_kmh(i) >= 40 & v_kmh(i) < 55
                gtt(i) = g(3);
        elseif v_kmh(i) >= 55 & v_kmh(i) < 80
                gtt(i) = g(4);
        elseif v_kmh(i) >=80
                gtt(i) = g(5);
        end
end


% make gtt a column vector
gt = gtt';


% Calculate engine rpm based ontransmission gear ratio 'gt'
% the differential gear ratio 'gd' and the tire rpm 't_rpm'. If car is stopped (t_rpm==0), e_rpm = eid.
e_rpm1 = gd .* t_rpm .* gt ;
for i=1:size(v,1),
        if e_rpm1(i) <= eid
                e_rpm(i) = eid;
                else
                e_rpm(i) = e_rpm1(i) ;
        end
end
% Calculate alternator rpm based on engine rpm 'e_rpm' and engine-alternator
% gear ratio 'gea'
alt_rpm = gea .* e_rpm;


% engine torque tau_e
for i=1:size(v,1),
        tau_e(i) = ( Fe(i) * r ) / ( gd * gt(i) ) ;
end


% alternator torque tau_a
tau_a = tau_e / gea;
```

E.2   Dual-Controlled Alternator Characteristics

% Matlab script to produce plots for dual-controlled alternator
% based on the averaged model in PESC '99 paper
% Vahe Caliskan, MIT
% February 2, 2000

% Alternator parameters

```
scale = 1;                      % scale=1 (14V machine), scale=3 for (42V machine)
p = 12;                         % Number of poles
p2 = p/2;                       % Number of pole pairs
n0 = 1000;                      % Alternator speed at which current=0
Vo = 42;                        % Output (battery) voltage
Vd = 1;                         % Diode on-voltage
Vopp = Vd + Vo/2;               % Effective output voltage
Rs = (33e-3)*scale^2;           % Stator equivalent resistance (33m)
Rf = (3.5)*scale^2;             % Field Resistance (3.5)
Ls = (135e-6)*scale^2;          % Stator equivalent inductance (180u)
Vref = 14*scale;                % reference voltage of alternator
```


```
% define sweep variables
speed1=1500:100:6000;           % speeds of interest (rpm)
kif=scale*9e-3*ones(size(speed1,2),1);


Vxrange = [15 42 50];           % [14V machine]alt. output voltages of interest (V)
%Vxrange = 30:1:150;            % [42V machine]alt. output voltages of interest (V)



for kk=1:1:size(speed1,2),
            nn(kk) = speed1(kk);        % Alternator Drive speed (rpm)
        for mm=1:1:size(Vxrange,2),
            % 42V output
            if mm==2
                if -0.238*(nn(kk)/1000)+1.0713 > 1
                        duty(mm,kk)=1;
                elseif -0.238*(nn(kk)/1000)+1.0713 < 0
                        duty(mm,kk)=0;
                else
                        duty(mm,kk)=-0.238*(nn(kk)/1000)+1.0713;
                end

            % 50V output
            elseif mm==3
                if -0.2*(nn(kk)/1000)+1.06 > 1
                        duty(mm,kk)=1;
```

```
                    elseif  −0.2*(nn(kk)/1000)+1.06 < 0
                            duty(mm,kk)=0;
                    else
                            duty(mm,kk)=−0.2*(nn(kk)/1000)+1.06;
                    end


            % 14V output
            else
                    duty(mm,kk)=0;
            end
        end
end


factor = 1−duty;


for k=1:1:size(speed1,2),


        n(k) = speed1(k);           % Alternator Drive speed (rpm)
        Xs(k) = (pi/30)*n(k)*p2*Ls;  % Stator inductive reactance (function of n)
        Vs(k) = kif(k)*n(k);         % Back emf voltage peak (function of n)


        for m=1:1:size(Vxrange,2),
                Vx(m,k)= factor(m,k)*Vxrange(m);
                Vol(m,k) = 4*(Vx(m,k)/2 + Vd)/pi;


                % determine current out of alternator
                if n(k) > n0 & (Vs(k)^2 − Vol(m,k)^2)/( Vol(m,k)*Rs +...
                            sqrt(Xs(k)^2 *(Vs(k)^2 − Vol(m,k)^2) + Rs^2*Vs(k)^2) ) > 0
                        Ix(m,k) = (Vs(k)^2 − Vol(m,k)^2)/( Vol(m,k)*Rs +...
                            sqrt(Xs(k)^2 *(Vs(k)^2 − Vol(m,k)^2) + Rs^2*Vs(k)^2) );
                else
                        Ix(m,k) = 0.0;
                end
        end


end


% calculate average power out of the alternator
Palt = (3/pi) .* Ix .* Vx;


% Experimental Verification


fripple = [1.042 1.724 2.27 2.97 3.47];
speed = (5/3)*fripple*1000;
```

```
% Valt = 15V, at constant field current of 3.6A
i15 = [62 99 107.8 107.6 106.9];
v15 = [15.1 15.3 15.53 15.41 15.53];
p15 = i15 .* v15;


% Vout = 42V, at constant field current of 3.6A
i42 = [21.2 42.4 59.5 77.2 90.52];
p42 = 42 .* i42;


% Vout = 50V, at constant field current of 3.6A
i50 = [17.7 35 48 63.5 79];
p50 = 50 .* i50;


% Plot power out of alternator Palt vs. output voltage Vx with alt. speed as a parameter
figure(1);
plot(speed1,Palt(1,:),'g',speed1,Palt(2,:),'b',speed1,Palt(3,:),'r'),grid


figure(2);
% includes experimental data
plot(speed1,Palt(1,:),'g',speed1,Palt(2,:),'b',speed1,Palt(3,:),'r',...
        speed,p15,'gx--',speed,p42,'bx--',speed,p50,'rx--'),grid
```

E.3   Dual-Controlled Alternator Experimental Results

```
% Matlab script to produce plots for dual-controlled alternator
% based on the averaged model in PESC '99 paper
% December 14, 2000


% Alternator parameters
p = 12;                            % Number of poles
p2 = p/2;                          % Number of pole pairs
n0 = 1000;                         % Alternator speed at which current=0
Vo = 42;                           % Output (battery) voltage
Vd = 1;                            % Diode on-voltage
Vopp = Vd + Vo/2;                  % Effective output voltage
Rs = 33e-3;                        % Stator equivalent resistance (33m)
Rf = 3.5;                          % Field Resistance (3.5)
Ls = 135e-6;                       % Stator equivalent inductance (180u)
Vref = 14;                         % reference voltage of alternator
kif = [9e-3 9e-3 9e-3 9e-3 9e-3];  % kif = (Vref + 2*Vd)*(1/n0);
                                   % Speed voltage constant with En = kif*n


% define sweep variables
speed1 = [1800 3000 4000 5000 6000];   % speeds of interest (rpm)
Vxrange = 10:1:55;                     % alt. output voltages of interest (V)


for k=1:1:size(speed1,2),

        n(k) = speed1(k);              % Alternator Drive speed (rpm)
        Xs(k) = (pi/30)*n(k)*p2*Ls;    % Stator inductive reactance (function of n)
        Vs(k) = kif(k)*n(k);           % Back emf voltage peak (function of n)


    for m=1:1:size(Vxrange,2),
            Vx(m,k)=Vxrange(m);
            Vol(m,k) = 4*(Vx(m,k)/2 + Vd)/pi;


            % determine duty ratio
            if Vx(m,k) < Vo
                    duty(m,k) = 1 - Vx(m,k)/Vo;
            else
                    duty(m,k) = 0;
            end


            dutyp(m,k) = 1 - duty(m,k);


            % determine current out of alternator
            if n(k) > n0 & (Vs(k)^2 - Vol(m,k)^2)/( Vol(m,k)*Rs +...
```

```
                        sqrt(Xs(k)^2 *(Vs(k)^2 - Vol(m,k)^2) + Rs^2*Vs(k)^2) ) > 0
                Ix(m,k) = (Vs(k)^2 - Vol(m,k)^2)/( Vol(m,k)*Rs +...
                        sqrt(Xs(k)^2 *(Vs(k)^2 - Vol(m,k)^2) + Rs^2*Vs(k)^2) );

        else
                Ix(m,k) = 0.0;

        end

    end

end


% calculate average power out of the alternator
Palt = (3/pi) .* Ix .* Vx;


% calculate average current through the boost diode (which is delivered to the battery)
Idavg = Ix .* dutyp;


% calculate rms current going through the boost switch
Iqrms = sqrt(duty) .* Ix;


% max power, Pmax at voltage, Vmax (Vx at Pmax)
[Pmax, maxk] = max(Palt);
Vmax = Vx(maxk);


% Experimental Verification
fripple = [1.042 1.724 2.27 2.97 3.47];
speed = (5/3)*fripple*1000;


% Experimental results (exp1.m)
% Valt = 10V, at constant field current of 3.6A
ia10 = [85.4 108 108 107.4 107.2];
va10 = [10.46 10.65 10.67 10.77 10.76];
if10 = [3.6 3.6 3.6 3.6 3.6];
pa10 = ia10 .* va10;


% Valt = 15V, at constant field current of 3.6A
ia15 = [62 99 107.8 107.6 106.9];
va15 = [15.1 15.3 15.53 15.41 15.53];
if15 = [3.6 3.6 3.6 3.6 3.6];
pa15 = ia15 .* va15;


% Valt = 20V, Vfield = 12V
ia20 = [36 90 101 108.8 108.2];
va20 = [20.04 20.37 20.44 20.38 20.44];
if20 = [3.57 3.55 3.54 3.56 3.55];
pa20 = ia20 .* va20;
```

```
% Valt = 25V, Vfield = 12V
ia25 = [3.7 75.4 96.2 104.2 108.6];
va25 = [24.98 25.4 25.06 25.13 25.17];
if25 = [3.55 3.52 3.55 3.53 3.52];
pa25 = ia25 .* va25;


% Valt = 30V, starting at 3000 rpm, Vfield = 12V
ia30 = [999 56.94 84.2 95.8 101];
va30 = [999 29.7 30.08 30.16 30.17];
if30 = [999 3.44 3.44 3.42 3.40];
pa30 = ia30 .* va30;


% Valt = 35V, starting at 3000 rpm,
% Vfield = 12V for first data point at 3000rpm
% field current constant at 3.6A for all subsequent speeds
ia35 = [999 37.4 76.6 92.6 101.4];
va35 = [999 35.1 35.19 35.3 35.13];
if35 = [999 3.51 3.6 3.6 3.6];
pa35 = ia35 .* va35;


% Valt =40V, field current constant at 3.6A
% data starts at 3000rpm
ia40 = [999 16.6 60.2 84 95.7];
va40 = [999 39.99 40 40.1 39.99];
if40 = [999 3.6 3.6 3.6 3.6];
pa40 = ia40 .* va40;


% Valt =45V, field current constant at 3.6A
% data starts at 4000 rpm
ia45 = [999 999 45.4 75.4 89.6];
va45 = [999 999 45.12 45.07 45.1];
if45 = [999 999 3.6 3.6 3.6];
pa45 = ia45 .* va45;


% Valt =50V, field current constant at 3.6A
% data starts at 4000 rpm
ia50 = [999 999 31.8 65.6 83];
va50 = [999 999 50.06 49.94 50.07];
if50 = [999 999 3.6 3.6 3.6];
pa50 = ia50 .* va50;


% Valt =55V, field current constant at 3.6A
% data starts at 4000 rpm
ia55 = [999 999 13.4 53.4 75];
va55 = [999 999 54.89 54.71 54.97];
```

```
if55 = [999 999 3.6 3.6 3.6];
pa55 = ia55 .* va55;


% current/voltage/power vectors at various speeds
i1800 = [ia10(1) ia15(1) ia20(1)];
v1800 = [va10(1) va15(1) va20(1)];
p1800 = [pa10(1) pa15(1) pa20(1)];


i3000 = [ia10(2) ia15(2) ia20(2) ia25(2) ia30(2) ia35(2) ia40(2)];
v3000 = [va10(2) va15(2) va20(2) va25(2) va30(2) va35(2) va40(2)];
p3000 = [pa10(2) pa15(2) pa20(2) pa25(2) pa30(2) pa35(2) pa40(2)];


i4000 = [ia10(3) ia15(3) ia20(3) ia25(3) ia30(3) ia35(3) ia40(3) ia45(3) ia50(3) ia55(3)];
v4000 = [va10(3) va15(3) va20(3) va25(3) va30(3) va35(3) va40(3) va45(3) va50(3) va55(3)];
p4000 = [pa10(3) pa15(3) pa20(3) pa25(3) pa30(3) pa35(3) pa40(3) pa45(3) pa50(3) pa55(3)];


i5000 = [ia10(4) ia15(4) ia20(4) ia25(4) ia30(4) ia35(4) ia40(4) ia45(4) ia50(4) ia55(4)];
v5000 = [va10(4) va15(4) va20(4) va25(4) va30(4) va35(4) va40(4) va45(4) va50(4) va55(4)];
p5000 = [pa10(4) pa15(4) pa20(4) pa25(4) pa30(4) pa35(4) pa40(4) pa45(4) pa50(4) pa55(4)];


i6000 = [ia10(5) ia15(5) ia20(5) ia25(5) ia30(5) ia35(5) ia40(5) ia45(5) ia50(5) ia55(5)];
v6000 = [va10(5) va15(5) va20(5) va25(5) va30(5) va35(5) va40(5) va45(5) va50(5) va55(5)];
p6000 = [pa10(5) pa15(5) pa20(5) pa25(5) pa30(5) pa35(5) pa40(5) pa45(5) pa50(5) pa55(5)];


% calculate max power and voltage it occurs a for 1800rpm, duty for boost
[p1800max,v1800maxk]=max(p1800);
v1800max=v1800(v1800maxk);
d1800max=1 − v1800max./Vo;
d1800maxx= Vo ./ (Vo+v1800max);


% calculate max power and voltage it occurs a for 6000rpm, duty for boost
[p6000max,v6000maxk]=max(p6000);
v6000max=v6000(v6000maxk);


% make some max vectors
vmax1 = [v1800max v6000max];
pmax1 = [p1800max p6000max];


% Generate plots
% Plot power out of alternator Palt vs. output voltage Vx with alt. speed as a parameter
figure(1);
% analytical and experimental
plot(Vx,Palt(:,1),'b',Vx,Palt(:,2),'r',Vx,Palt(:,3),'g',Vx,Palt(:,4),'b',Vx,Palt(:,5),'r',...
            Vmax,Pmax,'k-',v1800,p1800,'bx--',v3000,p3000,'rx--',v4000,p4000,'gx--',...
            v5000,p5000,'bx--',v6000,p6000,'rx--',vmax1,pmax1,'k--'),
```

% analytical and experimental - no maxpaths
plot(Vx,Palt(:,1),'b',Vx,Palt(:,2),'r',Vx,Palt(:,3),'g',Vx,Palt(:,4),'b',Vx,Palt(:,5),'r',...
          v1800,p1800,'bx--',v3000,p3000,'rx--',v4000,p4000,'gx--',...
          v5000,p5000,'bx--',v6000,p6000,'rx--'),
% analytical only
plot(Vx,Palt(:,1),'b',Vx,Palt(:,2),'r',Vx,Palt(:,3),'g',Vx,Palt(:,4),'b',Vx,Palt(:,5),'r',Vmax,Pmax,'k-'),
% analytical - no max path
plot(Vx,Palt(:,1),'b',Vx,Palt(:,2),'r',Vx,Palt(:,3),'g',Vx,Palt(:,4),'b',Vx,Palt(:,5),'r'),

% Plot alternator average current Ix vs. output voltage Vx with alt. speed as a parameter
figure(2);
plot(Vx,Ix(:,1),'b',Vx,Ix(:,2),'r',Vx,Ix(:,3),'g',Vx,Ix(:,4),'c',Vx,Ix(:,5),'k'),
grid, xlabel('V_x (V)'), ylabel('I_x (W)'),
title('I_x vs. V_x for various alternator speeds at full field excitation')

% Plot the average current through the boost diode vs. duty ratio
figure(3);
plot(duty(:,1),Idavg(:,1),'b',duty(:,2),Idavg(:,2),'r',duty(:,3),Idavg(:,3),'g',...
          duty(:,4),Idavg(:,4),'c',duty(:,5),Idavg(:,5),'k'),axis([0 0.667 0 80]),
grid, xlabel('d (-)'), ylabel('I_{d,avg} (A)'),
title('I_{d,avg} vs. d for various alternator speeds at full field excitation')

% Plot the rms current through the boost switch vs. duty ratio
figure(4);
plot(duty(:,1),Iqrms(:,1),'b',duty(:,2),Iqrms(:,2),'r',duty(:,3),Iqrms(:,3),'g',...
          duty(:,4),Iqrms(:,4),'c',duty(:,5),Iqrms(:,5),'k'),axis([0 0.667 0 100]),
grid, xlabel('d (-)'), ylabel('I_{q,rms} (A)'),
title('I_{q,rms} vs. d for various alternator speeds at full field excitation')

% Plot the average current through the boost diode vs. alt. voltage Vx
figure(5);
plot(Vx(:,1),Idavg(:,1),'b',Vx(:,2),Idavg(:,2),'r',Vx(:,3),Idavg(:,3),'g',...
          Vx(:,4),Idavg(:,4),'c',Vx(:,5),Idavg(:,5),'k'),axis([14 42 0 80]),
grid, xlabel('V_x (V)'), ylabel('I_{d,avg} (A)'),
title('I_{d,avg} vs. V_x for various alternator speeds at full field excitation')

% Plot the rms current through the boost switch vs. alt. voltage Vx
figure(6);
plot(Vx(:,1),Iqrms(:,1),'b',Vx(:,2),Iqrms(:,2),'r',Vx(:,3),Iqrms(:,3),'g',...
          Vx(:,4),Iqrms(:,4),'c',Vx(:,5),Iqrms(:,5),'k'),axis([14 42 0 100]),
grid, xlabel('V_x (V)'), ylabel('I_{q,rms} (A)'),
title('I_{q,rms} vs. V_x for various alternator speeds at full field excitation')

References

[1] J.G. Kassakian, H.-C. Wolf, J.M. Miller, and C.J. Hurton, "Automotive electrical systems circa 2005," *IEEE Spectrum*, vol. 33, no. 8, pp. 22–27, August 1996.

[2] K.K. Afridi, *A Methodology for the Design and Evaluation of Advanced Automotive Electrical Power Systems*, Ph.D. thesis, Massachusetts Institute of Technology, Department of Electrical Engineering and Computer Science, February 1998.

[3] M. Naidu, N. Boules, and R. Henry, "A high-efficiency high-power-generation system for automobiles," *IEEE Transactions on Industry Applications*, vol. 33, no. 6, pp. 1535–1543, November/December 1997.

[4] J.G.W. West, "Powering up – a higher system voltage for cars," *IEE Review*, pp. 29–32, January 1989.

[5] International Electrotechnical Commission, "Impact of current passing through the human body: Part I," Tech. Rep., International Electrotechnical Commission, 1984, Report IEC 479-1.

[6] Society of Automotive Engineers, "Vehicle system voltage – initial recommendation," Tech. Rep., Society of Automotive Engineers, June 1992, Report SAE J2232.

[7] J.K. Parmerlee, "Safety of higher voltage automotive electrical systems," Tech. Rep., ARAC, February 1990, ARAC Final Report on Project I-7194.

[8] A. Kusko and J. Rennecker, "Electrical system safety issues," MIT/Industry Consortium on Automotive Electrical/Electronic Components and Systems, June 1998.

[9] W.-D. Blauensteiner, "A brief history of 42V," MIT/Industry Consortium on Automotive Electrical/Electronic Components and Systems, March 1996.

[10] R. Frank, "Replacing relays with semiconductor devices in automotive application," in *SAE Proceedings*, 1988, SAE Paper 880177.

[11] A. Marshall and K.G. Buss, "Automotive semiconductor switch technologies," in *Proceedings of IEEE Workshop on Electronic Applications in Transportation*, October 1990, pp. 68–72.

[12] A. Graf, D. Vogel, J. Gantioler, and F. Klotz, "Intelligent power semiconductors for future automotive electrical system," in *Elektronik im Kraftfahrzeug (In-Car Electronics)*, June 1997.

[13] G. Kobe, "The 42-V revolution," *Automotive Industries*, pp. 30–33, August 1998.

[14] Daimler-Benz, "Draft specifications of a dual voltage vehicle electrical power system 42V/14V," MIT/Industry Consortium on Automotive Electrical/Electronic Components and Systems, March 1997.

[15] M. Zhu, "Design of feedforward active ripple filters for power converters," M.Eng. thesis, Massachusetts Institute of Technology, Department of Electrical Engineering and Computer Science, May 1999.

[16] T.C. Neugebauer, "Computer-aided design and optimization of dc/dc power converters," S.M. thesis, Massachusetts Institute of Technology, Department of Electrical Engineering and Computer Science, September 1999.

[17] Analogy Inc., *Guide To Writing Templates*, version 4.1 edition, October 1996.

[18] J.C. Byrum, "Comparative evaluation of dual-voltage automotive alternators," S.M. thesis, Massachusetts Institute of Technology, Department of Electrical Engineering and Computer Science, September 2000.

[19] H. Broeck, G. Henneberger, and M. Frister, "Fahrzeugbordnetzsystem," June 1989, German Patent DE 3743316A1.

[20] K. Mashino, S. Tezuka, T. Futami, and Y. Nakajima, "Electric power supply system for automobile," May 1990, European Patent 0370468A1.

[21] Y. Mori, K. Mashino, and A. Saitou, "Power supply device for vehicle," July 1990, European Patent 0379357A2.

[22] J.V. Hellmann and R.J. Sandel, "Dual/high voltage vehicle electrical systems," in *SAE Future Transportation Technology Conference and Exposition*, Portland, OR, August 1991, SAE paper 911652.

[23] G.A. Williams and M.J. Holt, "The future of vehicle electrical power systems and their impact on system design," in *SAE Future Transportation Technology Conference and Exposition*, Portland, OR, August 1991, SAE paper 911653.

[24] H. Harer, G. Henneberger, and J.D. VanWyk, "Power supply circuit for motor vehicles," December 1992, US Patent 5175439.

[25] K.K. Afridi, R.D. Tabors, and J.G. Kassakian, "Alternative electrical distribution system architectures for automobiles," in *IEEE Workshop on Power Electronics in Transportation*, October 1994, pp. 33–38.

[26] A. Williams, J. Smith, H. Evans, J. Scholfield, and J. Elvidge, "Advanced electrical architecture vehicle development," *Automotive Engineering*, pp. 101–105, February 1995.

[27] M.F. Matouka, "Design considerations for higher voltage automotive electrical systems," in *SAE Future Transportation Technology Conference and Exposition*, August 1991, SAE paper 911654.

[28] C.R. Smith, "Review of heavy duty dual voltage systems," in *International Off-Highway &* *Powerplant Congress and Exposition*, September 1991, SAE paper 911857.

[29] C. Patterson, "Dual voltage alternator for automotive applications," M.S. thesis, University College Dublin, Department of Electrical and Electronic Engineering, January 1997.

[30] C. Patterson J. O'Dwyer and T. Reibe, "Dual voltage alternator," in *IEE Colloquium on Machines for Automotive Applications*, London, England, November 1996.

[31] J. Becker, M. Pourkermani, and E. Saraie, "Dual-voltage alternators," in *International Truck and Bus Meeting and Exposition*, November 1992, SAE paper 922488.

[32] O.H. Schade, "Analysis of rectifier operation," *Proceedings of IRE*, vol. 31, no. 7, pp. 341–361, July 1943.

[33] P. Richman, "Wave factors for rectifiers with capacitor input filters, and other high crest factor loads," *IEEE Transactions on Industrial Electronics and Control Instrumentation*, vol. 21, no. 4, pp. 235–241, November 1974.

[34] A.G. Bogle, "Rectifier circuit performance: some new approximate formulas," *Proceedings of IEE*, vol. 124, no. 12, pp. 1127–1134, December 1977.

[35] A. Lieders, "Single-phase rectifier circuits with CR filters, part 1 – theory," *Electronic Components and Applications*, vol. 1, no. 3, pp. 153–163, May 1979.

[36] W.P. Gibbons, "Current and voltage waveform distortion analysis on three-phase "wye" power systems with rectifier loads," *IEEE Transactions on Industry Applications*, vol. 19, no. 2, pp. 181–190, March/April 1983.

[37] K.S. Hall, "Calculation of rectifier-circuit performance," *Proceedings of IEE - Part A*, vol. 127, no. 1, pp. 54–60, January 1980.

[38] J. Schaefer, *Rectifier Circuits: Theory and Design*, Wiley, 1965.

[39] G. Seguir, *Power Electronic Converters: AC-DC Conversion*, North Oxford Academic, 1986.

[40] V. Caliskan, D.J. Perreault, T.M. Jahns, and J.G. Kassakian, "Analysis of three-phase rectifiers with constant-voltage loads," in *IEEE Power Electronics Specialists Conference*, Charleston, SC, June–July 1999, pp. 715–720.

[41] J. G. Kassakian, M. F. Schlecht, and G. C. Verghese, *Principles of Power Electronics*, Addison Wesley, 1991.

[42] Robert Bosch GmbH, *Automotive Electric/Electronic Systems*, VDI-Verlag GmbH, Düsseldorf, 1988.

[43] S. Kuppers and G. Henneberger, "Numerical procedures for the calculation and design of automotive alternators," *IEEE Transactions on Magnetics*, vol. 33, no. 2, pp. 2022–2025, March 1997.

[44] A.E. Fitzgerald, C. Kingsley, and S.D. Umans, *Electric Machinery*, McGraw-Hill, 1983.

[45] G. Henneberger and S. Kuppers, "Field calculation and dynamic simulation of a claw-pole alternator," in *International Conference on Electrical Machines and Drives*, 1995.

[46] I. Kuo, "A methodology for sizing components in a dual-voltage automotive electrical system," M.Eng. thesis, Massachusetts Institute of Technology, Department of Electrical Engineering and Computer Science, February 1999.

[47] D.J. Perreault and V. Caliskan, "Load matched alternator system," *U.S. Patent pending*, 2000.

[48] G. Venkataramanan, B. Milkovska, V. Gerez, and H. Nehrir, "Variable speed operation of permanent magnet alternator wind turbines using a single switch power converter," *Journal of Solar Energy Engineering - Transactions of the ASME*, vol. 118, no. 4, pp. 235–238, November 1996.

[49] A.R. Prasad, P.D. Ziogas, and S. Manias, "Active power factor correction technique for three-phase diode rectifiers," *IEEE Trans. Power Electronics*, vol. 6, no. 1, pp. 83–92, January 1991.

[50] E.H. Ismail and R. Erickson, "Single-switch 3ϕ PWM low harmonic rectifiers," *IEEE Trans. Power Electronics*, vol. 11, no. 2, pp. 338–346, March 1996.

[51] D.J. Perreault and V. Caliskan, "Alternator jump charging system," *U.S. Patent pending*, 2000.

[52] D.J. Perreault, T.N. Neugebauer, V. Caliskan, T.M. Jahns, and J.G. Kassakian, "Progress report on dc/dc converters for dual-voltage electrical systems," MIT/Industry Consortium on Automotive Electrical/Electronic Components and Systems, December 1997.

[53] W. Tang, F.C. Lee, and R.B. Ridley, "Small-signal modeling of average current-mode control," *IEEE Transactions on Power Electronics*, vol. 8, no. 2, pp. 112–119, April 1993.

[54] L.H. Dixon, "Average current-mode control of switching power supplies," in *Unitrode Product and Applications Handbook*, Merrimack, NH, June 1993.

[55] *Motorola TVS/Zener Device Data*, Phoenix, AZ, second edition, 1994.

[56] S. Korn, "Automobiles need transient voltage suppression," *Power Conversion & Intelligent Motion*, vol. 15, no. 2, pp. 28–31, February 1989.

[57] Robert Bosch GmbH, "Zener diodes for 42V alternator applications," http://www.bosch.de.

[58] J.M. Miller, D. Goel, D. Kaminski, H.-P. Schoner, and T.M. Jahns, "Making the case for a next generation automotive electrical system," in *IEEE–SAE International Conference on Transportation Electronics (Convergence)*, Dearborn, MI, October 1998.

[59] D.J. Perreault and V. Caliskan, "Dual output alternator system," *U.S. Patent pending*, 2000.

[60] J.G. Kassakian, "Automotive electrical systems – the power electronics market of the future," in *IEEE Applied Power Electronics Conference*, New Orleans, LA, February 2000, pp. 3–9.

[61] J.G. Kassakian, J.M. Miller, and N. Traub, "Automotive electronics power up," *IEEE Spectrum*, vol. 37, no. 5, pp. 34–39, May 2000.

[62] V. Ostovic, J.M. Miller, V.K. Garg, R.D. Schultz, and S.H. Swales, "A magnetic equivalent circuit based performance computation of a lundell alternator," *IEEE Transactions on Industry Applications*, vol. 35, no. 4, pp. 825–830, July/August 1999.

[63] J.M. Miller, "Multiple voltage electrical power distribution system for automotive applications," in *31st Intersociety Energy Conversion Engineering Conference (IECEC)*, Washington, DC, August 1996.

[64] W. T. Balogh, "Boost converter regulated alternator," *U.S. Patent 5,793,625*, August 11, 1998.